Cameron, Patrick (2024) *Shaping the spatial correlations of photon pairs for quantum imaging applications.* PhD thesis.

https://theses.gla.ac.uk/84605/

Shaping the Spatial Correlations of Photon Pairs for Quantum Imaging Applications

---

Patrick Cameron

Submitted in fulfilment of the requirements for the
Degree of Doctor of Philosophy

School of Physics and Astronomy
College of Science and Engineering
University of Glasgow

March 2024

Abstract

The field of quantum imaging exploits the quantum properties of light to surpass fundamental classical limits and to develop novel imaging modalities. For example, the use of nonclassical states of light can offer enhanced resolution, increased sensitivity, and improved noise performance compared to classical techniques. In recent years, significant advances in non-classical sources - particularly sources of photon pairs - and camera technologies have enabled many new quantum imaging schemes, primarily in the form of proof of concept experiments, but increasingly approaching real-world applications.

In parallel, light structuring techniques have strongly developed in the realm of classical imaging. Revolutionary tools, such as spatial light modulators (SLMs), allow the manipulation of the phase and amplitude of coherent light beams with extremely high precision. Shaping light with such digital holograms can, for example, enable imaging through scattering media or transforming light from one transverse spatial mode to another. Over the past few years, such tools have had a significant impact on various fields of optics, including metrology, imaging, microscopy, and communications.

This thesis investigates how the concepts of classical light shaping can be adapted and applied to improve techniques of quantum imaging with photon pairs. A theoretical framework describing such shaping is developed, and the key differences between classical and photon-pair shaping are highlighted. These concepts are then applied to the practical problem of imaging through aberrations. A novel adaptive optics method to correct for aberrations in an imaging system is demonstrated, with potential applications in classical and quantum microscopy. Beyond imaging, some applications of two-photon shaping for quantum communications are also explored.

Acknowledgements

I would first like to thank my supervisor Hugo Defienne for the invaluable guidance, support, and constant inspiration you have given me during my PhD. Thank you especially for giving me the chance to come and work with you in Paris for a year and for all of the work that involved on your part; my time there was unforgettable. I would also like to thank my secondary supervisor Daniele Faccio for giving me the opportunity to pursue this PhD in the first place.

I would like to thank all of the members of the Extreme Light research group for their friendship and for making it so enjoyable to come into work every day. I would also like to thank everyone in the Nanostructures and Optics group in Paris for making me feel so welcome during my stay there, especially to Chloé, Baptiste, Raj, and Emma. Extra thanks to Chloé and Baptiste for helping me navigate the infamous French bureaucracy, and to Raj for proofreading my thesis.

Thanks to my friends, especially to Calum and Douglas for living with me for two and a half years during my PhD and putting up with my terrible jokes. A special thanks to my dad for proofreading my thesis as well. And finally, thanks to Mum, Dad, Grace, Charlotte, and Rebecca for all of your love and support, not just during my PhD but through my whole life.

Declaration of Originality

I declare that, with the exception of Chapter 1 and Sections 2.1, 2.2, and 2.3 which contain introductory material, this thesis is the result of my own work.

I declare that this thesis does not contain work submitted for any other degree at the University of Glasgow or any other institution.

Summary of Publications

The following is a list of paper I have written or contributed to during my PhD.

- [1] Hugo Defienne, **Patrick Cameron**, Bienvenu Ndagano, Ashley Lyons, Matthew Reichert, Jixuan Zhao, Edoardo Charbon, Jason W. Fleischer, and Daniele Faccio. “Pixel super-resolution using spatially-entangled photon pairs”. Nature Communications, June 2022. DOI: 10.1038/s41467-022-31052-6
- [2] Baptiste Courme, **Patrick Cameron**, Daniele Faccio, Sylvain Gigan, and Hugo Defienne. “Manipulation and Certification of High-Dimensional Entanglement Through a Scattering Medium”. PRX Quantum, January 2023. DOI: 10.1103/PRXQuantum.4.010308
- [3] **Patrick Cameron**, Baptiste Courme, Chloé Vernière, Raj Pandya, Daniele Faccio, and Hugo Defienne. “Adaptive Optical Imaging with Entangled Photons”. Science, March 2024. DOI: 10.1126/science.adk7825
- [4] **Patrick Cameron**, Baptiste Courme, Daniele Faccio, and Hugo Defienne. “Shaping the Spatial Correlations of Entangled Photon Pairs”. Journal of Physics: Photonics, June 2024. DOI: 10.1088/2515-7647/ad50b1

Contents

List of Figures

List of Abbreviations

AO Adaptive optics.

BBO β-barium borate.

CCD Charge-coupled device.

CMOS Complementary metal oxide semiconductor.

CW Continuous wave.

DM Dichroic mirror.

EMCCD Electron-mulitplying charge-coupled device.

EPR Einstein-Podolsky-Rosen.

ETPA Entangled two-photon absorption.

FF Far field.

HOM Hong-Ou-Mandel.

ISM Image scanning microscopy.

LiDAR Light detection and ranging.

MLA Micro-lens array.

NF Near field.

NIR Near-infrared.

OAM Orbital angular momentum.

OPO Optical parametric oscillation.

PBS Polarising beam splitter.

PDMS Polydimethylsiloxane.

PMT Photo-multiplier tube.

PSF Point-spread function.

QAO Quantum-assisted adaptive optics.

QKD Quantum key distribution.

ROI Region of interest.

SAM Spin angular momentum.

SLED Superluminescent diode.

SLM Spatial light modulator.

SNR Signal-to-noise ratio.

SNSPD Superconducting nanowire single photon detector.

SPAD Single-photon avalanche diode.

SPDC Spontaneous parametric down conversion.

SSIM Structural similarity index measure.

TM Transmission matrix.

TPA Two-photon absorption.

Chapter 1

Introduction

1.1 Introduction to Quantum Imaging

Quantum imaging is the field that exploits the quantum properties of light to improve imaging techniques. The aim of this section is to introduce this topic and review the state of the art to motivate and give context to the work presented in this thesis.

1.1.1 A Brief History of Quantum Mechanics

Quantum imaging is a branch of quantum optics with pioneering experiments conducted in the 1960s-1970s. In this subsection I give some context and background for this development by summarising some of the key developments in quantum mechanics and optics from the 20th century.

At the end of the 19th century it appeared that the existing theories of physics fully described our universe and that there was little more to be discovered. Lord Kelvin, an eminent physicist from the University of Glasgow, is said to have concluded in 1897 that *“There is nothing new to be discovered in physics now. All that remains is more and more precise measurement.”* However, some problems were apparent, notably in the theory describing thermal radiation emitted by objects with non-zero temperatures. The theory, called the Rayleigh-Jeans law, predicted that the amount of emitted radiation was inversely proportional to its wavelength, suggesting the amount of radiation emitted by any object tended to infinity at short wavelengths. In 1900, Max Planck presented a mathematical remedy by suggesting that black bodies could only emit radiation in a discrete spectrum as hypothetical packets or ‘quanta’ of energy. Then, in 1905, Albert Einstein postulated that these quanta were not just a mathematical trick but real particles that we now know as photons. He demonstrated the existence of photons, i.e. the need for a quantised electromagnetic field in the description of light-matter interactions, in his work on the photoelectric effect [5] for which he won the Nobel Prize in Physics in 1921.

The photon is an indivisible particle of light whose energy E is directly proportional to its frequency ν as

$$E = h\nu, \tag{1.1}$$

where h, called Planck's constant, comes from the minimum quanta of energy of an emitter, given by Max Planck. This posed another problem however as experiments up to this point seemed to show that the wave description of light given by Maxwell's equations was also correct. Is light then made of particles or waves? It wasn't until 1923 that Louis de Broglie suggested that particles could exhibit wave-like properties, and vice-versa [6]. This idea of wave-particle duality gave birth to the field of quantum mechanics.

One of the key concepts of quantum mechanics is that of the wavefunction. This says that, until a particle is detected, its state is not determined. We can only say that it has a certain probability of being measured in a certain state. Mathematically, this is given by a probability amplitude that is described by the particle's wavefunction, usually denoted Ψ. For example, the probability P of detecting a particle at a position x is given by the square-magnitude of its probability amplitude at that position, $\Psi(x)$:

$$P(x) = |\Psi(x)|^2. \tag{1.2}$$

These amplitudes can be complex-valued functions, and the wavefunction for a given system is the solution to the Schrödinger wave equation. Another key concept of quantum mechanics is the Heisenberg uncertainty principle. This says that, for two conjugate observables such as position and momentum, the precision with which they can be known simultaneously is limited. Specifically, the product of the uncertainties in position, Δx, and momentum, Δp, is limited by

$$\Delta x \Delta p \geq \frac{\hbar}{2}, \tag{1.3}$$

where $\hbar = h/2\pi$ is the reduced Planck's constant.

By the 1930s the concept of measurements of quantum states had matured. A physical system can be represented by a complex Hilbert space $\mathcal{H}$, and the wavefunction of a state within this system is represented by an element, or vector, in this space. Measurements of observable quantities are then represented by unitary operators[1] that act on these state vectors. The action of performing a measurement is written $\hat{A}\left|\psi\right\rangle$. If $\hat{A}$ is a discrete observable, the possible measurement outcomes are given by its eigenvalues a_i, with the probability of a specific outcome given by the inner product of the corresponding eigenvector with the state:

$$P_i = |c_i|^2, \quad \text{where} \quad c_i = \left\langle a_i \middle| \psi \right\rangle. \tag{1.4}$$

---

[1] A unitary operator is defined as an operator that is equal to it's Hermitian conjugate i.e. complex conjugate transpose. $\hat{A}$ is unitary if $\hat{A}^\dagger = (\hat{A}^*)^T = \hat{A}$

The notation $\langle f| = (|f\rangle^*)^T$. As it turns out, the state $|\psi\rangle$ can be written as a linear combination of these eigenstates:

$$|\psi\rangle = \sum_i c_i \, |a_i\rangle \, . \tag{1.5}$$

The measurement of observable $\hat{A}$ 'collapses' the state onto one of the eigenstates $|a_i\rangle$. Following this, any further measurement of $\hat{A}$ will not yield a different outcome, since by definition $\hat{A} \, |a_i\rangle = a_i \, |a_i\rangle$. This can also be extended to continuous observables. A full description can be found in most quantum mechanics textbooks, for example in Refs. [7, 8].

Up to this point we have only considered states of single particles. What happens if we have a two-particle state? Since we're interested in quantum optics, I use photons as example particles. Say we're interested in a two-photon state $|\psi\rangle$ where the individual photons have states $|\phi_1\rangle$ and $|\phi_2\rangle$. A possible two-photon state could be written as

$$|\Psi\rangle = |\phi_1\rangle \otimes |\phi_2\rangle = |\phi_1, \phi_2\rangle_{12} \, , \tag{1.6}$$

where $\otimes$ denotes a tensor product and the subscript indicates which photon is in which state[2] . The state $|\Psi\rangle$ is a vector in a joint Hilbert space $\mathcal{H}_1 \otimes \mathcal{H}_2$, where $\mathcal{H}_1, \mathcal{H}_2$ are the Hilbert spaces of the individual photons. States that can be written in such a way are called separable states, since they can be separated into a product of two single-photon states. However, not all two-photon states can be written as product states. The state may also be non-separable and an interesting effect arises from this non-separability. Imagine preparing two photons in the following joint state:

$$|\psi\rangle = \frac{1}{\sqrt{2}}\big(|H, V\rangle + |V, H\rangle\big) \tag{1.7}$$

where $|H\rangle$ and $|V\rangle$ are the horizontal and vertical polarisation states, respectively. Now, if one photon is measured to have horizontal polarisation, the polarisation of the other must be vertical. The vertical and horizontal component of each photon are therefore (anti-) correlated. But these correlations are stronger than classical correlations, as they hold regardless of the measurement basis used. For example, measuring the polarisation of one photon of $|\psi\rangle$ in the diagonal-anti-diagonal basis ($|D\rangle \, , |A\rangle$) and finding it to be have polarisation $|D\rangle$ means that the other photon must also have polarisation $|D\rangle$. This is true for all measurement bases on the polarisation degree of freedom. In mathematical terms, one can express the state using the diagonal-anti-diagonal

---

[2] This subscript is often implicit, and in fact is only needed if the particles are assumed to be distinguishable. In the second quantisation formalism this is not the case, but this is not within the scope of this summary.

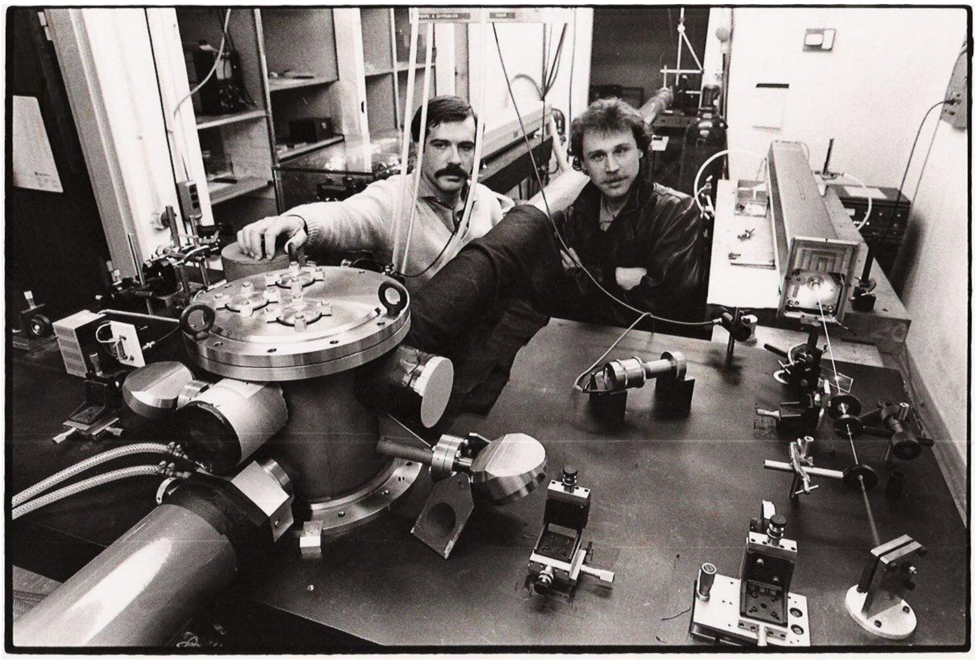

Figure 1.1: **Alain Aspect (left) in his lab in 1981.** © Collections, Ecole Polytechnique. Image taken from the Nobel Prize website (Ref. [10]).

and circular left-right bases ($|L\rangle, |R\rangle$) as:

$$|\psi\rangle = \frac{1}{\sqrt{2}}\big(|D, D\rangle - |A, A\rangle\big) \tag{1.8}$$

$$= \frac{1}{\sqrt{2}}\big(|R, R\rangle - |L, L\rangle\big) \tag{1.9}$$

Before the measurement on the first photon, the second photon was genuinely in a superposition of $|H\rangle$ and $|V\rangle$, so measuring one photon can affect the state of the other. Even if the photons are separated to opposite ends of the universe, the action of measuring one will instantaneously affect the other. This is called entanglement and it represents one of the most astonishing features of quantum mechanics and plays a significant role in quantum-based applications, including quantum imaging.

In 1935, Einstein, Podolsky and Rosen laid out the famous EPR paradox based on this phenomenon of entanglement [9]. Einstein famously did not like the non-deterministic nature of quantum mechanics, saying *"God does not play dice with the universe"*. The EPR paradox questioned the implications of quantum mechanics, suggesting that it gave an incomplete description of reality and that there are so-called hidden variables that govern the behaviour of quantum states.

Almost 30 years later in 1964, John Bell published a solution to this paradox, known as Bell's Theorem [11]. He derived a mathematical inequality that must be satisfied if a hidden-variable description of the universe is to be correct. Multiple experiments trying to violate Bell's inequality were performed in the 1980s and 1990s, with the first violation by Alain Aspect and coworkers in 1982 [12], for which he (jointly) received the 2022 Nobel Prize.

1.1.2 Quantum Imaging: The Early Years

Bell's work paved the way for investigations into the possible benefits of using entangled particles, leading to the development of many modern fields of quantum optics like quantum communications and quantum imaging. In this section, I elaborate on the pioneering experiments and developments in the field of quantum imaging, specifically those conducted between the 1980s and 2010s. Then the next section (Subsection 1.1.3) will focus on the most recent works that are directly relevant to my PhD work.

There are two elements needed for a quantum imaging experiment: a source of non-classical light, and highly sensitive light detectors that are typically capable of detecting photons one by one. While detectors in the form of photo-multiplier tubes (PMTs) were available from the 1930s, sources weren't developed until the 1960s.

Emergence of the First Non-classical Sources

The first source of entangled photons was demonstrated in 1967 using atomic cascades to generate polarisation-entangled states [13]. Especially interesting for this thesis is the first observation of photon pairs generated with spontaneous parametric down conversion (SPDC) in 1970 [14]. SPDC is a nonlinear process that converts one pump photon into two lower energy photons which, by convention, are called the signal and idler photons. I go in to much more detail about SPDC in Section 2.1. SPDC has become ubiquitous in quantum optics, and all of the experiments described in this thesis use it as a photon pair source.

In the '80s, SPDC and other non-linear processes such as four-wave mixing were also used to generate another type of non-classical light called squeezed light [15]. In squeezed states of light, the photons are not described by the Poisson statistics that govern laser light, and instead follow so-called sub-Poissonian statistics. The wavefunction of an optical state can be described in terms of quadratures of the electromagnetic field: $\hat{X}$ represents the amplitude quadrature of the field in a specific mode and $\hat{Y}$ represents the phase quadrature. The quadrature variances obey Heisenberg's uncertainty relation:

$$\Delta^2 X \Delta^2 Y \geq \frac{1}{16}, \tag{1.10}$$

with Δ^2 representing the variance. For a coherent state i.e. laser light, we have symmetric variance, i.e. $\Delta^2 X = \Delta^2 Y = 1/4$. However, if we are not interested in the phase, for example, we can decrease the amplitude variance $\Delta^2 X$ at the cost of increasing $\Delta^2 Y$. This is called squeezing,

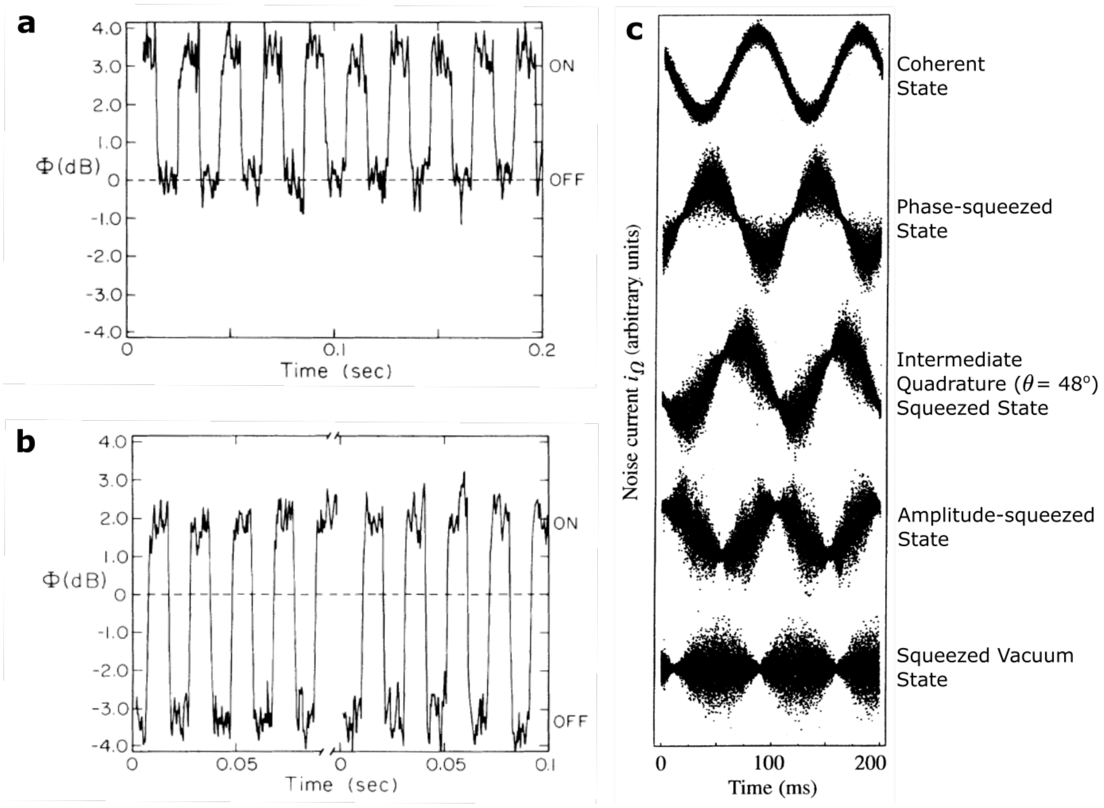

Figure 1.2: **Examples of measurements with non-classical light. a,b,** Example of sub-shot noise sensitivity in an interferometric phase measurement. A relative phase in one arm of the interferometer is induced with a phase modulator gated with an on-off signal at 50 Hz. Φ is the level of fluctuations of the difference photocurrent between two photo-detectors at each output port of the interferometer. **a,** Time trace with vacuum-state input in the interferometer. **b,** Time trace with a squeezed state input in the interferometer, with an improvement of 3 dB in signal-to-noise ratio. The dashed line gives the vacuum signal with no phase modulation and no squeezed light input. **a** and **b** reprinted with permission from Ref. [17]. Copyright 1987 by the American Physical Society. **c,** Noise plots for various types of squeezed states. The points of minimum noise (i.e. variance) depend on the quadrature that is squeezed. **c** reprinted with permission from Ref. [18]. Copyright 1997 by Springer Nature.

and it can be used to reduce the shot noise in a given quadrature. For example, optical parametric oscillation (OPO), where the parametric down-conversion process takes place inside a cavity, is an efficient experimental way to generate squeezed states of amplitude or phase [16].

Sub-shot-noise Imaging with Squeezed Light

The interest in squeezed states for imaging comes from their associated sub-Poissonian statistics. Indeed, when performing a measurement - even with an idealised and noiseless photo-detector - the random fluctuations due to the successive detection of photons will still introduce noise. The variance in the number of photons detected over a certain amount of time is called the shot noise, and is a fundamental limitation of classical light. For a measurement over a given time interval, the amplitude of the shot noise is proportional to the average number of photons detected

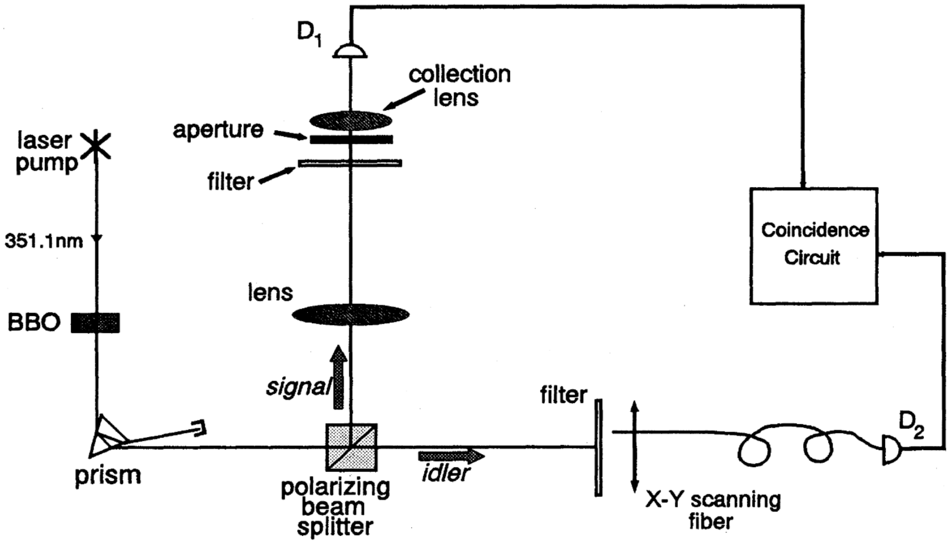

Figure 1.3: **Diagram of ghost imaging experiment from Ref. [23].** Photon pairs are generated via Type II SPDC in a BBO crystal. Signal and idler are then separated by a polarising beam splitter. Signal photon is collected by a lens and detected by D_1, erasing all spatial information. Idler photon is collected by an X-Y scanning fibre and detected by D_2. An object in the signal arm can be reconstructed by measuring coincidences between D_1 and D_2 even though photons measured at D_1 contain no spatial information about the object. Reprinted with permission from Ref. [23]. Copyright 1995 by the American Physical Society.

in that interval. Using squeezed light, it is possible to operate below this fundamental limit, which is very interesting for optical sensing and by extension optical imaging. Experiments using squeezed states demonstrated not just noise reduction but also improvements in spatial resolution [17, 19]. Following this, it was realised that this noise reduction can also be achieved with any state that has sub-Poissonian statistics, leading to similar demonstrations with single photon states [20, 21]. Examples of such experiments are shown in Figure 1.2. In fact, photon number and phase are conjugate observables [22], so single photon states are a specific type of squeezed state for which the uncertainty in photon number has been completely minimised at the expense of the phase uncertainty.

Correlation-based Quantum Imaging with Entangled Photons

The first quantum imaging experiment based on photon pairs was the demonstration of ghost imaging in 1995 [23]. In this experiment, shown in Figure 1.3, a source of position-momentum entangled photon pairs is used to illuminate an object. The object is placed in the path of one of the photons, which is measured by a single-pixel bucket detector, i.e. a detector with no spatial resolution. The other photon does not interact with the object, and is measured by a single-pixel scanning detector that can resolve spatial information. Due to the entanglement, the photons in each pair are correlated in position and momentum. If photon coincidences are measured, the spatial structure of the object can be retrieved. This is the first example of coincidence-based quantum imaging exploiting the spatial correlations of photon pairs. Ghost imaging was actually replicated, with lower contrast, by exploiting classical correlations in the early 2000s [24–26].

Improved spatial resolution is another benefit enabled by entangled photons. In the context of lithography, Boto et. al. showed theoretically that states of N photons, called Fock states, behave as if they were one photon with a wavelength N times smaller than that of the actual photons [27]. This means that the diffraction spot of an N-photon state is N times smaller than the diffraction spot of classical light with the same wavelength, which was experimentally demonstrated by d'Angelo et. al. in 2001 [28]. This effect was (relatively) recently used to achieve super-resolved imaging with photon pairs [29].

In fact, photon pair states can also be used to achieve sub shot-noise imaging. An imaging scheme based on photon pairs was proposed by Brambilla et. al. [30]. Considered individually, each photon of a pair will still exhibit shot noise. However, since the photons are correlated temporally and spatially, a differential measurement can be made to reduce the noise in an intensity measurement. Following this work, an experiment demonstrating sub-shot noise imaging was done in 2010 by Brida et. al. [31].

Imaging with Undetected Photons

Finally, imaging with undetected photons is another application of photon pair states. Normally, photons from different pairs are incoherent and do not interfere with each other. However, it is possible to make these previously incoherent photons act coherently in a phenomenon called induced coherence without induced emission.

In the original theoretical work of 1991 [33], the authors consider generating two sets of pairs by pumping two different SPDC crystals with the same coherent beam. If the idler photon from the first crystal is perfectly overlapped with the idler from the second, then the signal photons from each crystal, which were previously incoherent, become coherent and start to display interference fringes. If some of the idler photons from the first crystal are blocked before they reach the second crystal, the visibility of these fringes is reduced. Only the signal photons need to be detected to see this decrease in visibility, the idlers can be discarded. This means that, with spatially multimode pairs, an object can be illuminated by idler photons and its intensity - and, in fact, phase - can be retrieved by only detecting signal photons that never interacted with it. This is imaging with undetected photons, and was first demonstrated by the group of Anton Zeilinger, another 2022 Nobel Laureate, in the work of Lemos et. al. [32]. A diagram of an imaging with undetected photons experiment is shown in Figure 1.4. Notably, this method does not require any correlation measurements, as all of the information becomes encoded in the intensity of the signal photons. The application potential of this type of imaging scheme becomes apparent when using pairs of photons that are not degenerate in frequency. In this case it is possible to illuminate an object

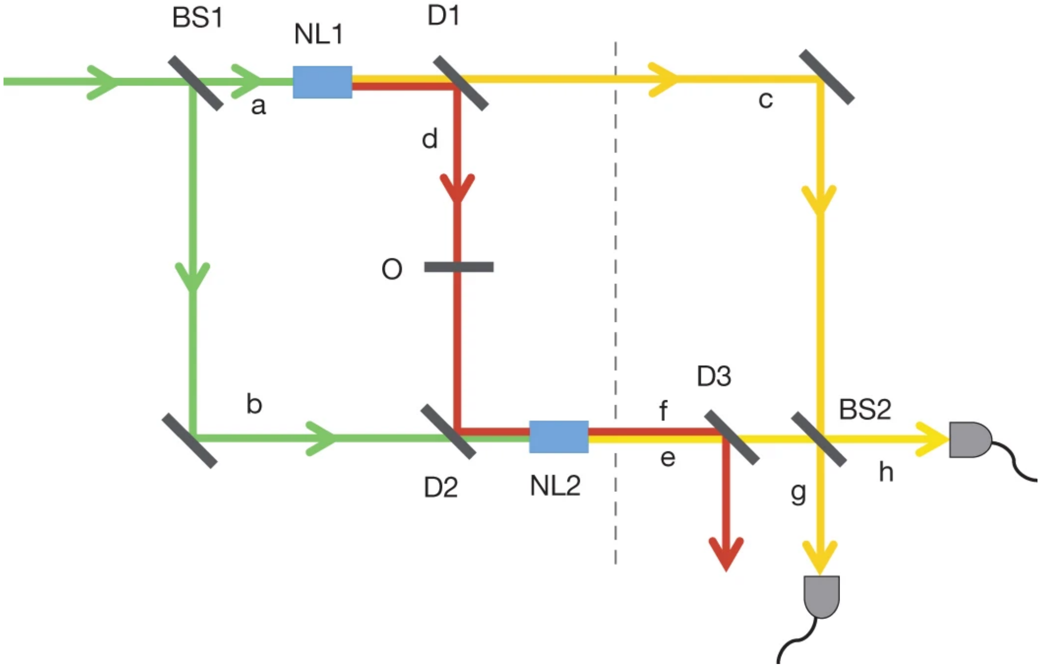

Figure 1.4: **Diagram of imaging with undetected photons experiment from [32].** The pump laser (green) is split into two beams, a and b, coherently pumping nonlinear crystals $NL1$ and $NL2$. Beam a pumps crystal $NL1$ generating pairs of signal (yellow) and idler (red) photons at different wavelengths. The same occurs at crystal $NL2$. The idler photon from $NL1$ is aligned with the idler photon from $NL2$ with dichroic mirror $D2$ so that the final idler after $NL2$ contains no information about which crystal produced the photon pair. The idler photons are then discarded. This results in interference between the two signal photon beams (c and e) when they are combined at beam splitter $BS2$. An object is placed in path d between the crystals can introduce some distinguishability between the two idler photons, resulting in a measurable difference in the interference between the signal photons. Reprinted with permission from Ref. [32]. Copyright 2014 by Nature Springer

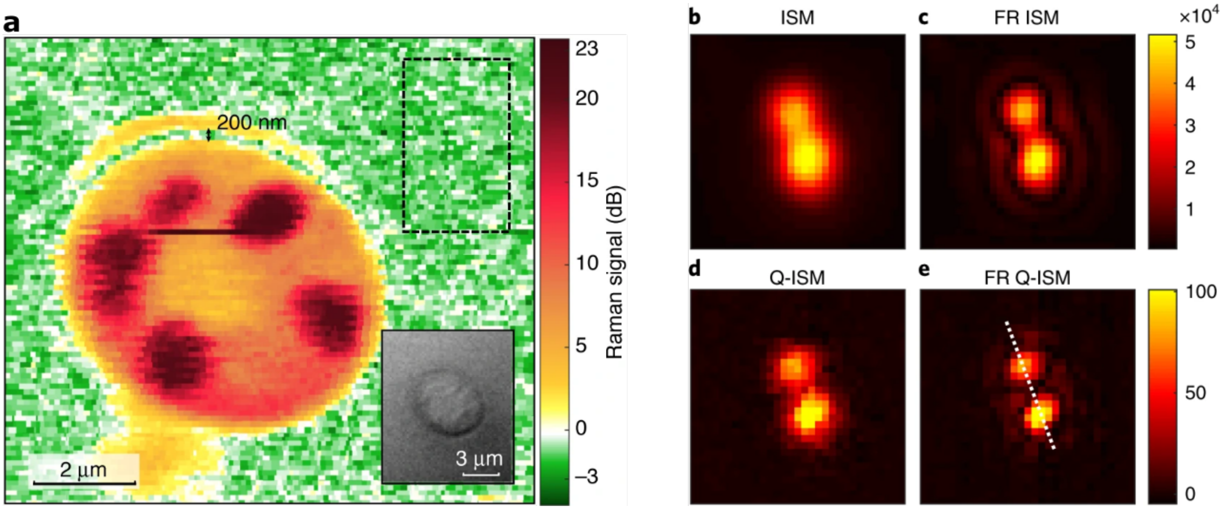

Figure 1.5: **Examples of quantum-enhanced imaging. a,** Raman-microscope image of a yeast cell. Measurement noise reduced by 1.3 dB below shot noise by using an amplitude-squeezed state for illumination, representing a 35% increase in SNR. **b-e,** Confocal scan of quantum dot emitters. **b,** Classical image scanning microscopy (ISM) image. **c,** Fourier-re-weighted classical ISM image. Colour bars of **b,c** represent detected photon counts. **d,** Super-resolved Quantum image scanning microscopy image (Q-ISM). Image retrieved by measuring the photon antibunching signal between two detectors. **d,** Fourier-re-weighted Q-ISM image. Colour bars of **d,e** represent number of missing detected photon pairs. **a** reproduced from Ref. [34] **b-e** reproduced from Ref. [35]

at a certain wavelength - for example, in the Near Infrared (NIR), which is quite challenging to detect with a camera - but to form the image at the wavelength of the other photon, typically in the visible spectrum where detection is more convenient.

1.1.3 State of of the Art

We now arrive at the present day, where the field of quantum imaging is continuing to develop and mature. In this subsection I will outline the current state of the art of the field, covering the most relevant works, and with a particular focus on correlation-based imaging with photon pairs.

Squeezed Light Imaging

As mentioned above, squeezed states of light are interesting because their statistics can be manipulated to improve the signal-to-noise ratio (SNR) of measurements. Nowadays, squeezed states are typically generated via non-linear processes such as OPO [36–38] and four-wave mixing [15, 39, 40], with squeezing up to 15 dB having been achieved via OPO [41]. Note that the increase in SNR is relative to a classical source at the same brightness i.e. increasing brightness of a classical source will always also increase the SNR. Squeezed states are interesting, then, when it is not possible to increase the brightness due to source or sample limitations.

Although it is not exactly an imaging experiment, it is worth mentioning perhaps the most famous example of enhanced measurements using squeezed states in the detection of gravitation waves at LIGO, where squeezing was used to improve sensitivity by several orders of magnitude [37, 38, 42–44]. In addition, squeezed light has been employed in cases involving photosensitive samples, such as biological imaging [45], for example in particle tracking in optical tweezers experiments [46, 47]. Raman microscopy, which operates at the samples' damage threshold, is another important technique in biological imaging [48, 49] that has also benefited from squeezed light to reduce noise [34]. Figure 1.5a shows a Raman-microscopy image whose SNR has been enhanced by using an amplitude-squeezed state for illumination from Ref. [34].

Imaging with Single-photon Emitters

Fluorescence microscopy is another technique in biological imaging that has become ubiquitous in the field. It is used to improve contrast and resolution, as well as give information about the physical and chemical properties of a sample [50]. Fluorescent dyes are based on molecules which, after being excited to a high-energy electronic state, de-excite to their ground state by emitting light. While they may not initially be thought of as 'quantum', fluorescent emitters are also a source of non-classical light. Due to the nature of the excitation and emission process, the vast majority of these emitters emits only one photon at a time, with a delay between each photon so that photons are never emitted together. If the light from such a source is sent through a beam splitter, there will be a dip in the intensity correlations detected between the two output ports when compared to the same intensity correlations of a coherent emitter[3]. This dip is called anti-bunching, and is a signature of the non-classical statistics of the emitters [52]. As such, single-photon emitters have been used in super-resolution and localisation methods involving direct anti-bunching measurements [20, 35, 53], and indirect photon-statistics-based approaches [54]. Figures 1.5b-e show a comparison between classical and anti-bunching-enhanced images from Ref. [35].

Photon-pair-based Correlation Imaging

Photon pairs are particularly interesting because their quantum correlations offer a much richer source of information than simple intensity measurements. The often-cited examples for this are the aforementioned works demonstrating sub-diffraction-limited optical resolution [27], and sub-shot-noise imaging [31], an example of which can be seen in Figure 1.6a.

Originally, photon correlations were measured by raster-scanning two single-pixel detectors and counting the coincidences between them. Now, multi-pixel cameras (see Section 2.2) are used to measure correlations. Electron-multiplying charge-coupled device (EMCCD) and, more re-

---

[3] This is called a Hanbury-Brown-Twiss experiment after the work of Hanbury-Brown and Twiss in measuring the intensity correlations in the light emitted by separate stars [51].

cently, single-photon avalanche diode (SPAD) array cameras form the basis of most modern quantum imaging detection schemes. These types of detectors are now regularly used for correlation measurements, and have been used to achieve super-resolution with photon pairs [55, 56]. An example of enhanced resolution imaging with photon pairs is shown in Figure 1.6b.

Photon pairs can also offer improved sensitivity for phase measurements if they are prepared as a N00N state. A N00N state is an N-photon state $|\phi\rangle$ that has the form

$$|\phi\rangle = |N, 0\rangle + |0, N\rangle, \tag{1.11}$$

where $|N, 0\rangle$ represents the state in which N photons are in one mode of a two-mode system, and $|0, N\rangle$ is the state in which N photons are in the other mode. These N00N states can be used to increase sensitivity in phase measurements, yielding a fundamental sensitivity increase of $\sqrt{N}$ compared to classical light [57]. Photon pairs can be prepared in the form of Equation 1.11 with $N = 2$. A number of works using photon pair states to perform phase measurements have demonstrated this improved sensitivity in recent years [1, 58–60].

Staying with the topic of phase imaging, works exploiting the Hong-Ou-Mandel (HOM) effect have also been demonstrated recently [61, 62]. The HOM effect is a quantum interference effect arising from the indistinguishable nature of quantum particles that was first demonstrated by Hong, Ou, and Mandel in 1987 [63]. If two identical bosons, e.g. photons, arrive at different input ports of a beamsplitter, their wavefunctions interfere so that they will always exit together from the same port in a phenomenon called bunching. Photon coincidences between the two output ports will drop to zero when the input photons are completely indistinguishable. Introducing some distinguishability, in the form of a group delay between the photons for example, will increase the coincidences. This change can be used to measure the relative group delay between the different photons. A phase-only object introduces such a delay which can therefore be measured using HOM interference, with up to sub-nanometre precision.

Photon pairs can allow for techniques that can surpass classical limits, but they can also enable novel methods that don't have a direct classical equivalent. A good example of this is the development of photon-pair-based holography schemes [64, 65]. Holography is the name given to techniques aiming to capture full-field information, i.e. amplitude and phase, of a light field. In classical holography a beam of light passes through a sample and is then made to interfere with a reference beam with a known phase, ϕ_{ref} [66]. The sample introduces an unknown relative phase shift ϕ_{obj} between the two beams. The measured intensity of the interfered beams is then dependent on ϕ_{obj} and ϕ_{ref}. By taking multiple intensity measurements with different, known values of ϕ_{ref}, ϕ_{obj} can be recovered through a technique called phase-shifting holography [67]. Entanglement-enabled holography [65] uses a similar principle, but now the object phase ϕ_{obj} is

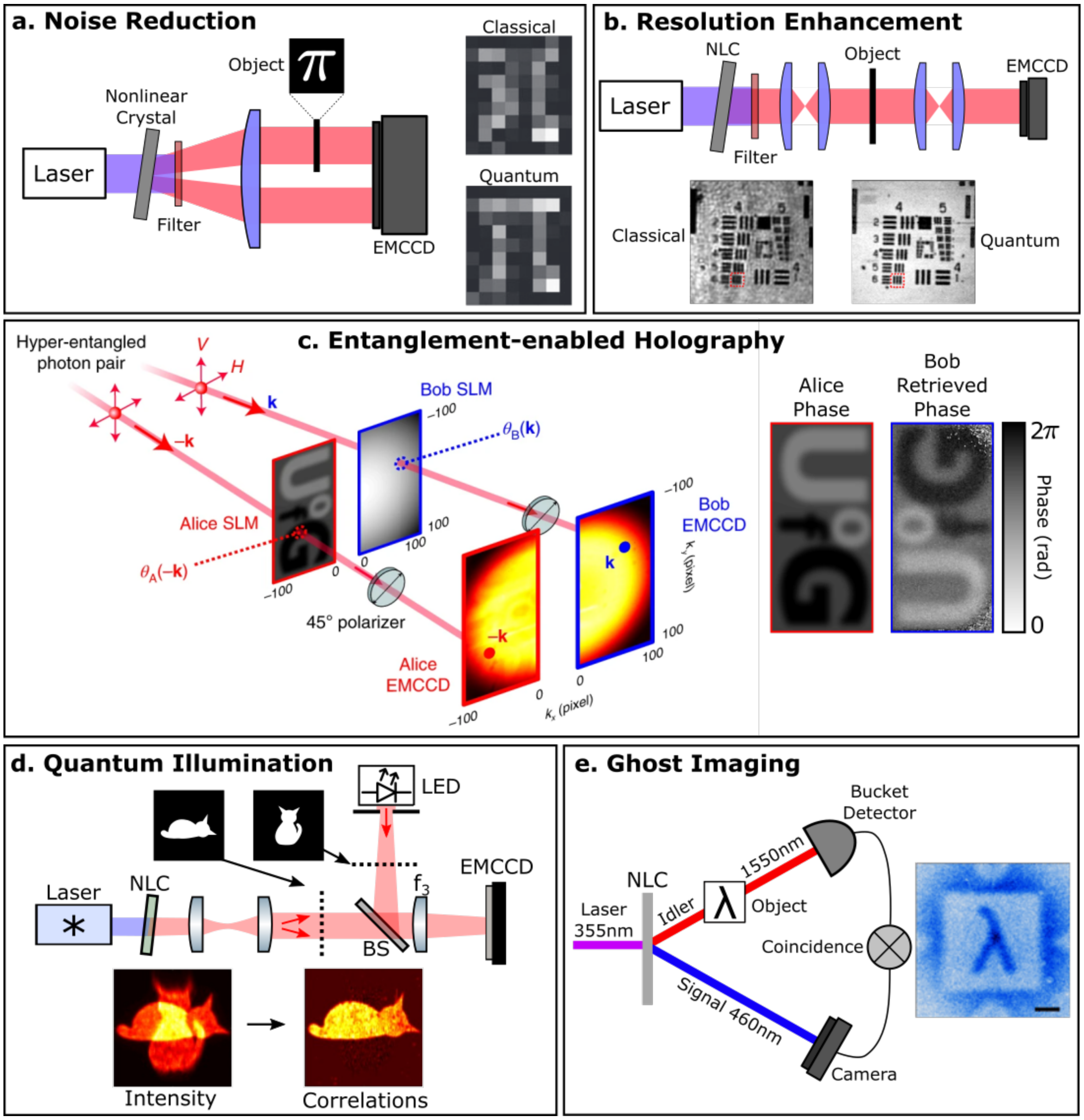

Figure 1.6: **Examples of photon-pairs-based quantum imaging schemes. a,** Sub-shot-noise imaging via photon pair correlations, reproduced from Ref [68]. **b,** Quantum-enhanced resolution via photon-pair imaging, reproduced from Ref. [55]. **c,** Entanglement-enabled holography. A phase image is encoded by Alice in the entanglement between two photons. The phase is then retrieved by Bob by measuring photon pair correlations reproduced from Ref. [65]. **d,** Non-degenerate ghost imaging, reproduced from [69]. **e,** Quantum illumination. The image of an object (sleeping cat) illuminated with photon pairs is separated from a classical background (up-right cat), reproduced from Ref. [70].

encoded as a phase in a quantum state, as

$$|\psi\rangle = \sum_k \left(|V\rangle_k |V\rangle_{-k} + e^{i\phi_{obj}(k)} |H\rangle_k |H\rangle_{-k}\right), \tag{1.12}$$

where $k, -k$ are the wavevectors of the photons in a given pair. When the pairs pass through the object, its phase is encoded as a coherent phase in the superposition of $|H\rangle$ and $|V\rangle$ states. Following this, the state is projected onto a diagonal polarisation which makes the photon pair coincidence rate proportional to the phase difference. This allows the phase to be reconstructed via a phase-shifting holographic technique. Interestingly, after the state is generated, the two beams never need to interact locally. Due to the hyper-entanglement - that is entanglement in multiple degrees of freedom - the object can be placed in one arm and the phase shifting apparatus in the other. Figure 1.6c shows an illustration of entanglement-enabled holography from Ref. [65]. In the configuration demonstrated in Ref. [65], the object must be birefringent so that only one polarisation acquires the phase, but this is not a fundamental limitation. Additionally, since the phase is encoded in the entanglement itself, this technique offers stronger robustness to noise, higher spatial resolution, and has applications in quantum state characterisation.

Entanglement-enabled holography is not the only case in which photon pairs offer more robustness to noise. Quantum illumination allows for a signal of correlated photon pairs to be extracted from a large background [71]. Photon pairs are strongly correlated in position and in time, whereas sources of background noise are not. Measuring photon correlations allows only photon pairs to be accepted as a signal, and all other photons to be rejected. This was first demonstrated with a simple proof-of-principle experiment by Lopaeva et. al. [72], and was later used to 'distil' images carried by photon pairs from a large background [70, 73]. It has since been used in quantum-enhanced target detection [74], light detection and ranging (LiDAR) [75, 76] and hidden communications [77] applications. An example of quantum image distillation is shown in Figure 1.6d.

Photon pairs have also enabled a range of other techniques, such as hyperspectral imaging, where the strong spatio-temporal correlations of the pairs are used to acquire images over very broad wavelength ranges without sacrificing spatial resolution [78]. Reconfigurable phase-contrast microscopy is another example that exploits the position-momentum correlations of pairs to enable post-acquisition control of illumination angle and field-of-view [79]. Finally, while ghost imaging is possible classically, non-degenerate ghost imaging, where the illumination and detection wavelengths are different, is a fully quantum technique [69], as is ghost imaging with entanglement-swapped photons [80]. An example of non-degenerate ghost imaging is shown in Figure 1.6e.

Whilst imaging with photon pairs clearly offers many potential advantages, there are still some major drawbacks to overcome. Bright sources of photon pairs have not yet been developed, and current sources such as SPDC have a maximum brightness in the picowatt to nanowatt range[81]. While there have been significant developments in camera technology, their speed is still the main limiting factor for acquisition times. With the most advanced cameras, a full correlation measurement will take tens of minutes and, with the more widely available cameras, acquisition times are closer to tens of hours. Due to these disadvantages, there has not yet been a practical implementation of a quantum imaging scheme.

1.2 Introduction to Light Shaping

The goal of my PhD was to apply light shaping techniques to quantum imaging. The context is still very much centred on quantum imaging, but I also include a brief summary of light shaping here. I am using light shaping as an umbrella term to cover any method that controls the amplitude or phase of a light beam for imaging or communications applications. Note that here we won't discuss techniques related to spectral and temporal shaping, as I did not use these in my PhD. This is already an extremely broad field in classical optics with a huge number of both academic and real-world applications. In this section, I will summarise these applications in classical optics, and how they have been applied to quantum optics.

1.2.1 Shaping Classical Light

Light shaping is widely used in classical imaging. Structured illumination microscopy is one example of this. The principle is to illuminate a fluorescent sample with a beam of light whose intensity profile has been tailored to achieve a higher resolution [82]. Adaptive optics (AO) is another example of light shaping applied to microscopy [83]. AO techniques correct for optical aberrations in microscope imaging systems by using controllable corrective elements like deformable mirrors and spatial light modulators (SLMs). These devices underpin most modern light shaping techniques, and a more detailed description of them can be found in Chapter 3.

AO targets relatively smooth, low-order aberrations. Wavefront shaping operates in the extreme regime of high-order scattering aberrations [84]. A scattering medium allows light to propagate through, but scrambles it so that the initial spatial structure of the light is completely lost. By measuring how the light is scrambled [85], or by optimising a focus target [86], an SLM can be used to render these normally opaque materials transparent. This shaping can also be used to optimise and control light propagation through multimode optical fibres [87], which has important applications in not only imaging but communications as well.

The techniques described thus far are all based on controlling the transverse spatial profile of scalar light fields. The topic of structured light explores the shaping of all the degrees of freedom of light, for many different applications [88]. For example, the capacity of optical fibres can be increased if information is encoded in multiple spatial modes simultaneously [89]. This technique, called mode-multiplexing, uses the fact that the modes of a system are orthogonal, so each mode effectively acts as different communications channel. States based on angular momentum, called orbital angular momentum (OAM) modes, are a particularly useful example of this mode-multiplexing.

OAM states are based on the Laguerre-Gauss transverse modes [90], which can be generated in a number of ways, for example with spiral phase plates [91, 92] or, more commonly today, SLMs [93, 94]. OAM arises from the helical wavefront of the LG modes, and is distinct from the spin angular momentum (SAM) originating from circular polarisation [95, 96]. Aside from communications, OAM has other applications such as in optical spanners to rotate particles in optical traps [95]. The polarisation of light also plays an important role in structured light. The vectorial nature of light is a rich resource for communications applications and especially quantum communications, which we will see in the following section.

1.2.2 Shaping Quantum Light

Structured Light

Structured quantum light is a relatively recent field, only emerging in the last 20 years [97], although it is well-suited to quantum optics. For example, encoding quantum information in the form of 2-dimensional polarisation entangled states, called qubits, seems the natural choice for photonic quantum communications. However, entanglement in transverse spatial modes is also possible [98], and in fact can offer many advantages over polarisation qubits. Individual photons can carry OAM, which can be used to encode information in their spatial degrees of freedom. While it is possible to use spatial-mode qubits, it turns out that higher dimensional qudit states can offer many advantages over these 2-dimensional qubits.

A key example of quantum communications that has been extended to high dimensional states is quantum key distribution (QKD). These techniques exploit entanglement to transmit cryptographic keys in such a way that they are provably secure due to the quantum no-cloning theorem [99]. QKD with high dimensional states has been demonstrated in Refs. [100–103], offering higher key rates, lower error rates, and stronger robustness to noise. All of these implementations use the concepts of structured light to encode information in the high-dimensional spatial degrees of freedom of photonic states.

Aberration and Scattering Correction

While quantum light shaping in the form of structured light has seen a lot of development in recent years, aberration and scattering correction with quantum light is still a relatively small topic.

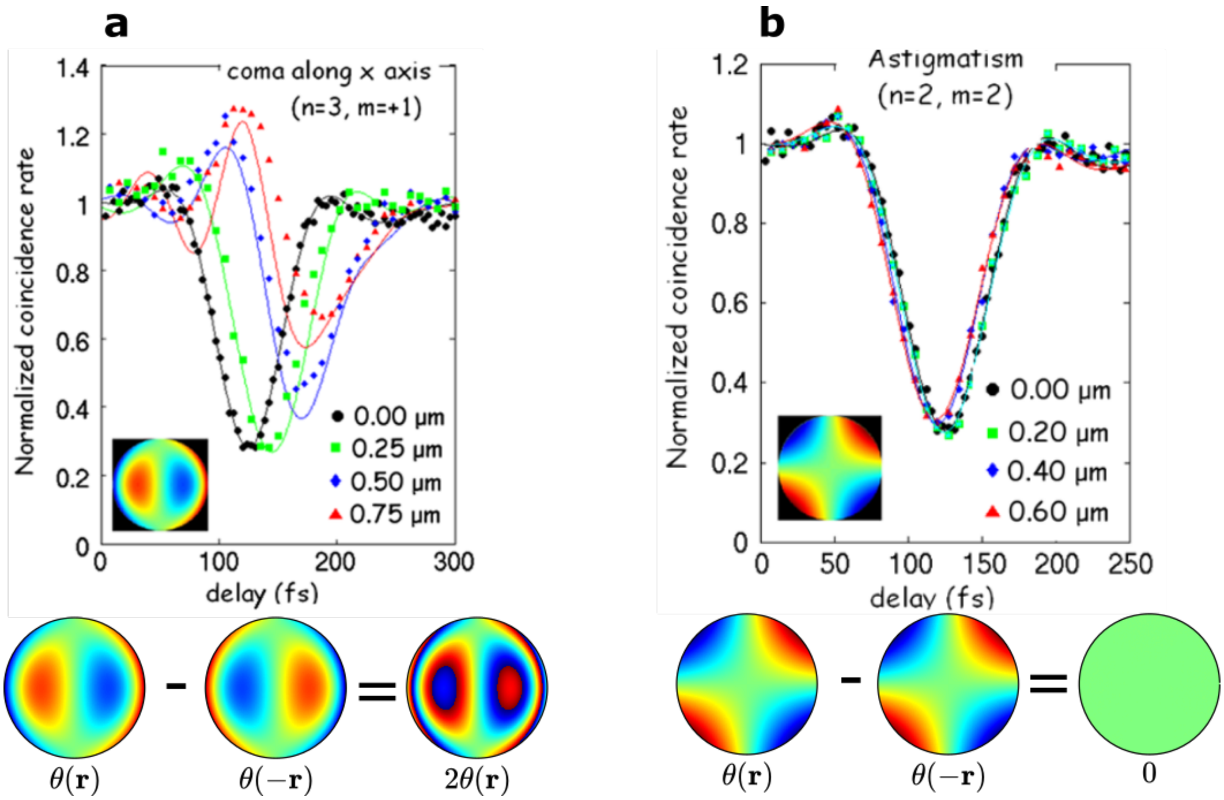

Figure 1.7: **Even order aberration cancellation with SPDC photon pairs.** Plots of coincidence rate vs relative delay in a photon pair interferometer with phase aberrations applied to one photon in each pair. **a,** With odd-order aberration (coma). **b,** With even-order aberration (astigmatism). Coincidence rate is modulated by an effective phase mask that is equal to $\theta(\mathbf{r})-\theta(-\mathbf{r})$, where θ is the aberration phase mask that is applied to one photon. This results in the even-order aberrations being cancelled out due to the rotational symmetry. Reprinted with permission from Ref. [104]. Copyright 2008 by the American Physical Society

In the context of quantum imaging, much of the work has focused on exploiting the spatial symmetries of photon pairs to passively cancel aberrations. The photon pairs generated via SPDC exhibit certain symmetries in their angular spectrum. Specifically, for a well collimated pump laser, the photons in any resulting pair must be strongly anti-correlated in their transverse momenta $\mathbf{q}$, i.e. $\mathbf{q}_{signal} = -\mathbf{q}_{idler}$. More details on SPDC can be found in Section 2.1. Due to this symmetry, photon pairs' spatial correlations are unaffected by so-called even orders of aberrations, that is aberrations that are symmetric under coordinate inversion. This cancellation effect was demonstrated for quantum interferometry experiments to negate even-order aberrations [104] and to correct for spatial dispersion effects [105], and was later demonstrated in a ghost imaging experiment [106]. This concept was extended further by manipulating the symmetries of a photon pair source [107]. The relationship is not trivial to show, but the circular symmetry in how the photons in each pair are emitted leads to a cancellation phase aberrations that are symmetric under coordinate inversion. Figure 1.7 shows an example of this even-order aberration cancellation with spatially anti-correlation photon pairs.

Aberration correction in the context of quantum communications has had more attention in recent years. Quantum communications involves transmitting entangled states over long distances. Almost all practical quantum communications protocols have to deal with distortion in the form of aberrations and scattering during the transmission. In free-space QKD, the cryptographic keys are transmitted as an entangled state through the atmosphere. The turbulence in the atmosphere can distort this signal, making it difficult to implement such a QKD scheme. However, in recent years a free-space QKD implementation was reported in Ref. [108], where the authors use an adaptive-optics approach to correct for spatial and temporal distortions.

It is also useful to transmit quantum states through multi-mode optical fibres. These fibres support multiple spatial modes, so they have a high information capacity, however they also scramble the spatial information that is transmitted through them, similarly to scattering materials. Because of this scattering behaviour of fibres, the application of wavefront shaping to photon pairs is another active area of research. By using the transmission matrix approach of Popoff et. al. [109], spatial entanglement can be recovered through a scattering layer, as demonstrated in Refs. [2, 110, 111]. Subsection 3.5.1 gives a more detailed discussion of this concept, specifically as it relates to the work reported in Ref. [2]. Finally, entangled photon pairs offer the possibility of remote aberration correction where one photon in each pair experiences the aberration, and correction is applied to the other photon. Remote cancellation of low-order aberrations was demonstrated by Black et. al. [112]. This topic is further discussed in Chapter 5.

The aforementioned works rely on knowing the transmission matrix which often involves a separate measurement using a classical source of light. This may not always be possible, which is why it is also interesting to consider the optimisation-based approach. Lib et. al. demonstrate a real-time shaping technique by optimising the SPDC pump beam that has been allowed to copropagate with the photon pairs [113]. The work of Weiss and Katz [114] highlights a slightly different approach. While they are not directly measuring photon-pair correlations, they measure the signal from a two-photon absorbing fluorescent sample. The non-linear nature of this signal allows it to be used as an optimisation target for in-situ wavefront shaping in fibre-bundle imaging.

1.3 Discussion

As we have seen, there are many potential advantages of quantum imaging. However these have not yet been translated into practical implementations. Development of sources and detectors is ongoing and is constantly yielding improvements; in the last ten years we have gone from raster scanning single pixel detectors to high-speed, high-resolution single photon sensitive cameras. A less-explored avenue to improve quantum imaging schemes is to apply the benefits of classical light shaping to quantum schemes. Shaping in the context of structured quantum light is quite a broad field, but shaping for quantum imaging is mostly unexplored.

This thesis presents a series of works that aim to fill some of this gap, bringing the concepts of adaptive optics and wavefront shaping to quantum imaging. The results presented here demonstrate improvements in quantum imaging and communications schemes, as well as potential new applications of quantum light to improve classical imaging methods.

Chapter 2

Introduction to Experimental Imaging with Photon Pairs

In this chapter I give an introduction to the experimental and technical aspects of quantum imaging. I introduce the source of photon pairs, and the detectors that one may use. I also describe how to build and run a quantum imaging experiment. Finally I use the work presented in Ref [1], to which I contributed, as a practical example of the concepts from this chapter.

2.1 Source of Photon Pairs: Spontaneous Parametric Down Conversion

All of the experimental work shown in this thesis uses spontaneous parametric down conversion as the photon-pair source. SDPC is a non-linear optical process in which a single pump photon at frequency ω_p is converted into a pair of lower energy photons[115]. These are traditionally called the signal and idler photons, at frequencies ω_s and ω_i, respectively, but it is also common to use subscripts 1 and 2 to denote them i.e. ω_1 and ω_2. Conservation of energy and momentum imposes so-called phase matching conditions so that frequency of the photons are related by

$$\omega_p = \omega_s + \omega_i, \tag{2.1}$$

and their wavevectors are related by

$$\mathbf{k}_p = \mathbf{k}_s + \mathbf{k}_i. \tag{2.2}$$

Figure 2.1 shows an illustration of these phase-matching conditions. For a plane wave in free space, the magnitude of the wavevector is $k = 2\pi/\lambda = \omega/c$ and its direction is the normal vector to the wavefront. The following explanation is based on the textbook ‘Nonlinear Optics’ by Boyd [116]. SPDC is a second-order non-linear process, so it can only take place in a material

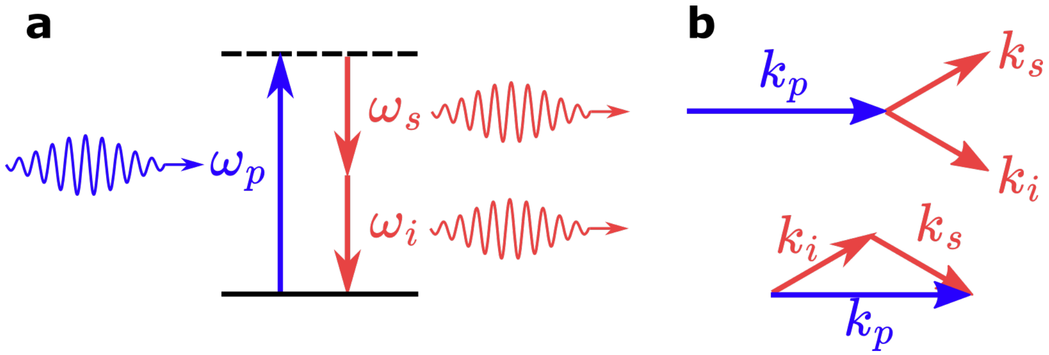

Figure 2.1: **Schematics of the SPDC process.** **a,** Energy level diagram for SPDC. A high-energy pump photon (blue) excites the material to a virtual energy level. This de-excites by spontaneously emitting two lower energy photons (red). This illustrates the energy conservation conditions of Equation 2.1 **b,** Wave-vector diagram for SPDC. A single pump photon is converted into a signal and idler photon whose momenta sum to that of the pump. This illustrates the momentum conservation conditions of Equation 2.2

with a non-zero second-order non-linear susceptibility, $\chi^{(2)}$. To understand what this means, consider an electromagnetic wave in a material. The electric field $\mathbf{E}(t)$ of this wave causes positive and negative charges in the material to become slightly separated forming a dipole moment in the material. This dipole moment is oriented in the same direction as electric field and is called the material polarisation $\mathbf{P}(t)$. From Maxwell's equations, the wave equation in such a material is then

$$\nabla^2\mathbf{E} - \frac{1}{c^2}\frac{\partial^2\mathbf{E}}{\partial t^2} = \frac{1}{\epsilon_0 c^2}\frac{\partial^2\mathbf{P}}{\partial t^2}, \tag{2.3}$$

where c is the speed of light in vacuum, and ϵ_0 is the permittivity of free space. Equation 2.3 says that the electromagnetic wave induces a wave in the material polarisation, which in turn drives more electromagnetic waves. In the general case, material polarisation will be composed of a linear and non-linear response to the electric field. It can be expressed via a Taylor series as

$$\mathbf{P}(t) = \epsilon_0\left[\chi^{(1)}\mathbf{E}(t) + \chi^{(2)}\mathbf{E}^2(t) + \chi^{(3)}\mathbf{E}^3(t) + ...\right] \tag{2.4}$$

where $\chi^{(n)}$ is known as the n^{th} order susceptibility. If only the linear susceptibility term $\chi^{(1)}$ is non-zero then $\mathbf{P}(t) = \epsilon_0\chi^{(1)}\mathbf{E}(t)$, so the polarisation is directly proportional to the electric field. However, if the material has some non-linear susceptibility ($\chi^{(n)} \neq 0, n > 1$), then the polarisation wave can contain frequencies that are not present in the original light. From Equation 2.3, the additional frequencies in $\mathbf{P}$ will drive electromagnetic waves at these frequencies. Physically, some of the incident light is converted to light at new frequencies. This describes classical non-linear processes like second-harmonic generation, and sum- and difference-frequency generation (see Boyd [116]). SPDC however, requires a quantum description of light.

A full description of the quantisation of the electromagnetic field can be found in most quantum optics textbooks, for example in Ref. [117]. In summary, the quantised electromagnetic field behaves like an harmonic oscillator with discrete modes. The creation ($\hat{a}_l^\dagger$) and annihilation ($\hat{a}_l$) operators act to add or remove a photon from these modes, where the subscript denotes the specific electromagnetic mode l. These operators act as follows:

$$\begin{aligned} \hat{a}_l^\dagger \left| vac \right\rangle &= \left| 1_l \right\rangle \\ \hat{a}_l \left| 1_l \right\rangle &= \left| vac \right\rangle , \end{aligned} \tag{2.5}$$

where $|vac\rangle$ is the vacuum state containing no photons, and $|1\rangle_l$ is the state with one photon in mode l. From Ref. [115], the interaction Hamiltonian of SPDC is then

$$\hat{H}_{SPDC} = i\hbar\kappa \left(\hat{a}_s \hat{a}_i \hat{a}_p^\dagger e^{i\mathbf{\Delta k}.\mathbf{r} - i\Delta\omega t} + \hat{a}_s^\dagger \hat{a}_i^\dagger \hat{a}_p e^{-i\mathbf{\Delta k}.\mathbf{r} + i\Delta\omega t} \right), \tag{2.6}$$

where $\hbar$ is the reduced Planck's constant, κ is a constant, $\mathbf{\Delta k} = \mathbf{k}_p - \mathbf{k}_s - \mathbf{k_i}$, $\Delta\omega = \omega_p - \omega_s - \omega_i$, and $i = \sqrt{-1}$ is the imaginary number. The second term corresponds to SPDC, with the annihilation of a photon in the pump mode and creation of photons in the signal and idler modes. The first term corresponds to the inverse process i.e sum-frequency generation. Typically we assume that the signal and idler are degenerate in frequency, so $\omega_p = 2\omega_s = 2\omega_i$. Solving for this Hamiltonian and making a first-order approximation gives

$$|\Psi\rangle \approx C_0 \left| 0_s, 0_i, N_p \right\rangle + \kappa C_1 e^{-i\mathbf{\Delta k}.\mathbf{r}} \left| 1_s, 1_i, (N-1)_p \right\rangle \tag{2.7}$$

where C_0 and C_1 are constants with $C_0 >> C_1$. The first term corresponds the case in which the pump photon simply passes through the crystal with no interaction. The second term corresponds to a pair being generated with probability proportional to $|\kappa C_1|^2$. This means that SPDC is an extremely inefficient process with the vast majority of pump photons simply passing through the crystal. The exact efficiency depends on the wavelengths of the photons and on the properties of the crystal, but photon pair generation rates are typically around 10^{-6}-10^{-7} pairs per pump photon [81]. This inefficiency is a fundamental limitation of SPDC. The pump power can only be increased so far before the first-order approximation becomes invalid and higher order terms come into play. For high enough pump powers the probability of generating two or more pairs simultaneously becomes non-negligible. In fact, due to the spontaneous nature of SPDC, it is an entirely probabilistic process and is not able to generate pairs deterministically.

SPDC is well-suited to imaging as it produces spatially multi-mode photon pair states. More specifically, the pairs generated with SPDC can exist in a large number of position and momentum modes. Due to the phase matching conditions (Equations 2.1 and 2.2), the photons in each pair are strongly correlated in their spatial (position-momentum) and temporal (time-frequency) degrees of freedom. It is these correlations that we exploit to do quantum imaging. A large number of spatial modes means there is a high capacity for encoding and transmitting spatial information, which is essential for imaging.

Practical Considerations

Here I summarise some important points to consider when using SPDC practically in an experiment. Since it occurs in a non-linear material, the refractive index of the material must be taken into account. In this case, since the pump, signal, and idler photons do not have the same polarisation, the phase matching conditions can only be satisfied if the non-linear material is birefringent, i.e. a materials whose refractive index depends on the polarisation of the light [115]. The second-order material polarisation is then

$$P_i^{(2)} = \epsilon_0 \sum_{jk} \chi_{ijk}^{(2)} E_j E_k \tag{2.8}$$

where ijk are indices denoting the orthogonal components of each field vector. For a birefringent material, $\chi^{(2)}$ is a tensor. In practice, birefringent crystals are typically used as non-linear materials, and experiments in this thesis were all done using β-barium borate (BBO) crystals. These crystals are typically cut to specific dimensions which dictate the specific phase matching that will occur. The crystal dimensions determine the relative polarisations of the photons, classified into types:

$$\begin{aligned} (\text{Type 0 } &: \mathbf{o} \rightarrow \mathbf{o} + \mathbf{o}) \\ \text{Type I } &: \mathbf{o} \rightarrow \mathbf{e} + \mathbf{e} \\ \text{Type II } &: \mathbf{o} \rightarrow \mathbf{e} + \mathbf{o}, \end{aligned} \tag{2.9}$$

where we have **pump→signal+idler**, and **o** and **e** denote ordinary and extraordinary polarisations, respectively.

Type I SPDC generates pairs whose photons have the same polarisation. This is useful for a co-propagating imaging configuration where both photons travel through the same system. Most of the works in this thesis use Type I SPDC. Type II SPDC generates pairs whose photons have orthogonal polarisations, which can be used to separate the photons. Type 0 SPDC is a slightly special case, as it occurs in engineered crystals with periodic poling such as periodically-poled potassium titanyl phosphate (ppKTP). The output polarisation state is effectively the same as Type I, however periodically-poled crystals can be longer and therefore more efficient. There is a trade-off, however, as longer crystals produce pairs with a smaller angular spectrum which is less useful for imaging.

The spatial properties of the photon pairs are determined by the width and angular spectrum of the pump, and by the length of the crystal along the optical axis. The state written in the momentum-space basis is given by

$$|\Psi\rangle = \iint_{-\infty}^{\infty} \Psi(\mathbf{k}_1, \mathbf{k}_2) \, |\mathbf{k}_1, \mathbf{k}_2\rangle \, d\mathbf{k}_1 d\mathbf{k}_2, \tag{2.10}$$

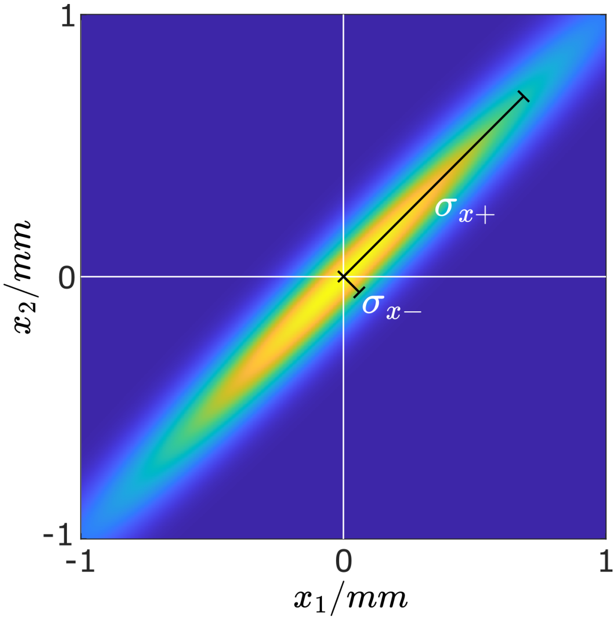

Figure 2.2: **Example of a one-dimensional position wavefunction.** Generated using the Double Gaussian approximation (Equation 2.13) with $\sigma_+ = 0.75$ and $\sigma_- = 0.1$ and $\mathbf{r}_1 = x_1, \mathbf{r}_2 = x_2$. Adapted from Ref. [118].

where $\mathbf{k}_1, \mathbf{k}_2$ are the wavevectors of photons 1 and 2, respectively. $\Psi(\mathbf{k}_1, \mathbf{k}_2)$ is the two-photon wavefunction in momentum space, which describes the joint probability density of the photon pairs. For a well-collimated pump beam, the momentum-space two photon wavefunction for SPDC is given by

$$\Psi(\mathbf{k_1}, \mathbf{k_2}) = \Psi(\mathbf{q_1}, \mathbf{q_2}) = \mathcal{N}\mathrm{sinc}\left(\frac{L_z\lambda_p}{8\pi}|\mathbf{q_1} - \mathbf{q_2}|^2\right)\exp\left(-\sigma_p^2|\mathbf{q_1} + \mathbf{q_2}|^2\right), \tag{2.11}$$

where $\mathcal{N}$ is a normalisation constant, L_z is the crystal length, λ_p is the pump wavelength, σ_p is the pump width, and $\mathbf{q_1}, \mathbf{q_2}$ are the transverse (i.e. perpendicular to the optical axis) components of the signal and idler momenta $\mathbf{k_1}, \mathbf{k_2}$, respectively [118]. The sinc term in Equation 2.11 arises from the assumption that the crystal has a rectangular shape in the z-direction and acts as the photon pair amplitude envelope. The dependence on L_z means that a short crystal will result in pairs with a broader angular spectrum than a long crystal. The Gaussian term gives the correlation width of the pairs in transverse momentum space, which is inversely proportional to the transverse spatial pump width σ_p.

For a short crystal and broad pump beam, the photon pairs are strongly correlated in the $\mathbf{q}_1 + \mathbf{q}_2$ coordinate. Physically, this means that the photons in a pair are strongly anti-correlated in transverse momentum. We can see this from conservation of momentum where Equation 2.2 also holds for transverse momenta: $\mathbf{q}_p = \mathbf{q}_1 + \mathbf{q}_2$. When the pump is well-collimated we have $\mathbf{q}_p \approx 0$ meaning the transverse signal and idler momenta must be related by $\mathbf{q}_1 \approx -\mathbf{q}_2$.

Also interesting is the state written in the position basis:

$$|\Phi\rangle = \iint_{-\infty}^{\infty} \Phi(\mathbf{r}_1, \mathbf{r}_2)\, |\mathbf{r}_1, \mathbf{r}_2\rangle\, d\mathbf{r}_2 d\mathbf{r}_2, \tag{2.12}$$

where $\mathbf{r}_1, \mathbf{r}_2$ are the position vectors of photon 1 and 2, respectively, and $\Phi(\mathbf{r}_1, \mathbf{r}_2)$ is the position-space two-photon wavefunction. Φ can be found by taking the 2-dimensional Fourier transform of Ψ. However, the sinc function in Ψ is not easily integrated, so it is typically approximated as a Gaussian function. In this so-called Double-Gaussian approximation [119], the position-space wavefunction is

$$\Phi(\mathbf{r}_1, \mathbf{r}_2) = \frac{1}{\sqrt{2\pi\sigma_{r+}\sigma_{r-}}} \exp\left(-\frac{\left(\mathbf{r}_1 + \mathbf{r}_2\right)^2}{4\sigma_{r+}^2}\right) \exp\left(-\frac{\left(\mathbf{r}_1 - \mathbf{r}_2\right)^2}{4\sigma_{r-}^2}\right), \tag{2.13}$$

where $\sigma_{r+}^2 = 2\sigma_p^2$ and $\sigma_{r_-}^2 = L_z\lambda_p/12\pi$. The first Gaussian term corresponds to the photon pair amplitude envelope, the width of which is directly proportional to the width of the pump beam. The second term gives the correlation width in the position basis, which is proportional to the crystal length. Figure 2.2 shows a simulated example of a position wavefunction for photon pairs evolving in one spatial dimension. Both photons in a pair are created at effectively the same location, dependent on the position of the pump photon that birthed them. A longer crystal introduces more uncertainty into the pump photon position, which in turn introduces more uncertainty into the so-called birth zone of the pair. This in turn translates to an increase in the transverse-position correlation width. For a full discussion, I recommend seeing the work of Schneeloch and Howell [118].

2.2 Detectors

With SPDC as the source for photon pairs, we need a way of measuring these pairs. In modern quantum imaging, single-photon-sensitive cameras are the go-to devices for this. Currently, several technologies exist, two of which are very popular. These are electron-multiplying charge-coupled device (EMCCD) and single photon avalanche diode (SPAD) based cameras, both of which I have used during my PhD.

Electron Multiplying CCD Cameras

The following information is taken from the Oxford Instruments Learning Centre [120]. A standard charge-coupled device (CCD) camera has a photo-active region that converts incident photons into charge, called photoelectrons. These photo-electrons are then moved to a layer behind the photo-active region called the storage region. This allows the next exposure of the photo-sensitive region to begin immediately, in parallel with the readout of the previous frame. From

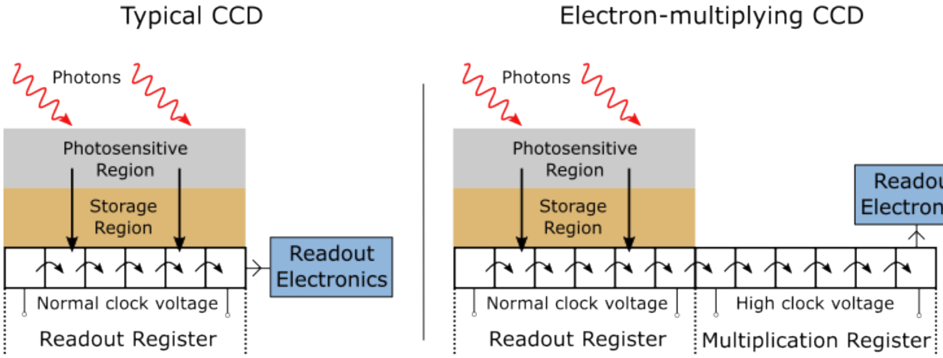

Figure 2.3: **Schematic of an EMCCD camera.** Photons incident on the sensor excite electrons in the photosensitive region which are subsequently moved back to the storage region. They are then transferred to the readout register. This is followed by the multiplication register which amplifies the signal before the readout electronics step.

the storage region the photoelectrons are trapped in potential wells. The readout process is then performed by transferring the photoelectrons along a register of these wells to the readout electronics. This is done by sending a voltage pulse along the register in a process called clocking. The charges are then amplified by a readout amplifier, which adds noise thereby reducing sensitivity. This noise can be reduced if the readout process is performed slowly but this is prohibitively slow in many cases.

EMCCD cameras circumvent this by amplifying the signal before the readout electronics. This amplification is achieved by adding a multiplication register to the electronics, as shown in Figure 2.3. A problem in CCD cameras is clock-induced charge. This comes from the photoelectrons exciting additional electrons during the clocking process. Typically this is something manufacturers try to minimise, but EMCCDs use this effect to multiply the number of photoelectrons before the readout amplifier, which greatly increases sensitivity while retaining high frame rates. A typical EMCCD has frame-rates of around 200 fps, with the fastest reaching 1000-2000 fps. Sensor sizes range range from 128×128 to 1024×1024 pixels. It should be noted that EMCCDs are not capable of performing direct coincidence measurements as they do not have the necessary timing resolution. Instead, photon pair correlations must be estimated based on statistics accumulated from a very large number of frames, as described in Ref. [121].

EMCCDs have very high quantum efficiencies at close to 80% for light at 800 nm. This means that 80% of all 800 nm photons incident on the sensor are converted into a detection signal. The main drawback of EMCCD cameras is their relatively slow speed. To measure the full spatial correlation distribution of a photon pair source typically takes $>$ 10 hours.

SPAD Cameras

SPAD cameras are based on a different technology to EMCCDs. Figure 2.4 shows the operation of a SPAD detector. A reverse bias voltage high above the breakdown voltage is applied across

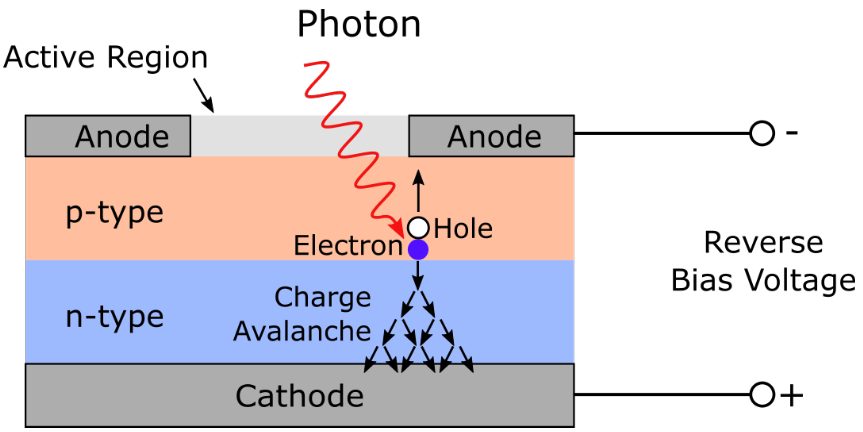

Figure 2.4: **Schematic of a SPAD detector.** A photon is absorbed, exciting an electron-hole pair. The large bias voltage across the junction causes the electron to rapidly accelerate towards the cathode. The electron has enough energy to ionise atoms in the lattice creating more free electrons. These are also accelerated towards the cathode, in turn creating more free electrons, thus causing the charge avalanche effect. This creates a voltage spike across the junction that can be read out as a detection signal.

a p-n semiconductor junction. This is an unstable configuration where any excitation causes a charge avalanche effect. A single photon incident on the detector can excite an electron-hole pair. The bias voltage causes the electron to accelerate towards the cathode. Due to the high voltage, the electron reaches a high enough energy to collide with and excite secondary electrons. These in turn are accelerated and excite more electrons, resulting in the desired avalanche effect. This generates a very fast voltage spike that can be read out. With fast enough timing electronics, SPADs are able to time-tag the arrival of photons with picosecond precision.

SPAD cameras, also called SPAD arrays, are made up many of these individual SPAD detectors, along with various readout and timing electronics. We can generally distinguish two categories of SPAD cameras: time-correlated single photon counting (TCSPC) SPAD cameras and time-gated SPAD cameras [122]. During my PhD I only used time-gated cameras so the focus here will be on them. They can be operated in different regimes depending on the application. Most devices can be operated in frame-based and time-gated modes. In the frame-based mode, each pixel is exposed simultaneously and the full sensor is read out as a frame. In this operating mode, the temporal resolution is given by the frame exposure time. The frame-based mode can be used to measure the spatial correlations of photon pairs using the method in Ref. [121] with much faster acquisition times compared with EMCCDs.

In the time-gated mode, an external pulse is used to trigger the camera. All of the pixels are then turned on for a specific duration, called the gate, and any photon that lands on the sensor during this window is detected. In this mode, the temporal resolution is given by the gate length. Time-gated mode allows for spatially resolved tagging of photons that can be used to measure photon time-of-flight for LiDAR imaging, or spatially resolved fluorescence lifetime imaging.

	Spatial Resolution	Temporal Resolution	Frame-rate	Detection Efficiency at 810nm	Pixel Fill-factor
EMCCD	High (up to 1024×1024 pixels)	Low (ms)	Low (up to 1.5 kpfs with cropped sensors)	Up to 80%	100%
SPAD	Low ($< 100 \times 100$ pixels)	High (ns or less)	High (100 kfps)	Low (<5% with MLA, <1% without)	Moderate (up to 75% with MLA, <5% without)

Table 2.1: **Comparison between EMCCD and SPAD array cameras.** MLA - microlens array.

Finally, event-based SPAD arrays are currently in development that operate in an asynchronous regime [122, 123] . Detection events are recorded as and when they occur so that, instead of a series of frames, the data is in the form of a list of pixel location and detection time i.e. (x, y, t). This is advantageous as it allows for direct, spatially resolved coincidence detection of photon pairs with no need for raster scanning or background subtraction.

SPAD array cameras with up to megapixel (1920 × 1080 pixels) resolutions have been demonstrated [124], but ready-to-use commercial devices tend to have less than 100 × 100 pixels. For example, the Hermes SPAD camera from MicroPhotonic Devices has a resolution of 32 × 64 pixels, with a maximum frame-rate of 100kpfs. A major drawback of SPAD devices is their low quantum efficiency. The pixels in most SPAD cameras have the timing and readout electronics side-by-side with their photon-detecting region. This means that only a small sub-region of each pixel can actually detect photons. This is typically less than 1% of the pixel area, but it can be improved by putting small lenses in front of each pixel to focus more light at the active region. This is called a micro-lens array (MLA). The Hermes camera has a photon detection probability of around 5% for light at 810nm.

Other Technologies

In addition to EMCCD- and SPAD-based technology, single-photon-sensitive cameras based on other technologies do exist. Intensified complementary metal oxide semiconductor (iCMOS) devices have been used to measure photon correlations [125], however they suffer from higher noise and lower quantum efficiencies. Scientific CMOS (sCMOS) devices are CMOS-based detectors whose noise has been drastically reduced. This technology has enabled cameras that can resolve the number of photons that arrive at each pixel which has potential for quantum imaging applications [126].

Another important technology at the time of writing is the intensified Tpx3Cam from Amsterdam Scientific Instruments. These cameras are event-based, like the event-based SPADs mentioned previously, but the technology is further developed. Time-tagging cameras can produce a prohibitively large amount of data, especially at higher spatial and temporal resolutions. The advantage of event-based detectors is that they only produce data when a photon is actually detected, in the form of an (x, y, t) coordinate. The Tpx3cam is a silicon-based sensor made up of 256×256 pixels, each of which can be read out with a 1.6 ns timing resolution. The sensor itself cannot detect single photons, so a photo-multiplying intensifier is needed for quantum imaging applications. This camera has been used recently in a number of quantum optics experiments, such three-dimensional imaging [127], and more robust entanglement verification in scattering media [128].

Finally, superconducting nanowire single photon detectors (SNSPDs) are another import technology. These consist of an extremely thin (i.e. nanometres) wire made of a superconducting material. This wire is cooled below its critical temperature so that it is in the superconducting regime, and a current is passed through it. It has no resistance due to its superconductivity so, by Ohm's law, no voltage is induced across the wire. However it is thin enough that a single photon can contain enough energy to heat it above its critical temperate, causing it to lose its superconductivity. This causes the resistance of the wire to rapidly return which, due to the current passing through the wire, results in a spike in the voltage across it that can be read out as a detection signal. SNSPDs have very low dark counts, high sensitivity over a broad spectral range, short dead times between detection, and very fast timing resolution [129, 130]. The state of the art for an SNSPD array is 500×800 pixels, demonstrated by Oripov et. al. [131]. However they must be operated at cryogenic temperatures which makes them impractical to use in many applications. Since they are not silicon-based, it is also difficult to integrate them on-chip with readout electronics. Due to these drawbacks, SNSPDs are better suited to quantum sensing and communications applications[132] than to quantum imaging.

2.3 Photon Pair Correlation Measurement With an EMCCD Camera

In this section I describe the method we use to measure photon pair correlations, originally reported in Ref. [121]. This technique allows photon correlations to be estimated without the need for detecting photons pair-per-pair. For photon pairs whose polarisation and frequency spectrum are the same, their joint state $|\phi\rangle$ arriving at the camera is given by

$$|\phi\rangle = \sum_{i,j \in [\![1,N]\!]} \phi_{ij} \, |i, j\rangle \,, \tag{2.14}$$

where N is the number of pixels, i (j) denotes the i^{th} (j^{th}) pixel, $|i, j\rangle$ is the state in which one photon is at pixel i and the other is at pixel j, and ϕ_{ij} is the discrete, position-basis wavefunction of the pairs. The probability of finding one photon at position i and the other at position j is $G^{(2)}_{ij} = |\phi_{ij}|^2$. Throughout this thesis the specific nature of this second order spatial correlation function, i.e. if it is discrete or continuous, will be made clear by use of subscript indices ($G^{(2)}_{ij}$) or continuous parameters ($G^{(2)}(x_1, x_2)$), respectively.

The goal of this method is to find $G^{(2)}_{ij}$ from direct intensity images. This is done by relating the measured intensity statistics from a very large number of frames to the underlying probability distribution of the photon pairs. The l^{th} frame of an acquisition is denoted $\{x^{(l)}_i\}_{i\in[\![1,N]\!]}$, where the subscript i denotes the i^{th} of N pixels. We can also compute a 'correlation image' from the l^{th} frame: $\{x^{(l)}_i x^{(l)}_j\}_{i,j\in[\![1,N]\!]}$. For a large number M of frames, and assuming stationary illumination, the mean of the direct intensity images is

$$\langle x^{(l)}_i \rangle = \lim_{M\to\infty} \frac{1}{M} \sum_{l=0}^{M} x^{(l)}_i = \sum_{x_i=0}^{\infty} x_i P(x_i), \tag{2.15}$$

where $P(x_i)$ is the probability of the camera sensor to return the value x_i at pixel i for any given frame. Likewise, the mean of the correlation images is

$$\langle x^{(l)}_i x^{(l)}_j \rangle = \lim_{M\to\infty} \frac{1}{M} \sum_{l=0}^{M} x^{(l)}_i x^{(l)}_j = \sum_{x_i=0}^{\infty} \sum_{x_j=0}^{\infty} x_i x_j P(x_i, x_j), \tag{2.16}$$

where $P(x_i, x_j)$ is the joint probability of the sensor to return the values x_i at pixel i and x_j at pixel j for any given frame. $P(x_i)$ and $P(x_i, x_j)$ are dependent on the input state probability distribution $G^{(2)}_{ij}$, and on the camera sensor response function.

To get an expression of $G^{(2)}_{ij}$ in terms of the measured image, some assumptions must be introduced. The first is that the camera response is uniform across the sensor. Physically, this means that the probability η of a photon incident on the sensor being converted into a photoelectron is the same for every pixel. It also assumes that dark count rate due to thermal fluctuations is the same for every pixel. The second assumption is that the detector response function I_k depends linearly on the number of photoelectrons k generated at the sensor so that $I_k = Ak + x_0$. The parameter A depends on the detector gain and the analogue-to-digital conversion. Finally, the third assumption is that the detected state is a pure two-photon state as in this case the $G^{(2)}$ is equal to the cross-correlation that is actually computed. For more information on these assumptions, see Ref. [121]. With these assumptions, we can write,

$$G^{(2)}_{ij} = \frac{1}{2A^2\tilde{m}\eta^2} \left[\langle x_i x_j \rangle - \langle x_i \rangle \langle x_j \rangle \right], \tag{2.17}$$

where $\tilde{m}$ is the mean photon pair rate. This equality is demonstrated in Ref. [121] and is not trivial. In particular, it strongly relies on the assumptions made. For a given acquisition, A, $\tilde{m}$, and η are constant so simply act as scaling factors. In terms of the direct intensity images measured at the camera, we can write

$$G_{ij}^{(2)} \propto \frac{1}{M} \sum_{l}^{M} x_i^{(l)} x_j^{(l)} - \frac{1}{M^2} \sum_{l,l',l \neq l'}^{M} x_i^{(l)} x_j^{(l')}. \tag{2.18}$$

The physical interpretation of Equation 2.18 is as follows. Many pairs of photons are detected in each frame and the first term in Equation 2.18 correspond to the correlations from these pairs. These are not the only correlations represented by this term, however. Since there are several pairs detected per image, and even single photons and noise, many of these correlations are accidental, i.e., they are not correlations between photons from the same pair. The second term of Equation 2.18 corresponds to an estimate of these accidental counts. The correlation time of a photon pair is considerably smaller than time between frames, so we know that two photons from a pair will never arrive across two different frames. Therefore, the correlations between a frame and the subsequent frame can only be from photons that are not from the same pair. This gives an estimate of the accidental correlations. Subtracting the second term from the first removes the accidental correlations, leaving only an estimate of the genuine correlations that is proportional to the joint probability distribution $G_{ij}^{(2)}$.

2.3.1 Example of $G^{(2)}$ Measurement in Practice

The previous section gives a mathematical description of a $G^{(2)}$ measurement, but it is also useful to have a more practical description.

Let's say we have a camera sensor with a resolution of $N_x \times N_y$ pixels, for a total of N pixels. A typical acquisition can require anywhere between 10^5 and 10^7 frames. It is not practical - and normally not even possible - to store this many frames for each acquisition, so instead we break the processing down into smaller blocks of M frames, and continuously sum the results of each block. The real and accidental coincidence terms from Equation 2.18 are computed separately and the subtraction is done after the acquisition. The m^{th} block of frames results in two $N \times N$ arrays corresponding to these terms, called $R^{(m)}$ and $A^{(m)}$ respectively. These are summed for each block to get the final arrays so that $R = \sum_m R^{(m)}$ and $A = \sum_m A^{(m)}$, and finally $G_{ij}^{(2)} = R_{ij} - A_{ij}$.

The following is a step by step breakdown of the acquisition procedure:

1. Initialise empty $N \times N$ arrays corresponding to R and A. $R^{(m)}$ and $A^{(m)}$ will be added to these arrays after each block, then discarded.
2. Fill the camera's internal buffer with frames and download them as a block to the processing computer.

3. When the buffer has been emptied begin the next acquisition to fill the buffer. At the same time, begin the processing on the most recent block of frames. See following for details on processing.
4. Add $R^{(m)}$ and $A^{(m)}$ to R and A and delete the current block of frames from memory.
5. Return to Step 2 and repeat until the required number of frames have been processed.
6. Finally, compute $G^{(2)} = R - A$.

The processing for each block is done as follows. The m^{th} block of M frames, labelled $I^{(m)}$, will be in the form of an $N \times M$ array where each column is a frame that has been unwrapped into a 1-dimensional vector. From this, $R^{(m)}$ can be computed via an outer product. In practice, this is simply a matrix multiplication with the array of frames:

$$R^{(m)} = \frac{1}{M} I^{(m)} I^{(m)^T}, \tag{2.19}$$

where X^T denotes the transpose of X.

$A^{(m)}$ is computed slightly differently. We define $I_1^{(m)}$ as $I^{(m)}$ with the last frame (i.e. column) removed. Similarly, we define $I_2^{(m)}$ as $I^{(m)}$ with the first frame (column) removed. $I_1^{(m)}$ and $I_2^{(m)}$ are both $N \times (M-1)$ arrays. Now, the accidental coincidence matrix is computed as

$$A^{(m)} = \frac{1}{2(M-1)} \left(I_1^{(m)} I_2^{(m)^T} + I_2^{(m)} I_1^{(m)^T} \right). \tag{2.20}$$

The two terms are the covariance matrix of a given frame with the next frame, and a given frame with the previous frame. For $N_x \times N_y$ pixel frames, $G^{(2)}$ is actually an $N_x \times N_y \times N_x \times N_y$ element 4-d array. However, this processing gives $G^{(2)}$ in an $N \times N$ form, where each column/row corresponds to a 2d conditional probability distribution that has been unwrapped into a 1d column/row vector with $N = N_x \times N_y$ elements.

2.3.2 Practical Considerations

Region of Interest

For $N_x, N_y >\sim 150$, the full $G^{(2)}$ starts to be too large to store in memory for processing. Therefore, for cameras with larger sensors, we reduce the beam to a suitable size and select a sub-area, or region of interest (ROI), of the sensor from which to acquire frames.

Temperature Stability

The processing is done in parallel to the acquisition of the next block of frames. For an EMCCD camera, the processing is faster than the acquisition, so the camera speed is still the limiting

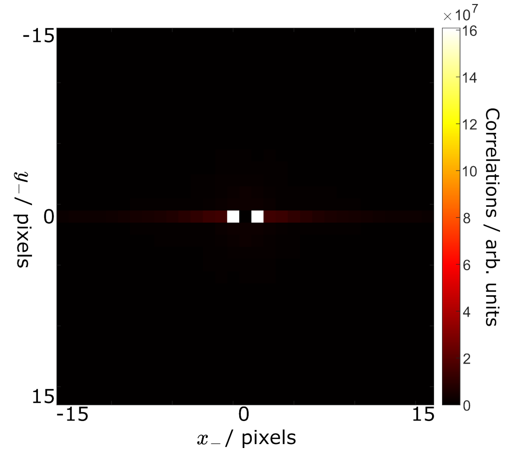

Figure 2.5: **Example of charge smearing artefact from a correlation measurement with an EMCCD camera.** Minus-coordinate projection of a $G^{(2)}$ measurement. Neighbouring pixels in each row are artificially correlated with each-other. It is predominately the direct neighbours but the artefact spreads across many pixels in each row. The central value has been set to zero.

factor. This is usually limited by the minimum exposure time, but may also be limited by the thermal performance of the camera. EMCCD camera sensors perform best at temperatures less than -60^{o}C. For cameras with larger sensors, such as the Andor Ixon Ultra 888, the temperature may be unstable at high frame-rates which can greatly impact SNR. To counteract this, a rest time between the acquisition of each block of frames can be added to allow the sensor to cool.

Saving Data

At the end of the processing we typically save R and A. The intensity images taken from the camera are all discarded as they are processed. Therefore, it is also useful save an average-intensity image that is simply the mean of all of the frames that have been acquired.

Correlations at the Same Pixel and Crosstalk

An individual pixel of an of EMCCD and SPAD camera cannot count the number of photons that land on it. This is because, in both cases, the signal resulting from a single photon detection event is not sufficiently distinguishable from the signal resulting from a two-photon (or greater) detection event. Therefore, no correlation information between a pixel and itself can be extracted. For this reason, we set the diagonal elements $G^{(2)}_{ijij}$ to the mean of the neighbouring elements. Alternatively, the diagonal elements could also be set to zero. In addition to this, most camera sensors also suffer from crosstalk between pixels. The signal from each pixel of sensor should be independent of each other pixel. However, in reality, the signal from one pixel can be affected by other pixels. For example, pixels in the same row of an EMCCD sensor suffer from high crosstalk. This cause of this crosstalk is an effect called charge smearing and is an artefact of the readout process. Recall from Section 2.2 that the charge from each pixel is shifted along a register during readout. This process is imperfect and, for a given bin in the register, there is often residual charge that is not shifted into the next bin when it should be. For the i^{th} bin, corresponding to the i^{th} pixel, it contains a charge Q_i, which is proportional to the intensity detected by that pixel. During the clocking process, the charge from bin i is shifted into bin $i+1$, the charge from bin $i-1$ is shifted into bin i etc. However, there is a residual charge R_i left behind in bin i that is proportional to Q_i. When the charge is shifted, R_i gets combined with the charge from the previous bin Q_{i-1} so we get $Q_{i-1} \rightarrow Q_{i-1} + R_i$. Since the signal that is read out for pixel $i-1$ is based on this value, it appears in the image as if pixel $i-1$ is brighter than it should be. The extra signal is proportional to the signal from the neighbouring pixel i. Since the readout is done row-by-row, this creates artificial correlations between pixels on the same row, as shown in Figure 2.5. Therefore, we set the correlation values between pixels in the same row to the mean of the correlations between neighbouring rows. Alternatively, these correlations could also be set to 0.

2.4 Interpreting the Measured $G^{(2)}$

The spatial correlations of the photon pairs are described by the quantity $G^{(2)}$. As stated above, for a measurement of two-dimensional transverse position or momentum correlations, this is a 4-dimensional object: for a photon at discrete location (i, j) and the other at (k, l) we have $G^{(2)}_{ijkl}$. The 4-d nature of $G^{(2)}$ makes it hard to visualise. In the previous section it is reshaped and expressed as a 2-d matrix for convenience, but this unwrapped form still does not lend itself well to visualisation. To aid us in visualisation and interpretation, there a number of projections that can be used to extract 2-dimensional images.

Reduced-dimension $G^{(2)}$

At first it is actually more pedagogical to consider the case of a correlation measurement for only one dimension of space - e.g. a detector with only one row of N pixels. In this case $G^{(2)}$ is a 2-dimensional matrix. Now, remember that $G^{(2)}$ is simply a measured joint probability distribution for the photon pairs. The i, j^{th} element of $G^{(2)}$ gives the probability of detecting a photon at the i^{th} pixel while simultaneously detecting another photon at the j^{th} pixel, i.e. $P(i, j) = G^{(2)}_{ij}$. We can also extract conditional probability distributions. The probability distribution for detecting photon 1, given that photon 2 has been detected at pixel a is given by the a^{th} column of $G^{(2)}$, i.e. $P(i|j = a) = G^{(2)}_{i;j=a}$. Likewise for the conditional distribution of photon 2 given that photon 1 has been detected at pixel b is given by the b^{th} row of $G^{(2)}$: $P(j|i = b) = G^{(2)}_{i=b;j}$. Figure 2.6b shows an example of two conditional distributions for photon pairs that are strongly correlated in position.

The conditional distributions contain useful information, but lengthy acquisitions - typically 10

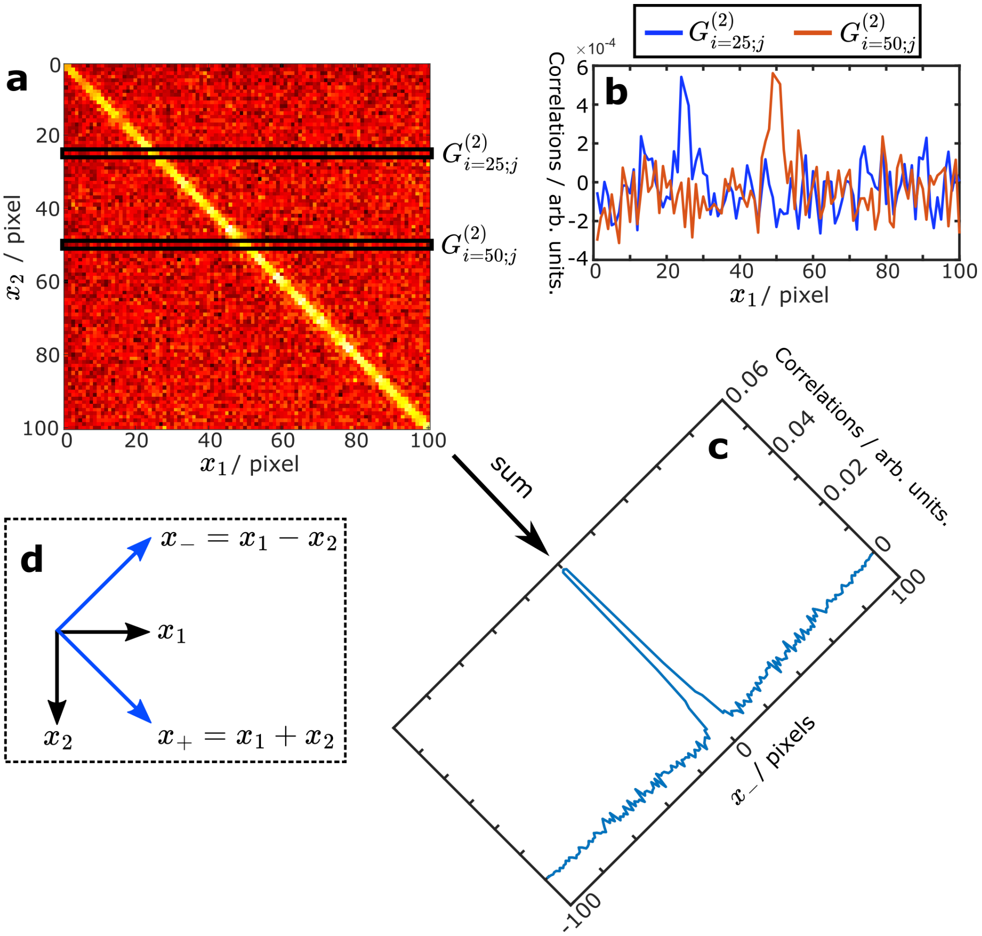

Figure 2.6: **Position-correlated $G^{(2)}$ for 1-dimensional transverse position measurement. a,** Experimentally measured $G^{(2)}$. Full 2-d position data was acquired and $G^{(2)}$ for a single row of pixels was extracted after measurement. Notice the bright diagonal which is due to the photon pairs being strongly correlated in position. **b,** Conditional probability distributions extracted from $G^{(2)}$. Black boxes highlight the extracted rows. Notice the peaks around the corresponding pixels. **c,** Minus-coordinate $(x_1 - x_2)$ projection of $G^{(2)}$ obtained by summing along the diagonal direction. Notice that the SNR of the peak in this projection is much larger than the SNR of the peaks in the conditional distributions. **d,** Illustration of the sum- and minus-coordinates. Data obtained from processing 10^7 frames, acquired with the Andor Ixon Ultra 888 EMCCD at 2 ms exposure time and an ROI of 100×100 pixels. The diagonal elements $G^{(2)}_{ii}$ correspond to the correlations between a pixel and itself. EMCCD camera pixels cannot resolve photon numbers, so these value are don't give any real information. Therefore they are set to the mean of the neighbouring elements.

hours or more - are required to get a high enough signal-to-noise ratio (SNR) to see it in practice. By exploiting the symmetries of the photon pairs we can obtain some distributions with better SNR. From Equation 2.13 we can see that, for a short crystal, the photon pairs are strongly correlated in position at the plane of the crystal. If an imaging system is used to optically relay the plane of the crystal onto a camera, the photons will also be strongly correlated in position at the camera. This means that, when a photon lands on pixel i, the other photon is very likely to land on or nearby the same pixel. This means that correlations will be concentrated in the diagonal and near-diagonal elements $G^{(2)}_{i;j\approx i}$. This can be seen in Figure 2.6a. By summing along this sum-coordinate direction, labelled x_+, most of the high-valued elements will be summed into the same locations. The result of this sum is shown in Figure 2.6c. We have projected the $G^{(2)}$ along the sum-coordinate direction onto the minus-coordinate (x_-) axis. The projection shown in Fig 2.6c is therefore called the minus-coordinate projection. We denote this C^-, and it is computed for one dimensional correlations by

$$C^-_{i_-} = \frac{1}{N - |i_-|} \sum_i^N G^{(2)}_{i(i-i_-)} \tag{2.21}$$

where $\{i_-\} \in [-N+1, N-1]$, and term outside the sum is a normalisation factor that accounts for the fact that the i_-^{th} off-diagonal contains $N - |i_-|$ elements. A similar projection can be used when measuring the momentum correlations of the photon pairs. Instead of an imaging system that relays the surface of an SPDC crystal onto a camera, imagine a Fourier-imaging lens that images the Fourier plane of the crystal onto the camera, so we are measuring in transverse momentum space. Now, since the pairs are strongly anti-correlated in transverse momentum, the anti-diagonal and near-anti-diagonal elements $G^{(2)}_{i;j\approx N-i}$ will contain most of the correlations, as seen in Figure 2.7a. These correspond to correlations between pixel i the opposite pixel $N-i$, symmetric about the central pixel $N/2$ (assuming that the beam is well-centred on the camera). In this case, we want to sum along this anti-diagonal instead to collect most of the correlations in the same location in the projection. Now, we are projecting onto the sum-coordinate axis, so this is called the sum-coordinate projection. This is denoted C^+, and is computed for one-dimensional correlations by

$$C^+_{i_+} = \frac{1}{N - |i_+|} \sum_i^N G^{(2)}_{i(i_+-i)}, \tag{2.22}$$

where $\{i_+\} \in [-N+1, N-1]$. Both of these projections can be seen as an average of all of the conditional distributions, after re-centring the conditionals on their corresponding conditional pixel.

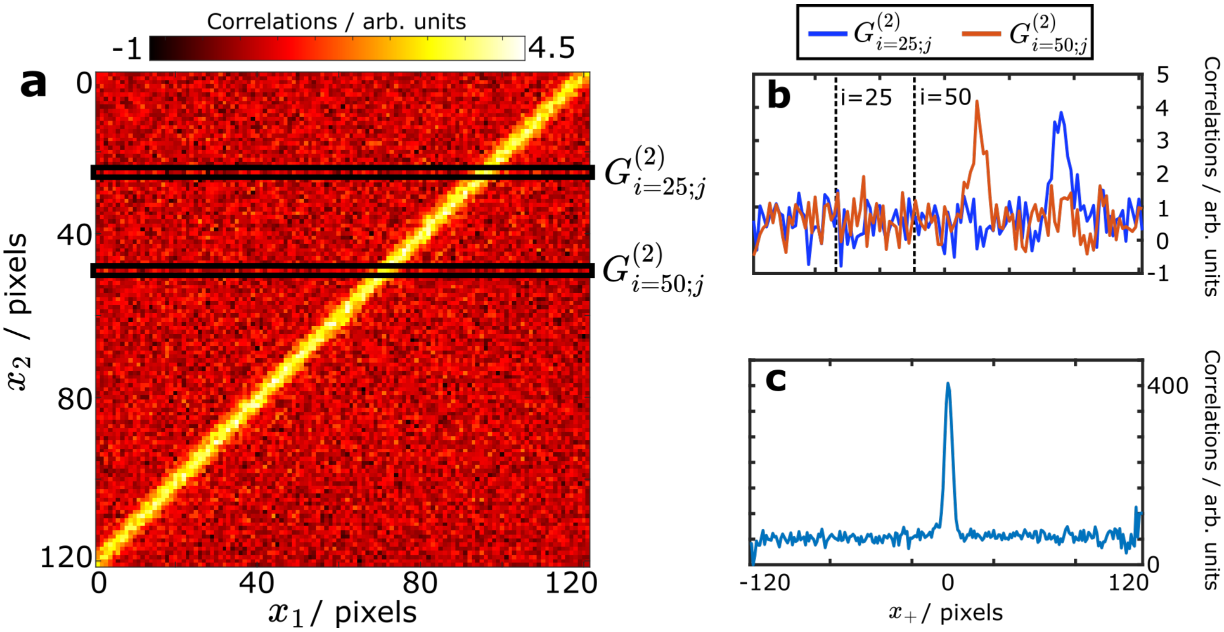

Figure 2.7: **Anti-correlated $G^{(2)}$ for a 1-dimensional transverse momentum momentum measurement. a,** Experimentally measured $G^{(2)}$ with camera in the Fourier-plane of the non-linear crystal. Full 2-d position data was acquired and $G^{(2)}$ for a single row of pixels was extracted after measurement. Notice the bright anti-diagonal which is due to the photon pairs being strongly anti-correlated in momentum. **b,** Conditional probability distributions extracted from $G^{(2)}$. Black boxes highlight the extracted rows. Notice the peaks around the opposite pixels, symmetric about the centre pixel. **c,** Sum-coordinate ($x_1 + x_2$) projection of $G^{(2)}$ obtained by summing along the anti-diagonal direction. Negative values arise due to an over-estimate of the global accidentals rate. Data obtained from processing 9×10^6 frames, acquired with the Andor Ixon Ultra 897 EMCCD at 2 ms exposure time and an ROI of 121×121 pixels.

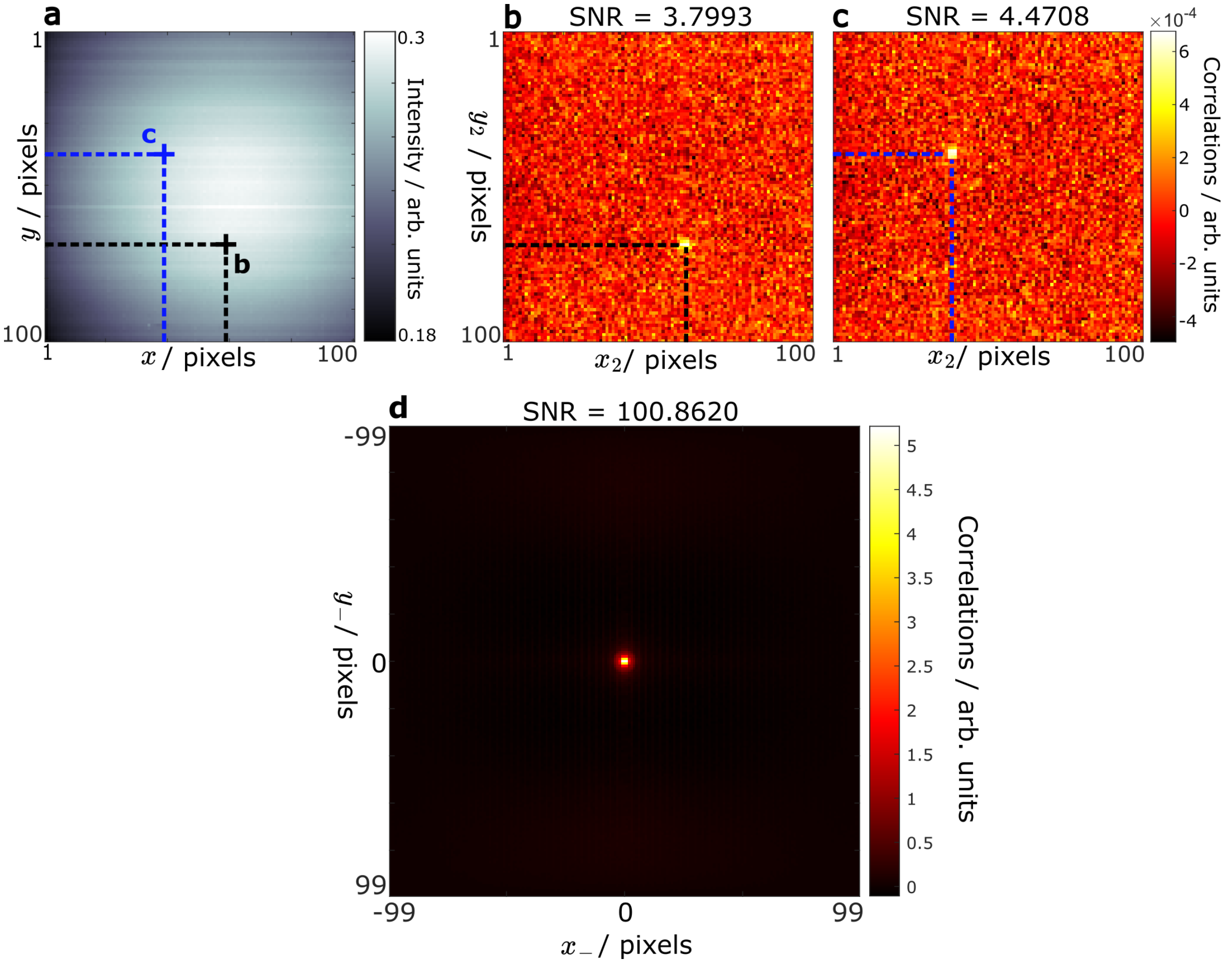

Figure 2.8: **Position-correlated $G^{(2)}$ projections for a 2-dimensional transverse position measurement. a,** Average direct intensity image. **b,c,** Conditional distributions for ($i = 69, j = 59$) and ($i = 40, j = 39$), respectively. Notice the bright spots centred around the pixel that the distribution has been conditioned on. **d,** Minus-coordinate projection of measured $G^{(2)}$. Since the correlations were measured in 2-dimensional transverse position, this is a 2-d image. The bright peak at the centre indicates that the pairs are strongly correlated in position. Again, notice that the SNR in C^- is much higher than in the conditional images. Images are from the same dataset as in Figure 2.6 i.e. an acquisition of 10^7 frames with the Andor Ixon Ultra 888 EMCCD at 2 ms exposure time, with an ROI of 100×100 pixels. For the SNR calculation, the signal is taken as the mean of a 3×3 area of pixels. For this conditionals, this is centred around the chosen conditional pixel; for the projection, this is centred on the central pixel. The noise is calculated as the standard deviation of the image with the peak and neighbouring area of 9×9 pixels removed. Then, SNR = signal/noise.

Full 4-dimensional $G^{(2)}$

The aim of these examples was to give a more intuitive, visual description of the projections we use to visualise $G^{(2)}$. The underlying concepts are exactly the same for the full 4-dimensional $G^{(2)}$, but now the projections are 2-dimensional quantities. Figure 2.8 shows examples of two conditionals and a minus-coordinate projection. Figs. 2.8b and c show the conditional distributions, conditioned on pixels $(59, 69)$ and $(39, 40)$, respectively. These are now 2-dimensional 'images' that give the probability distribution of detecting a photon on the camera, given that its twin was detected at the chosen pixel. The pairs in this example are strongly correlated in position, so the conditionals distributions are narrow peaks centred on the corresponding pixel. The bright, narrow peak at the centre of the minus-coordinate projection, shown in Figure 2.8d, means that the pairs are strongly correlated in position. Likewise, Figure 2.9 shows examples of conditional images and a sum-coordinate projection for a $G^{(2)}$ that was measured in the far-field of a nonlinear crystal. The acquisition time here was approximately 8 hours. The formulae for the minus- and sum-coordinate projections are easily adapted to the case of a 4-dimensional $G^{(2)}$ with $N_x \times N_y \times N_x \times N_y$ elements. For the minus-coordinate projection:

$$C^{-}_{i_- j_-} = \frac{1}{N_x - |i_-|} \frac{1}{N_y - |j_-|} \sum_{i}^{N_x} \sum_{j}^{N_y} G^{(2)}_{ij(i-i_-)(j-j_-)}, \tag{2.23}$$

and for the sum-coordinate projection

$$C^{+}_{i_+ j_+} = \frac{1}{N_x - |i_+|} \frac{1}{N_y - |j_+|} \sum_{i}^{N_x} \sum_{j}^{N_y} G^{(2)}_{ij(i_+-i)(j_+-j)}, \tag{2.24}$$

where now $\{i_-, i_+\} \in [-N_x + 1, N_x - 1]$ and $\{j_-, j_+\} \in [-N_y + 1, N_y - 1]$.

2.4.1 Discussion of the Effects of Acquisition Time on Signal-to-noise Ratio

For any imaging experiment the signal-to-noise ratio of the images is important. In most classical imaging schemes with bright illumination it rarely causes any practical problems. However in quantum imaging with SPDC, it becomes more of a factor. The SNR of a $G^{(2)}$ measurement scales as $\sqrt{M}$, where M is the total number of frames [133]. This can be seen by examining the photon pair statistics. The probability of detecting one pair (i.e. one coincidence) is independent of any prior or future detection events. Therefore, pair detections can be modelled by a Poissonian distribution. For a given pair of pixels i and j, the probability P of detecting k coincidences between these pixels in any given frame is

$$P_{ij}(k, \lambda) = \frac{\lambda^k \mathrm{e}^{\lambda}}{k!}, \tag{2.25}$$

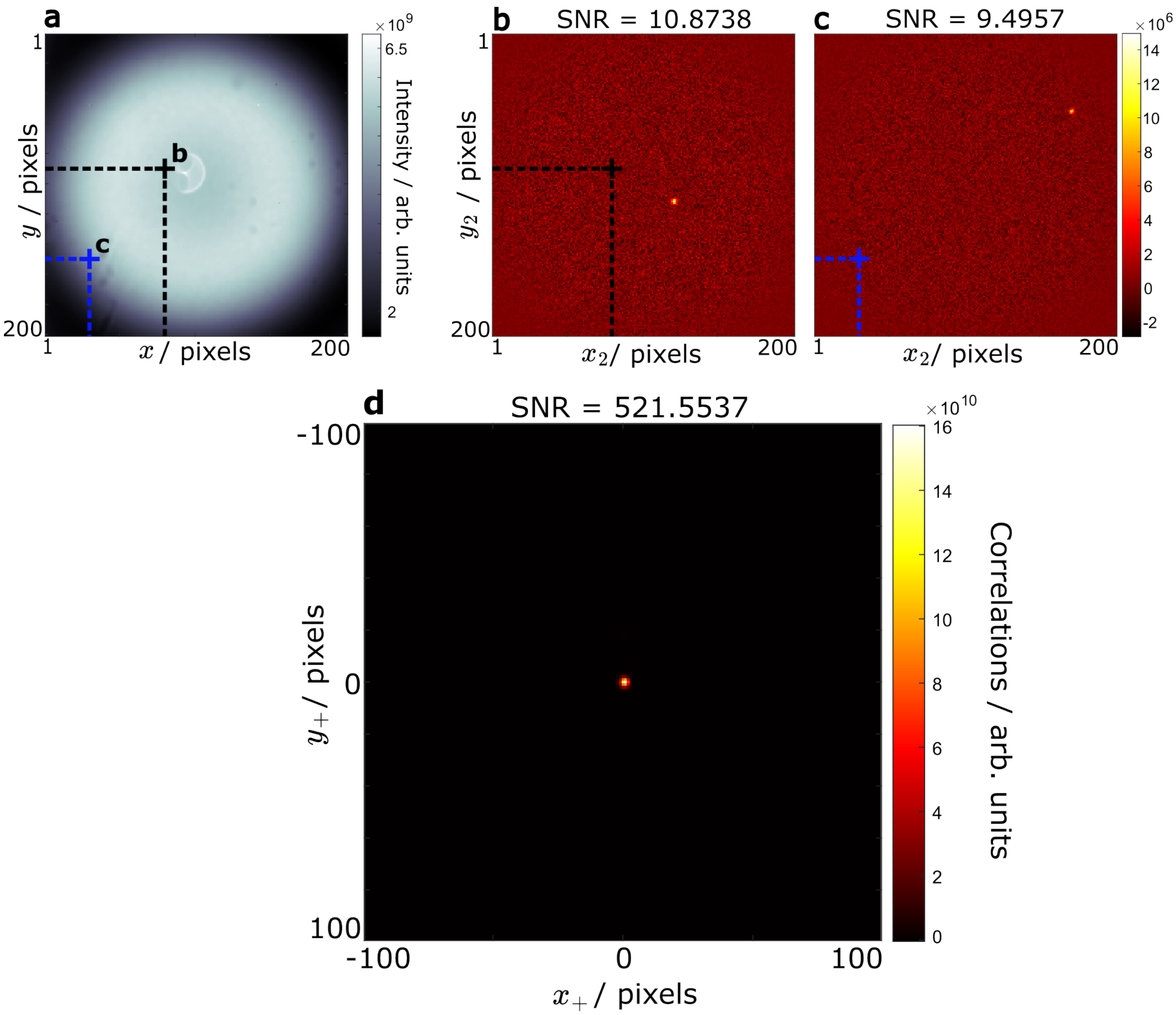

Figure 2.9: **Anti-correlated $G^{(2)}$ projections for a 2-dimensional transverse momentum measurement. a,** Average direct intensity image. **b,c,** Conditional distributions for $(i = 80, j = 30)$ and $(i = 30, j = 150)$, respectively. Notice the bright spots centred around the pixel that is diametrically opposite the pixel that the distribution has been conditioned on. **d,** Cropped sum-coordinate projection of measured $G^{(2)}$. The bright peak at the centre indicates that the pairs are strongly anti-correlated in momentum. Images are from an acquisition of 9×10^6 frames with the Andor Ixon Ultra 897 EMCCD at 2 ms exposure time, with an ROI of 200×200 pixels. The SNR is calculated in the same way as Figure 2.8

where λ is the mean of this distribution and is a function of the underlying pair production distribution (i.e. $|\Psi|^2$ or $|\Phi|^2$), the system losses, and detector properties. For a Poisson distribution, the variance σ^2 is also equal to λ. Now, each frame samples from this distribution, so the mean and variance of the number coincidences between i and j over M frames is

$$\mathrm{E}_M[k] = \mathrm{Var}_M[k] = \lambda M. \tag{2.26}$$

Finally, the noise in the detected coincidences between i and j is given by the standard deviation $\sigma = \sqrt{\mathrm{Var}_M[k]} = \sqrt{\lambda M}$. The SNR is equal to the mean value $\mathrm{E}_M[k]$ divided by this noise, so we find

$$\mathrm{SNR} = \frac{\mathrm{E}_M[k]}{\sqrt{\mathrm{Var}_M[k]}} = \frac{\lambda M}{\sqrt{\lambda M}} = \sqrt{\lambda M} \propto \sqrt{M}. \tag{2.27}$$

The SNR scales as the square root of the number of frames. Therefore, there are diminishing returns in SNR improvements for increasing the number of frames.

The above analysis assumes a constant pump power and constant exposure time for each frame. Naively, one might think that increasing these quantities will also give an increase in SNR, and with an ideal detector this is true. However with the method of Ref. [121], it is not the case. Since we operate in a regime of multiple pairs per frame, we detect a large number of accidental coincidences. These are estimated and subtracted as per Equation 2.18, however the quality of this estimate is dependent on the number of pairs per frame. As we expect, if there are too few, then each frame contains mostly noise resulting in a lower SNR. However if there are too many pairs the number of accidentals will be too high and the SNR will also suffer. There exists then an optimal photon flux, which can be predicted from the camera parameters [133], but in practice it is more efficient to find the optimal exposure time via a trial-and-error approach.

This is assuming a fixed pump power. Generally, it is best to maximise the pump power and then minimise the exposure time, since the SNR scales with the number of frames (Eq. 2.27). For a typical experiment we have a pump power of 100 mW and an exposure time of 2 ms.

2.5 Building a Quantum Imaging Experiment

A quantum imaging experiment consists of a source, an imaging system, and a camera. As discussed previously, the source a nonlinear crystal. In all of the works described in this thesis we have used a BBO crystal pumped by a continuous-wave laser with a frequency of 405 nm. This generates photon pairs via SPDC with a central wavelength of 810 nm. We are typically only interested in degenerate pairs, i.e. pairs whose photons have approximately the same frequency, so a band-pass filter at 810 ± 5 nm is used to remove non-degenerate pairs. A long-pass filter is also used to filter the pump beam after it has passes through the BBO crystal. The camera and detection methods have already been discussed at length. So far, however, I have not described

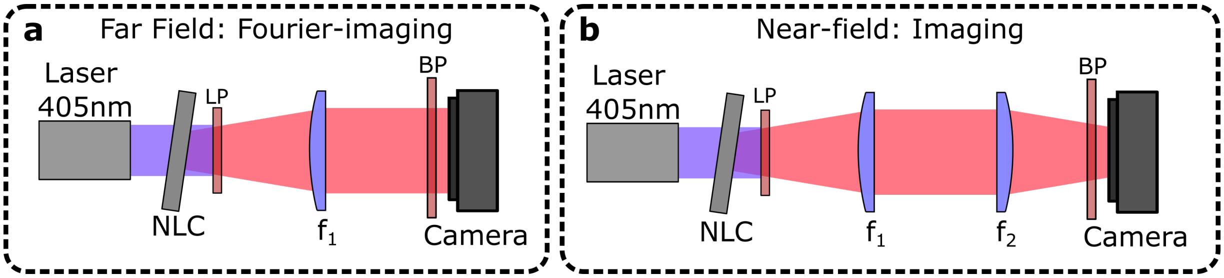

Figure 2.10: **Near-field and far-field imaging setups. a,** Fourier-imaging of a nonlinear crystal (NLC) placed at the front focal plane of lens f_1 with the camera placed at the back focal plane of f_1. Data presented in Figures 2.7 and 2.9 acquired in a FF imaging configuration. **b,** Imaging of a non-linear crystal placed at the input plane of a 4-f system composed of lenses f_1 and f_2. Data presented in Figures 2.6 and 2.6 acquired in a NF imaging configuration. BP - band-pass filter.

how we build an imaging experiment with photon pairs or how photon pair correlations can actually be used to retrieve information about an object. In this section, therefore, I will introduce the basic principles of imaging and I describe how we actually build and align a quantum imaging experiment.

2.5.1 Elements of Fourier Optics

I will start with a very brief overview of the core concepts of Fourier optics that we use when designing and building an imaging experiment. I closely refer to the textbook 'Introduction to Fourier Optics' by Goodman [134]. The most important concept from Fourier optics is that an ideal lens performs a 2-dimensional Fourier transform. More specifically, for monochromatic light, the field at the back (i.e. output) focal plane of a lens is equal to the Fourier transform of the field at the front (input) focal plane. Mathematically, the field at back focal plane E_{out} is related to the field at the front focal plane E_{in} by

$$E_{out}(\mathbf{r}') = \int_{-\infty}^{\infty} E_{in}(\mathbf{r}) \mathrm{e}^{-\frac{2\pi i}{f\lambda}\mathbf{r}.\mathbf{r}'} d\mathbf{r}, \tag{2.28}$$

where f is the focal length of the lens and λ is the wavelength of the light. Notice that, for a given wavelength, the effect of the focal length is to scale the profile of the output field by a factor f. Such a Fourier-transforming lens is called a 2-f system, since it consists of propagation by a distance f, transmission through the lens, followed by another propagation by a distance f. An example of a 2-f imaging system to image the Fourier plane of a nonlinear crystal is shown in Figure 2.10a.

Now, one of the properties of a Fourier transform is that $\mathcal{F}\{\mathcal{F}\{E(\mathbf{r})\}\} \propto E(-\mathbf{r})$. If we put two 2-$f$ systems back to back so that the output plane of the first system is the input plane of the second, we can relay the field at the input plane of the first to the output plane of the second. For obvious reasons, this is called a 4-f imaging system or 4-f relay. If the first lens has focal length f_1 and the second has focal length f_2, the output field is

$$E_{out}(\mathbf{r}') = E_{in}\left(-\frac{f_1}{f_2}\mathbf{r}\right), \tag{2.29}$$

where we have omitted the constant multiplication factor. We have magnified E_{in} by a factor $M = -f_2/f_1$ and relayed it to the output plane. Relaying the electric field from a given plane to another plane is the basis of imaging. We are interested in the intensity and/or phase of a field e.g. at the plane of a sample, but we cannot put a camera in this plane. Imaging is the act of transmitting the information from this plane to another plane, where we can place a detector. This property of a 4-f system to magnify and relay a field to a desired plane makes it the main building block for an imaging system. An example of a 4-f imaging system that images the surface of a nonlinear crystal onto a camera is shown in Figure 2.10b. In addition to the 4-f imaging system there are other two-lens systems that can be used. If the distance between the two lenses is not equal to the sum of their focal lengths, the intensity at the input plane will still be relayed and magnified to the output plane but the field will not. That is, $|E_{out}(\mathbf{r}')|^2 = \left|E_{in}(M\mathbf{r})\right|^2$, but $E_{out}(\mathbf{r}') \neq E_{in}(M\mathbf{r})$. The system introduces an additional phase to the field.

It is also useful to do imaging with a single lens. This is a classic result from ray optics, not Fourier optics, but it is still worth mentioning here. From the thin lens approximation, for a lens with focal length f, an object placed at a distance d_1 before the lens will create an image at a distance d_2 after the lens, where d_1 and d_2 are related by

$$\frac{1}{f} = \frac{1}{d_1} + \frac{1}{d_2}, \tag{2.30}$$

and the resulting image is magnified by a factor $M = -d_2/d_1$. A special case is $d_1 = 2f$, so that $d_2 = d_1$ and $M = 1$. This can be used to swap between imaging and Fourier-imaging without altering any distances. If the lens in a 2-f system is replaced by a lens $f' = 0.5f$, then the field at the input plane will now be imaged onto the output plane. It is important to note that, as with non-4-f two-lens systems, in such single-lens imaging systems it is not the field that is relayed from the object plane to the image plane, but only its intensity. In both cases, since a camera is sensitive only to the intensity of the field, this is generally sufficient for a simple imaging system. However, it has its limitations in systems that measure the spatial phase of the field.

Lastly, for an imaging system comprised of multiple 4-f relays, there are multiple planes in which the field is either equal to (up to some magnification) the input field, or equal to the (scaled) Fourier transform of the input field. Throughout this thesis, the planes which contain an image of the input field we will call near-field (NF) planes. In general, any near-field plane will be separated from any other near-field plane by an even number of lenses. On the other hand, the planes which contain the Fourier transform of the input field are called far-field (FF) planes. This name comes from Fraunhofer diffraction, which says that as the field from a plane propagates to infinity, i.e. the far-field, the propagated field looks like the Fourier transform of the original field. In general, any far-field plane is an odd number of lenses away from any near-field plane, and an even number of lenses away from any other far-field plane.

2.5.2 Aligning a Quantum Imaging Experiment

The power of the light from SPDC is on the order of tens of picowatts making it invisible to the naked eye and most cameras (hence the need for EMCCDs, SPADs, etc). Aligning a system directly with photon pairs is therefore very difficult. Instead, we use an alignment laser at the same wavelength as the photon pairs. Actually, the alignment beam must only be strongly spatially coherent; strong temporal coherence is not necessary. For this reason, we use a super-luminescent diode (SLED). This is effectively a diode laser in which the light only has a single pass through the gain medium so no lasing occurs. SLEDs have high spatial coherence but have a relatively broadband frequency spectrum. This allows a band-pass filter to be used to precisely match the SLED frequency with that of the photon pairs.

Typically a filter with a bandwidth of 10 nm is sufficient to filter out the majority of non-degenerate photon pairs. Care should be taken to ensure that the central wavelength of the filter is well matched to the central wavelength of the pairs. If the filter is not symmetric about the central wavelength of the pairs it will asymmetrically filter one photon in each pair more than the other. This can result in a significant reduction in measured correlations without a drop in the total intensity.

Photon pairs are very sensitive to the alignment so we mount both the crystal and the lens immediately after the crystal on separate translation stages to finely control their positioning. Once the system is mostly aligned by hand we then precisely align the final lens and crystal by optimising the photon pair correlation width via the sum- and minus-coordinate projections. The basic concept is that the pairs are strongly correlated in the image plane of the crystal, and strongly anti-correlated in the Fourier plane of the crystal. If the correct plane is not imaged well onto the camera due to some misalignment, for example, then the measured correlation width will appear broader. Conversely, minimising the correlation width is a good way to ensure the system is well aligned. For more details on the effects of misalignment and aberrations on the pairs' spatial correlations, see Chapters 3 and 4.

I will now describe how to align an imaging system to relay and magnify the NF or FF plane of a nonlinear crystal onto a camera.

1. **Co-align SLED and pump.** To ensure the SLED will follow the same path as the pairs, it

must be aligned with the pump beam. A dichroic mirror (DM) is used to superimpose the pump onto the SLED. Two mirrors in the path of the SLED can fully control the position and angle, whilst one mirror plus the DM are sufficient for the pump. The two beams can be aligned with each other by ensuring they both pass through two distantly separated irises. After they are co-aligned, do not move the DM or any mirror before it. Note that if the SLED is at 810 nm, an IR viewing card will be necessary to see the beam.

2. **Place mirrors.** Now that the SLED is aligned with the pump, place the required mirrors and align them with the SLED so that the beam follows the desired path. Try to keep the beam as close to the centre of each mirror as possible. This is to avoid cutting any light since, once the lenses are places, the beam at the mirrors may be substantially expanded.

3. **Place lenses.** Assuming you need to align n lenses, label them f_1-f_n, where f_1 is the first lens after the crystal, and f_n is the last lens, immediately before the camera. We start with f_n and work backwards. The process is as follows:

    (a) Place the camera in the desired position and ensure the SLED is well-centred on the sensor. Put lens f_n before the camera, and adjust it's position to obtain the best possible focus. The best focus is found empirically i.e. by moving the lens and viewing the focus spot width and intensity. The centre of the focused and collimated beams should be at approximately the same position. To adjust this, change the lateral position of the lens. With all lenses, ensure they are perpendicular to the optical path. We can swap between imaging and Fourier-imaging the beam by swapping lens f_n with one that has half the focal length, $0.5f_n$.

    (b) Swap lens f_n with lens $0.5f_n$.

    (c) Place lens f_{n-1} and position this to achieve the best focus. Again, the beams should be roughly centred at the same position on the sensor.

    (d) To place lens f_{n-2}, replace $0.5f_n$ with f_n and find the best focus.

    (e) For every subsequent lens, first swap $f_n \leftrightarrow 0.5f_n$ and then position the new lens to get the best focus. Always make sure that the collimated beam and focused spots are centred at around the same point at the camera. This ensures that the beam is passing perpendicularly through the centre of each lens.

    (f) Finish by placing the lens f_1. Generally, this lens has a short focal length, typically between 25 mm and 50 mm. This lens should be mounted on a translation stage for fine control of its alignment. More precise alignment will be done in the following step, but you should still aim for the best alignment possible by hand first.

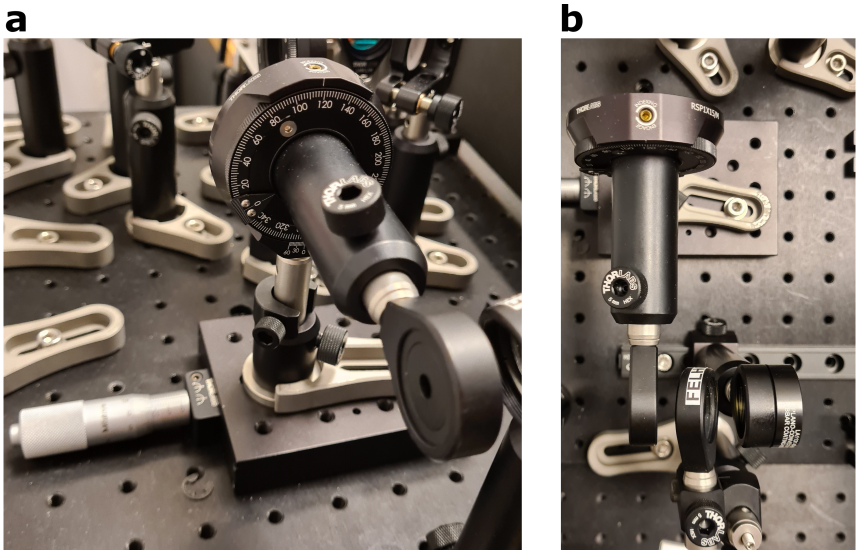

Figure 2.11: **Example of a rotatable crystal mount. a,** Image of full mount and translation stage. The crystal is mounted on a circular lens mount and post. This itself is mounted horizontally on a rotation mount to enable simple control over the crystal angle. Finally, everything is mounted on a (manually actuated) translation stage for precise control over the crystal position. **b,** Top-down image of the same crystal mount to show the crystal followed by a short-pass spectral filter and short focal length lens (f_1). The filter is tilted to direct the reflection of the pump to a desired location.

4. **Precisely align lens f_1 and crystal.**

   The photon-pair correlations are particularly sensitive to the positions of lens f_1 and the crystal. The reason is that it is generally necessary to use a lens with a short focal length just after the crystal. Indeed, this allows for a sufficiently large numerical aperture to collect all the k-vectors emitted by the crystal. It is therefore important to align these well.

   (a) First, choose between the lens with focal length f_n or $0.5 f_n$ in order to image the front focal plane of lens f_1 onto the camera. This configuration is called near-field imaging configuration. Now we are imaging the plane in which we want to put the crystal. The crystal is transparent to the SLED, but it will likely have dust/imperfections on its surface. It can be put in roughly the correct plane by getting these imperfections in-focus. If there are no visible imperfections, another option is use a cross target or similar object that can be easily swapped with the crystal without moving the entire crystal mount. For an example of the mount we have used, see Figure 2.11.

   (b) Now that all of the lenses and the crystal are positioned, the SPDC light should be visible on the camera. In the following steps we will measure and use the photon-pair spatial correlations to precisely adjust the positions of the lens and crystal. From here, remove as much background light as possible by covering the setup and turning off all other light sources.

(c) Now, put the setup in the far-field imaging configuration i.e. choose between the lens with focal length f_n or $0.5f_n$ in order to image the back focal plane of lens f_1 onto the camera. We will align the lens f_1 first since, in the far-field configuration, the correlation width does not depend on the distance between the lens and crystal.

(d) Tilt the crystal around its horizontal axis until a ring (or rings if the crystal is a Type II or paired Type I) is visible on the camera. Slowly tilt the crystal until this ring is collapsed almost to a disk, and fits into a suitable ROI on the camera. A disk is preferred because, for imaging, we want a uniform illumination profile.

(e) Find the position of the stage that optimises (i.e. focuses best) the sum-coordinate projection. A short, i.e. <5 minutes, acquisition should be necessary to resolve a signal in the projection.

(f) Once the peak of the sum-coordinate projection in the far-field imaging configuration is optimised, move to the near-field imaging configuration. Now, repeat the process above (skipping the step of tilting the crystal) for the position of the crystal instead of the lens, and optimise the peak in the minus-coordinate projection of $G^{(2)}$ instead.

2.6 An Example of Experimental Quantum Imaging: Pixel Super-resolution

This section is based on the published article *'Pixel super-resolution with spatially entangled photons'* by authors Hugo Defienne, Patrick Cameron, Bienvenu Ndagano, Ashley Lyons, Matthew Reichert, Jixuan Zhao, Andy R. Harvey, Edoardo Charbon, Jason W. Fleischer and Daniele Faccio [1]. I was involved in this project at the beginning of my PhD. Hugo Defienne conceived of the concept and wrote the majority of the paper. The data presented in Figures 2.13 and 2.14 was acquired by Hugo Defienne. Subsection 2.6.2 is based on the theoretical explanation given in the paper. My contribution to the paper was acquiring data for and performing the slanted edge frequency analysis.

I will now describe an example of a quantum imaging experiment where the photon pair correlations can be exploited to obtain additional information that would not be present in a direct intensity image. This is the method of achieving pixel super-resolution with spatially entangled photon pairs.

2.6.1 Encoding an Image in the Spatial Correlations

Up to this point I have described how to measure the $G^{(2)}$ for a photon pair source using an imaging system, but I have not described how we can encode and extract information from an

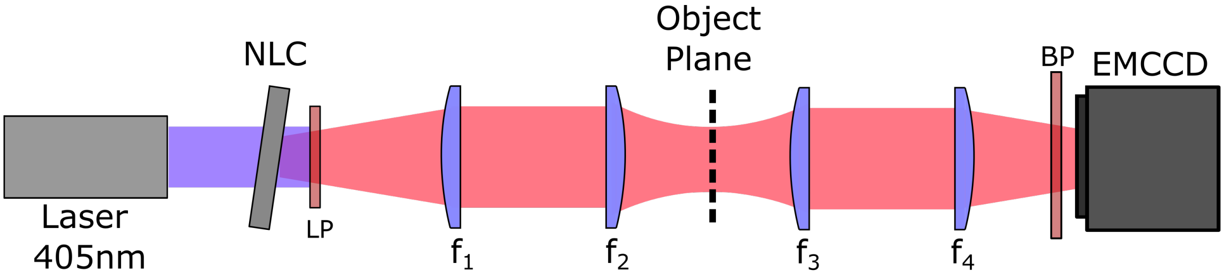

Figure 2.12: **Diagram of a simple quantum imaging experiment.** A laser at 405 nm pumps a nonlinear crystal (NLC), and the remaining pump beam is filtered with a long-pass filet (LP). The plane of the crystal is relayed to an object plane

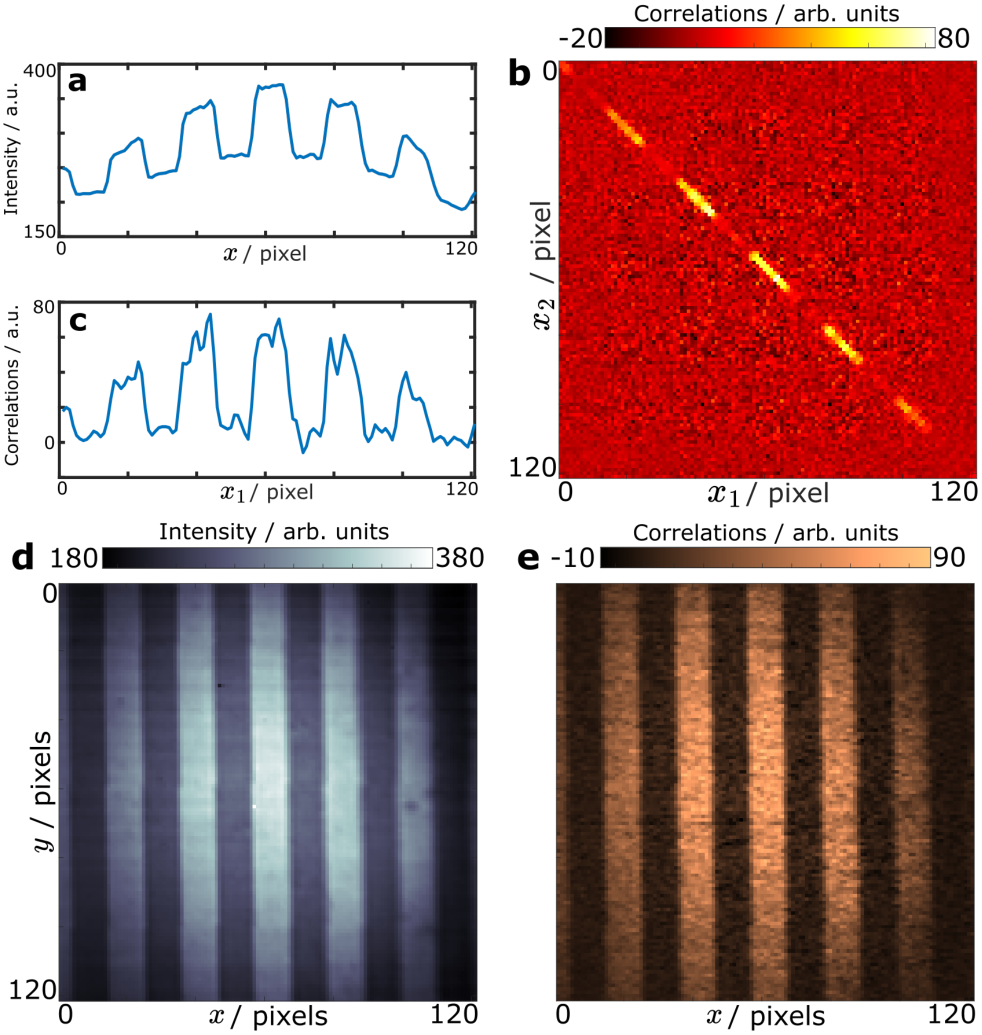

Figure 2.13: **Image encoded in diagonal elements of $G^{(2)}$. a,** 1-d direct intensity image of a grating object in the NF plane of a BBO crystal, measured with one row of pixels ($i = 52$). **b,** $G^{(2)}$ measured with the same row of pixels. **c,** Diagonal elements of the 1-d $G^{(2)}$ shown in **b** i.e. $G^{(2)}_{ii}$. **d ,** Full 2-d intensity image of the grating. **e** Diagonal elements of full 4-d $G^{(2)}$ i.e $G^{(2)}_{(ij)(ij)}$. An ROI of 121 × 121 pixels was used for all measurements. 1-d data was extracted post-acquisition. All data from an acquisition of 1.7×10^7 frames with Andor Ixon Ultra 897 EMCCD with an exposure time of 2 ms.

object in a quantum imaging system. Figure 2.12 shows a diagram of basic NF quantum imaging setup. A 4-f system (lenses f_1, f_2) is used to relay the photon pair field from the crystal plane to the object plane. Since the photons are strongly correlated in position at the crystal, they will also be strongly correlated in position at the object. The plane of the object is then relayed onto the camera to perform the measurement. In fact, if one looks only at the direct intensity of a photon pair source, it behaves exactly as a classical, incoherent light source (see Subsection 3.3.3 for a more information). The intensity profile at the camera is then just an image of the object:

$$I_{ij} \propto |t(x_i, y_j)|^2, \tag{2.31}$$

where (i, j) is the camera pixel centred at position (x_i, y_j) and t is the transmission profile of the object.

With photon pairs, this is not the full story however; we must also look at how an object affects the correlations. For perfectly correlated pairs, $G^{(2)}_{ijkl} = \delta_{(ij)(kl)}$, where

$$\delta_{(ij)(kl)} = \begin{cases} 1 & \text{for } (ij) = (kl) \\ 0 & \text{for } (ij) \neq (kl) \end{cases}$$

is known as the the Kronecker delta. Both pairs pass through exactly the same point in the NF plane. If the object from above, $t(x_i, y_j)$ is placed in a NF plane, as in Figure 2.12, then both photons will be attenuated by the same point in the object. Since they are perfectly correlated, they both arrive at pixel (i, j) on the camera. This results in correlations of the form

$$G^{(2)}_{ijkl} = \delta_{(ij)(kl)} |t(x_i, y_j) t(x_k, y_l)|^2, \tag{2.32}$$

so that the diagonal elements are

$$G^{(2)}_{ijij} = |t(x_i, y_j)|^4. \tag{2.33}$$

The extra power of 2 arises because both photons of each pair are attenuated by the object. The probability of one photon being absorbed by the object is proportional to $|t(x_i, y_i)|^2$. The probability of both photons being absorbed is therefore proportional to $|t(x_i, y_i)|^4$.

The profile of the object has been encoded in the diagonal of $G^{(2)}$. In reality the photons are not perfectly correlated; they have a finite correlation width that broadens the bright diagonal (or anti-diagonal) of the $G^{(2)}$. However, the object is still encoded in this broader diagonal, as demonstrated in Figure 2.13. Here we see how the object modulates the correlations (Figure 2.13a) such that an image of the object can be extracted by taking the diagonal elements (Figures 2.13c and e). This diagonal image is usually the quantity of interest in a correlation-based quantum imaging experiments, such as quantum image distillation [70] and resolution enhancement [135].

As discussed previously however, the pixel resolution for quantum imaging is typically limited to less than 150 × 150 pixels which will often negate the improved optical resolution afforded by correlation imaging in the first place. The pixel super-resolution method reported in Ref. [1] offers a potential solution to this problem by artificially increasing the effective pixel resolution using extra information present in the $G^{(2)}$.

2.6.2 Additional Information Contained in the $G^{(2)}$

From Figure 2.13b we can see that the object is not only encoded in the main diagonal, but also in some of the off-diagonals as well. As a reminder, the diagonal elements $G^{(2)}_{ii}$ correspond to the correlations between pixel i and itself. With an object, this corresponds to pairs whose photons both pass through the object at position x_i, and is proportional to the square of direct intensity image of the object as discussed above. The first off-diagonal elements $G^{(2)}_{i(i\pm1)}$ correspond to the correlations between a pixel i and its neighbouring pixels $i \pm 1$. This corresponds to pairs that are centred in between pixels i and $i \pm 1$. We can say that these photons sample the object at position $x_{i\pm1/2}$, i.e. halfway between x_i and $x_{i\pm1}$. The images extracted from the off-diagonals therefore sample different positions within the object compared to the main diagonal image. The diagonal and off-diagonal images, which have the same pixel-resolution as the camera sensor, can be combined into a higher resolution image with twice the number of pixels.

The images can be combined by taking the sum-coordinate projection of the $G^{(2)}$, which interleaves the elements of the diagonal and off-diagonal images. To see this, recall from the definition of the sum-coordinate projection from Equation 2.22, that the even elements are given by

$$C^{+}_{i_+=2k} = G^{(2)}_{kk} + 2\sum_{l=0}^{N} G^{(2)}_{(k-2l)k}, \tag{2.34}$$

and the odd elements by

$$C^{+}_{i_+=2k+1} = 2G^{(2)}_{k(k+1)} + 2\sum_{l=1}^{N} G^{(2)}_{(k-2l-1)k}. \tag{2.35}$$

Now we introduce the assumption that the correlation width σ is smaller than the pixel pitch Δ. This means that the correlations between non-neighbouring pixels is negligibly small and can be omitted, so we are left with

$$\begin{aligned} C^{+}_{i_+=2k} &= G^{(2)}_{kk}, \\ C^{+}_{i_+=2k+1} &= 2G^{(2)}_{k(k+1)}. \end{aligned} \tag{2.36}$$

Therefore, the sum-coordinate projection is equal to a combination of the diagonal and first off-diagonal images. In reality, the $G^{(2)}$ consists mostly of noise which, when it is summed, dominates the true signal in the final high-resolution image. To avoid this the $G^{(2)}$ is filtered by removing the weak correlation values. In this case it means setting all of elements outside of the diagonal and off-diagonals to zero. These elements contain little to no correlation information so this allows us to retain the object information while removing the excess noise contributions.

Lastly, recall that the diagonal elements do not actually contain any real correlation information for most cameras. The values of these elements are estimated by taking the mean of the neighbouring elements. However this means that, for a 1d measurement, the diagonal doesn't contain any more information than the off-diagonals. We can still extract more information in the case of a 2d measurement. In 1d, there are two off diagonals corresponding to correlations between pixel i and the pixels $i \pm 1$. In 2d there are now eight off-diagonals, corresponding to the correlations between pixel (i, j) and all neighbouring pixels: $(i, j \pm 1), (i \pm 1, j), (i+1, j \pm 1), (i-1, j \pm 1)$. The diagonal elements can be estimated from the off-diagonals in one direction e.g. j which gives a high-resolution image the i direction. This way, two images with pixel super-resolution in the horizontal and vertical directions can be retrieved. Unfortunately, it is not possible to increase the resolution in both directions with an EMCCD camera due to charge smearing obscuring the adjacent-pixel correlations along the rows. It should be noted that this pixel super-resolution technique can also work in the far-field illumination configuration, where the object and camera are in FF planes of the crystal. The main difference is that the object is now encoded in the anti-diagonal and off-anti-diagonals of the $G^{(2)}$ instead. A FF illumination scheme also circumvents the need to estimate the diagonal elements, since the correlations are now between diametrically opposite pixels. It is also possible to avoid this diagonal estimation in a NF configuration if the pairs are separated and imaged onto two cameras (or two separate regions of the same camera), as in Refs. [62, 64].

2.6.3 Demonstration of Pixel Superresolution and Image Frequency Analysis

Figures 2.14 a-c show an example of an object - a horizontal grating - where there appears to be an improvement of the resolution in the sum-coordinate projection image. To verify that we have actually sampled more of the object and not just artificially added pixels we use the tools of Fourier analysis. The Fourier transform of an image gives the spatial frequency content of that image. In this case, since the object only has structure in one direction, we use the 1-d Fourier transform. Figure 2.14d shows the frequency content of a direct intensity image, a $G^{(2)}$ diagonal image, and a sum-coordinate projection image. A fundamental concept in sampling theory is the Nyquist-Shannon limit [136]. This states that the maximum frequency in a signal that can be sampled without aliasing[1] is equal to half the sampling rate. Practically, this means

---

[1] Aliasing is the introduction of artefacts into a signal due to discrete sampling. The most common example of this is the illusion of wheels spinning backwards on camera when they are rotating with a frequency near the camera

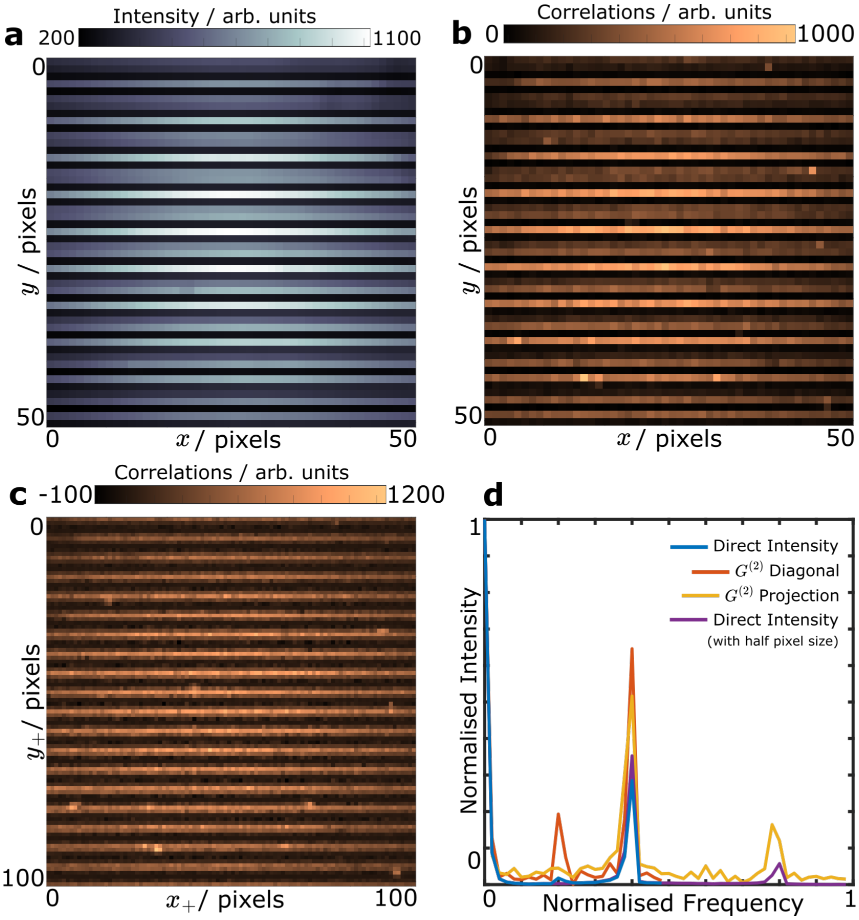

Figure 2.14: **Demonstration of $G^{(2)}$ pixel super-resolution. a,** Direct intensity image of grating object with a period close to twice the camera pixel pitch i.e. the Nyquist-Shannon limit. **b,** Image of the grating from diagonal elements of $G^{(2)}$. **c,** Sum-coordinate projection of $G^{(2)}$ after filtering elements with no correlation information. **d,** Vertical spatial frequency spectrum of images **a-c** and spectrum of a direct intensity image captured using a camera with half the pixel pitch (i.e. twice the pixel resolution). The rightmost peak in the projection image spectrum (yellow) is due to the extra frequency information recovered by doing the sum-coordinate projection. This is corroborated by the peak in the double-resolution intensity image spectrum (purple) at the same location. The leftmost peak in the diagonal image spectrum (red) is due to aliasing of frequencies in the object that are above the Nyquist-Shannon limit. All data is from an acquisition of 5×10^6 frames, using the Andor Ixon 897 EMCCD camera with an exposure time of 2 ms and an ROI of 100×100 pixels. The data was then binned into 2×2 macropixels before processing the $G^{(2)}$ to emulate a camera with a lower pixel resolution.

that structures smaller than twice the pixel pitch will not be properly resolved by a camera. We see this in Figures 2.14a,b,d, where the grating appears to contain extra frequencies that are not really present.

Slanted-edge Experiment

My primary contribution to this project was in performing an alternative frequency-analysis experiment to verify the super-resolution concept. This was based on the slanted-edge method to recover the system's modulation transfer function (MTF) [137, 138]. The MTF is the modulus of the optical transfer function (OTF), denoted $H(\nu_x, \nu_y)$, which describes how the spatial frequencies of an object signal are modulated by the image system and is a characteristic quantity of the system. The MTF can be measured by imaging a sharp edge, typically a razor blade, with the imaging system. For a sharp enough edge, we can assume that its transmission can be described as a step function

$$t(x) = \begin{cases} 1 & \text{for } x \geq 0 \\ 0 & \text{for } x < 0. \end{cases} \tag{2.37}$$

Then, the image of the edge at the camera will be blurred by the point-spread function (PSF) of the system. The resulting blurred image of an ideal edge object gives the edge-spread function (in the direction of the edge) of the system. Then, the derivative of the edge-spread function is equal to the 1-d point-spread function in the the direction of the edge. Finally, we can take the Fourier transform of this PSF to retrieve the MTF of the system. There is a slight problem with this method, however, as the image we measure at the camera is a discrete sampling of the edge profile. If the sampling rate is lower than the maximum frequency of the MTF, then we cannot retrieve the full information. This is where the slanted edge is useful. If we use an edge that is at a small angle relative to the horizontal axis, then each column of pixels effectively samples an image of the edge that is shifted by a distance less than the pixel pitch. By re-centring and summing the edge-spread function captured by each column we can combine these shifted samples to greatly increase the sampling rate and accurately measure the system MTF. The results are shown in Figure 2.15.

The slanted edge method gives a different measure of the frequency content to the Fourier transform of the grating object images. While it is always useful to have two separate measurements of the same quantity for confirmation, the slanted edge method is not actually best suited to our specific experiment. To understand why, it is important to highlight the difference between optical resolution and pixel resolution. The optical resolution of an imaging system tells us that the smallest feature size (i.e smallest detail) that is resolvable assuming an ideal camera whose pixels are infinitesimally close together (i.e. one with an infinite spatial sampling rate). This is limited by factors such as the lenses, system geometry, and the wavelength of light being used.

---

framerate.

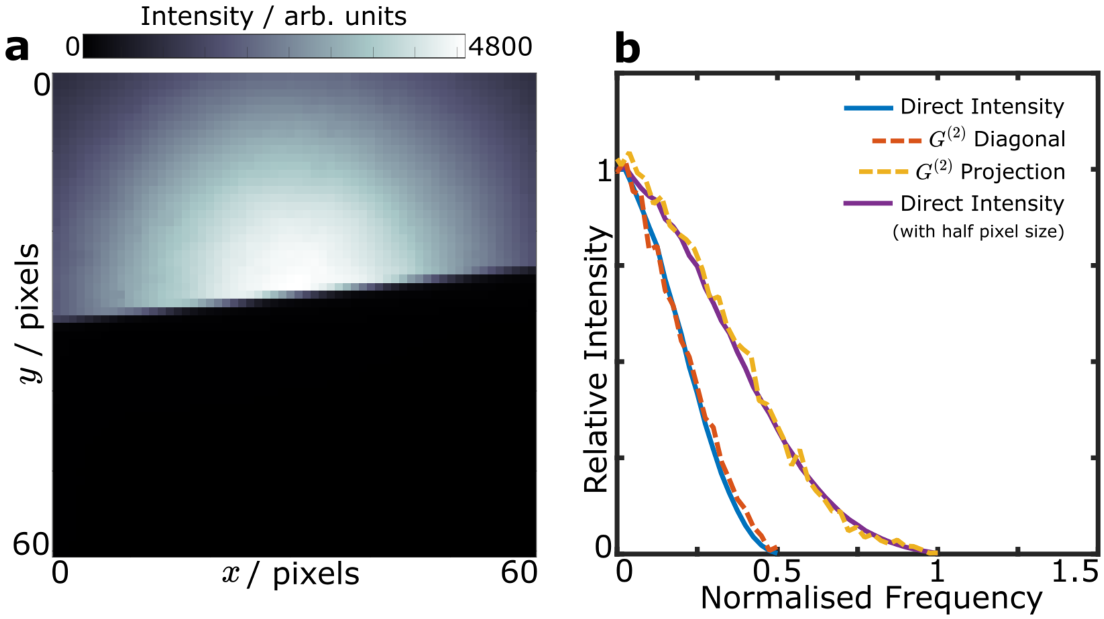

Figure 2.15: **Slanted edge frequency analysis. a,** Direct intensity image of slanted razor blade object. **b,** Modulation transfer functions for direct intensity, $G^{(2)}$ diagonal, $G^{(2)}$ projection, and double-resolution direct intensity images. Curves show the intensity of spatial frequency components relative to the DC (i.e. non-oscillating) value. Data from an acquisition of 6×10^6 frames with the Andor Ixon 897 EMCCD at a 2 ms exposure time, with an ROI of 120×120 pixels.

Mathematically, it is given by the width of the system PSF. Pixel resolution on the other hand is given by the size, or more accurately the spacing, of the camera pixels i.e. the sampling rate of the measurement. These are two independent quantities that can both limit the minimum resolvable feature size.

The primary purpose of the slanted edge method is to quantify the optical resolution of an imaging system without being limited by the camera's pixel resolution. Since we are interested in quantifying the increase in pixel resolution, it is not necessarily the best tool. However, when the pixel resolution is the limiting factor over the optical resolution, it still gives a measure of the spatial frequency content of the pixelised image. We can see from Figure 2.15b that the MTF has a cutoff at a higher frequency which confirms that the sum-coordinate projection images genuinely contain more spatial information.

2.6.4 Application to Other Quantum Imaging Techniques

This pixel super-resolution method has the benefit that it can be applied in many other pre-existing quantum imaging techniques. It does not require any experimental modification; the only requirement is to process the data in a different manner. Figure 2.16 shows the results of applying pixel superresolution to other quantum imaging applications, namely quantum image distillation [70] and entanglement-enabled holography [65].

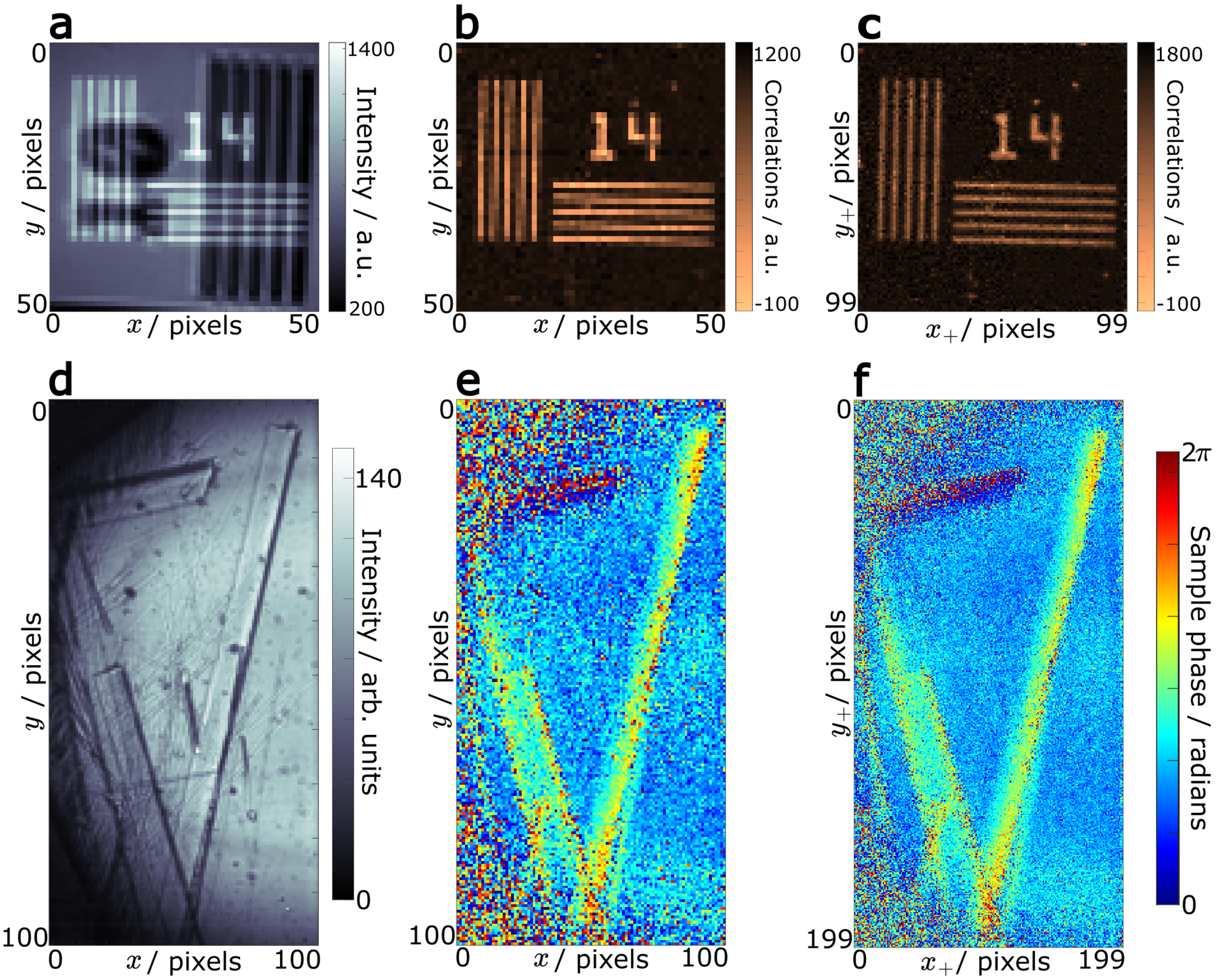

Figure 2.16: **Pixel super-resolution applied to other quantum imaging techniques. a-c,** Quantum image distillation (Ref [70]). **a,** Direct intensity image with desired object (number 14 and thin bars, light) illuminated with photon pairs plus undesired background light (number 10 and thick bars). **b,** 'Distilled' image containing only desired object, reconstructed from diagonal elements of $G^{(2)}$. **c,** 'Distilled' image with enhanced resolution obtained by projecting the measured $G^{(2)}$ onto the sum-coordinate axis. **d-e,** Entanglement-enabled holography. **a,** Direct intensity image of sample - a piece of a bird feather. **e,** Phase image of sample. **f,** Super-resolved phase image of sample. Data from Ref. [1].

2.7 Discussion

The aim of this chapter was to introduce a quantum imaging ‘toolkit’; a collection of concepts, techniques and equipment that I have used to build and run all of the experiments described in this thesis. This is not a comprehensive list -as we saw in Chapter 1 quantum imaging covers a broad range of techniques - but it gives the foundation for this thesis. SPDC is the go-to source for photon pairs because, despite its low power, it requires a relatively simple experimental setup - a continuous-wave laser and a crystal - and it can generate spatially multi-mode states that are essential for imaging. Single photon sensitive cameras allow for rapid, parallel measurement of these multi-mode states, enabling the capture of the rich information that is contained within the photon-pair correlations in the form of the spatial $G^{(2)}$. Pixel-superresolution was chosen as an example because it illustrates the main concepts of imaging with photon pairs. Specifically, it demonstrates that images can be encoded in the pairs’ spatial correlations, and that the correlations genuinely do contain extra information that can be extracted by performing the appropriate projection on the $G^{(2)}$.

The diagonal projections are particularly useful. As discussed in this chapter, they allow the correlation width of the pairs to be evaluated in a fraction of the time it would take to characterise the full $G^{(2)}$. As we will see in the next chapters, the sum- and minus-coordinate projections actually capture a wealth of information about the pairs’ correlations and how they are affected by the environment in which the pairs propagate. The focus of this chapter was on introducing the practical, experimental concepts of quantum imaging. In the follow chapter I introduce another experimental concept: that we can shape and control the photon pair correlations. Along with the practical consideration, I also introduce the theoretical framework that we use to describe the propagation and shaping of photon pair states.

Chapter 3

Shaping the two-photon wavefunction

This chapter is based on the work presented in Ref. [4] titled *'Shaping the Spatial Correlations of Entangled Photon Pairs'* by authors Patrick Cameron, Baptiste Courme, Daniele Faccio, and Hugo Defienne. This is an invited paper for a tutorial issue of the Journal of Physics: Photonics on the topic of wavefront shaping. The manuscript is currently in review.

3.1 Introduction

As I have discussed in the previous chapters, one of the main benefits of imaging with photon pairs is that it allows us to beat the classical limits of resolution [27] and sensitivity [68, 139]. Many new methods based on exploiting the correlations of photon pairs have been enabled in the last decade with the advent of EMCCD and SPAD camera technology, and with easy-to-implement photon pair sources based on SPDC (see Chapter 2). However, these sources are still very low intensity, and camera technology is still limited in terms of temporal resolution, detection efficiency, and acquisition speed. While improvements to all of these factors are very likely to happen in the future, quantum imaging concepts are not yet compatible with real-word applications.

While we wait for brighter sources and faster cameras, we can focus on developing other aspects of quantum imaging methods. In this regard, it is interesting to take inspiration from concepts in classical microscopy. In fact, microscopy is already quite compatible with quantum imaging. Most quantum imaging methods require precise control over the source of illumination, as this is typically where the 'quantum' aspects originate from. Also, due to the sensitivity requirements of single-photon or photon-pair measurements, they must also be done in controlled, low-light environments. Microscopes in lab environments clearly allow for both of these requirements, and so microscopy is an obvious direction for quantum imaging. Luckily, there is already a vast amount of research and development dedicated to improving classical microscopes, the concepts

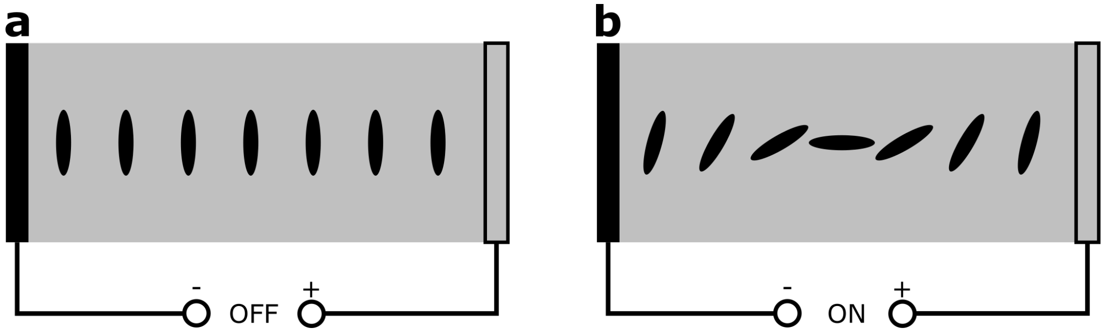

Figure 3.1: **Schematic of a liquid crystal SLM pixel. a,** Liquid crystal orientation with no voltage applied across electrodes. **b,** Liquid crystal orientation with an applied voltage.

of which can potentially be adapted to quantum imaging. In particular, in this chapter I will focus on the concepts and techniques of light shaping.

Light shaping can refer to a large number of techniques and methods to control one or more of the degrees of freedom of light. Pulse shaping aims to manipulate the temporal properties of a beam, while polarisation shaping controls the electric field vector. Here we are only doing spatial light shaping; controlling the spatial properties of the electric field, restricted to linearly polarised light. To perform this shaping, a device that can control the wavefront, i.e. the phase profile, of a light beam is used. These devices are known as Spatial Light Modulators (SLMs). While there are many devices based on different technologies and principles, in this thesis I have used only liquid crystal SLMs.

SLMs are arrays of liquid crystal cells whose birefringence can be controlled on an individual pixel level. The liquid crystals are made up of long molecules that tend to become aligned together, leading to optical anisotropy. For a single pixel, the liquid crystals are contained in a layer between two electrodes. If a voltage is applied across these electrodes then the liquid crystal molecules become oriented along the direction of the electric field. The refractive index of the liquid crystal layer depends on this orientation and can therefore be controlled by the applied voltage across the electrode. The crystals' anisotropy also means they are birefringent so their refractive index also depends on the polarisation of the incident light. For linearly polarised, monochromatic light, the refractive index and therefore optical path length of each pixel can be precisely set. This can be used to imprint (almost) arbitrary phase profiles on an incident beam. Figure 3.1 shows a schematic diagram of an SLM pixel.

Such control has many applications, especially in imaging and microscopy [140]. Examples include structured illumination microscopy [82], which aims to improves imaging resolution by illuminating the sample with a specifically tailored pattern of light, adaptive optics [83] and wavefront shaping [141], which use SLMs to correct for optical aberrations and scattering, and even contrast-enhanced and quantitative phase imaging methods [142, 143]. Clearly, light shaping is an extremely powerful tool, and it is interesting to see how it can be used to improve quantum

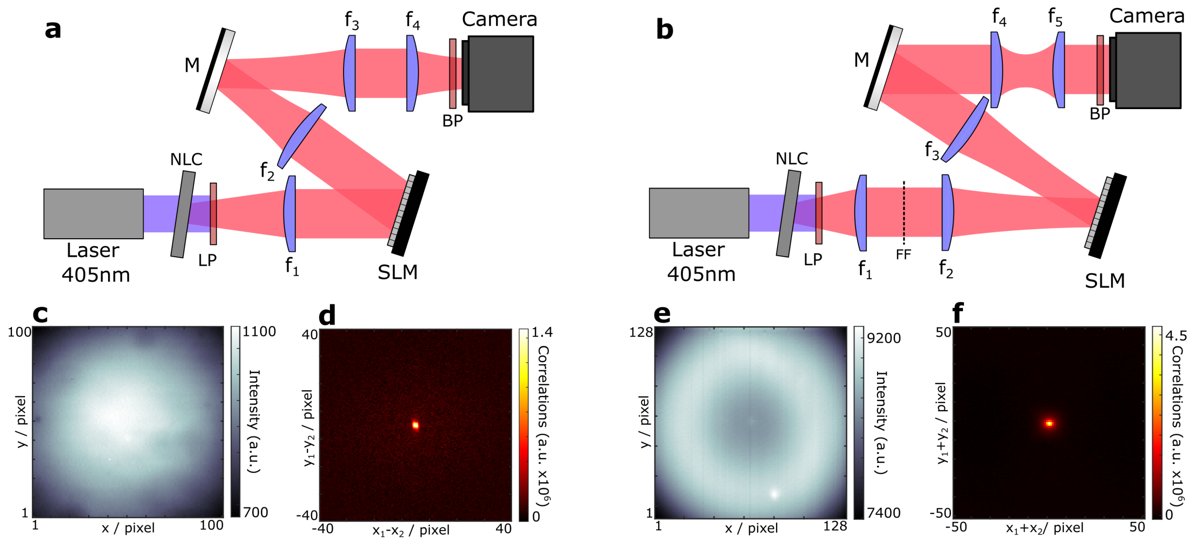

Figure 3.2: **Experimental setup for shaping the two-photon correlations.** Spatially entangled photon pair at ~ 810 nm are produced via Type I spontaneous parametric down conversion (SPDC) using a collimated, continuous-wave laser at 405 nm and a thin β−Barium Borate nonlinear crystal (NLC). Pump photons are filtered out by a long-pass filter (LP) at 650 nm. A band-pass filter at 810±5 nm before the single-photon sensitive camera filters out any non-degenerate pairs. **a,** Diagram of a near-field (NF) imaging configuration. The plane of the NLC is imaged onto the camera using two 4-f relays ($f_1 - f_2$ and $f_3 - f_4$). The spatial light modulator (SLM) is placed in the Fourier plane, or far-field, of the crystal. In this configuration, the photons are correlated at the camera, and anti-correlated at the SLM. **b,** Diagram of a far-field (FF) imaging configuration. The Fourier plane of the BBO is imaged into the camera with two 4f relays ($f_2 - f_3$ and $f_4 - f_5$). The SLM is placed in the near-field plane of the NLC. In this configuration, the photons are anti-correlated at the camera, and correlated at the SLM. **c,e,** Direct intensity images from the camera in the NF imaging and FF imaging configurations, respectively. **d,** Minus-coordinate projection of the measured $G^{(2)}$ in the NF imaging configuration. **f,** Sum-coordinate projection of the measured $G^{(2)}$ in the FF imaging configuration. **c,d** are from an acquisition of 2.5×10^5 frames. **e,f** are from an acquisition of 6×10^6 frames. M - mirror.

imaging applications. In this chapter I describe two simple photon-pair shaping experiments that illustrate some of the important differences between classical and quantum shaping, as well as the theoretical framework we use to describe photon-pair-based imaging. I also discuss some interesting applications of such two-photon shaping that go even beyond imaging. For example, we will see that this type of control can also be very useful for quantum communications (Subsection 3.5.1).

3.2 Experiment

When shaping and detecting correlated photon pairs, there are two main configurations that can be used. These are the near-field (NF) and the far-field (FF) imaging configurations. Figure 3.2 **a,b** shows schematics of these two configurations. These are named for the optical plane in which camera is placed. In the far-field case, the lenses are such that the plane of the crystal surface is conjugate to the SLM. Similarly, in the near-field case the Fourier-plane of the crystal is conjugate to the SLM plane. Due to the phase matching conditions in the SPDC process, the photons at the plane of the crystal are strongly correlated in transverse position ($\mathbf{r}$) and strongly anti-correlated in transverse momentum ($\mathbf{q}$). Both of these types of correlations can be exploited, hence the two experimental configurations.

In both cases, the source of photon pairs is a thin BBO crystal that is pumped by a continuous-wave (CW) laser with a wavelength of 405 nm via Type I SPDC. This generates photon pairs centred at 810 nm. Immediately after the crystal a 650 nm cutoff long-pass filter is used to filter the pump photons while allowing the photon pairs to propagate through the rest of the system. After propagating through the system the pairs are detected using an EMCCD camera, and the spatial correlations are measured using the method described in Ref. [121] and in Section 2.3. In both cases, an SLM placed in a Fourier plane of the camera is used to control the light. Finally, a band-pass filter at 810 ± 10 nm is placed immediately before the camera to ensure that only approximately degenerate photon pairs are detected.

The near-field (NF) imaging configuration is shown in Figure 3.2a. As the name suggests, the crystal surface is imaged onto the EMCCD camera and the SLM is positioned in a Fourier plane of the crystal. Figure 3.2 **c** shows an example of the intensity at the camera. The shape of this is mostly dependent on the intensity profile of the pump. Figure 3.2 **d** shows the minus-coordinate projection of the measured $G^{(2)}$ of the photon pairs. The bright, narrow peak, as seen in Figure 3.2**d**, tells us that the pairs are strongly correlated in position. Physically, this means that when a photon from a pair is detected at a position (x_1, y_1), it is very likely that its twin will be detected within a very small area around the same pixel $(x_2, y_2) \approx (x_1, y_1)$. No phase mask was displayed on the SLM to perform this measurement.

The far-field (FF) imaging configuration is shown in Figure 3.2b. Here, the EMCCD is now in a Fourier plane of the crystal and the SLM is positioned instead in a conjugate plane of the crystal's surface. Figure 3.2 **e** shows an example of the intensity at the camera. Here, the classic SPDC ring can be seen. The thickness of this ring is proportional to the bandwidth of the pairs, and the radius is dependent on the angle between the optical axis and the normal to the crystal surface. Figure 3.2 **f** shows the sum-coordinate projection of the measured $G^{(2)}$. It represents the probability of measuring two photons from a pair on two anti-symmetric pixels of the camera (x_1, y_1) and (x_2, y_2), with the barycentre positioned at $(x_1 + x_2, y_1 + y_2)$. In this case, the presence of an intense peak at the centre indicates strong spatial anti-correlation. This tells us that, when a photon from a pair is detected at a position (x_1, y_1), it is very likely that its twin will be detected within a very small area around the diametrically opposite pixel $(x_2, y_2) \approx (-x_1, -y_1)$. No phase mask was displayed on the SLM to perform this measurement.

3.3 Classical and Quantum Shaping Theory

I will now introduce the theoretical framework that we use to describe photon pair imaging experiments. Since this idea of shaping is inspired from classical imaging, it is interesting to compare classical and quantum shaping. A convenient way to do this is to work with the spatial correlation functions, specifically the first and second order functions $G^{(1)}$ and $G^{(2)}$ [144]. The quantities that we measure in experiment can be written in terms of these functions, and they can be used to derive expressions for propagation through optical systems. First we introduce the relevant measured quantities, and how they are written in terms of the correlation functions.

For classical imaging and shaping, the quantity of interest is the intensity of the electric field, $I(\mathbf{r}) = |E(\mathbf{r})|^2$. It can be written in terms of the first-order spatial correlation function of the field as

$$\begin{aligned} I(\mathbf{r}) &= G^{(1)}(\mathbf{r}, \mathbf{r}) && (3.1) \\ &= \langle \hat{E}^{(-)}(\mathbf{r}) \hat{E}^{(+)}(\mathbf{r}) \rangle. && (3.2) \end{aligned}$$

Here, $\langle ... \rangle$ denotes an ensemble average, and $\hat{E}^{(+)}$ and $\hat{E}^{(-)}$ are, respectively, the positive and negative frequency components of the quantum operator associated with the electric field. In practice, the intensity is typically measured by accumulating photons at each pixel of a camera. The camera signal at each pixel is therefore proportional to the intensity at that pixel.

As we have seen, when working with photon pairs we are instead more interested in the second-order spatial correlation function of the intensity, $G^{(2)}(\mathbf{r_1}, \mathbf{r_2})$. It can be written in terms of the second-order spatial correlation function of the field as:

$$G^{(2)}(\mathbf{r_1}, \mathbf{r_2}) = \langle \hat{E}^{(-)}(\mathbf{r_1}) \hat{E}^{(-)}(\mathbf{r_2}) \hat{E}^{(+)}(\mathbf{r_1}) \hat{E}^{(+)}(\mathbf{r_2}) \rangle. \qquad (3.3)$$

In classical imaging, information is typically encoded and transmitted in the intensity of the field. The interest of photon-pair imaging is the richer information available in this $G^{(2)}$. In practice, we measure $G^{(2)}(\mathbf{r_1}, \mathbf{r_2})$ by detecting photon coincidences between pairs of spatial positions $\mathbf{r_1}$ and $\mathbf{r_2}$. It can also be reconstructed using the method described in [121] and in Section 2.3. It gives the probability of simultaneously detecting a photon at position $\mathbf{r_1}$ and a photon at position $\mathbf{r_2}$. As we will see, if we have a pure two-photon state with spatial wavefunction ϕ, the intensity correlations can be related to this wavefunction as $G^{(2)}(\mathbf{r_1}, \mathbf{r_2}) = |\phi(\mathbf{r_1}, \mathbf{r_2})|^2$. We see the same relationship between $G^{(2)}$ and ϕ in the two-photon case as we see between I and E in the classical case. We will see by the end of this section that we can shape these two quantities in similar manners.

Since we want to see how we can shape the distributions I and $G^{(2)}$, it is useful to know how they propagate through an imaging system. Any linear system can be fully described by its complex

PSF. This is written $h(\mathbf{r}', \mathbf{r})$, where the coordinates in the input plane are represented by $\mathbf{r}$, and the coordinates in the output plane by $\mathbf{r}'$. Given the PSF, the correlation functions can be propagated through a linear system as:

$$G^{(1)}(\mathbf{r_1}', \mathbf{r_2}') = \int G^{(1)}(\mathbf{r_1}, \mathbf{r_2}) h^*(\mathbf{r_1}', \mathbf{r_1}) h(\mathbf{r_2}', \mathbf{r_2}) d\mathbf{r_1} d\mathbf{r_2} \tag{3.4}$$

and

$$\begin{aligned} G^{(2)}(\mathbf{r_1}', \mathbf{r_2}', \mathbf{r_3}', \mathbf{r_4}') = \int & G^{(2)}(\mathbf{r_1}, \mathbf{r_2}, \mathbf{r_3}, \mathbf{r_4}) h^*(\mathbf{r_1}', \mathbf{r_1}) h^*(\mathbf{r_2}', \mathbf{r_2}) \\ & h(\mathbf{r_3}', \mathbf{r_3}) h(\mathbf{r_4}', \mathbf{r_4}) d\mathbf{r_1} d\mathbf{r_2} d\mathbf{r_3} d\mathbf{r_4}. \end{aligned} \tag{3.5}$$

These expressions are the most general form for describing how the first and second-order correlation functions propagate through a system. If we know the form of the correlation functions at the input and we know the PSF describing the system, then we can derive expressions relating the input and output states. In the following we will consider the simple shaping configuration introduced in the previous section, and shown in Figure 3.2. In this experiment, we say that the input plane is immediately before the SLM, and the output plane is that of the camera. Since the action of the SLM is simply to impart a phase profile $\theta(\mathbf{r})$ onto the beam, the PSF can be written

$$h(\mathbf{r}', \mathbf{r}) = h_{lens}(\mathbf{r}', \mathbf{r}) \exp\left[i\theta(\mathbf{r})\right], \tag{3.6}$$

with

$$h_{lens}(\mathbf{r}', \mathbf{r}) = \exp\left[-\frac{2\pi i \mathbf{r}\mathbf{r}'}{f\lambda}\right], \tag{3.7}$$

where f is the focal length of the lens immediately after the SLM, λ is the wavelength of the light being used, $\mathbf{r}$ and $\mathbf{r}'$ are the transverse coordinates in the SLM and camera plane, respectively. Note that the normalisation coefficient of h_{lens} has been omitted for clarity. Now that we know the PSF of our system, let's consider some different states of light that are of interest to us.

3.3.1 Shaping Coherent Light

First we consider a well-collimated laser at the input. In the ideal case, a laser is a perfectly spatially coherent source. The first-order correlation function for such a source is given by [144]

$$G^{(1)}_{coh}(\mathbf{r_1}, \mathbf{r_2}) = E^*(\mathbf{r_1}) E(\mathbf{r_2}), \tag{3.8}$$

where $E(\mathbf{r})$ is the electric field at position $\mathbf{r}$ and * denotes the complex conjugate. Thus, from equations 3.2 and 3.4, the intensity after the system is given by

$$I_{coh}(\mathbf{r}') = \left| \int E(\mathbf{r}) h(\mathbf{r}', \mathbf{r}) d\mathbf{r} \right|^2 . \tag{3.9}$$

Using equation 3.6 and simplifying, we get the intensity at the camera

$$I_{coh}(\mathbf{u}) = \left| \left[\mathcal{F}\left[E(\mathbf{r})\right] * \mathcal{F}\left[e^{i\theta(\mathbf{r})}\right] \right] \left(\frac{\mathbf{r}'}{f\lambda} \right) \right|^2 , \tag{3.10}$$

where $\mathcal{F}[...]$ is the 2-dimensional Fourier transform, and $\mathbf{u} = \mathbf{r}'/f\lambda$. The $*$ denotes the 2-dimensional convolution operation such that

$$[f * g](\mathbf{r}') = \int_{-\infty}^{\infty} f(\mathbf{r}) g(\mathbf{r}' - \mathbf{r}) d\mathbf{r}. \tag{3.11}$$

This is the expected result from Fourier-optics and says that the field measured at the camera is simply the (scaled) Fourier transform of the mask on the SLM. The intensity correlation function for a coherent source is

$$G^{(2)}(\mathbf{r_1}, \mathbf{r_2}) = I_{coh}(\mathbf{r_1}) I_{coh}(\mathbf{r_2}). \tag{3.12}$$

Clearly, if the intensity is known, then the intensity correlations can be fully reconstructed so they do not contain any additional information when the light is perfectly coherent.

3.3.2 Shaping Incoherent Light

At the opposite extreme to coherent light we have incoherent light. In the case of a perfectly incoherent source, e.g. an extended thermal source, the first-order correlation function has the form

$$G^{(1)}_{inc}(\mathbf{r_1}, \mathbf{r_2}) = I_0(\mathbf{r_1}) \delta(\mathbf{r_1} - \mathbf{r_2}), \tag{3.13}$$

where $\delta(\mathbf{r})$ is the Dirac-delta distribution and $I_0(\mathbf{r})$ is the intensity profile of the beam. As before, we find an expression for the intensity after the system:

$$I_{inc}(\mathbf{r}') = \int I_0(\mathbf{r}) |h(\mathbf{r}', \mathbf{r})|^2 d\mathbf{r}. \tag{3.14}$$

Since $|h|$ is a constant for our system, we get

$$I_{inc}(\mathbf{r}') = \int I_0(\mathbf{r}) d\mathbf{r}. \tag{3.15}$$

In other words, the SLM effectively does nothing to incoherent light in this configuration. The intensity correlations for an incoherent source are given by the Siegert relation [145]

$$G^{(2)}_{inc}(\mathbf{r_1}, \mathbf{r_2}) = I_{inc}(\mathbf{r_1}) I_{inc}(\mathbf{r_2}) + |I_{inc}(\mathbf{r_1}) \delta(\mathbf{r_1} - \mathbf{r_2})|^2. \tag{3.16}$$

3.3.3 Shaping Entangled Photon Pairs

Now let's consider a two-photon state. Here we will see that entangled photon pairs exhibit both coherent and incoherent properties, depending on the quantity that we look at. We want to see how our state propagates from the input to the output of the system. The state at the input plane - the plane immediately before the SLM in the example of Figure 3.2 - is written

$$|\phi\rangle = \iint \phi(\mathbf{r_1}, \mathbf{r_2}) \, |\mathbf{r_1}, \mathbf{r_2}\rangle \, d\mathbf{r_1} d\mathbf{r_2}, \tag{3.17}$$

where $\phi(\mathbf{r_1}, \mathbf{r_2})$ is the position-basis wavefunction which describes the state, and $\mathbf{r_1}, \mathbf{r_2}$ are the transverse position vectors for photon 1 and photon 2 respectively. In this simplified notation, $|\mathbf{r_1}, \mathbf{r_2}\rangle = |\mathbf{r_1}\rangle_1 \otimes |\mathbf{r_2}\rangle_2$ denotes the state in which photon 1 is at position $\mathbf{r_1}$ and photon 2 is at position $\mathbf{r_2}$. The $G^{(1)}$ for such a state is given by

$$G^{(1)}_{pairs}(\mathbf{r_1}, \mathbf{r_2}) = \int \phi^*(\mathbf{r_1}, \mathbf{r}) \phi(\mathbf{r_2}, \mathbf{r}) d\mathbf{r}. \tag{3.18}$$

and direct intensity is then

$$I_{pairs}(\mathbf{r_1}) = \int \left|\phi(\mathbf{r_1}, \mathbf{r})\right|^2 d\mathbf{r}. \tag{3.19}$$

Additionally, one can compute the second-order field correlations as:

$$G^{(2)}_{pairs}(\mathbf{r_1}, \mathbf{r_2}, \mathbf{r_3}, \mathbf{r_4}) = \phi^*(\mathbf{r_1}, \mathbf{r_2}) \phi(\mathbf{r_3}, \mathbf{r_4}), \tag{3.20}$$

giving the intensity correlations :

$$G^{(2)}_{pairs}(\mathbf{r_1}, \mathbf{r_2}) = \left|\phi(\mathbf{r_1}, \mathbf{r_2})\right|^2. \tag{3.21}$$

From here we can see that the direct intensity is simply the marginal sum of the intensity correlations i.e. $I(\mathbf{r_1}) = \int G^{(2)}(\mathbf{r_1}, \mathbf{r}) d\mathbf{r}$. Now, using equations 3.4 and 3.5, I_{pairs} and $G^{(2)}_{pairs}$ can be expressed in the output (i.e. camera) plane as

$$I_{pairs}(\mathbf{r_1}') = \int \left| \int \phi(\mathbf{r_1}, \mathbf{r_2}) h(\mathbf{r_1}', \mathbf{r_1}) d\mathbf{r_1} \right|^2 d\mathbf{r_2}, \tag{3.22}$$

and

$$G^{(2)}_{pairs}(\mathbf{r_1}', \mathbf{r_2}') = \left| \iint \phi(\mathbf{r_1}, \mathbf{r_2}) h(\mathbf{r_1}', \mathbf{r_1}) h(\mathbf{r_2}', \mathbf{r_2}) d\mathbf{r_1} d\mathbf{r_2} \right|^2 \tag{3.23}$$

where $\mathbf{r_1}'$ and $\mathbf{r_2}'$ are the transverse positions in the camera plane, $\phi(\mathbf{r_1}, \mathbf{r_2})$ is the two-photon wavefunction in the SLM plane and h is the PSF.

Now we consider the two shaping configurations shown in Figures 3.2a and b. In both cases, the imaging system from the SLM to the camera, h, is the same (up to a different magnification factor), but the input states are different. We start with the configuration of Figure 3.2a. Here, the SLM is positioned in the Fourier plane of the crystal. In our experimental conditions the collimated pump beam diameter is much larger than the crystal thickness. Therefore, we assume that photon pairs can be considered to be near-perfectly anti-correlated in the plane immediately before the SLM. That is, the wavefunction $\phi(\mathbf{r_1}, \mathbf{r_2}) \approx \phi_0(\mathbf{r_1} - \mathbf{r_2})\delta(\mathbf{r_1} + \mathbf{r_2})$ [146], where ϕ_0 is the amplitude envelope of the two-photon wavefunction in the crystal Fourier plane. It is linked to the intensity measured in the SLM plane as $I(\mathbf{r}) = |\phi_0(\mathbf{r})|^2$. In practice, it takes the shape of a disk or a ring, as shown in Figure 3.2.e, and its spatial phase is assumed to be uniform. After performing the change of variables $\mathbf{r}_+ = (\mathbf{r_1} + \mathbf{r_2})/2$ and $\mathbf{r}_- = (\mathbf{r_1} - \mathbf{r_2})/2$, the intensity correlations in the camera plane can be expressed as

$$G^{(2)}(\mathbf{r}'_+, \mathbf{r}'_-) = \left| \left[\mathcal{F}\left[\phi_0(\mathbf{r})\right] * \mathcal{F}\left[e^{i\psi(\mathbf{k})}\right] \right] \left(\frac{2\mathbf{r}'_-}{f\lambda} \right) \right|^2 \tag{3.24}$$

where $\psi(\mathbf{k}) = \theta(\mathbf{k}) + \theta(-\mathbf{k})$ and all global constants are omitted for clarity. Now we consider the configuration in Figure 3.2b. Here we are imaging the crystal plane onto the SLM. Since we have thin crystal and a large pump diameter, we can assume that the photon pairs are perfectly correlated, i.e. $\phi(\mathbf{r_1}, \mathbf{r_2}) \approx \phi'_0(\mathbf{r_1} + \mathbf{r_2})\delta(\mathbf{r_1} - \mathbf{r_2})$ [146], where ϕ'_0 is the amplitude envelope of the two-photon wavefunction in the crystal plane. It is linked to the intensity measured in the SLM plane as: $I(\mathbf{r}) = |\phi'_0(\mathbf{r})|^2$. In practice, it takes the shape of the pump beam, as shown in Figure 3.2.c, and its spatial phase is assumed to be uniform. Then, the intensity correlations at the camera are given by

$$G^{(2)}(\mathbf{r}'_+, \mathbf{r}'_-) = \left| \left[\mathcal{F}\left[\phi'_0(\mathbf{r})\right] * \mathcal{F}\left[e^{i2\theta(\mathbf{k})}\right] \right] \left(\frac{2\mathbf{r}'_+}{f\lambda} \right) \right|^2 . \tag{3.25}$$

Additionally, we find that the intensities I are uniform in both configurations. Thus, as would be the case for a perfectly spatially incoherent source, the phase programmed on the SLM does not modulate the intensity measured in the Fourier plane. Indeed, in our experimental conditions, the spatial coherence length in the SLM plane is very small, notably smaller than the variations in phase programmed on the SLM. By changing the crystal and the illumination conditions [147], it would be possible to work in an intermediate regime with partially spatially coherent light, allowing modulation of both the intensity and the intensity correlations.

Comparing equations 3.10, 3.25 and 3.24 we see that the spatial intensity correlations can be shaped in a manner that is almost equivalent to spatial intensity shaping in the classical case.

Under our experimental conditions, $\mathcal{F}[E(\mathbf{r})]$, $\mathcal{F}[\phi_0(\mathbf{r})]$ and $\mathcal{F}[\phi'_0(\mathbf{r})]$ are very sharply peaked. Therefore, they can be considered as Dirac-Delta distributions, allowing for the simplification of the equations to focus on the role played by the SLM:

- Classical: $I = \left|\mathcal{F}\left[e^{i\theta(\mathbf{r})}\right]\right|^2$,
- Pairs - NF imaging: $G^{(2)} = \left|\mathcal{F}\left[e^{i\psi(\mathbf{r})}\right]\right|^2$,
- Pairs - FF imaging: $G^{(2)} = \left|\mathcal{F}\left[e^{i2\theta(\mathbf{r})}\right]\right|^2$.

With entangled photon pairs we find that, depending on the configuration, the shaping behaves slightly differently. In the case of near-field imaging, we see that the phase on the SLM affects the projection in the form of the function $\psi(\mathbf{r}) = \theta(\mathbf{r}) + \theta(-\mathbf{r})$. In the case of far-field imaging, we see that the projection is affected by a $2\theta(\mathbf{r})$ phase term. As a reminder, the SLM is always in a far field plane relative the camera and the names of the configurations come from the position of the SLM relative to the crystal. In both cases the photon pairs effectively ‘see’ a phase mask that is different from the mask that is actually displayed on the SLM. In the case of NF imaging, the pairs’ spatial correlations are modulated by an effective mask that is equal to the real phase mask plus a spatially inverted version of it. Intuitively this makes sense, as the photons in each pair are modulated by symmetrically opposite pixels on the SLM. In the FF imaging case, the spatial correlations are modulated by twice the real phase mask. Again this makes sense as, in this case, both photons in each pair are modulated by the same SLM pixel. In the following section I show some experimental results which demonstrate these two-photon shaping effects.

3.4 Experimental Results

As discussed in the previous chapter, the spatial $G^{(2)}$ that we measure is a 4-dimensional object, and is therefore inconvenient for us to visualise. Therefore, we project the $G^{(2)}$ onto 2-dimensional images. In fact, we see that these projections are extremely convenient for viewing the spatial correlations. In Section 2.4 I introduced the discrete-variable projections $C^+_{i_+}$ and $C^-_{i_-}$. Now we are interested in the continuous-variable projections, which are defined as

$$C^-(\mathbf{r}_-) = \int_S G^{(2)}(\mathbf{r}_-, \mathbf{r}_+) d\mathbf{r}_+ \tag{3.26}$$

for the minus-coordinate projection, and

$$C^+(\mathbf{r}_+) = \int_S G^{(2)}(\mathbf{r}_-, \mathbf{r}_+) d\mathbf{r}_- \tag{3.27}$$

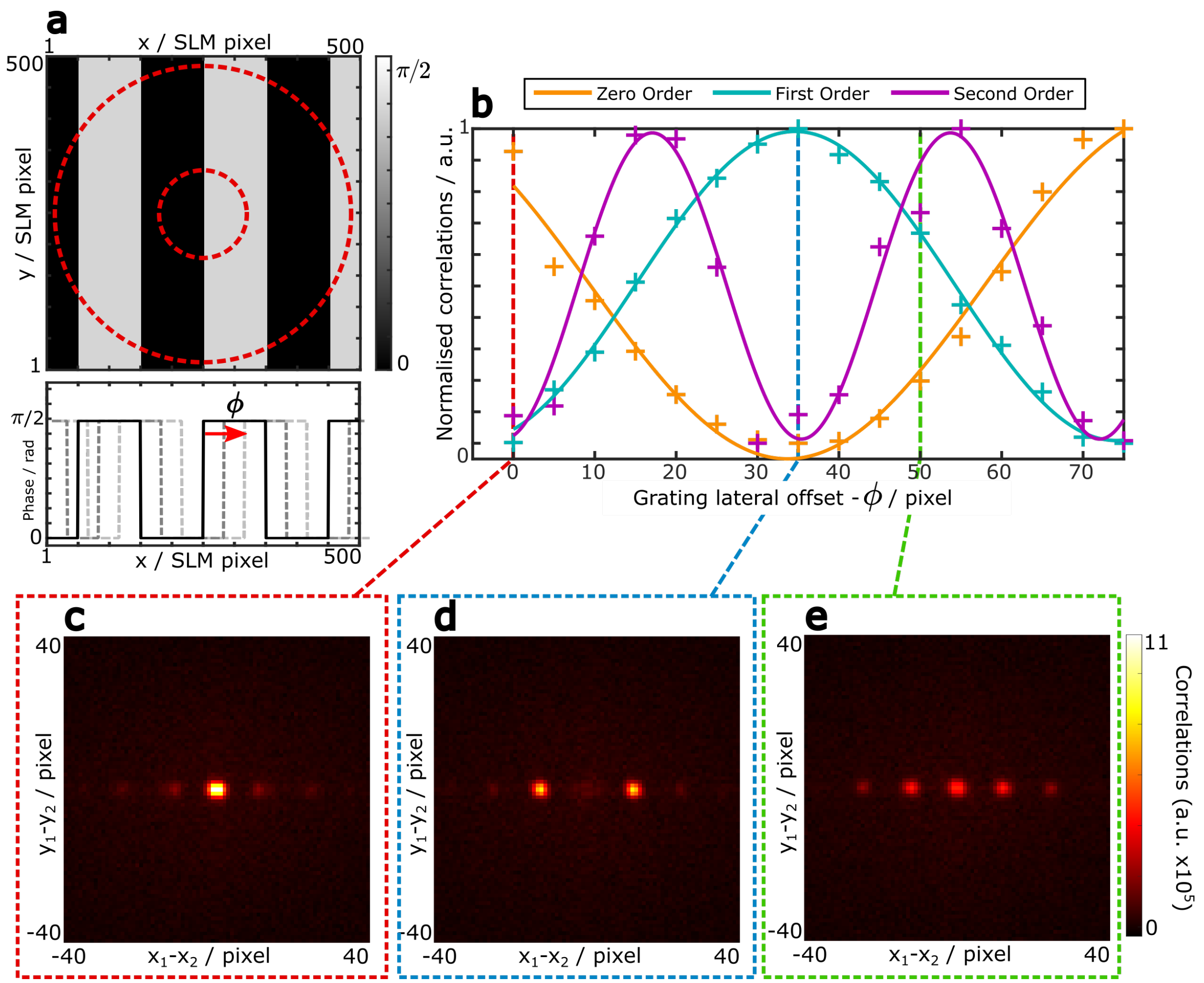

Figure 3.3: **Shaping the two-photon correlations in a near-field (NF) imaging configuration.** A phase grating (**a**) is displayed on the illuminated region of the SLM. Line plot shows a single row of the grating. Red dashed circles are illustration of approximate position of SPDC ring on the SLM. Grating width is exaggerated for illustrative purposes. The actual period used in acquisition was 75 pixels. **b,** Magnitude of correlation peaks as a function of grating lateral offset β. Crosses are data points, solid lines are sine fits. Data is normalised for each order individually to allow better visual comparison. **c-e,** Minus-coordinate projections of $G^{(2)}$ for $\beta = 0$ (**c**), $\beta = 35$ pixels (**d**), and $\beta = 70$ pixels (**e**) peaks (cropped). Correlations for each grating offset are from an acquisition of $\sim 1.8 \times 10^6$ frames.

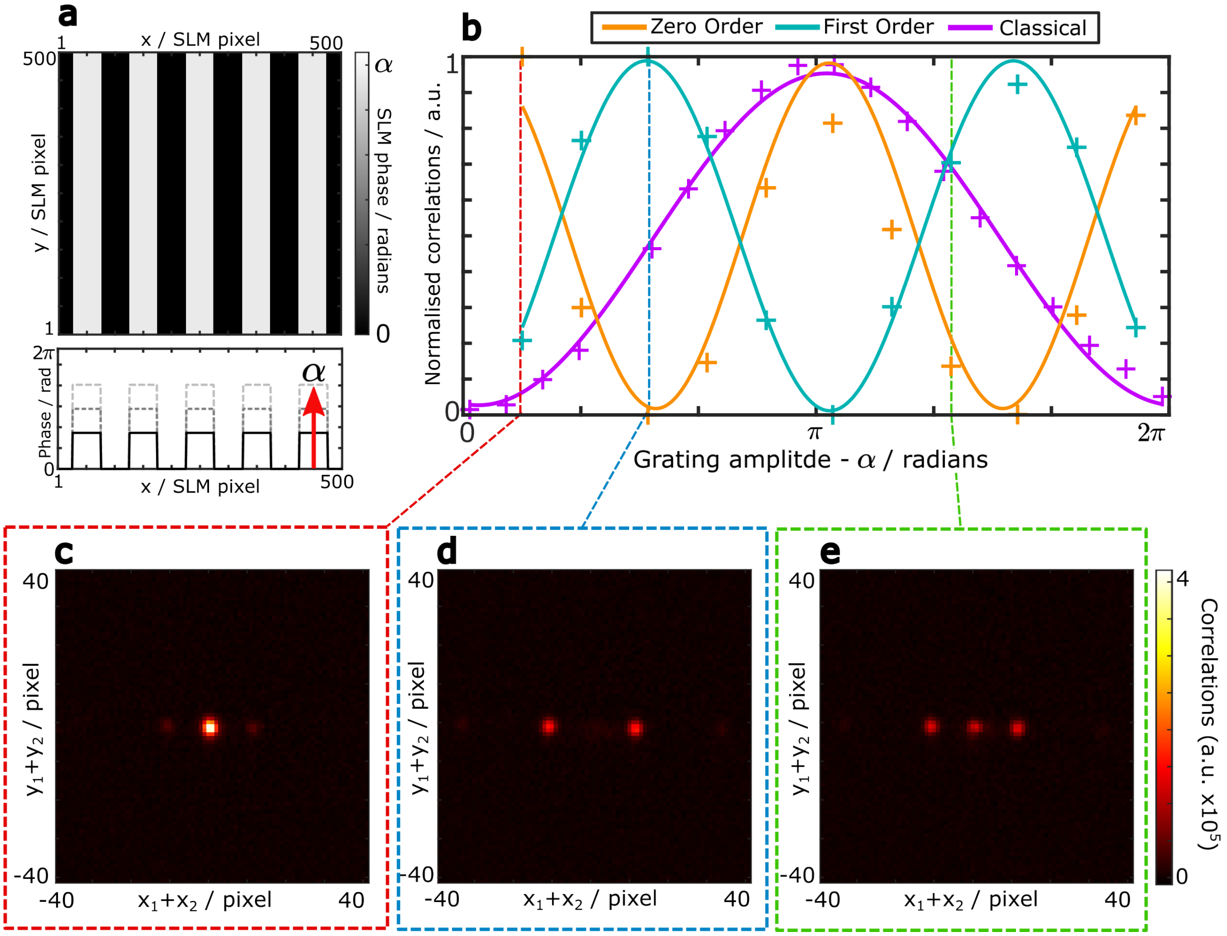

Figure 3.4: **Shaping the two-photon correlations in a far-field (FF) imaging configuration.a,** Phase grating displayed on the illuminated region of the SLM. Line plot shows a single row of the grating. **b,** Magnitude of correlation peaks as a function of grating amplitude α. Crosses are data points, solid lines are sinusoidal fits. Data is normalised for each order individually to allow better visual comparison. Classical data (purple) has scale of intensity, rather than correlations. **c,d** Sum-coordinate projections of $G^{(2)}$ for grating amplitude $\alpha = \pi/6$ (**c**), $\alpha = \pi/2$ (**d**) and $\alpha = 2\pi/9$ (**e**). Correlations for each grating amplitude are from an acquisition of $\sim 5 \times 10^5$ frames.

for the sum-coordinate projection, where $G^{(2)}$ is expressed here in the rotated basis $(\mathbf{r}_+, \mathbf{r}_-)$ and S is the integration area. $(\mathbf{r}_+, \mathbf{r}_-)$ are related to $(\mathbf{r}_1, \mathbf{r}_2)$ by

$$\begin{aligned} \mathbf{r}_+ &= \frac{1}{2}(\mathbf{r}_1 + \mathbf{r}_2) \\ \mathbf{r}_- &= \frac{1}{2}(\mathbf{r}_1 - \mathbf{r}_2) \end{aligned} \tag{3.28}$$

The projections expressed in the usual basis $(\mathbf{r}_1, \mathbf{r}_2)$ are

$$C^-(\mathbf{r}_-) = \int_S G^{(2)}(\mathbf{r}, \mathbf{r} + 2\mathbf{r}_-)d\mathbf{r} \tag{3.29}$$

and

$$C^+(\mathbf{r}_+) = \int_S G^{(2)}(\mathbf{r}, 2\mathbf{r}_+ - \mathbf{r})d\mathbf{r}. \tag{3.30}$$

Clearly, due to the symmetries of the measured $G^{(2)}$, these projections allow us to directly view the modulated correlations with no loss of information:

$$C^-(\mathbf{r}_-) \propto \left|\mathcal{F}\left[e^{i\psi(\mathbf{r})}\right]\right|^2 \quad \text{(NF)} \tag{3.31}$$

$$C^+(\mathbf{r}_+) \propto \left|\mathcal{F}\left[e^{i2\theta(\mathbf{r})}\right]\right|^2 \quad \text{(FF).} \tag{3.32}$$

Figure 3.3 shows the results for the NF imaging configuration, where we are imaging the surface of the crystal on the camera (Figure 3.2a). As a simple demonstration, we use a $\pi/2$-modulated phase grating pattern, shown in Figure 3.3a. According to Equation 3.24, the photon pairs in this system 'see' the actual grating plus a spatially inverted version. Therefore, if $\theta(\mathbf{r}) + \theta(-\mathbf{r}) = constant$, then we expect to see no modulation of the minus-coordinate projection. To demonstrate this, the grating is displayed on the SLM and translated laterally, measuring C^- at each lateral shift. Figure 3.3b shows the values of each diffraction order as a function of lateral shift. If the grating is positioned such that one of the steps is at the centre of the SPDC beam, then we have $\psi(\mathbf{r}) = \pi/2 = constant$ and we expect no modulation in the ideal case. Figure 3.3c shows the minus-coordinate projection measured in such a case. Even though we do not observe a complete extinction of higher orders, mainly due to the fact that the phase pattern is not perfectly asymmetric in practice, the measurements in Figure 3.3a confirm that these higher orders are minimised while the zero order is maximised. Instead, if the grating is positioned $1/4$ of a grating period away from this, then we get $\psi(\mathbf{r}) = 2\theta(\mathbf{r})$, and the correlations should be maximised in the first-order diffraction peaks. This can be seen in Figure 3.3d. At the intermediate grating positions, $\psi(\mathbf{r})$ contains higher frequency components, and we see second-order diffraction peaks. Furthermore, it's interesting to note that replicating this experiment with classical coherent light would not yield any change in the intensity-measured diffraction pattern. Indeed, a lateral shift in the phase pattern in the Fourier plane would only influence the spatial phase component of the diffraction pattern, which the camera is not sensitive to.

According to Equation 3.25, we expect a different phenomenon in the case of the FF imaging configuration (Figure 3.2b). As before, we put a phase grating on the SLM (Fig 3.4a) but, since we instead have the $2\theta(\mathbf{r})$ phase term, lateral translation has no effect on C^+. Instead, we vary the amplitude of the phase grating α from 0 to 2π radians, and measure C^+ at each step. Figure 3.4b shows the values of the diffraction orders at each grating amplitude. As a comparison, we also performed the same experiment using classical coherent light and recorded the first-order diffraction peak intensity in function of α (pink curve). As expected, it follows a sinusoidal pattern reaching its maximum at $\alpha = \pi$. In the case of entangled photon pairs, we see the oscillation but, since C^+ is modulated by twice the phase mask, the frequency of this oscillation is doubled. Figures 3.4c-e show examples of the sum-coordinate projections measured for α equals to $\pi/6$, $\pi/2$ and $2\pi/9$, respectively.

These results show that we are able to control the intensity correlations of photon pairs, but what is the physical interpretation of this? The first thing to note is that, in these experiments, the direct intensity measured on the camera does not depend on the SLM phase mask. This is due to the incoherent behaviour that the photon pairs have when we are only looking at intensity. Thinking of photons as particles, this means that the probability of a detecting a photon at any given pixel does not change with the different phase masks. Instead, by modulating the $G^{(2)}$, we are manipulating the joint probability of simultaneously detecting two photons at two specific camera pixels. Considering this, we can interpret our experimental results. In the case of Figure 3.3d, there is no longer a sharp peak at the centre, but two peaks at some distance either side. This means the photons no longer arrive strongly correlated in position at the camera, instead arriving some constant distance apart. Similarly, in the case of Figure 3.4d, the phase mask prevents the photons from arriving at the camera strongly anti-correlated in position. Ultimately, this means that we can control the collective behaviour of photon pairs without changing their individual behaviour.

This shaping is not limited to simple phase grating patterns. Figure 3.5 shows the resulting minus-coordinate projections for helical phase masks displayed on the SLM in a near-field imaging configuration. As in the classical case, imparting a helical phase results in correlations in the shape of a ring whose radius is dependent on the number of times l that the helical phase changes from 0 to 2π[1] In fact, a helical phase is an interesting case where, due to the rotational symmetry, the phase mask $\theta(\mathbf{r}) = \theta(-\mathbf{r})$ $(+const.)$, so the effective phase mask is equal to twice the SLM phase, i.e. $\psi(\mathbf{r}) = 2\theta(\mathbf{r})$. Note that this double phase effect is for the joint two-photon state: each photon acquires an OAM of l, so the two-photon state acquires an OAM of $2l$.

---

[1] l is also known as the orbital angular momentum number, since a beam with a helical phase carries OAM in discrete values proportional to l.

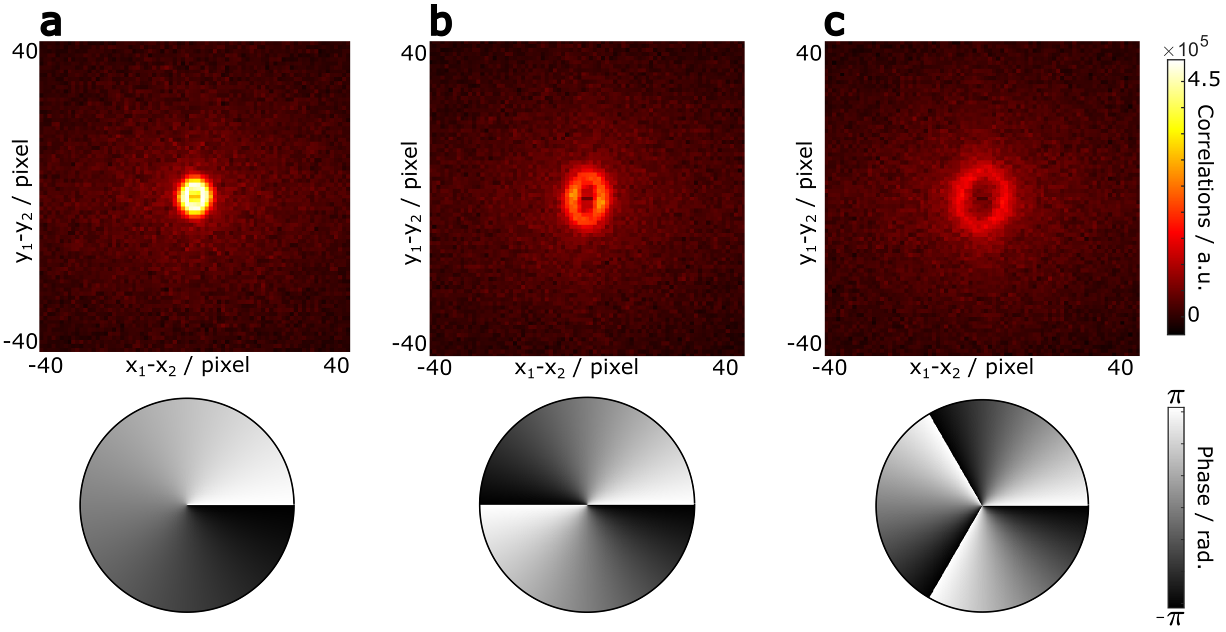

Figure 3.5: **Correlation shaping with helical phase masks.** Minus-coordinate projections and and corresponding phase masks for $l = 1$ (**a**), $l = 2$ (**b**), and $l = 3$ (**c**). Data from acquisitions of 2.5×10^6 frames with Andor Ixon Ultra 888 camera at an exposure time of 2 ms.

3.5 Application of Two-photon Shaping

3.5.1 Quantum Communication: Entanglement Recovery Through a Scattering Medium

One example where two-photon shaping can be applied is in field of quantum communications. In general, quantum communications is the name given to methods for sending a quantum state from one place to another, with the motivation being that sending information encoded in quantum states can be more secure than doing so classically [148]. Traditionally, this quantum information is encoded in two-level systems called qubits. Some typical two-level systems are the spin of an electron ($|\uparrow\rangle, |\downarrow\rangle$), or the polarisation of a photon ($|H\rangle, |V\rangle$). If two photons are then entangled in their polarisations, we say this is a state with two-dimensional entanglement.

The two-photon states we get from SPDC are actually entangled in multiple degrees of freedom due to the phase matching conditions within the nonlinear crystal. When considering the spatial degrees of freedom (position-momentum), the two-photon states produced in this way are said to be entangled in high dimensions [149]. This is because each photon in the state can exist in a large number of spatial modes. Such states, called qudits, have been shown to have a higher robustness to noise [150], better loss tolerance [151], and greater information capacities [101] compared to qubits. Therefore, they are of great interest for communications applications where all of these benefits would be extremely valuable. One major hurdle to overcome, however, is that this entanglement can be disrupted and become unusable if the photons encounter optical aberration

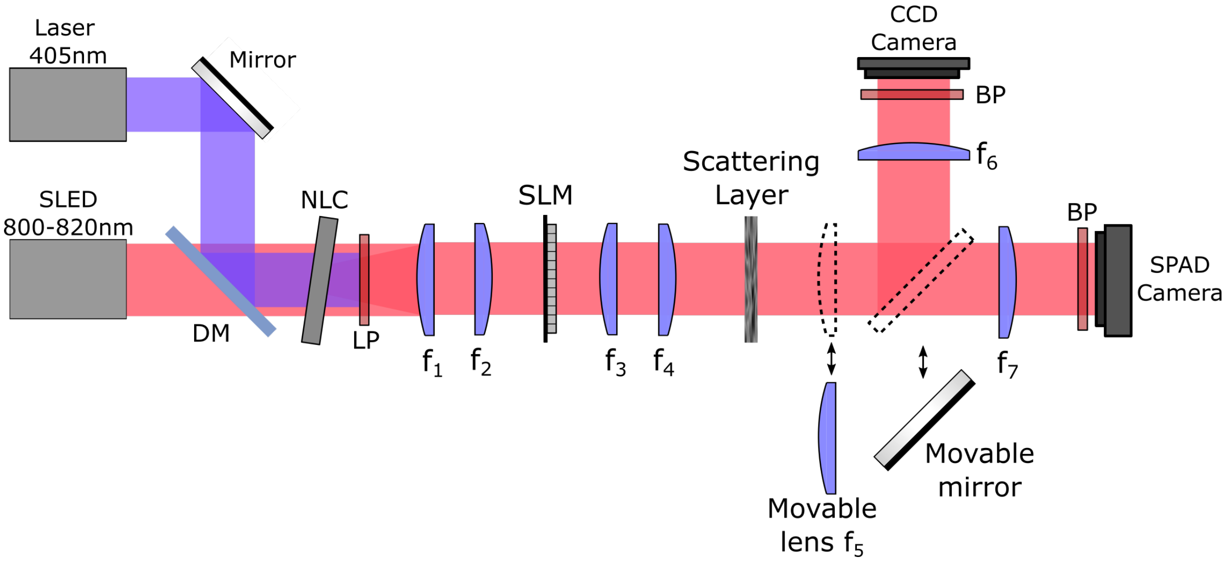

Figure 3.6: **Experimental setup for entanglement recovery through a scattering medium.** Spatially entangled photon pairs are produced by Type I SPDC by illuminating a BBO crystal (0.5 mm thickness) with a vertically polarised collimated laser diode at 405 nm. Simultaneously, horizontally polarised collimated light emitted by a superluminescent diode (SLED) is co-aligned to the pump beam using a dichroic mirror (DM). A long-pass filter (LP) with cutoff at 650 nm filters the pump photons after the crystal, and a band-pass (BP) filter at 810 ± 5 nm filters the classical beam. A two-lens system f_1-f_2 images the surface of the crystal onto an SLM which itself is imaged onto a scattering medium by lenses f_3-f_4. In the momentum-basis configuration, a single lens Fourier-imaging system (f_6 or f_7) is used to image the far-field of scattering layer onto either a SPAD camera (without movable mirror) or onto a CCD camera (with movable mirror). In the position-basis configuration, a movable lens f_5 is inserted to image the scattering layer onto the cameras. Figure adapted from Ref. [2]

or scattering that mixes spatial modes, as is the case in transmission through atmosphere or through multimode fibres. Using wavefront shaping, we demonstrate that this scrambling can be negated and entanglement can be restored through a thin scattering medium. Such an application of two-photon shaping is described in details in Ref. [2]. I participated in this work by analysing experimental data, producing simulations, and contributing to the writing of the paper.

Experimentally, the presence of entanglement is typically verified by computing a criterion for the correlations measured in multiple degrees of freedom. In this case, the criterion was the one derived by Giovanetti et. al [152] which states that separable systems satisfy the product:

$$\Delta \mathbf{r}_{-} \Delta \mathbf{k}_{+} > \frac{1}{2} \tag{3.33}$$

where $\Delta \mathbf{r}_{-} = \Delta(\mathbf{r_1} - \mathbf{r_2})$ and $\Delta \mathbf{k}_{+} = \Delta(\mathbf{k_1} + \mathbf{k_2})$ are uncertainties which correspond to the two-photon correlation widths of the $G^{(2)}$ measured in position and momentum, respectively. In other words, for a non-entangled state, there is a lower bound to the product of the position and momentum uncertainties, as we expect from the uncertainty principle. If the product of these uncertainties, i.e. correlation widths, is below this bound then we can say that the photon pairs are entangled in the position-momentum degrees of freedom. In fact, these widths are simply the widths of the peaks visible in the projections C^{+} and C^{-}, where the variable $\mathbf{k}$ is used to highlight that it represents measurements in momentum-space. Therefore, this verification can be done by measuring the width of the minus-coordinate projection while imaging the near-field of the crystal and the width of the sum-coordinate projection while imaging the far-field of the crystal.

In Ref. [2], the scattering medium was a thin layer of parafilm stretched over a glass slide, placed in a near-field plane of the nonlinear crystal. An SLM was placed in another near-field plane of the crystal to compensate for the scattering layer. If the scattering layer is assumed to be sufficiently thin and non-absorbing, then we can express the projections in this configurations as

$$C^{-}(\mathbf{r}_{-}) \propto \left| \mathcal{F}\left[\phi_0(\mathbf{r})\right] \right|^2 \qquad \text{(Imaging NF)} \tag{3.34}$$

$$C^{+}(\mathbf{r}_{+}) \propto \left| \mathcal{F}\left[\phi_0'(\mathbf{r})\right] * \mathcal{F}\left[e^{i2(\theta(\mathbf{r})+S(\mathbf{r}))}\right] \right|^2 \qquad \text{(Imaging FF),} \tag{3.35}$$

where $\theta(\mathbf{r})$ is the phase mask on the SLM as before, and $S(\mathbf{r})$ is a function corresponding to the unknown phase imparted by the scattering layer. The first thing to notice is that the minus-coordinate projection doesn't depend on the scattering layer. This is because it is a phase-only object and the camera is insensitive to phase. If it were placed in a different plane, or was sufficiently thick, it would modulate both projections. Secondly, notice that when $\theta(\mathbf{r}) = -S(\mathbf{r})$, the effect of the scatterer is negated entirely. When $\theta(\mathbf{r}) \neq -S(\mathbf{r})$, the spatial correlations are affected and will diverge from the ideal case, meaning $\Delta \mathbf{k}$ will increase and, beyond a certain amount of scattering, the entanglement verification will fail.

Clearly, we want to display a phase mask $\theta = -S$ on the SLM. However, S is different for every scattering layer, and is effectively random, so finding the optimal θ is not trivial. Luckily, the techniques of wavefront shaping exist to solve this exact problem. There are two main approaches to finding the best correction pattern on the SLM. The first is to optimise the intensity at a target camera pixel when illuminating the system with spatially coherent (laser) light, as demonstrated by Vellekoop and Mosk [86]. The second, which is the method we use, is to directly measure the transmission matrix of the scatterer and use this to compute the ideal phase mask using the techniques introduced by Popoff et. al. [109] where the transmission matrix can be seen as the discrete version of the PSF.

While the transmission matrix measurement could be done directly with photon pairs in theory, the low SNR and long acquisition times of correlation measurements make this very challenging (see Subsection 5.3.3). Therefore, the transmission matrix is actually measured using a SLED at 810 nm, as used for alignment. Finally, since we are working with the transmission matrix which is a discrete quantity, we also work practically in a discrete, matrix-based formalism. In this formalism the two-photon state Ψ^{in} is propagated with matrix multiplications. For a system with an SLM followed by the scatterer we have

$$\Psi^{out} = TD\Psi^{in}D^{t}T^{t}, \tag{3.36}$$

where D is a diagonal matrix representing propagation through the SLM and Ψ^{out} is the matrix associated with the two-photon state at the output. Satisfying the criteria that $\theta = -S$ can be ideally done by shaping the SLM so that $D = T^{-1}$. This would give $\Psi^{out} = \Psi^{in}$, thereby recovering the entanglement that was scrambled by the scatterer. For practical reasons, detailed in Ref. [2], we use the transpose conjugate of the transmission matrix to program the SLM i.e. $D = T^{\dagger}$. Figures 3.7d-f show examples of the sum-coordinate projections measured after a thin scattering medium with and without applying a correction on the SLM. The experimental setup used to obtain these results is described in Ref. [2], and is also shown in Figure 3.6.

3.5.2 Quantum Imaging: Adaptive Optical Imaging with Entangled Photons

Two-photon correlations shaping can also be used in an imaging context to do AO. We have demonstrated this in a work reported in Ref. [3]. It is described in detail in the whole of the following chapter (Chapter 4), and so I only briefly mention it here. AO aims to correct for optical aberrations in imaging systems to improve imaging performance. Typically, an SLM is used to optimise a so-called ‘guide star’ i.e. some structure or emitter in the object that is assumed to be point-like. However, in the absence of a guide star, the optimisation target can be

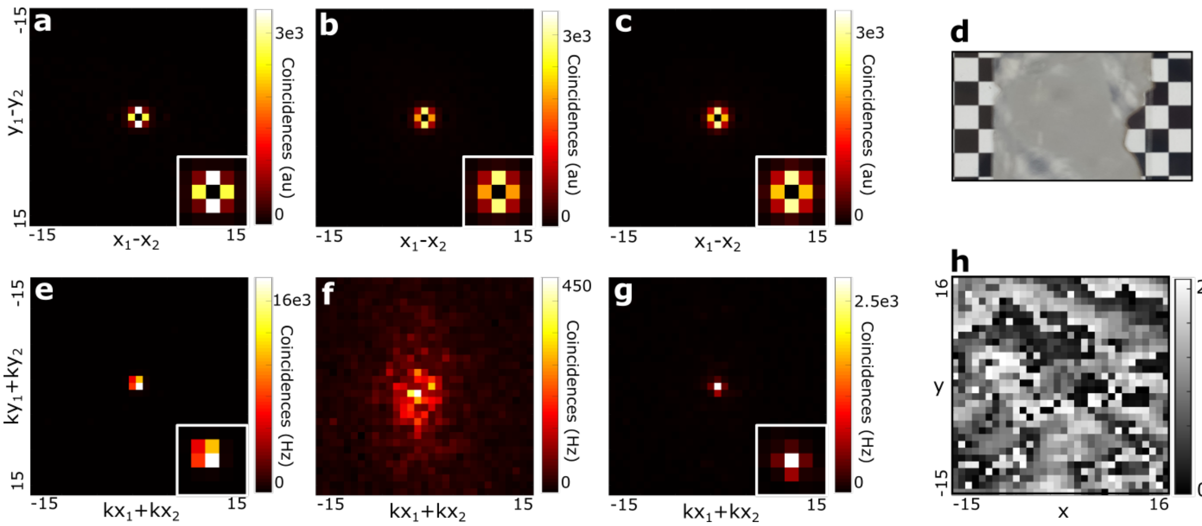

Figure 3.7: **Application of two-photon shaping: Entanglement transmission through a scattering medium. a-c,** Minus-coordinate projections in the near-field imaging configuration with: **a,** no scattering layer; **b,** scattering layer and no correction; **c,** scattering layer and correction. In this configuration, the scattering layer is in the plane being imaged so we see no distortion of the minus-coordinate projection. **e-g,** Sum-coordinate projections in the Fourier-imaging configuration with: **e,** no scattering layer; **f,** scattering layer and no correction; **g,** scattering layer and correction. In this configuration, the scattering layer is in the Fourier-plane of the camera so we see a speckle pattern in the sum-coordinate projection.**d,** Photograph of the scattering layer (a layer of parafilm on a microscope slide). **h,** Correcting phase mask on SLM, found by inverting the classically measured transmission matrix. Figure reproduced from Ref. [2]

unclear. The concept of this quantum-assisted adaptive optics is to use the spatial correlations of SPDC photon pairs as an effective guide star. Optimising the maximum value of the relevant $G^{(2)}$ projection with an SLM will also optimise the imaging performance of the system, with some interesting benefits and differences compared classical, image-based AO. For a complete description of this work, see Chapter 4.

3.5.3 Fundamental Quantum Effects: Investigating Entangled Two-photon Absorption

Another application for two-photon correlation shaping is the investigation of entangled two-photon absorption. This is an ongoing project that I have been involved in. I contributed to the experimental design and construction and to some of the data analysis.

Fluorescence is the process by which a molecule absorbs a photon at one wavelength and, after a short delay, emits a photon at a different wavelength. Usually the molecule absorbs a photon of a specific energy, ω_p, and enters an excited state. Some of this energy is dissipated as heat, and the rest is emitted as a photon with energy $\omega_e < \omega_p$. However, if two photons with energies ω_1 and ω_2 arrive simultaneously at the same location in material, they can be absorbed if $\omega_1 + \omega_2 \geq \omega_p$, as shown in Figure 3.8a. This is called two-photon absorption (TPA). If the two absorbed photons are independent, then the rate of absorption Γ_{TPA} is proportional to the square of the photon flux.

This quadratic scaling with photon flux can be used to achieve improved resolution and imaging depths in scanning and fluorescence microscopy [153]. This is because the size of the TPA region is proportional to the square of the illumination profile. For the same reason, TPA is also used in lithography to achieve smaller feature sizes [154]. TPA is also used in spectroscopy to access otherwise forbidden electronic states [155]. However, the quadratic scaling also makes TPA unsuitable for low-light applications.

Entangled two-photon absorption (ETPA) is a specific case of TPA in which the two absorbed photons are entangled. This means that the photons are no longer independent, and in fact the entangled two-photon absorption rate Γ_{ETPA} is predicted to scale linearly with photon flux [156]. Consider spatially correlated photon pairs from SPDC. The photons are correlated so that they will always arrive as a pair at the same position in space (in a NF plane of the crystal). In addition to this linear scaling in the low-flux regime, SPDC photon pairs are also spectrally correlated. For these reasons, there is strong interest in using ETPA for low-light spectroscopy applications [157, 158].

While an enhancement from using entangled photons has been reported [159–161], there is still much debate around the advantage it is expected to offer in the low-flux regime [162, 163]. The aim of our project is to offer a new angle to investigate ETPA by demonstrating a novel method

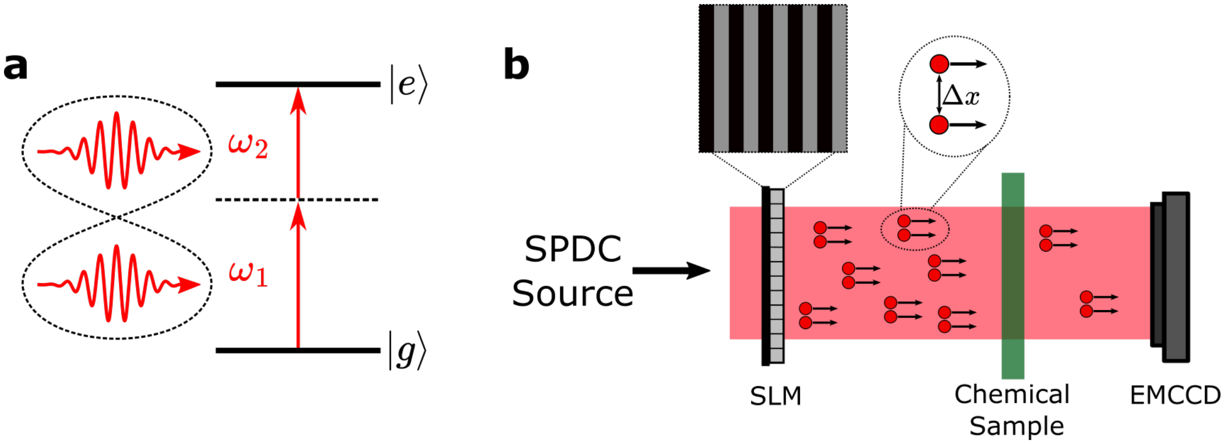

Figure 3.8: **Schematic of entangled two-photon absorption experiment. a,** Energy level diagram of two-photon absorption. **b,** Illustration of ETPA experiment. A grating is displayed on the SLM which allows the spatial separation Δx between signal and idler to be controlled.

for measuring and quantifying the rate of ETPA.

Figure 3.8b shows an illustration of this method. The concept is to use an SLM to control the spatial correlations of photon pairs that are illuminating a two-photon absorbing sample. For this, we work in near-field imaging configuration where the sample and camera are in optical planes conjugate to the nonlinear crystal. As we have seen in this chapter, we can modulate the spatial correlations of photon pairs with an SLM without modulating the overall intensity profile of the beam. This can be used to probe the effect of spatial correlations on ETPA while keeping the total photon flux on the sample the same. By displaying a phase grating on the SLM, the separation of the photons at the sample, Δx, can be precisely controlled, as in Figure 3.3. With no grating on the SLM, we expect Γ_{ETPA} to increase since the photons are arriving at the sample strongly correlated. Then, if a phase grating is displayed, we expect Γ_{ETPA} to decrease. We can measure this difference by taking the ratio of the peaks of the minus-coordinate projections in both cases.

This method could add a new perspective on the ongoing debate by providing a way to measure ETPA based on quantum correlations. The experiment is ongoing, with only preliminary results secured thus far. However, it provides an alternative approach to investigating ETPA and highlights well the diversity of applications of two-photon shaping.

3.6 Discussion

In summary, we have shown how one can shape the correlations of a spatially entangled two-photon state with both a theoretical description and an experimental demonstration. By using a Fourier-optics-based formalism, we have shown that the two-photon correlations can be shaped in an analogous manner to coherent classical states, with some important differences. Depending on the state at the SLM, the photon pairs ‘see’ a different version of the phase displayed on the SLM. For a correlated state, it is modulated according to twice the phase mask and, for an anti-correlated state, it is modulated by the combination of the phase mask and its spatial inverse. We demonstrate this experimentally, showing that there are in fact cases where we see no modulation of the correlations even when a non-flat phase mask is displayed on the SLM. In the context of my thesis, I have focused solely on two simple configurations, i.e., NF and FF imaging. However, one could imagine more complex situations, for instance, positioning the SLM in an intermediate plane that is in neither the NF or FF of the crystal, or even by using multiple SLMs is different planes. It would be interesting in the future to study these configurations. In particular, they could allow for modulation so that correlations will change depending on the spatial region of the beam they occupy.

Chapter 4

Adaptive Optical Imaging with Entangled Photons

This chapter is based on the work presented in Ref. [3] titled *'Adaptive Optical Imaging with Entangled Photons'* by authors Patrick Cameron, Baptiste Courme, Chloé Vernière, Raj Pandya, Daniele Faccio, and Hugo Defienne. This paper has been accepted for publication in the journal Science.

4.1 Introduction

In all imaging applications there is a finite limit to the size of features that can be resolved. For an imaging lens with focal length f and aperture diameter D, this is typically expressed as the Rayleigh criterion [164]:

$$\Delta l \approx 1.22\frac{f\lambda}{D}, \tag{4.1}$$

where Δl is the smallest resolvable distance, and λ is the wavelength of the light being used. While this is not a fundamental physical limit, it encapsulates well the main factors affecting spatial resolution. For a given imaging system, f and D are fixed, and the resolution is limited by the wavelength of the light being used, called the diffraction limit of light.

Label-free microscopes are essential for studying biological systems in their most native states. Unlike fluorescence microscopes, they do not require the samples to be stained with fluorescent markers. In standard label-free microscopes, the sample is illuminated with an external source and the same light is collected to form its image. The contrast mechanisms correspond to the change in phase and amplitude of the light diffracted by the sample. As discussed in Chapter 1, the use of non-classical light sources can enhance imaging performance in a number of ways, and such quantum-enhanced imaging techniques are particularly well-suited for microscopy. To

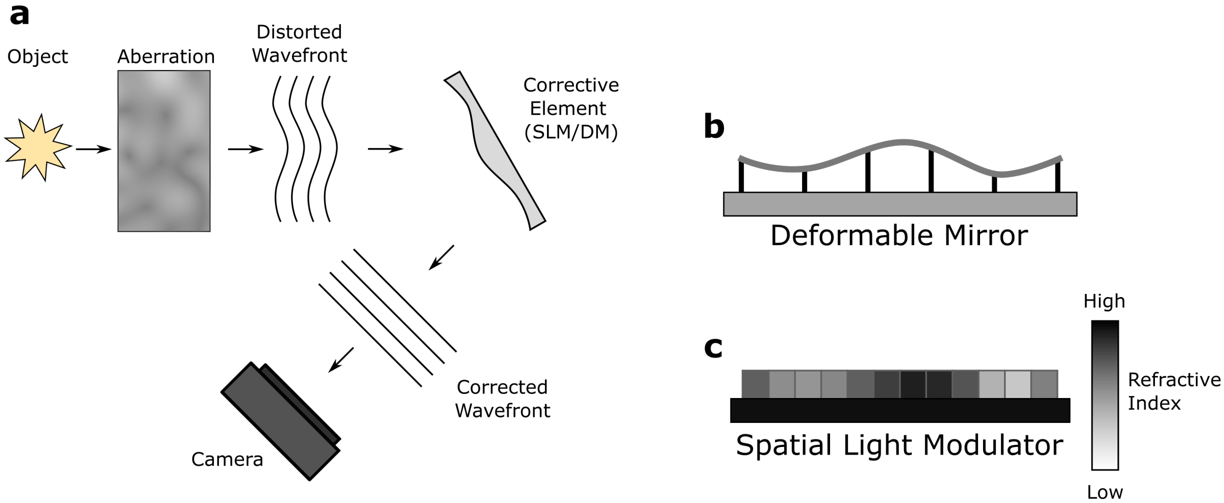

Figure 4.1: **Principle of Adaptive Optics. a,** Illustration of the correction of a distorted wavefront using a corrective device such as a spatial light modulator (SLM) or deformable mirror. **b,** Illustration of a deformable mirror. A flexible mirror membrane is mounted on actuators that can deform the mirror to control the wavefront of the reflected beam. **c,** Illustration of a spatial light modulator. The refractive index of individual pixels can be controlled to modulate the wavefront of the reflected beam.

summarise the relevant points, entangled-photon imaging has been used in bright-field imaging configurations to enhance spatial resolution [1, 27, 56, 165], achieve sub-shot-noise imaging [31] and improve the contrast in the presence of noise and losses [70, 73]. In phase imaging, they can be utilised to augment the contrast in both confocal [58] and wide-field [60, 166] differential interference contrast (DIC) systems, and are at the basis of new modalities including quantum holography [65, 167], reconfigurable phase-contrast microscopy [79] and 3D-imaging [127]. Finally, they can also improve time-gated imaging protocols, such as optical coherence tomography (OCT), by reducing dispersion [168, 169] and enhancing depth sensitivity [61]. However, all of these enhancements are based on the assumption that the system is diffraction limited. In many practical situations this is not the case, as it is common to have optical aberrations present in the imaging system. Generally speaking, the field of adaptive optics (AO) aims to correct for these aberrations to optimise the resolution of an imaging system.

AO originated in astronomy to improve the resolution of ground-based telescopes [170]. The light from stars and other astronomical objects has a flat wavefront which can be ideally focused. However, once it reaches the Earth, variations in the density, and therefore refractive index, of the atmosphere introduce distortions to this wavefront. This results in blurred images and reduces the resolution of the telescope. If the shape of these distortions can be measured, e.g. with a Shack-Hartmann sensor, then an SLM or deformable mirror can be used to compensate for them, thereby restoring the imaging performance and recovering a diffraction-limited resolution. Figure 4.1 shows an illustration of the principle of adaptive optics.

The concepts of AO were soon applied to improve the resolution of classical microscopes. Instead of originating from the turbulent atmosphere, aberrations in microscopy are typically caused by variations in the refractive index of the sample itself, known as specimen-induced aberration. In addition to this, the optical elements within the microscope itself can introduce systematic aberrations. In many cases it is not actually practical to directly measure the distortions. Instead, a point-like source or structure called a guide star is identified in the sample. Since it is point-like, the image of this guide star should, by definition, look like the point-spread function of the microscope. Therefore, it can be used as an optimisation target to correct for aberrations. In the past decades, AO has played a major role in the development of advanced imaging systems, particularly fluorescence microscopes [171, 172].

In the absence of a guide star, however, the PSF and thus the aberration information is not directly accessible. This is typical for most label-free and linear microscopy systems. To circumvent this issue, wavefront sensorless, image-based AO methods have been developed [172–174]. They are based on the principle that the image, resulting from the convolution between the specimen structure and the PSF, has optimum quality only when the aberrations have been fully compensated. In practice, an image metric is first defined and then optimised by acting with the wavefront shaping device. The appropriate choice of the metric depends on the image formation process of the microscope used and the nature of the sample. The most commonly used metrics include the total output intensity [175], image contrast [176], low frequency content [177] and sharpness [178, 179]. In recent years, this has enabled aberration correction in several label-free microscope modalities, such as bright-field [177], quantitative phase-contrast [180], differential interference contrast (DIC) [181] and OCT [182].

One of the primary hurdles in achieving effective image-based AO lies in the requirement to define distinct metrics for each microscope modality and for varying specimen types. Furthermore, certain metrics may introduce systematic errors. For instance, when capturing volumetric samples, a defocus correction based on an image sharpness metric can yield multiple solutions corresponding to different transverse planes within the sample.

In this Chapter I describe a novel method called quantum-assisted adaptive optics (QAO) that exploits the spatial correlations of entangled photon pairs to correct for aberrations, as introduced in Ref. [3]. This method harnesses the fact that the PSF of an imaging system is directly encoded in the spatial correlations of photons pairs that have propagated through it. This allows direct optimisation of the PSF without the need for a guide star in the sample. The performance of QAO is independent of the imaging modality and structure of the specimen under investigation, and can outperform classical AO methods in some conditions.

4.2 Concept and Theory Behind Quantum-assisted Adaptive Optics

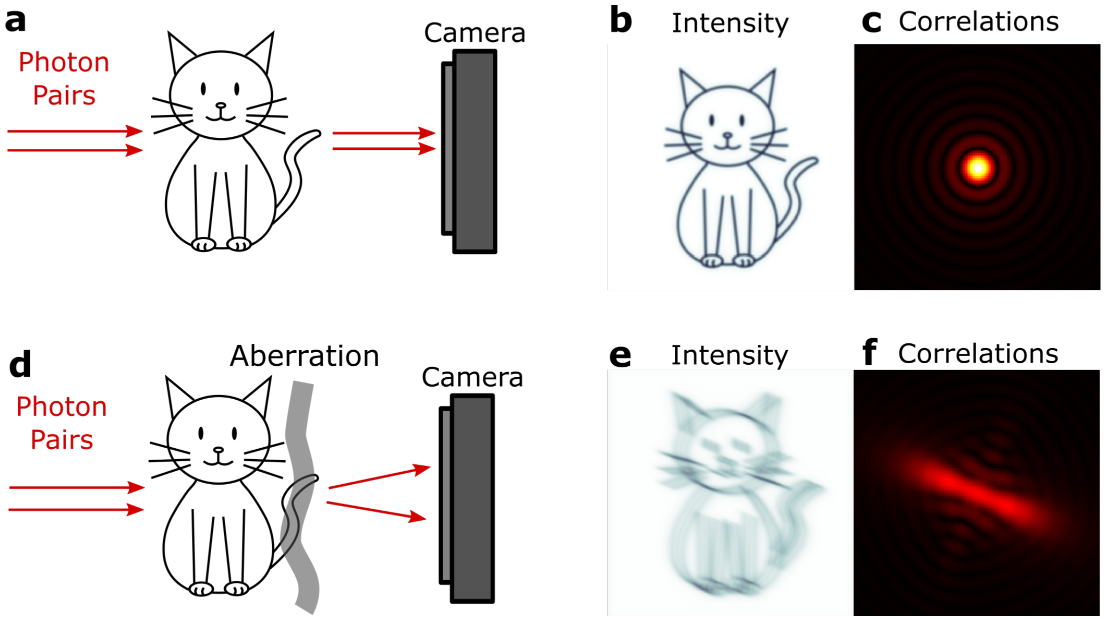

Figure 4.2: **Concept of Quantum-assisted Adaptive Optics (QAO). a,** An object is illuminated by spatially entangled photon pairs and imaged onto a single-photon sensitive camera. The imaging system between the object and the camera is not represented for clarity. Photon pairs are strongly correlated in the object plane. Without optical aberrations, a **(b)** sharp intensity image of the object is acquired and photon pairs are still correlated at the camera plane. Photon pairs correlations are visualised by **(c)** measuring the spatial second-order correlation function, $G^{(2)}$, and projecting it onto specific coordinates. Such a $G^{(2)}$ projection is proportional the system's point-spread function (PSF) and shows a narrow peak at its centre. **d**, With aberrations present, the system is not limited by diffraction and the pairs are no longer correlated at the camera plane, resulting in a **(e)** blurred intensity image and a **(f)** distorted $G^{(2)}$ projection. In QAO, aberrations are corrected using a spatial light modulator (SLM) to maximise the central value of the $G^{(2)}$ projection.

In our QAO scheme, spatially-entangled photon pairs generated via SPDC are incident on an object (t) which is then imaged onto a single-photon sensitive camera (Figure 4.2.a). From this, we have information from two quantities in parallel. From Subsection 3.3.3 we know that the light from SPDC behaves like spatially incoherent light if we measure only direct intensity. In the most general case, this intensity has the form given in Equation 3.14: $I(\mathbf{r}') = \int \phi_0(\mathbf{r})|h(\mathbf{r}',\mathbf{r})|^2 d\mathbf{r}$ where ϕ_0 the the intensity envelope of the photon pairs. If the PSF is shift-invariant (the same at each point of the sample) then, as in classical incoherent illumination, the intensity image (I) produced at the camera simply results from a convolution between the magnitude-squared PSF (h) and the object as

$$I = |h|^2 * |t|^2. \tag{4.2}$$

Simultaneously, the photons are also pair-wise correlated, and exhibit strong spatial correlations which arises from their entanglement [183]. Therefore, in addition to this intensity information, the intensity correlations will also contain information about the system. Modifying to include the effects of the object t, Equation 3.22 can be extended to describe the intensity correlations at the output of our imaging systems as

$$G^{(2)}(\mathbf{r}_1', \mathbf{r}_2') = \left| \iint \phi(\mathbf{r}_1, \mathbf{r}_2) t(\mathbf{r}_1) t(\mathbf{r}_2) h(\mathbf{r}_1', \mathbf{r}_1) h(\mathbf{r}_2', \mathbf{r}_2) d\mathbf{r}_1 d\mathbf{r}_2 \right|^2, \tag{4.3}$$

where, as before, $\phi(\mathbf{r}_1, \mathbf{r}_2)$ is the position-basis wavefunction of our two-photon state. This is clearly a complicated function that depends on the PSF, the object, and the spatial correlations of the photon pairs at the source, and may not seem particularly practical. However, under specific experimental conditions, we will see that the sum-coordinate projection of this $G^{(2)}$ can be approximated as:

$$C^+(\mathbf{r}_+) \approx K \left| [h * h](2\mathbf{r}_+) \right|^2, \tag{4.4}$$

where K is a constant representing the photon-pair transmission rate through the object and is independent of h. Equation 4.4 says that the PSF of the imaging system is directly encoded in C^+ via an autoconvolution. Therefore, maximising the central projection value $C_0^+ = C^+(\mathbf{r}_+ = \mathbf{0})$ is equivalent to maximising the sharpness of the PSF. This in turn is the same as optimising the imaging performance (see Eq. 4.2). Thus, we can do AO by optimising the photon-pair spatial correlations. Importantly, Equation 4.4 also says that the only influence of the object t on this projection is in the global factor K. This means that, under the right conditions, the shape of C^+ does not depend on the structure of the object we are imaging. In other words, $C^+(\mathbf{r}_+)$ can be used as a 'universal guide star' that quantifies imaging performance independently of the structure of the sample under observation.

4.2.1 Derivation of Equation 4.4

In this section, I describe the steps used to derive Equation 4.4, which is central to understanding the QAO process. Starting from Equation 4.3, we can introduce some assumptions on the state and on the aberrations that allow it to be simplified, eventually yielding Equation 4.4. The initial assumptions are as follows:

1. We assume that the PSF is shift-invariant. Mathematically, such a PSF can be written as $h(\mathbf{r}', \mathbf{r}) = h(\mathbf{r}' - \mathbf{r})$. Physically, this means that for point source at location $\mathbf{r}$, the output will simply have the shape of the PSF centred at this point. Although it will simplify our calculations, this assumption is not strictly necessary.

2. We assume that the input plane (i.e. sample plane) is positioned in a Fourier plane of the crystal. This imaging configuration is the one in which we chose to operate in our study. A diagram of the experimental setup is shown in Figure 4.6. We chose to work in

this configuration because it presents certain practical advantages, especially for efficiently measuring correlations with a camera. A full description of the experimental setup is given in Section 4.3. However, it should be noted that it is also possible to use an alternative configuration in which the crystal's surface is imaged onto the object. Such a configuration is theoretically described in Subsection 4.2.3. It has not been explored experimentally in the context of my thesis but could be in the future.

Here, we thus image the Fourier plane of the crystal onto the object. In this plane the photons are almost perfectly anti-correlated and the two-photon wavefunction can be approximated as:

$$\phi(\mathbf{r}_1, \mathbf{r}_2) \approx \delta(\mathbf{r}_1 + \mathbf{r}_2). \tag{4.5}$$

The assumption that the pairs are perfectly anti-correlated in the sample plane is justified under our experimental conditions, since the crystal is illuminated by a collimated beam (0.8mm diameter), and its thickness (0.5mm) is much smaller than the corresponding Rayleigh length ($\sim$ 1m) [118, 146]. Note that, in Equation 4.5, the photon pair illumination beam is assumed to be infinitely large. To account for the fact that, in reality, the beam has a finite diameter, we can simply modify the definition of object t and include edges $t(\mathbf{r}) \rightarrow t(\mathbf{r})\mathrm{rect}(\mathbf{r}/a)$, where a^2 is the illumination area.

Under these assumptions, Equation 4.3 becomes:

$$G^{(2)}(\mathbf{r}_1', \mathbf{r}_2') = \left| \iint \delta(\mathbf{r}_1 + \mathbf{r}_2) t(\mathbf{r}_1) t(\mathbf{r}_2) h(\mathbf{r}_1' - \mathbf{r}_1) h(\mathbf{r}_2' - \mathbf{r}_2) d\mathbf{r}_1 d\mathbf{r}_2 \right|^2. \tag{4.6}$$

Then, using the following change of variables:

$$\begin{aligned} \mathbf{r}_+ &= \frac{1}{2}(\mathbf{r}_1 + \mathbf{r}_2), \\ \mathbf{r}_- &= \frac{1}{2}(\mathbf{r}_1 - \mathbf{r}_2), \end{aligned} \tag{4.7}$$

the intensity correlations can be expressed as:

$$\begin{aligned} G^{(2)}(\mathbf{r}_+', \mathbf{r}_-') &= \left| \iint \delta(\mathbf{r}_+) t(\mathbf{r}_+ + \mathbf{r}_-) t(\mathbf{r}_+ - \mathbf{r}_-) h(\mathbf{r}_+' + \mathbf{r}_-' - (\mathbf{r}_+ + \mathbf{r}_-)) h(\mathbf{r}_+' - \mathbf{r}_-' - (\mathbf{r}_+ - \mathbf{r}_-)) d\mathbf{r}_+ d\mathbf{r}_- \right|^2 \\ &= \left| \int t(\mathbf{r}_-) t(-\mathbf{r}_-) h(\mathbf{r}_+' + \mathbf{r}_-' - \mathbf{r}_-) h(\mathbf{r}_+' - \mathbf{r}_-' + \mathbf{r}_-) d\mathbf{r}_- \right|^2. \end{aligned} \tag{4.8}$$

From there, we use another change of variables: $\mathbf{r} = \mathbf{r}_+' + \mathbf{r}_-' - \mathbf{r}_-$. This gives

$$G^{(2)}(\mathbf{r}_+', \mathbf{r}_-') = \left| \int t(\mathbf{r}_+' + \mathbf{r}_-' - \mathbf{r}) t(-\mathbf{r}_+' - \mathbf{r}_-' + \mathbf{r}) h(\mathbf{r}) h(2\mathbf{r}_+' - \mathbf{r}) d\mathbf{r} \right|^2. \tag{4.9}$$

Using again the change of variable i.e. $(\mathbf{r_1}, \mathbf{r_2}) \rightarrow (\mathbf{r}_+, \mathbf{r}_-)$, and recalling the definition of the sum-coordinate projection C^+ (Equations 3.27 and 3.30), we can express it as:

$$\begin{aligned} C^+(\mathbf{r}_+) &= \int G^{(2)}(\mathbf{r_1}, 2\mathbf{r}_+ - \mathbf{r_1}) d\mathbf{r_1} \\ &= \iint G^{(2)}(\mathbf{r_1}, \mathbf{r_2}) \delta(\mathbf{r_2} - (2\mathbf{r}_+ - \mathbf{r_1})) d\mathbf{r_1} \\ &= \int G^{(2)} \left(\mathbf{r}_+, \mathbf{r}_- \right) d\mathbf{r}_-. \end{aligned} \tag{4.10}$$

Equation 4.10 can then be expanded as:

$$\begin{aligned} C^+(\mathbf{r}_+) &= \int \left| \int t\left(\mathbf{r}_+ + \mathbf{r}_- + \mathbf{r}\right) t\left(-\mathbf{r}_+ - \mathbf{r}_- + \mathbf{r}\right) h(\mathbf{r}) h(2\mathbf{r}_+ - \mathbf{r}) d\mathbf{r} \right|^2 d\mathbf{r}_- \\ &= \iiint t\left(\mathbf{r}_+ + \mathbf{r}_- + \mathbf{r_A}\right) t\left(-\mathbf{r}_+ - \mathbf{r}_- + \mathbf{r}\right) h(\mathbf{r_A}) h(2\mathbf{r}_+ - \mathbf{r_A}) \\ &\quad t^*\left(\mathbf{r}_+ + \mathbf{r}_- + \mathbf{r_B}\right) t^*\left(-\mathbf{r}_+ - \mathbf{r}_- + \mathbf{r_B}\right) h^*(\mathbf{r_B}) h^*(2\mathbf{r}_+ - \mathbf{r_B}) d\mathbf{r_A} d\mathbf{r_B} d\mathbf{r}_- \\ &= \iint \left[\int t\left(\mathbf{r}_+ + \mathbf{r}_- + \mathbf{r_A}\right) t\left(-\mathbf{r}_+ - \mathbf{r}_- + \mathbf{r}\right) t^*\left(\mathbf{r}_+ + \mathbf{r}_- + \mathbf{r_B}\right) \right. \\ &\quad \left. t^*\left(-\mathbf{r}_+ - \mathbf{r}_- + \mathbf{r_B}\right) d\mathbf{r}_- \right] h(\mathbf{r_A}) h(2\mathbf{r}_+ - \mathbf{r_A}) h^*(\mathbf{r_B}) h^*(2\mathbf{r}_+ - \mathbf{r_B}) d\mathbf{r_A} \mathbf{r_B} \\ &= \iint K(\mathbf{r_A}, \mathbf{r_B}) h(\mathbf{r_A}) h(2\mathbf{r}_+ - \mathbf{r_A}) h^*(\mathbf{r_B}) h^*(2\mathbf{r}_+ - \mathbf{r_B}) d\mathbf{r_A} \mathbf{r_B}, \end{aligned} \tag{4.11}$$

where the effects of the object t are grouped into the function K. Using the change of variable $\mathbf{r} = \mathbf{r}_+ + \mathbf{r}_- - \mathbf{r_A}$, $K(r_A, r_B)$ can be simplified as:

$$\begin{aligned} K(\mathbf{r_A}, \mathbf{r_B}) &= \int t\left(\mathbf{r}_+ + \mathbf{r}_- - \mathbf{r_A}\right) t\left(-\mathbf{r}_+ - \mathbf{r}_- + \mathbf{r_A}\right) \\ &\quad t^*\left(\mathbf{r}_+ + \mathbf{r}_- - \mathbf{r_B}\right) t^*\left(-\mathbf{r}_+ - \mathbf{r}_- + \mathbf{r_B}\right) d\mathbf{r}_- \\ &= \int t\left(\mathbf{r}\right) t\left(-\mathbf{r}\right) t\left(\mathbf{r} + (\mathbf{r_A} - \mathbf{r_B})\right) t\left(-\mathbf{r} - (\mathbf{r_A} - \mathbf{r_B})\right) d\mathbf{r}. \end{aligned} \tag{4.12}$$

As a result, we have shown that $C^+(\mathbf{r}_+)$ can be written:

$$C^+(\mathbf{r}_+) = \iint K(\mathbf{r_A}, \mathbf{r_B}) h(\mathbf{r_A}) h(2\mathbf{r}_+ - \mathbf{r_A}) h^*(\mathbf{r_B}) h^*(2\mathbf{r}_+ - \mathbf{r_B}) d\mathbf{r_A} d\mathbf{r_B}. \tag{4.13}$$

where

$$K(\mathbf{r_A}, \mathbf{r_B}) = \int t\left(\mathbf{r}\right) t\left(-\mathbf{r}\right) t^*\left(\mathbf{r} + (\mathbf{r_A} - \mathbf{r_B})\right) t^*\left(-\mathbf{r} - (\mathbf{r_A} - \mathbf{r_B})\right) d\mathbf{r}. \tag{4.14}$$

Equation 4.13 is the most general form of C^+. The only assumption we have made about the aberrations is that they are shift-invariant which, as stated above, is not strictly necessary up to

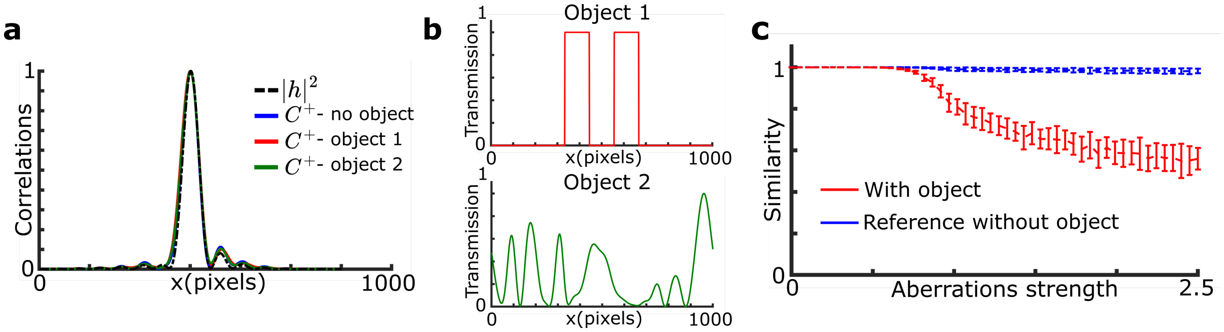

Figure 4.3: **Simulations of sum-coordinate projections C^+ with and without an object. a,** Sum-coordinate projections C^+ obtained in the presence of aberrations with strength $f_{ab} = 0.9$ without object (blue curve), with a simple object (red curve) and with a more complex object (green curve). The absolute-squared of the PSF is also represented by the dashed-black line. All curves are plotted after normalisation to their maximum value. **b**, Simple and more complex object used in the simulations. **c - Blue curve,** Similarity values obtained by comparing the sum-coordinate projection simulated with an object and this without object. To obtain a similarity value, 400 correlation values were calculated using the Matlab function `corrcoef` between the reference sum-coordinate projection (no object) and 400 sum-coordinate projections generated for 20 different randomly generated aberration patterns and 20 different randomly generated objects. Random aberrations are used here to show the effect of the aberration strength in general. **c - Red curve,** Similarity values obtained with the same process but using the absolute value squared-PSF as the reference.

this point. To obtain Equation 4.4 we must introduce another assumption. If we assume that the optical aberrations present in the system are sufficiently weak, Equation 4.13 can be further simplified. Indeed, if the aberrations are weak - meaning there is no scattering or absorption - then the PSF h is quite narrow i.e. non-negligible only close to 0. This implies that the term $h(\mathbf{r_A})h(2\mathbf{r_+} - \mathbf{r_A})h^*(\mathbf{r_B})h^*(2\mathbf{r_+} - \mathbf{r_B})$ is non-negligible only for small values of $|\mathbf{r_A}|$ and $|\mathbf{r_B}|$. In this case, the values $|\mathbf{r_A} - \mathbf{r_B}|$ are also small, and Equation 4.14 simplifies into:

$$K(\mathbf{r_A}, \mathbf{r_B}) \approx \int |t(\mathbf{r})\, t(-\mathbf{r})|^2 d\mathbf{r} = K. \tag{4.15}$$

Under this assumption, K is now a constant that does not depend on $\mathbf{r_A}$ and $\mathbf{r_B}$, and therefore can be taken out of the integral. Equation 4.13 can now be simplified and expressed as a convolution, allowing us to obtain Equation 4.4. The validity of the weak aberration hypothesis is confirmed by the simulations in the following section.

4.2.2 Justification of Weak-Aberration Assumption

Here I will show some simulated and experimental results which justify the assumptions made in the preceding derivation. Effectively, Equation 4.4 says that the shape of the sum-coordinate projection does not depend on the structure of the object t if the aberrations are sufficiently weak. We can confirm this by comparing C^+s acquired with different objects. Figure 4.3 shows some

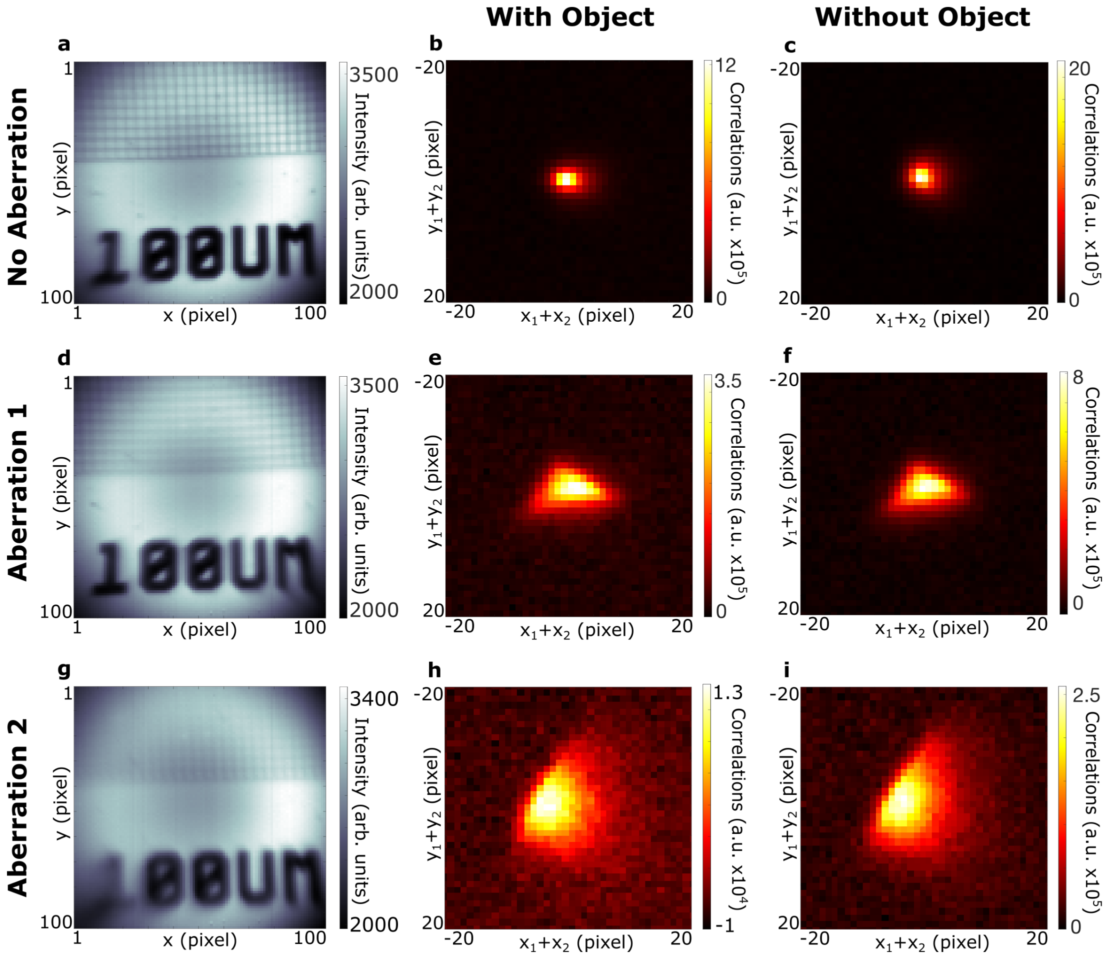

Figure 4.4: **Experimental data of sum-coordinate projection with and without the presence of an object.** First row (**a,b,c**) acquired with no induced aberrations. Second row (**d,e,f**) acquired with weak aberrations. Third row **g,h,i** acquired with different weak aberrations. First column (**a,d,g**) shows direct intensity images with the object, a 100μm resolution target grid. Second column (**b,e,h**) shows sum-coordinate projections acquired with the object present. Third column (**c,f,i**) shows the sum coordinate projection without the object present. Each intensity and sum-coordinate image acquired from 10^7 frames, taking ~ 5 hours. All experimental results were acquired using the setup detailed in Figure 4.6, in which the aberrations were induced using a second SLM placed at plane A2. a.u. - arbitrary units.

results from simulations of Equation 4.13. Here, we consider only one dimensional objects and fields, so that $\mathbf{r} \rightarrow x$. Aberrations are modelled as random phases. The strength of the aberrations, which we call here f_{ab} is defined as the inverse of the correlation length of this random phase. It is controlled by modulating the Fourier-spectrum of an initial random phase (generated using Matlab's `rand()` function) by a Gaussian filter of width $\sigma_{filter} = 1/f_{ab}$. General details on the simulations can be found in Appendix B. Figure 4.3a shows the normalised sum-coordinate projections with different objects (Fig 4.3b) for fixed, low-strength aberrations. It also shows the absolute value squared of the PSF for comparison. These simulations demonstrate that, for low aberrations, the object has a negligible effect on the shape of the sum-coordinate projection. To be more quantitative, Figure 4.3c shows the similarity C^+ with and without objects for increasingly strong aberrations. C^+ is computed with and without an object and the correlation coefficient between these cases is computed via Matlab's `corrcoeff()` function. For each value of f_{ab}, 20 random aberrations and 20 random objects were generated, and the average correlation coefficient for each of these was computed. As the aberration strength increases, the projection with an object becomes less similar to the reference projection without an object. However, for low-strength aberrations, there is no appreciable difference between them. This is the regime in which Equation 4.4 is valid.

Figure 4.4 shows experimental justification that, in this study, we operate in such a low-aberration regime. These results are acquired using the experimental setup shown in Figure 4.6 which will be described in detail in Section 4.3. Sum-coordinate projections were measured with varying levels of aberration (implemented with an SLM and staying in the range of low-aberrations), with and without an object present. The main effect of the object is to decrease the maximum value of the measured C^+ while the shape remains effectively the same, as expected from Equation 4.4.

4.2.3 QAO with Photons Correlated in Position

In the derivation of Equation 4.4, we assumed that the object is in the Fourier-plane of the nonlinear crystal and so the photons arrive with near perfect anti-correlations at the object. As explained above, this is the illumination configuration that we have chosen to focus on in my PhD work. However, we know that the photons from SPDC exhibit strong position correlations in addition to these momentum anti-correlations. Therefore, it is also possible to arrive at a similar result if we consider the case of an object (and camera) in a plane conjugate to the crystal. In this section, we derive the Equations to use QAO for such a configuration. As before we can assume that the PSF is shift-invariant, and also that photons are perfectly correlated in position:

$$\phi(\mathbf{r_1}, \mathbf{r_2}) \approx \delta(\mathbf{r_1} - \mathbf{r_2}). \tag{4.16}$$

Starting from Equation 4.3 and performing the same change-of-variables, namely $(\mathbf{r_1}, \mathbf{r_2}) \rightarrow (\mathbf{r}_+, \mathbf{r}_-)$, we obtain:

$$G^{(2)}(\mathbf{r}'_+, \mathbf{r}'_-) = \left| \int t(\mathbf{r}_+)^2 h(\mathbf{r}'_+ + \mathbf{r}'_- - \mathbf{r}_+) h(\mathbf{r}'_+ - \mathbf{r}'_- - \mathbf{r}_+) d\mathbf{r}_+ \right|^2 . \tag{4.17}$$

From there, we use another change of variables: $\mathbf{r} = \mathbf{r}'_+ + \mathbf{r}'_- - \mathbf{r}_+$, to obtain:

$$G^{(2)}(\mathbf{r}'_+, \mathbf{r}'_-) = \left| \int t(\mathbf{r}'_+ + \mathbf{r}'_- - \mathbf{r})^2 h(\mathbf{r}) h(\mathbf{r} - 2\mathbf{r}'_+) d\mathbf{r} \right|^2 . \tag{4.18}$$

Then, recalling the minus-coordinate projection of $G^{(2)}$, defined as:

$$C^-(\mathbf{r}_-) = \int G^{(2)}(\mathbf{r_1}, \mathbf{r_1} + 2\mathbf{r}_-) d\mathbf{r_1} \tag{4.19}$$

and using again the change of variable i.e. $(\mathbf{r_1}, \mathbf{r_2}) \rightarrow (\mathbf{r}_+, \mathbf{r}_-)$, one can express C^- as:

$$C^-(\mathbf{r}_-) = \int G^{(2)} \left(\mathbf{r}_+, \mathbf{r}_- \right) d\mathbf{r}_+ . \tag{4.20}$$

Then, we can expand and simplify the previous equation as follow:

$$C^-(\mathbf{r}_-) = \iint K_-(\mathbf{r_A}, \mathbf{r_B}) h(\mathbf{r}) h(\mathbf{r_A} - 2\mathbf{r}_-) h^*(\mathbf{r_B}) h^*(\mathbf{r_B} - 2\mathbf{r}_-) d\mathbf{r_A} d\mathbf{r_B}, \tag{4.21}$$

where:

$$K_-(\mathbf{r_A}, \mathbf{r_B}) = \int t\left(\mathbf{r}\right)^2 t^* \left(\mathbf{r} + (\mathbf{r_A} - \mathbf{r_B}) \right)^2 d\mathbf{r}. \tag{4.22}$$

Equation 4.21 is the most general form of C^-. Under the same weak aberration hypothesis as before so that $|\mathbf{r_A} - \mathbf{r_B}|$ is small, Equation 4.22 simplifies into:

$$K_-(\mathbf{r_A}, \mathbf{r_B}) \approx \int |t\left(\mathbf{r}\right)|^4 d\mathbf{r} = K_- . \tag{4.23}$$

Under this assumption, K_- is now a constant that can be pull out of the integral in Equation 4.21. Finally, the minus-coordinate projection can be expressed as:

$$C^-(\mathbf{r}_-) \approx K_- |[h \star h](2\mathbf{r}_-)]|^2, \tag{4.24}$$

where we use $\star$ to denote the 2-dimensional correlation product, such that

$$[f \star g](\mathbf{r}') = \int_{-\infty}^{\infty} f(\mathbf{r}) g(\mathbf{r}' + \mathbf{r}) d\mathbf{r}. \tag{4.25}$$

Equation 4.24 has a very similar form to Equation 4.4 and shows that, in principle, QAO can work equally with correlated or anti-correlated photons.

The choice of which configuration to use is solely a practical one. We preferred to work in the anti-correlated (i.e. far-field imaging) regime due to technical restraints of the cameras. Most single-photon sensitive cameras cannot detect coincidences between a single pixel and itself. If photons are strongly correlated, it is very likely that they will arrive together at the same pixel. Much of the correlation information is then lost, as these coincidences cannot be measured. This can be somewhat circumvented if the correlations are spread over a few pixels. However, most cameras - including EMCCD and SPAD cameras - also suffer from pixel crosstalk, which further reduces the ability to detect coincidences at nearby pixels. For these reasons, we chose to operate in the anti-correlated regime i.e. illuminating the object with anti-correlated photon pairs.

4.2.4 QAO with Entangled vs Classically Anti-Correlated Photons

At this stage, it is interesting to discuss whether entanglement is truly necessary to perform QAO, or if classical correlations would be sufficient. To compare the results, let's go through the full reasoning with classically anti-correlated photons.

We consider a hypothetical experiment exploiting photons that are only classically anti-correlated, with no entanglement. We assume the existence of a point in the sample plane emitting perfectly anti-correlated photons, modelled by the following joint probability density function:

$$p_0(\mathbf{r}_1, \mathbf{r}_2) = \delta(\mathbf{r}_1 + \mathbf{r}_2) \tag{4.26}$$

When propagating photons through the imaging system, the blurring process caused by the system PSF can be described by introducing a random variable $\mathbf{N}$ to their initial positions in the object plane:

$$\mathbf{r}_k \to \mathbf{r}_k + \mathbf{N}_k, k \in 1, 2 \tag{4.27}$$

Since both photons are influenced by the system independently, it is necessary to introduce a distinct random spread term for each of them. Their probability density function is determined by the PSF of the imaging system: $P_{\mathbf{N}_k}(\mathbf{n}) = |h(\mathbf{n})|^2$. Applying basic statistics, we obtain the probability density in the image plane:

$$p_i(\mathbf{r}'_1, \mathbf{r}'_2) = \iint p_0(\mathbf{r}_1, \mathbf{r}_2)|t(\mathbf{r}_1)h(\mathbf{r}'_1 - \mathbf{r}_1)|^2|t(\mathbf{r}_2)h(\mathbf{r}'_2 - \mathbf{r}_2)|^2 d\mathbf{r_2} d\mathbf{r}_1, \tag{4.28}$$

where t is an object. Following the same mathematical reasoning as in Section 4.2.1, we obtain the following result:

$$p_i(\mathbf{r}'_+, \mathbf{r}'_-) = \int |t(\mathbf{r}'_+ + \mathbf{r}'_- - \mathbf{r})t(-\mathbf{r}'_+ - \mathbf{r}'_- + \mathbf{r})h(\mathbf{r})h(2\mathbf{r}'_+ - \mathbf{r})|^2 d\mathbf{r}. \tag{4.29}$$

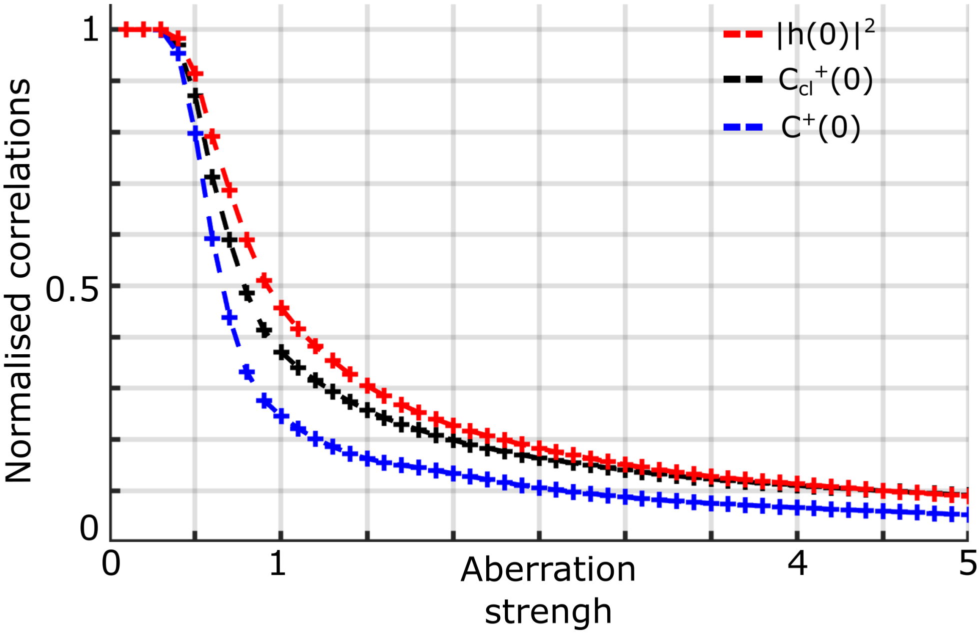

Figure 4.5: **Comparison of the sensitivity of QAO with entangled vs classically correlated photons.** Variation of the central values (blue) $C^+(\mathbf{0})$ and (black) $C_{cl}(\mathbf{0})^+$ in function of the aberrations strength. $C^+(\mathbf{0}) \propto |[h * h](\mathbf{0})|^2$ in the case of entangled photons, and $C^+_{cl}(\mathbf{0}) \propto |h|^2 * |h|^2(\mathbf{0})$ in the case of classically correlated photons. As a comparison, the red curve shows also the variations of $|h|^2(0)$, which corresponds to the case of classical AO.

Finally, we define the classical analogue to the sum-coordinate projection

$$C^+_{cl}(\mathbf{r}_+) = \int p_i(\mathbf{r_1}, 2\mathbf{r}_+ - \mathbf{r_1}) d\mathbf{r_1} = \int p_i\left(\mathbf{r}_+, \mathbf{r}_-\right) d\mathbf{r}_-, \tag{4.30}$$

and obtain:

$$\begin{aligned} C^+_{cl}(\mathbf{r}_+) &\approx K_{cl} \iint |h(\mathbf{r}) h(2\mathbf{r}_+ - \mathbf{r})|^2 d\mathbf{r} \\ &\approx K_{cl}\left[|h|^2 * |h|^2(2\mathbf{r}_+)\right], \end{aligned} \tag{4.31}$$

where

$$K_{cl} = \int |t\left(\mathbf{r}\right) t\left(-\mathbf{r}\right)|^2 d\mathbf{r}. \tag{4.32}$$

As one can see, classically anti-correlated photons would lead to a result that is similar but formally different from that obtained with entanglement. However, the QAO algorithm could still work, just in a less efficient manner. Indeed, simulations show that $|h * h|^2$ is more sensitive to the deformations of the PSF than $|h|^2 * |h|^2$, as demonstrated in Figure 4.5. As a result, the same holds for their central values i.e. $C^+(0)$ and $C^+_{cl}(0)$. We observe that the central value decreases more rapidly when increasing the aberration strength with entangled photons than with classical correlations. This increased sensitivity is a genuine advantage provided by entanglement. In addition, the red curve shows the variation $|h(0)|^2$, corresponding to the case of classical AO, which is even less sensitive. This sensitivity comes from the fact that h is complex, i.e. it has magnitude and phase. C^+ is sensitive to the phase of h since the autoconvolution is done before the absolute-value is taken, while in the classical case it is done after. Intuitively, one can see this extra sensitivity as arising due to the relative phase acquired by entangled photons, to which classically correlated photons are not sensitive. Furthermore, one can demonstrate through similar calculations that pairs of classically correlated photons (i.e., $p_0(\mathbf{r_1}, \mathbf{r_2}) = \delta(\mathbf{r_1} - \mathbf{r_1})$) lead to a similar result but with a correlation product instead of a convolution product: $C^-_{cl}(\mathbf{r}_-) \propto \left[|h|^2 \star |h|^2\right](2\mathbf{r}_-)$. Comparing this with Equation 4.24 we can see that correlated pairs also result in a phase sensitivity that is not present with classically correlated pairs.

In addition to this fundamental difference, there are some practical considerations to take into account. Other than SPDC, a source of strongly anti-correlated photon is unknown, so such a source would need to be engineered. A simple way to do this would be to rapidly scan two focused points of light in the object plane, in an anti-correlated manner. However, QAO would not be necessary in this case, since each of these scanned points would allow the PSF to be directly measured at the output. Thermal light is a widely used form of classically correlated light, but here the photons are correlated in position, where the correlation measurement suffers from the inability to resolve single-pixel correlations and from pixel crosstalk, as discussed in the previous section.

4.3 Experimental Details

In this section, I will now describe the experiments that utilise the QAO technique, and present experimental results demonstrating its effectiveness.

4.3.1 Experimental Setup

Figure 4.6 shows the experimental setup. Spatially entangled photon pairs are SPDC in a thin β-barium borate (BBO) crystal cut for Type I phase matching. Using lens f_1, the output surface of the crystal is Fourier-imaged onto the sample. Subsequently, the sample is imaged onto the camera using two $4f$ imaging systems, namely f_2-f_3 and f_4-f_5. Specimen- and system-induced aberrations can be introduced in the imaging system in planes A1 and A2, respectively. An SLM, used to correct for aberrations, is placed in a Fourier plane of the sample. Photon pairs transmitted through the system are detected at the output using an EMCCD camera. This is utilised for measuring both conventional intensity images and photon correlations, following the technique described in Ref. [121] and in Section 2.3.

The following sections detail the results of aberration correction with QAO in various experimental conditions, and with various samples as test objects.

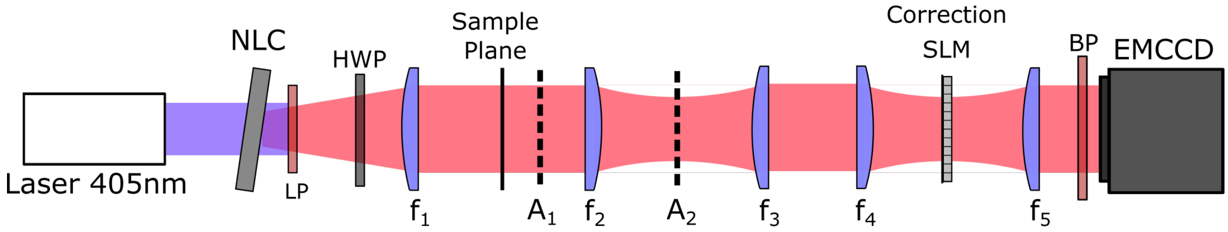

Figure 4.6: **Experimental setup for QAO.** Spatially-entangled photon pairs centred at 810 nm are produced via Type I Spontaneous Parametric Down-Conversion (SPDC) using a 405 nm collimated continuous-wave laser and a 0.5mm-thick β-barium borate nonlinear crystal (NLC). Blue photons are then filtered out by a low-pass filter (LP) at 650 nm. The sample is illuminated by the photon pairs while being positioned in the Fourier plane of the crystal ($f_1 = 100mm$). It is subsequently imaged (with a magnification of 1) onto the electron-multiplying charge-coupled device (EMCCD) camera using two 4-f imaging systems, $f_2 - f_3$ and $f_4 - f_5$. The spatial light modulator (SLM) used to correct aberrations is positioned in a Fourier plane of the sample between f_4 and f_5. For clarity, it is depicted in transmission, but in practice, it operates in reflection. Optical aberrations can be introduced at either the optical planes A1 (near the sample plane) or A2 (Fourier plane). Note that plane A1 is deliberately placed at a small distance from the object plane to introduce sufficient aberrations. To detect only near-degenerate photon pairs, a band-pass filter (BP) at 810 ± 10 nm is positioned in front of the camera.

4.3.2 Modal-based Optimisation Approach

To correct aberrations, we employ a modal-based adaptive optics algorithm that utilises C_0^+ as a feedback parameter, where $C_0^+ = C^+(\mathbf{r}_+ = 0)$. In this work, the Zernike polynomials are used as the modal basis for correction, since they form an orthonormal basis on the unit disk and result in a smooth phase mask [184]. The phase masks $\theta(\psi, \rho)$ are generated using

$$\theta(\psi,\rho) = \sum_{n=n_{min}}^{n_{max}} \sum_{m=-n}^{n} \alpha_{mn} Z_n^m(\psi,\rho), \tag{4.33}$$

where α_{mn} is the coefficient for the m, n^{th} Zernike polynomial Z_n^m, and $\psi = \text{arctan2}(y, x)$, $\rho = \sqrt{x^2 + y^2}$ are the 2-dimensional radial coordinates. Note that $Z_n^m = 0$ when $m + n$ is odd, so the total number of modes is given by $N = \frac{1}{2}[(n_{max} + 1)(n_{max} + 2) - n_{min}(n_{min} + 1)]$ with the condition that $n_{max} \geq n_{min} \geq 0$. The correction is done modally, meaning the best correction for each Zernike mode is found independently of each other mode. To reduce the errors due to any crosstalk between modes, the correction is repeated starting from the phase mask found during the previous iteration. In this work, we consider all modes with radial numbers $n \leq 5$ and azimuthal numbers $|m| \leq n$, excluding piston, tip, and tilt. For each Zernike mode (Z_n^m), we record five sum-coordinate projections with distinct, known bias amplitudes (α_{nm}). In each measurement, the correcting SLM phase θ_{nm} is thus modulated according to the equation:

$$\theta_{nm} = \theta_{nm-1} + \alpha_{mn} Z_n^m, \tag{4.34}$$

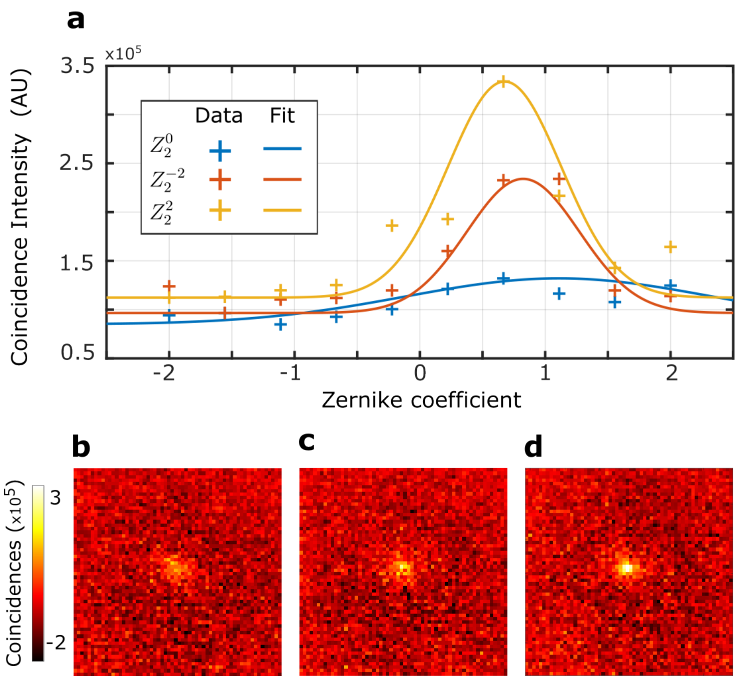

Figure 4.7: **Modal optimisation of C_0^+.** For each Zernike function, we find the coefficient α_{mn}^{corr} that maximises C_0^+, then add this to our correction mask. **a,** Value of the peak of the sum-coordinate projection plotted as a function of correction strength for each of the n=2 Zernike functions. Solid line shows the fitted Gaussian function for each mode. **b,c,d,** $C^+(r)$ after optimising C_0^+ for Z_2^0, Z_2^{-2}, Z_2^2, respectively. Data taken with Nuvu Cameras HNu 128 EMCCD. a.u. - arbitrary units

where θ_{nm-1} represents the optimal phase correction obtained for the previous mode. Such a phase modulation approach is commonly used in classical modal AO [174].

For each mode mn, a set of sum-coordinate projections is acquired for a range of correction coefficients α_{mn}. The maximum value for each projection is fitted as a function of α_{mn}, and the value of α_{mn}^{corr} that maximises the projection peak is calculated. Figures 4.7b-d and Figure 4.8h show examples of acquisition and fitting for different modes. We use a Gaussian model to fit the data.

From experimental observations, we assume that the correlation peak C_0 can be written as a function of correction coefficient α_{mn} with the form

$$C_0(\alpha_{mn}) = \beta + A\exp\left[-\frac{1}{\sigma^2}(\alpha_{mn} - \alpha_{mn}^{corr})^2\right]. \tag{4.35}$$

That is, $C_0^+(\alpha_{mn})$ is a Gaussian that is centred at the best correction α_{mn}^{corr}. β represents the noise floor of the measurements, since C_0^+ typically never goes to 0, as can be seen in Figure 4.7a. A is the amplitude of the Gaussian function, and σ is the width, both of which are dependent on acquisition time for $C^+(\mathbf{r}_+)$. MATLAB's curve fitting functionality is used to perform the fits, and the value of α^{corr} is extracted.

Figure 4.7 shows in more details another example where the aberrations consist of three modes: Z_2^0, Z_2^{-2}, Z_2^2 (defocus, vertical astigmatism, and oblique astigmatism). The coincidence image peak was calculated for a range of 10 different values of α_{mn}^i for each mode, plotted in Figure 4.7a. In principle, the fitting can be done with as few as two points per mode plus one value for zero correction, allowing for correction with only $2N + 1$ points [185]. In practice we take more points per mode and update the correction mask after each mode which improves the SNR of C_0^+. This increase in SNR after correcting each mode can be seen in Figures 4.7b-d.

4.4 Results

4.4.1 Correction of System-induced Aberrations

To illustrate our method, we placed a biological sample - a honeybee mouthpiece on a microscope slide - in the sample plane and captured its intensity image in transmission (Figure 4.8a). In the absence of aberrations, the sum-coordinate projection exhibits a distinct and sharp peak, as shown in Figure 4.8d. However, when aberrations are present, the image becomes blurred, and the correlation peak is spread and distorted, as depicted in Figures 4.8b and 4.8e, respectively. In this demonstration, we induce aberrations by introducing a second SLM at plane A2 that displays a low-frequency random phase pattern. This configuration, with low-order Zernike modes in the camera Fourier-plane, most closely emulates a scenario with system-induced aberrations.

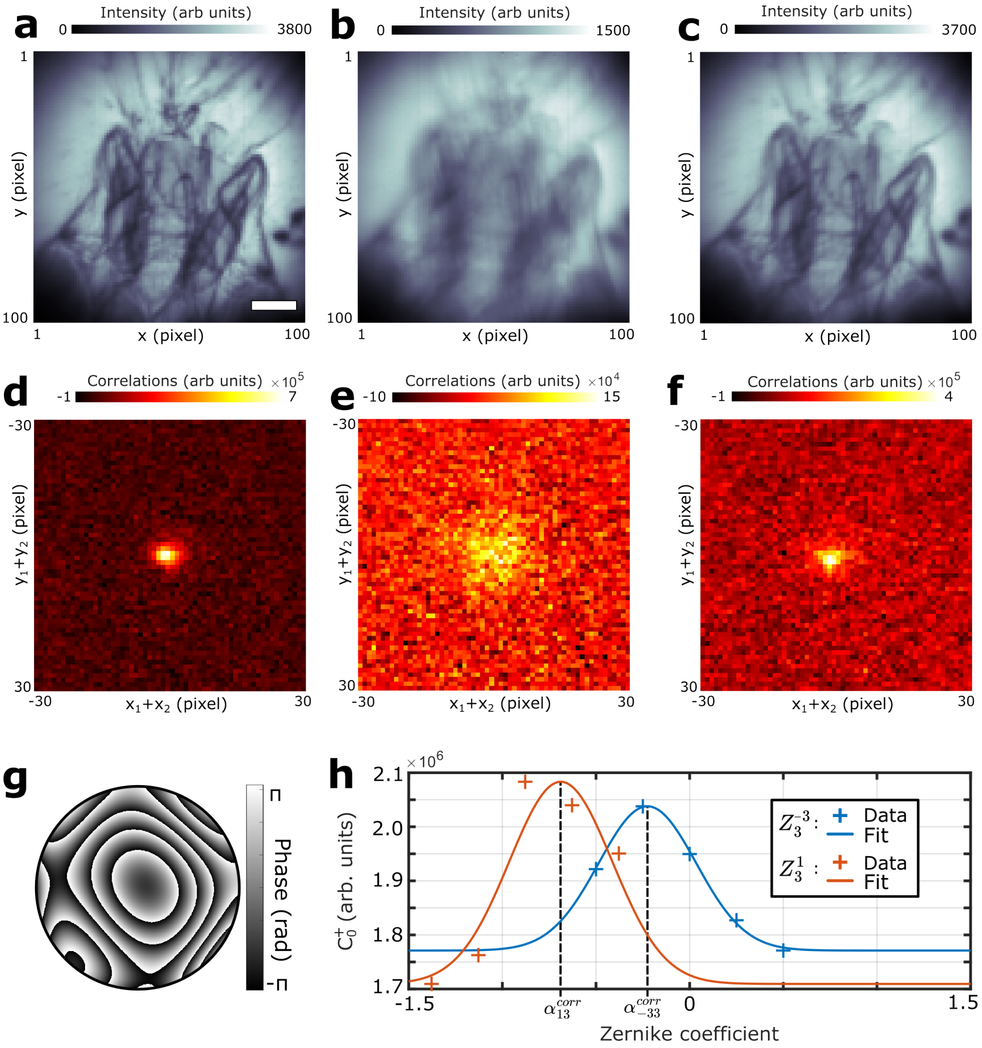

Figure 4.8: **Results of QAO correction. a-c**, Intensity images of a biological sample (bee head) acquired in transmission **(a)** without aberrations, **(b)** with aberrations before correction, and **(c)** after correction. Using the aberration-free intensity image as a reference, we find structural similarity values of $SSIM = 77.89\%$ and $SSIM = 98.41\%$ for the uncorrected image and the corrected image, respectively. **d-f**, Correlations images $C^{+}(\delta\mathbf{r}^{+} = \mathbf{r_1} + \mathbf{r_2})$ measured **(d)** without aberrations, **(e)** with aberrations before correction, and **(f)** after correction. **g,** Optimal phase pattern obtained after correction and displayed on the SLM. **h,** Values of the sum-coordinate projection peaks C_0^{+} in function of the coefficient α_{mn} for two Zernike modes Z_3^{-3} and Z_3^{1} (crosses). $\alpha_{-33}^{corr} = -0.2253$ and $\alpha_{13}^{corr} = 0.6881$ are the two optimal correction values for each mode returned by the fit (solid lines). Each intensity and sum-coordinate projection was obtained from 10^5 frames, approximately equivalent to a 2 min-acquisition. The white scale bar is 400 μm. Data taken with Nuvu Cameras HNu 128 EMCCD. a.u. - arbitrary units

For a practical example of the modal correction, the values of C_0^+ obtained from the sum-coordinate projections for the modes Z_3^{-3} and Z_3^1 are shown in Figure 4.8h. The positions of the maxima, denoted α_{-33}^{corr} and α_{13}^{corr}, representing the optimal corrections for their respective mode, are determined using Gaussian model described by Equation 4.35. After several optimisation steps, a narrow peak is recovered in the sum-coordinate projection (Figure 4.8f) and a sharp image appears in the intensity (Figure 4.8c).

Visual comparison with the aberration-free images shows a clear improvement after correction. Quantitatively, one can use the structural similarity index measure (SSIM) as a metric for image similarity. This metric takes into account properties of the human visual system. The SSIM between images A and B is calculated using

$$\mathrm{SSIM} = \frac{(2\mu_A\mu_B + C_1)(2\sigma_{AB} + C_2)}{(\mu_A^2 + \mu_B^2 + C_1)(\sigma_A^2 + \sigma_B^2 + C_2)}, \tag{4.36}$$

where μ_A, μ_B are the means of images A and B, σ_A, σ_B are the standard deviations of A and B, and σ_{AB} is the cross-covariance between A and B. $C_1 = 0.01L$ and $C_2 = 0.03L$ are regularisation constants where L is the dynamic range of image A. SSIM values can be expressed as a percentage similarity. For full details see Ref. [186].

Using the aberration-free image as a reference (Figure 4.8a), we find SSIM= 77.89% for the uncorrected image (Figure 4.8c) and SSIM = 98.41% for the corrected image (Figure 4.8b). Note that here, although the object is illuminated by a source of entangled photon pairs, whose quantum properties are crucial for measuring C^+ and thus correcting aberrations, the imaging process itself is purely 'classical' as the output image is obtained through a simple intensity measurement.

4.4.2 Defocus Correction with 3D Sample

QAO offers several advantages compared with classical AO. Firstly, as demonstrated in Figure 4.8, it does not require a guide star. All photon pairs forming the image possess information about the system aberrations at every point, because these are encoded in their spatial correlations. Additionally, as demonstrate in Subsection 4.2.2, the performance of QAO does not depend on the sample properties or the imaging modality. The spatial correlation structure is a property of the illumination itself, and is only affected by the system aberrations. This implies that QAO will converge irrespective of the observed sample type, ranging from nearly transparent samples (e.g. cells) to denser ones (e.g. layered minerals), regardless of their complexity or smoothness of structure.

In this aspect, QAO thus surpasses all image-based AO techniques, where the chosen metrics and optimisation performances depend on the properties of the sample. In this section we show that,

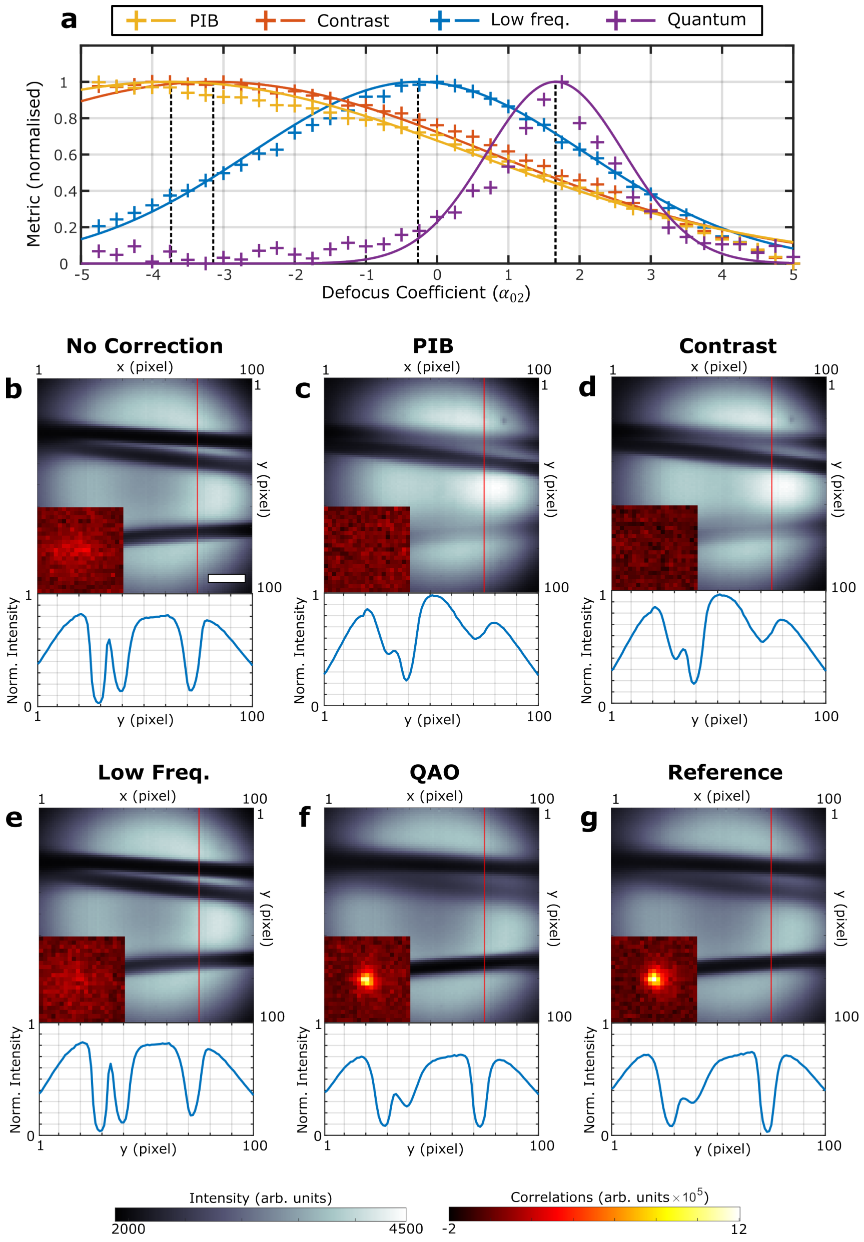

Figure 4.9: **Comparison between QAO and classical image-based AO**. **a,** Values of three image quality metrics (namely power in bucket, image contrast and low frequencies) and C_0^+ in function of the defocus correction coefficient α_{02}. Data is given by the crosses, and the fits used to find optimal values (α_{02}^{corr}) are given by solid lines. In this experiment, the object is 3-dimensional (three thin copper wires). **b-g,** Intensity images (grayscale), central regions of C^+ (inset) and intensity profile for a single column (line plot) for various defocus corrections on SLM: **b,** without correction ($\alpha_{02}^{corr} = 0$ and SSIM = 76.39%); **c,** Optimal correction found using a 'Power in Bucket' metric ($\alpha_{02}^{corr} = -3.1427$ and SSIM = 50.56%); **d,** Optimal correction found using a 'Image Contrast' metric ($\alpha_{02}^{corr} = -3.1427$ and SSIM = 52.29%); **e,** Optimal correction found using a 'Low Spatial Frequencies' metric ($\alpha_{02}^{corr} = -0.2677$ and SSIM = 72.61%); **f,** Optimal correction found using QAO ($\alpha_{02}^{corr} = 1.6622$ and SSIM = 96.83%); **g,** No aberration. Vertical red lines show selected column for profile plots. Each intensity image and sum-coordinate projection were obtained from 10^5 frames, approximately equivalent to a 2 min-acquisition. The white scale bar is 400μm. Data taken with Nuvu Cameras HNu 128 EMCCD. a.u. - arbitrary units

in certain imaging situations, image-based approaches can lead to systematic error in aberration correction, whereas QAO converges to the correct solution. We consider a situation where the sample has a 3-dimensional structure, which is very common in microscopy. In such a case, it is known that it is not possible to correct for defocus aberrations properly. Indeed, when using an image quality metric, it may optimise for the wrong focal plane within the sample. Since the sample structure has no effect in QAO, defocus correction is possible.

Here we show a simple proof-of-principle experiment to demonstrate this defocus correction. We chose an object consisting of three copper wires, each with an approximate thickness of 0.15 mm, and spaced approximately 5 mm apart along the optical axis. We then induced defocus aberration with strength $\alpha_{02}^{aber} = -2$ by placing a second SLM in plane A2. Sum-coordinate projection and intensity images are acquired for a wide range of defocus corrections ($\alpha_{02} \in [-5, 5]$) programmed on the correction SLM. At each step, values of three standard AO image quality metrics are calculated from the intensity image: power-in-bucket [175], image contrast [176], and low frequency content [177]. In addition, C_0^+ is also retrieved from the sum-coordinate projection. For an image I, the chosen metrics are defined as follows:

Power-in-Bucket: This metric is simply the sum of each pixel within a circular region of the image. The diameter of this region was chosen to be 100 pixels, i.e. the full width of the image.

$$M_{PIB} = \sum_{i=1}^{N_x} \sum_{j=1}^{N_y} I_{ij} \tau_{ij} \tag{4.37}$$

where

$$\tau_{ij} = \begin{cases} 1, & \text{if } (i - N_x/2)^2 + (j - N_y/2)^2 \leq r^2 \\ 0, & \text{otherwise,} \end{cases} \tag{4.38}$$

with $r = 50$.

Contrast: This metric is the difference between the maximum and minimum values of the intensity normalised image:

$$M_{contrast} = \max(I) - \min(I) \tag{4.39}$$

Since the illumination does not cover the full ROI, only the values within the same circular region τ as defined for the power-in-bucket are considered.

Low Frequencies: This metric is introduced in [177], where they show that optimising the low spatial frequency content of an image will optimise the image sharpness. The Fourier transform of the image is computed, and the sum of the low-frequency values are taken as the metric:

$$M_{LF} = \sum_{i=1}^{N_x} \sum_{j=1}^{N_y} a_{ij} \mathcal{F}[I]_{ij}, \tag{4.40}$$

where $\mathcal{F}[I]$ is the 2-dimensional fast Fourier transform of the image I, and a is an annulus where

$$a_{ij} = \begin{cases} 1, & \text{if } r_0^2 \leq (i - N_x/2)^2 + (j - N_y/2)^2 \leq r_1^2 \\ 0, & \text{otherwise,} \end{cases} \tag{4.41}$$

with $r_0 = 4$ and $r_1 = 10$.

Figure 4.9.a shows the four corresponding optimisation curves. First, we observe that the various classical AO metrics return different optimisation coefficients, highlighting their dependency on the object's structure. Then, by examining the intensity images captured while programming each optimal correction phase pattern (Figs. 4.9b-e), it becomes evident that none of these metrics properly corrected the aberrations. Indeed, the aberration-free image in Figure 4.9g clearly shows that only the bottom wire is in the focal plane, which is not the case in any of the intensity images shown in Figures 4.9b-e. It should be noted here that the goal is to optimise the image quality in a specific plane. This is desirable for example in sectioning microscopy techniques where the aim is to acquire images at different, known planes in the sample.

On the other hand, QAO converges to the correct solution, as seen in the intensity image shown in Figure 4.9f (SSIM = 96.83%). Interestingly, we also note that the optimum value found with QAO is $\alpha_{02}^{corr} = 1.622$, which differs slightly from the value of 2 (opposite of $\alpha_{02}^{aber} = -2$) that we would be expect to find. This is because QAO corrects not only for the intentionally introduced defocus aberrations in the A2 plane, but also for those inherent in the imaging system. This is also shown by the fact that the correlation peak in Figure 4.9.f (inset) is slightly narrower than the one in Figure 4.9.g (inset). This demonstration uses a very simple three-dimensional sample: three spaced wires. However, QAO can in principle be used with more complex three-dimensional samples as long as we remain within the regime of weak aberrations. Such samples are typically studied with optical tomography methods, where QAO can therefore be used after adapting the mathematical formalism to account for the thickness of these objects [127].

4.4.3 Correction of Specimen-induced Aberrations

The demonstrations up to this point have introduced aberrations using an SLM in plane A2 (Fig 4.6). These results act as a good proof-of-principle of QAO, but are not necessarily representative of a general AO scenario. It is also important to test the performance of QAO in cases with unknown, specimen-induced aberrations. To approximate the effects of specimen-

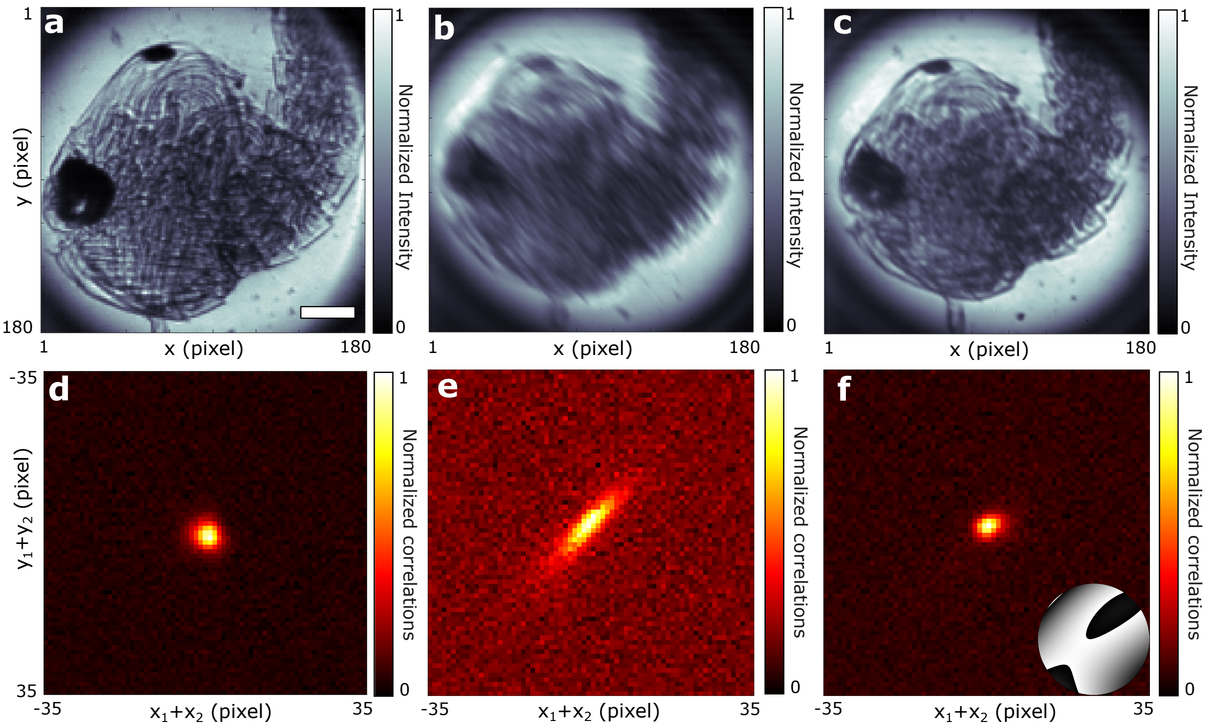

Figure 4.10: **Correction of Specimen-induced Aberrations**. These results were obtained using the experimental setup in Figure 4.11 but in a classical imaging configuration. Aberrations were induced by inserting the PDMS in plane A1. **a,b and c**, Direct intensity images acquired without aberrations, with aberrations and after QAO correction, respectively. **d,e and f**, Sum-coordinate projections acquired without aberrations, with aberrations and after QAO correction, respectively. The white scale bar represents 400μm. Data taken with Andor Ixon Ultra 897 EM-CCD. a.u. - arbitrary units

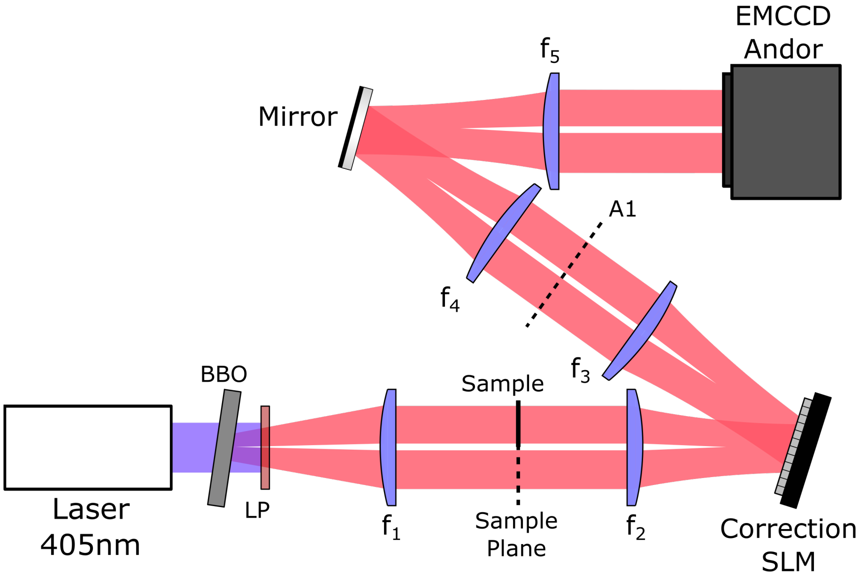

Figure 4.11: **Experimental setup for QAO applied to a quantum imaging experiment.**

induced aberrations we use a 1-cm thick layer of polydimethylsiloxane (PDMS), a clear polymer with a smooth but non-flat surface (shown in Figure 4.12). The PDMS layer is placed a short distance after the sample, corresponding to plane A1 in Figure 4.6. This emulates a layer of inhomogeneous clear tissue or sample support that is typically the source of sample-induced aberrations in practical microscopy. Figure 4.10 shows the results of applying QAO to correct for PDMS-induced aberrations. In this experiment, the sample is a mosquito pupa. The results clearly show that correction for specimen-induced aberrations is possible with QAO.

4.4.4 QAO Applied to a Quantum Imaging Setup

Finally, in order to showcase its potential for quantum imaging, QAO is applied to a ‘quantum’ variant of the bright-field imaging setup depicted in Figure 4.6. Such a quantum variant is detailed in Figure 4.11. In such a scheme, only one photon of a pair interacts with the object, while its twin serves as a reference. For this, the sample is placed on only one half of the object plane ($x > 0$), as observed in the intensity images shown in Figures 4.12.a and b. To interpret this specific arrangement with Equation 4.13, we theoretically define the object such that $t(x < 0) = 1$ and $t(x > 0)$ describes the object. Then, the final image R is obtained by measuring photon correlations between all symmetric pixel pairs of the two halves, i.e. $R(\mathbf{r}) \approx G^{(2)}(\mathbf{r}, -\mathbf{r})$. This image, shown in Figure 4.12.e, is the equivalent of the diagonal-encoded images introduced in Subsection 2.6.1 for an object illuminated by anti-correlated pairs. As demonstrated in previous studies [65, 73, 165], such a quantum scheme offers some advantages over its classical counterpart, including an enhanced transverse spatial resolution and increased resilience against noise and stray light.

In the presence of aberrations, however, we show that this imaging technique becomes highly

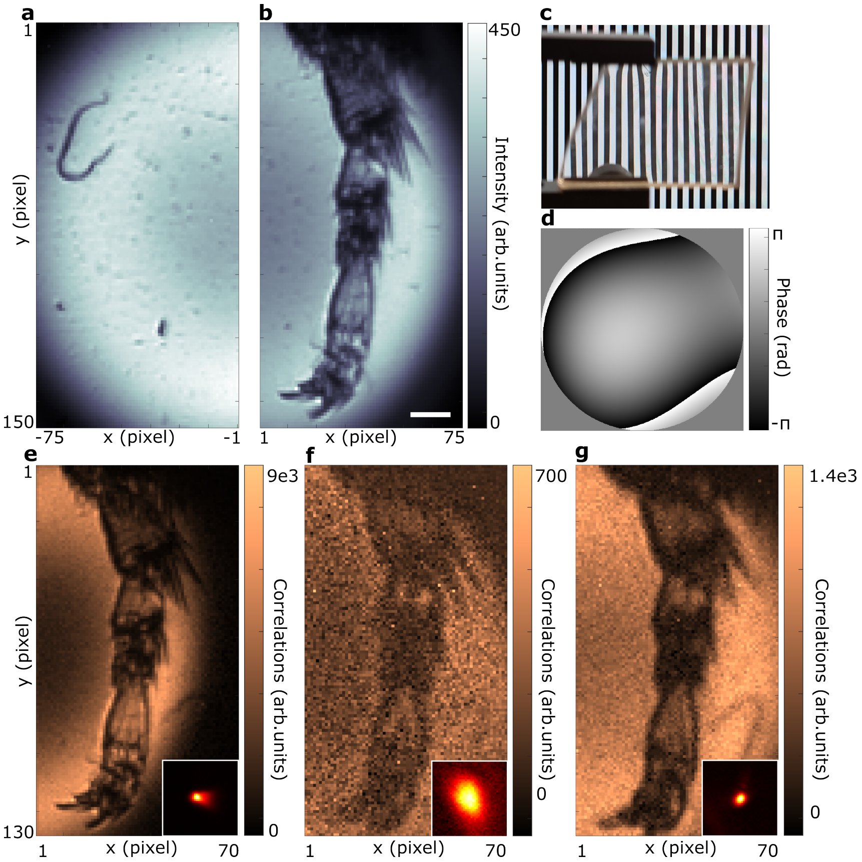

Figure 4.12: **Application of QAO to quantum imaging. a,** Intensity image formed by one photon of a pair used as a the reference photon. **b,** Intensity image formed by the other photon used to illuminate the sample, here a bee's leg. **c,** 1-cm-thick piece of PDMS inserted in plane A1 in the setup in Figure 4.6 to induce aberrations. **d,** Optimal phase pattern obtained after correction and displayed on the SLM. **e-g,** Anti-correlation images $R(\mathbf{r}) \approx G^{(2)}(\mathbf{r}, -\mathbf{r})$ obtained **(e)** without induced aberration (signal-to-noise ratio: SNR= 29), **(f)** with aberration ($SNR \approx 3$), and **(g)** after aberration correction ($SNR = 15$). Insets show the sum-coordinate projection in each case. Each sum-coordinate projection to achieve QAO was obtained from $2.2.10^4$ frames, approximately 3 minutes of acquisition, and each anti-correlation image was obtained from 10^7 frames, approximately 24 hours of acquisition. Note that the EMCCD camera used here is different from this used in Figures 4.8 and 4.9, and has a frame rate of just 130 fps. The total intensity (i.e. total number of photons) measured on the camera was the same in the presence of aberrations before and after correction. The white scale bar represents 400μm. Data taken with Andor Ixon 897 Life EMCCD.

impractical and thereby loses all its purported advantages. For example, Figure 4.12.f shows an anti-correlation image acquired after inserting a 1-cm-thick layer of PDMS, (shown in Figure 4.12.c) on both photon paths in plane A1 to induce optical aberrations. Not only is the resulting image blurred, leading to a complete loss of the expected resolution advantage, but also its signal-to-noise ratio is greatly reduced, rendering the sample almost indiscernible. We can compute the SNR by calculating the mean divided by the standard deviation of the pixel values in a bright (i.e. object-free) region of the image. In the presence of the PDMS, we find the SNR ≈ 3. After applying QAO, we retrieve an anti-correlation image in Figure 4.12.g that has a spatial resolution closer to that without aberrations and of much better quality (SNR= 15). The inset of Figure 4.12.g shows the corresponding sum-coordinate projection, exhibiting a much narrower and more intense peak, and Figure 4.12.d shows the optimal SLM phase pattern.

Aside from the loss of spatial resolution, the SNR has a large impact on the acquisition times of correlation-based quantum imaging experiments. In fact, recall from Chapter 2 that the SNR is proportional to the square-root of the acquisition time. The acquisition time with aberrations, T, that is needed to match the SNR of the corrected case is then

$$T \approx \left(\frac{SNR_{ab}}{SNR_{corr}} \right)^2 T_0 = \left(\frac{15}{3} \right)^2 T_0 = 25T_0, \tag{4.42}$$

where T_0 is original acquisition time. In our experiment, $T_0 \approx 24$ hours, meaning the required acquisition time to match SNR is on the order of 25 days. Clearly, this is beyond impractical, and in the vast majority of cases is too long to wait for one image to justify any quantum imaging benefits. QAO could therefore enable photon-pairs-based experiments that until now have not been feasible due to time constraints. Even if the correction process takes one full day, this would still give a total experiment time of two days, which is a considerable improvement.

Finally, when comparing carefully the sum-coordinate projections without aberrations (inset in Figs. 4.12.e) and after correction (inset in Figs. 4.12.g), we observe that QAO also corrected for a small PSF asymmetry present in the initial system. Compensating for this asymmetry results in a more uniform output image (Figure 4.12.g) than that obtained in the aberration-free case (Figure 4.12.e). By using QAO, we show a significant improvement of the output image quality in terms of resolution, SNR, and uniformity, effectively restoring the operational capability of this quantum imaging technique.

4.5 Discussion

We have introduced a QAO method that eliminates the need for a guide star. By optimising the spatial correlations of entangled photon pairs, we can directly optimise the system PSF and compensate for optical aberrations. QAO circumvents certain limitations linked to conventional image-based AO, and is particularly well-suited for classical and quantum full-field, label-free and linear microscopy systems.

In our study, we demonstrate QAO in the regime of weak optical aberrations. We use artificial layers to simulate aberrations commonly encountered in real-world microscopy systems, including system-induced (e.g. astigmatism, defocus, comatic aberrations due to objectives, and misalignment) and weak specimen-induced aberrations (e.g. translucent tissues surrounding the sample, immersion liquid, and sample support). Within this regime of weak aberrations, there are no fundamental barriers preventing the use of QAO in other, more advanced label-free imaging systems. For instance, QAO could improve current image-based approaches used in optical coherence tomography [187], be combined with 3D imaging techniques, some of which already utilised entangled photon pair sources [127], be employed in phase imaging and high-numerical aperture imaging schemes and adapted to reflection geometries by employing multiple SLMs. As with classical AO, the effectiveness of the correction found with QAO will always depend on the imaging modality and the nature of aberrations present. For instance, spatially variant aberrations will restrict the field of view in the corrected image, although this limitation might be circumvented by utilising alternative AO designs like conjugate and multi-conjugate AO [188, 189]. Finally, it is important to note that QAO is not yet adaptable in fluorescence microscopy, but this could change in the future with the emergence of photon-pairs emitting biomarkers [190].

In practice, the main limitation of QAO is its long operating time. Using an EMCCD camera, acquisition times of the order of one minute are required to measure one sum-coordinate projection. This means that correcting for multiple orders of aberration can take up to several hours. However, this technical limitation can be overcome by employing alternative camera technologies, some of which are already available commercially. For example, SPAD cameras have been employed to capture sum-coordinate projections at speeds up to 100 times faster than EMCCD cameras using similar photon pair sources [191, 192]. Another promising technology is the intensified Tpx3cam camera, which has recently been utilised for similar correlation measurements [128, 193, 194]. As technology advances, we anticipate that acquisition times will soon be reduced to seconds, leading to corresponding correction times in the order of minutes. In addition, here we chose Zernike polynomials as the basis set for aberration representation, even though they may not be optimal [195]. In particular, if the aberrations are more complex, wavefront shaping approaches using Hadamard or random bases should be considered [2, 86, 110, 113, 196].

In our demonstration, QAO employs entanglement between photons. Indeed, replacing our source by classically-anti-correlated photons would yield a formally different output measurement i.e. $C_{cl}^{+} = |h|^2 * |h|^2$ (Section 4.2.4). Such a metric could still be used for AO, but is genuinely less sensitive compared to entangled photons (Figure 4.5). Another benefit of photon pairs is their second-order coherence. This allows for coherent information - for example phase - to be extracted simultaneously to incoherent intensity information, which is not possible with classically correlated photons. In addition, producing such near-perfect classical anti-correlations is challenging in practice. One potential approach could use thermal light, that is naturally position-correlated, and adapt the output measurement by using the minus-coordinate projection of the $G^{(2)}$. This measurement will have lower contrast and sensitivity than entangled photons and will face issues with camera crosstalk, but could benefit from a higher brightness. Finally, it should also be noted that prior studies [104–107, 112] have explored the use of entangled photon pairs to correct specific types of optical aberrations, but without employing AO.

In summary, we have demonstrated that QAO works for bright-field imaging (classical and quantum) and that it can also extend to more complex label-free modalities, such as phase imaging and reflection configurations. Another crucial point is that QAO can be used in all the quantum versions of these systems [60, 61, 79, 166, 168, 169]. This could prove very useful because, as shown in the bright-field case in Figure 4.12, such quantum schemes are extremely sensitive to optical aberrations, to the point of preventing them from working. QAO thus has the potential to optimise the operation of any imaging system based on photon pairs, and could therefore play a major role in the development of future quantum optical microscopes.

Chapter 5

Future Directions

In this chapter I discuss some potential future directions in which to take the concepts that I have developed during my PhD. One of these directions is the extension of quantum imaging and shaping to experiments using Type II SPDC. As a reminder, Type II SPDC generates pairs in which the polarisation of the signal photon is orthogonal to that of the idler. This allows the pairs to be easily separated while maintaining their spatial distributions, which could enable more complex imaging schemes. I describe how the two-photon imaging and propagation theory can be extended to experiments in which the photons in each pair propagate through different systems. I then introduce the concept of 'non-local' or remote aberration correction for which I have some preliminary results. Lastly I discuss some other potential directions in which to take the work in this thesis.

5.1 Imaging with Type II SPDC

The main difference when imaging with Type II SPDC is that the two photons in each pair will, in general, not propagate through the same system. Since the signal and idler photons have orthogonal polarisations, i.e. H and V, a polarising beamsplitter (PBS) can be used to easily separate them. Actually, the signal and idler from a Type I source can also be separated using a d-shaped mirror in the far-field (as in Ref. [61]) but using a Type II source with a PBS is (moderately) easier to implement, and both the signal and idler beam retain their full angular spectrum. Figure 5.1 shows an example of a Type II experiment in which the signal and idler beams are separated and pass through different systems.

The mathematical formalism introduced in the previous chapters can be easily adapted to describe this. Since the signal and idler photons now propagate through two different systems, we now use two different point-spread functions h_1 and h_2. The two-photon propagation equation

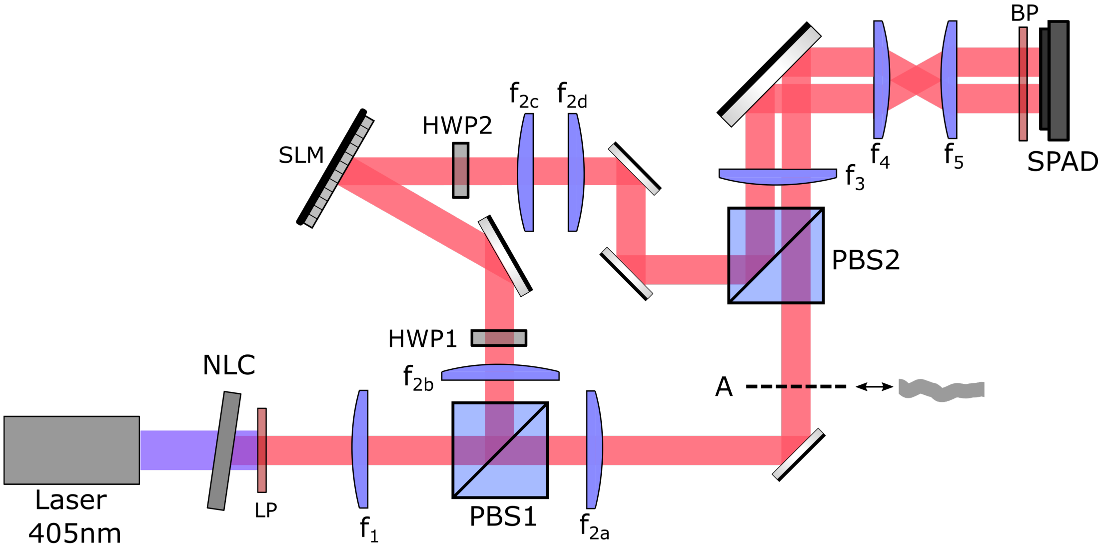

Figure 5.1: **Experimental setup for imaging with Type II SPDC.** A Type II BBO crystal (NLC) is pumped with a 405 nm CW laser generating pairs containing photons with orthogonal (H and V) polarisations. The remaining pump photons are removed with a 650 nm long-pass filter (LP). The photons in each pair are then separated using a polarising beamsplitter (PBS1). In the horizontal polarisation path there is plane A in which aberrations can be inserted, and in the vertical polarisation path there is an SLM. The SLM only modulates horizontally polarised light so a half-wave plate (HWP1) is used to rotate the polarisation of the photons. A second halfwave plate (HWP2) after the SLM is used to rotate the photons back to vertical so the two paths can be recombined with a polarising beamsplitter (PBS2). Both beams are imaged onto the camera with lenses f_3-f_5. The lenses are such that the SLM and aberration are in an optical plane conjugate to the crystal surface, and the SPAD is in a far-field plane. Distances between lenses are not to scale. Lens f_5 can be swapped for a lens $0.5f_5$ to image the crystal surface and measure the near-field correlation. An 810 ± 5 nm band-pass filter (BP) is used to select only degenerate photon pairs.

(Equation 3.23) then becomes

$$G^{(2)}(\mathbf{r}'_1, \mathbf{r}'_2) = \left| \iint \phi(\mathbf{r}_1, \mathbf{r}_2) h_1(\mathbf{r}'_1, \mathbf{r}_1) h_2(\mathbf{r}'_2, \mathbf{r}_2) d\mathbf{r}_1 d\mathbf{r}_2 \right|^2 . \tag{5.1}$$

In a Type II experiment the signal and idler beams can be directed onto different regions of the camera, or in fact onto separate cameras. Figures 5.2a and b show the signal and idler far-field intensities on two separate regions of the camera, captured with the experimental setup shown in Figure 5.1. Due to the additional 4-f imaging system in the SLM path (lenses f_{2c}, f_{2d}) the idler beam is spatially inverted relative to the signal beam. The photons are therefore correlated in the far-field and anti-correlated in the near-field so the relevant projection in each case is swapped. Figure 5.2d shows the minus-coordinate projection of the $G^{(2)}$ between the two regions.

Figure 5.2c shows the intensity at the camera in the NF configuration, and Figure 5.2e shows the sum-coordinate projection. The distortion in this projection is likely due to aberrations such as coma in the imaging system. The reason it does not affect the correlations in the far-field is likely because the physical origin of the aberrations is close to a Fourier plane of the imaging system. Such coma aberration in the imaging system will need to be corrected in the future to obtain cleaner results, for example, by slightly changing the system configuration and placing the PBS just before the camera. The camera used in this example is the Hermes SPAD Array from MicroPhotonic Devices. This camera has 32×64 pixels and a maximum achievable frame-rate of approximately 65 kfps when performing simultaneous correlation computations. In the following section I describe the concept for a remote aberration correction method that is an extension of the quantum-assisted adaptive optics method introduced in Chapter 4.

5.2 Remote Aberration Correction

5.2.1 Concept

Figure 5.1 shows the experimental setup for remote aberration correction. In this system there is some optical aberration in the path of one photon, which we say is the signal photon, and in the path of the idler photon there is an SLM. The lenses are such that the aberration and SLM are both positioned in image planes of the nonlinear crystal. After they are separated by PBS1 the signal and idler photons pass through different systems which we label h_1 and h_2, respectively. The photons are initially strongly correlated, i.e. $\mathbf{r}_1 \approx \mathbf{r}_2$ and $\mathbf{k}_1 \approx -\mathbf{k}_2$. However, as in Chapter 4, the aberrations will degrade these correlations. The concept of remote aberration correction is to manipulate the idler photon with the SLM such that strong correlations are recovered. To see why this works, I will apply the theoretical tools that were developed in Chapter 3 using the new two-photon propagation equation, Equation 5.1. If we take our input state as the signal and idler

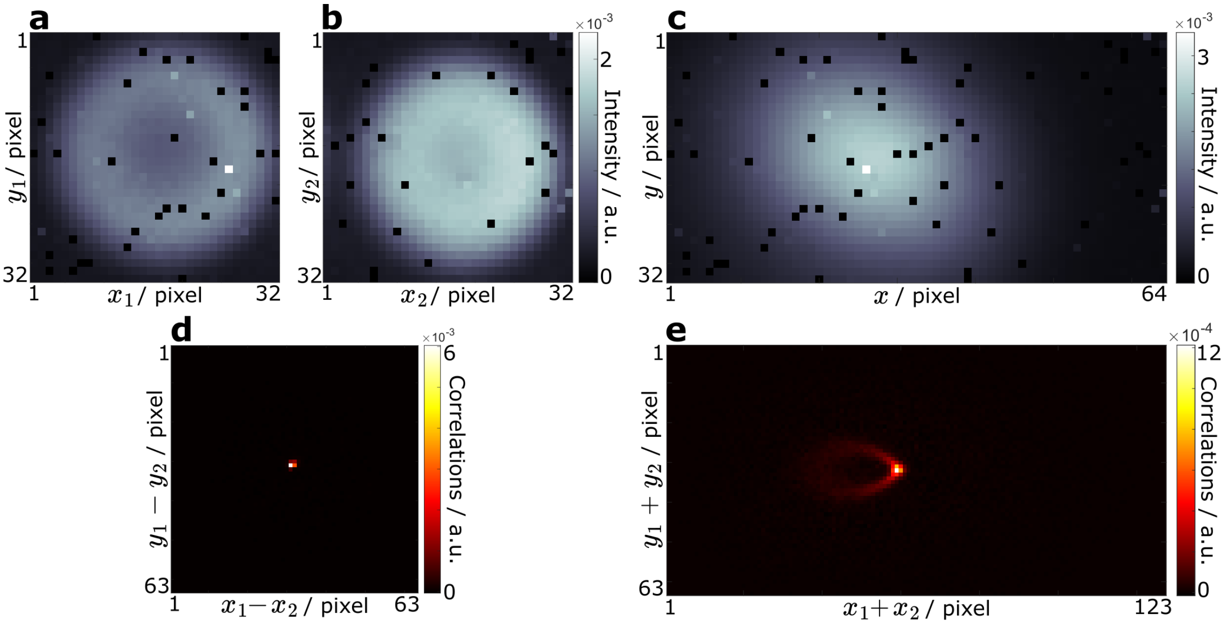

Figure 5.2: **Intensity and projections for Type II SPDC. a,b,** Direct intensity images of vertical (a) and horizontal (b) beams in the far-field imaging configuration. Beams were directed to left and right halves of the SPAD camera. **c,** Full direct intensity image taken in the near-field imaging configuration. Beams were superimposed in the near-field. **d,** Minus-coordinate projection of $G^{(2)}$ between horizontal and vertical beams. Note that even though this is a FF imaging configuration this is the *minus*-coordinate projection because the extra 4-f relay in the SLM path inverts one beam relative to the other, resulting in photons that are correlated in position. **e,** Sum-coordinate projection of $G^{(2)}$ measured in the NF configuration. As before, the extra 4-f causes the photons to be anti-correlated instead of correlated. All data captured using the MPD Hermes SPAD camera with an exposure time of 1 μs. FF data (a,b,d) from an acquisition of 6×10^6 frames taking approximately 5 minutes. NF data (c,e) from an acquisition of 5.9×10^7 frames taking approximately 45 minutes. Black pixels are abnormally hot pixels that have been artificially set to zero.

fields in the planes immediately before the SLM and plane A, respectively, then we can write $\phi(\mathbf{r_1}, \mathbf{r_2}) \approx \phi_0(\mathbf{r_1} + \mathbf{r_2})\delta(\mathbf{r_1} - \mathbf{r_2})$. If we assume that the aberrations are low-order then they can be expressed as a random phase mask $S(\mathbf{r})$ in the image plane of the crystal. The PSFs for each system are then

$$h_1(\mathbf{r}_1', \mathbf{r}_1) = \exp\left[iS(\mathbf{r}_1) - \frac{2\pi i}{f\lambda}\mathbf{r}_1\mathbf{r}_1'\right] \tag{5.2}$$

and

$$h_2(\mathbf{r}_2', \mathbf{r}_2) = \exp\left[i\theta(\mathbf{r}_2) + \frac{2\pi i}{f\lambda}\mathbf{r}_2\mathbf{r}_2'\right], \tag{5.3}$$

where $\theta(\mathbf{r})$ is the phase mask displayed on the SLM and the relative plus sign in the expression for h_2 represent the additional 4-f relay that spatially inverts the idler beam. Now, plugging these expressions for ϕ, h_1, and h_2 into Equation 5.1, the intensity correlations at the camera are

$$G^{(2)}(\mathbf{r}_1', \mathbf{r}_2') = \left| \int \phi_0(\mathbf{r}) \exp\left[i\left(\theta(\mathbf{r}) + S(\mathbf{r})\right)\right] \exp\left[-\frac{2\pi i}{f\lambda}\mathbf{r}(\mathbf{r}_1' - \mathbf{r}_2')\right] d\mathbf{r} \right|^2, \tag{5.4}$$

or, in the rotated basis $\mathbf{r}_+, \mathbf{r}_-$,

$$G^{(2)}(\mathbf{r}_+, \mathbf{r}_-) = \left| \left[\mathcal{F}[\phi_0(\mathbf{r})] * \mathcal{F}\left[\mathrm{e}^{i(\theta(\mathbf{r})+S(\mathbf{r}))}\right]\right] \left(\frac{\mathbf{r}_-}{f\lambda}\right) \right|^2. \tag{5.5}$$

From this expression of the $G^{(2)}$, it is clear that the minus-coordinate projection has the form

$$C_-(\mathbf{r}_-) \propto \left| \left[\mathcal{F}[\phi_0(\mathbf{r})] * \mathcal{F}\left[\mathrm{e}^{i(\theta(\mathbf{r})+S(\mathbf{r}))}\right]\right] \right|^2. \tag{5.6}$$

Equation 5.6 is remarkably similar to Equation 3.35 which was used in Ref. [2] to show how correlations can be recovered through a scattering material. If we have $\theta(\mathbf{r}) = -S(\mathbf{r})$ then the second Fourier term disappears and we are left with diffraction-limited correlations. However, unlike the case of Ref. [2], the aberrated photons never interact with the SLM and the photons that are controlled with the SLM never encounter the aberrations. This is what we call remote aberration correction, since the correction is done on photons that never see the aberrations.

5.2.2 Preliminary Results

In Ref. [2] the SLM mask $\theta(\mathbf{r})$ was computed after learning the transmission matrix of the scattering medium classically. However, learning the transmission matrix requires an SLM to be situated in the same path as the aberration as well as a classical coherent light source. We wanted to demonstrate a different approach where there was truly no shaping of the signal photon. For this, we applied QAO optimisation to find the best correction mask. A layer of PDMS was placed in Plane A and the $G^{(2)}$ measured in the FF imaging configuration. Figure 5.3a shows the minus-

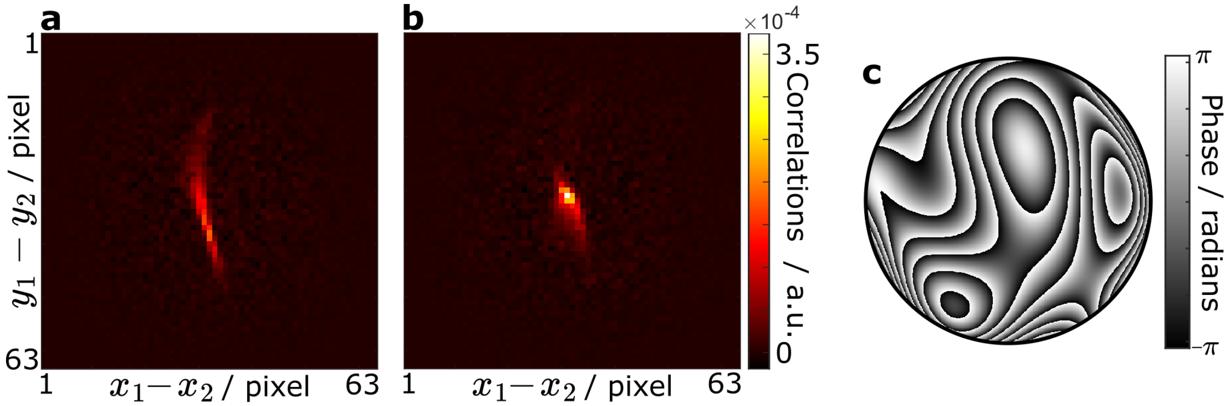

Figure 5.3: **Preliminary results of Remote Aberration Correction. a,** Minus-coordinate projection with PDMS layer in horizontal path and a flat phase mask on the SLM. **b,** Minus-coordinate projection after applying QAO to correct for the aberration. **c,** SLM phase mask found by optimising C_0^-. Data from acquisitions of 6.5×10^6 frames at 100 μs exposure time.

coordinate projection for a flat phase on the SLM. The QAO method was then used to optimise C_0^-. Figure 5.3b shows C^- after optimisation where there is a clear improvement compared to the initial image, suggesting that this is a promising direction in which to take this work.

5.3 Future Directions

5.3.1 Entanglement Recovery with Remote Aberration Correction

The current goal of the Type II experiment is to do entanglement verification through aberration, as demonstrated in Ref. [2], with two main differences: (i) The correction mask will be found by optimising the quantum correlations and will not require a classically-measured transmission matrix; (ii) the correction will be done remotely. However, optimising the correlations puts a limit on the complexity of aberrations that can be corrected. Even with the SPAD camera, it will be challenging to correct for high-order aberrations using the optimisation method introduced in Chapter 4. This is because, as the order of the aberrations increases, the number of modes that must be corrected also increases. On top of this, the measurable change in signal for each mode will also decrease as the number of aberration modes increases. For the future of this project, it will be necessary to improve both the optimisation method and the detection in order to work with complex aberrations.

5.3.2 Improving the QAO Optimisation process

Changing the Optimisation Target

One direction is to find a different optimisation target that more efficiently uses the information that is contained in projections. All of the demonstrations of QAO shown in this thesis were based on optimising the central value of the sum-coordinate projection, C_0^+. We know that this target will work, but in using it we effectively discard the information contained in all of the other pixels of the projection images. A much more efficient use of the information would be to define an optimisation target that is a function of all of the pixels in the projection. One possible candidate is the second central moment or (spatial) variance of the projection[1]. The second central moment of a distribution is just the variance of that distribution. In language of statistics, C^+ represents a probability density function. The random variable whose distribution this function describes is the location of one photon relative to its twin, denoted by the position vector $\mathbf{r}_+$. The second central moment μ_2 of this distribution can be computed via

$$\mu_2 = \int_{-\infty}^{\infty} (\mathbf{r}_+ - \mu)^2 C^+(\mathbf{r}_+) d\mathbf{r}_+, \tag{5.7}$$

where μ is the expected value of $\mathbf{r}_+$, i.e. the centroid of C^+. We can see from this definition that μ_2 is the average distance squared between each point $\mathbf{r}_+$ and mean position μ, weighted by the value of C^+ at that point. For a discrete, normalised projection C_{ij}^+ with $N_{x_+} \times N_{y_+}$ elements, μ_2 can be computed via

$$\mu_2 = \frac{1}{N_{x_+} N_{y_+}} \sum_{i}^{N_{x_+}} \sum_{j}^{N_{y_+}} \left((i - \mu_{x_+})^2 + (j - \mu_{y_+})^2 \right) C_{ij}^+, \tag{5.8}$$

where

$$\mu_{x_+} = \frac{1}{N_{x_+} N_{y_+}} \sum_{i}^{N_{x_+}} \sum_{j}^{N_{y_+}} i C_{ij}^+ \tag{5.9}$$

and

$$\mu_{y_+} = \frac{1}{N_{x_+} N_{y_+}} \sum_{i}^{N_{x_+}} \sum_{j}^{N_{y_+}} j C_{ij}^+ \tag{5.10}$$

are the expected values of x_+ and y_+. The second central moment uses the information contained in every pixel of the of the projection so could be a more efficient metric to use.

Improving the Iterative Algorithm

Another area where there is room for development is the optimisation algorithm itself. The sequential algorithm we use works well for correcting a relatively low number of modes, however for higher orders of correction it becomes slow. Here it would make sense to take inspiration from the field of classical AO, where there is a wide body of research on more sophisticated algorithms such as parallel gradient descent [197], genetic algorithms[198] and more [172]. In addition to these traditional optimisation approaches, the massive development in machine learning in recent years is providing an alternative method for finding optimal aberration correction [199].

---

[1] Thank you to Ilya Karuseichyk for this suggestion.

Region-specific QAO correction

Finally, something that has not yet been explored is the potential for region-specific correction with QAO. In the case of higher-order aberrations, the PSF of the system is no longer shift-invariant. Therefore, the correction mask that optimises one region of the field-of-view may not optimise another. Maximising the projection peak will give the best average improvement across the entire image, but may not give the best correction for a specific area. It would be interesting, therefore, to try to apply a region-specific QAO correction. Instead of computing C for the full $G^{(2)}$, we could take the projection of the subset of the $G^{(2)}$ corresponding to the desired region. Then, maximising this sub-projection should give the best correction for this region. There are some limitations to this. Firstly, since we are computing the projection from a smaller region, the signal-to-noise ratio will be reduced, necessitating longer acquisition times. Also, such region-specific correction is best suited to near-field imaging schemes where the pairs arrive correlated in position. In the far-field, since the pairs arrive diametrically opposite points, any sub-region would also need to be symmetric about the beam's centre, limiting the practicality in this configuration.

5.3.3 Towards fully-Quantum Wavefront Shaping

A natural direction to take these concepts in the long term is towards fully-quantum wavefront shaping i.e. correcting for a scattering medium without using any classical light. There are two main approaches for wavefront shaping. There is the optimisation approach first demonstrated by Vellekoop and Mosk [86] and the transmission matrix approach initially developed by Popoff [85]. In fact, QAO is effectively a fully-quantum wavefront shaping technique that is based on an optimisation approach. Due to practical limitations we have only demonstrated QAO in the low-order regime, but there is no fundamental restriction that would prevent the use of QAO to correct for scattering given bright enough sources and fast enough detectors. I discuss this idea here.

I described in Subsection 3.5.1 (Ref. [2]) how transmission-matrix-based wavefront shaping can be applied to photon pairs to allow entanglement to be transmitted through a scattering layer. However, this approach relies on prior characterisation of the scatterer using a separate classical source. Again, this is due to practical limitations of the sources and detectors, but theoretically the transmission matrix of a scattering medium could be measured with photon pairs. It would therefore be interesting to develop quantum wavefront shaping techniques further so that the classical characterisation is not necessary.

The classical characterisation process involves measuring speckle patterns caused by the scattering layer. A typical characterisation may involve measuring the electric field for each mode of an input basis. Typically the Hadamard basis is used. An SLM transforms the input state - a collimated Gaussian beam in the case of Ref. [2] - into the desired input mode. For each input mode the resulting output speckle is measured one by one. Using a 4-phase holographic reconstruction, the complex speckle for each input mode is measured. Each of these complex speckles is then a column of the transmission matrix (TM).

Interestingly, the photon pairs we generate with SPDC are already spatially multi-mode. This could be exploited to do a parallel measurement of the TM. For example, using a Type II source, the signal photon could be transmitted through the scatter layer and the idler used as a reference. With no scattering medium, the photons will be strongly correlated (or anti-correlated) upon detection. The conditional distributions of the signal photon for a given idler location will be a sharp peak about the corresponding location. With the scattering layer present, these conditionals will be speckle patterns instead. The idler locations give the input modes and the conditional signal distributions, which make up the columns of the measured $G^{(2)}$, give the output speckles. If the full field is measured via a holographic measurement then the resulting complex $G^{(2)}$ will actually be equivalent to the classically measured transmission matrix.

Currently, however, the practically achievable SNR of the $G^{(2)}$ measurement is simply too low. For example, consider the data shown in Figure 5.2d which is from a 5 minute long acquisition. The average SNR for each conditional of $G^{(2)}$ is 19.15. It is clear from the figure that the photons are strongly correlated in position here which means that the majority of the signal in each conditional is concentrated in a few pixels. If each conditional were a speckle pattern instead, the signal would be distributed across the whole image. If the speckle covered the full sensor then - on average - the signal at a given pixel will be reduced by a factor of $1/1024$. For a 5-minute acquisition time we can estimate that the SNR will be on the order of $19.15/1024 \sim 2\times10^{-2}$ i.e. the signal would be too weak to be detected. Of course, one could acquire more frames, but to even achieve an SNR of 2 would require a 10000-fold increase in acquisition time. Clearly, we must wait for brighter sources and faster, more efficient cameras for this to be viable.

5.4 Discussion

There are a number of potential directions that this work could take. The preliminary results shown in Figure 5.3 suggest that remote aberration correction is viable and could be to demonstrate remote recovery of entanglement through aberrations. This could be a relatively low risk, short term objective for the experiment as we know that, for low order aberrations, the QAO optimisation works well. Following this, an obvious long-term aim for the project is to extend the remote correction to the case with high-order aberrations, i.e. scattering. This could be done in a number of ways. One option is to first characterise the scatterer with a classical beam, as in Ref. [2]. However, as discussed above, the SLM and scattering medium are not in the same beam paths so this would likely require some experimental modification.

To solve this issue, it may be possible to do wavefront shaping by optimising the classical alignment SLED that is co-aligned with the pump. By using a polariser and half-wave plate to set the SLED polarisation to 45^o, the beam can be split equally between the SLM and aberration arms in the experiment. For a flat SLM we should expect to see a focused spot corresponding to the SLM arm on one region of the camera, and a speckle corresponding to the aberration arm on another region of the camera. Now, if we find the SLM mask that causes the focused spot to become a speckle that matches the aberration-arm speckle, we know that this phase mask matches the phase of the aberration. The negative of phase mask should therefore be the phase that optimises the photon pair correlations. However, while this may be interesting to investigate, remote aberration correction will have a broader range of applications if it does not rely on an auxiliary classical beam. To do this, the QAO optimisation process must be further developed to enable correction of scattering media.

We have seen that there are a number of avenues for improving QAO. A possible low hanging fruit is to find an optimisation target the uses the information from the projections more efficiently. Finding a more sophisticated optimisation algorithm will likely also be essential for applying QAO to correcting for scattering media. It is also worth noting that these improvements would not be specific to remote aberration correction and would improve QAO as a whole.

Remote wavefront shaping, i.e. remote correction of scattering media, is well-suited for applications in quantum communications through turbulent channels. However, the concept of remote correction of light has other interesting implications, for example in the field of microscopy. Consider a high-resolution, high numerical aperture microscope. These are relatively compact, sensitive devices that may not be easily modified to include an SLM to do AO. Instead of rebuilding the microscope to accommodate the SLM, remote shaping could allow for the SLM to be separate from the microscope. If a Type II SPDC source is used for illumination, then the signal could be sent through the microscope as normal, and the idler could be separated and sent to a bench-top setup where the SLM and any accompanying optics could be easily aligned and modified.

Chapter 6

Conclusion

The field of quantum imaging aims to improve and develop imaging technologies by exploiting the quantum-mechanical properties of light, offering advantages such as enhanced resolution and noise performance. The advent of single-photon sensitive cameras, as well as brighter sources of quantum light, has enabled many new developments in recent years, and we are now seeing quantum imaging techniques move closer and closer to real-word applications. While improved detectors and sources are certainly a key step towards this, it is also interesting to take inspiration from classical imaging techniques to see how quantum imaging methods can be improved.

In that respect, the initial aim for my PhD was to investigate and develop techniques for quantum imaging in scattering media. How can the techniques of classical wavefront shaping be applied to imaging with entangled photon pairs and, perhaps the more interesting question, how can the properties of such photons be exploited to improve wavefront shaping techniques? This goal has changed and shifted throughout my PhD, but it is still fair to say that the underlying motivation has remained more or less the same. How can classical light shaping concepts be applied to quantum imaging, and how can quantum imaging concepts be used to enhance classical imaging techniques?

To that end, I have presented in this thesis my work on the development of photon pair correlation shaping. Firstly, I have outlined the experimental techniques that we use to generate and image entangled photon pairs. In the work presented here we use the method of Defienne et. al. [121] along with EMCCD or SPAD cameras to measure the spatial correlations of photon pairs. With these methods I have demonstrated how a spatial light modulator can be used to shape and control photon pairs' spatial properties, and I have outlined a general theoretical framework to describe this. These results show that the way in which we can control the photon pair correlations is very similar to how we control classical, coherent light. For a simple case with an SLM in the Fourier plane of the camera, there are two standard configurations that each give slightly different results:

- **Near-field imaging**: The surface of the nonlinear crystal is imaged onto the camera. The SLM is in the far-field plane where the photons are anti-correlated in position. The photon pairs 'see' a phase mask that is equal to the mask on the SLM, $\theta(\mathbf{r})$, plus a spatially inverted version of the mask. The spatial correlations are modulated according to $\mathcal{F}[\mathrm{e}^{i\psi(\mathbf{r})}]$, with $\psi(\mathbf{r}) = \theta(\mathbf{r}) + \theta(-\mathbf{r})$.

- **Far-field imaging**: The Fourier plane of the nonlinear crystal is imaged onto the camera. The SLM is in the near-field plane where the photons are correlated in position. The photon pairs 'see' a phase mask that is equal to twice the phase mask on the SLM. The spatial correlations are modulated according to $\mathcal{F}[\mathrm{e}^{i2\theta(\mathbf{r})}]$.

It is important to emphasise that it is the *correlations* that are shaped, not the intensity. In fact, photon pairs generated by SPDC behave as if they are incoherent when measuring only their intensity and their higher order coherence is only revealed when measuring their correlations. This correlation shaping has potential applications in quantum communications [2] (Subsection 3.5.1), fundamental physics research (Subsection 3.5.3), and quantum and classical microscopy [3] (Chapter 4).

In the main project of my PhD we developed a novel method to measure and correct for aberrations in an imaging system called Quantum-assisted Adaptive Optics, as reported in Ref. [3]. Here, we exploit the fact that the point-spread function of an imaging system becomes encoded in spatial correlations of photon pairs that propagate through said system. This can be quantified by taking the appropriate projection C^+ or C^- of the measured two-photon joint probability distribution, called the $G^{(2)}$. By finding the corrective phase mask that optimises this projection, we show that this corrects for the aberrations and restores imaging performance.

One of the key benefits of this method is that the optimisation is (almost) entirely independent of the structure of the sample, unlike image-based AO methods. It is also not restricted to quantum imaging techniques; once the correction has been found, the images are direct, brightfield intensity images. Finally, many quantum imaging and communications experiments rely on strong spatial correlations for a suitable SNR and are very sensitive to aberrations. We show that QAO could be used to improve acquisition times up to a factor of 25, thereby enabling previously unfeasible experiments.

Finally, the work presented here could be taken in multiple directions. The following are some examples of potential routes this work could take:

1. **More efficient QAO optimisation.** Make more efficient use of the information contained $G^{(2)}$ projection, for example by optimising the second order central moment of the spatial correlation distribution. **Short-term**.

2. **Remote Aberration Correction.** Correct for aberrations in the path of one photon in a

pair by acting on the other. **Short/medium-term**.

3. **Improve QAO optimisation algorithm.** Develop a more sophisticated algorithm to find the best correction mask. **Medium-term**.
4. **Region-specific QAO.** In the case of shift-variant PSF, use QAO to find best correction in a specific region of field of view. **Medium-term**.
5. **Extend QAO to scattering media.** This would likely rely on improving the optimisation algorithm first. **Medium/long-term**.
6. **Fully-quantum transmission matrix measurement.** Measure the transmission matrix using only quantum light, i.e. photon pairs. **Long-term**.

To conclude, during my PhD I have developed methods to apply light shaping techniques to quantum imaging. I have demonstrated how the correlations of entangled photons can be controlled using spatial light modulators. Then, using these principles, I have demonstrated a novel scheme to correct for optical aberrations that may have potential benefits in classical microscopy. Quantum imaging is still in its adolescence, and there are many avenues for development and improvement that are yet to be explored.

Appendix A

Details on SLM Calibration

Here I will give a step by step method to calibrate the pixel response of an SLM. Example Matlab code for this process is given in Ref. [200]. This method requires a camera, a static scattering medium that produces a speckle, and a spatially coherent light source (here we use the SLED). It is assumed that the SLM is functioning and can display arbitrary grayscale images. It is simplest to control the camera and SLM using the same software, e.g. with the same Matlab or Python script. The SLM does not need to be perfectly aligned to perform this calibration step. The calibration is in two steps: the speckle correlation measurement, and the data processing. The measurement goes as follows:

1. Align the SLM and camera so that the SLED/laser is incident on the SLM and is visible on the camera. It is convenient to have Fourier-imaging lens between the SLM and camera, but the alignment of this lens does not need to be extremely precise at this stage.

2. Ensure that the SLM is blank, i.e. displaying a flat phase mask, and place the scattering medium after the SLM. It should be placed so that a wide speckle is shown on the camera. Save an image of this speckle; it will be used as the reference image, denoted $I_0(\mathbf{r})$. An example speckle is shown in Figure A.1a.

3. Randomly select approximately half of the pixels in the illuminated region of the SLM. It is best to group the pixels into larger macropixels. This region of the SLM is called the active region. The region containing the pixels that remain at zero is the passive region.

4. Now, for each grayscale value (i.e. integer G from 0 to 255), set the selected pixels to this value, display this mask on the SLM, and save an image of the speckle at each step. This image is denoted $I_G(\mathbf{r})$, where G is the grayscale value. An example image of the speckle for non-zero grayscale values is shown in Figure A.1b.

5. Calculate the correlation coefficient, M, between each image ($I_G(\mathbf{r})$) and the reference

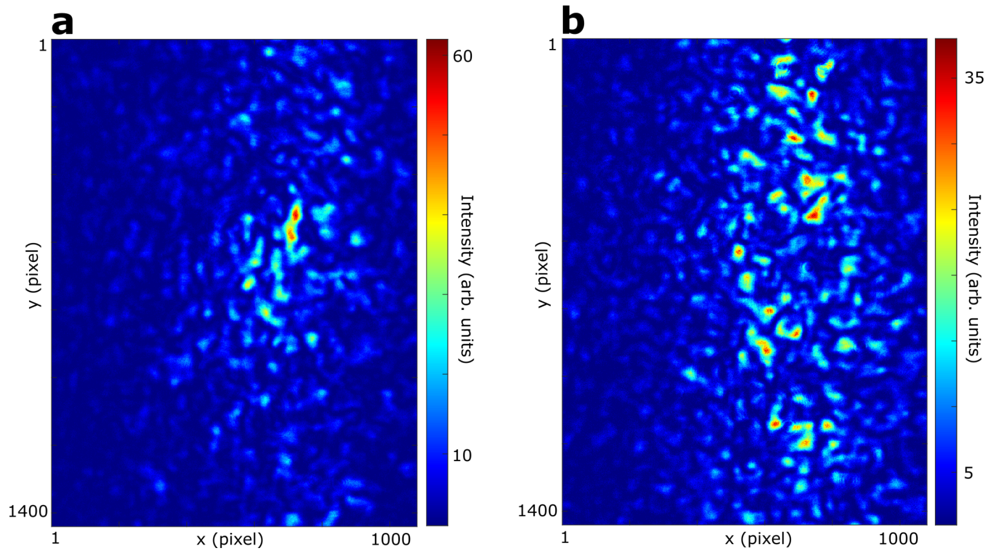

Figure A.1: **Speckle patterns. a,** Reference speckle pattern measured with a flat phase programmed on the SLM. **b,** Speckle pattern measured with random subset of SLM pixels set to the gray value $G = 117$. Images were acquired with with Thorlabs Zelux 1.6 MP Monochrome CMOS camera. The SLM is an Holoeye Pluto NIR-II.

image ($I_0(\mathbf{r})$). Here, this is done in Matlab using the function `corr2`.

6. Plot the correlation coefficient M as a function of grayscale pixel value, as shown in Figure A.2a.

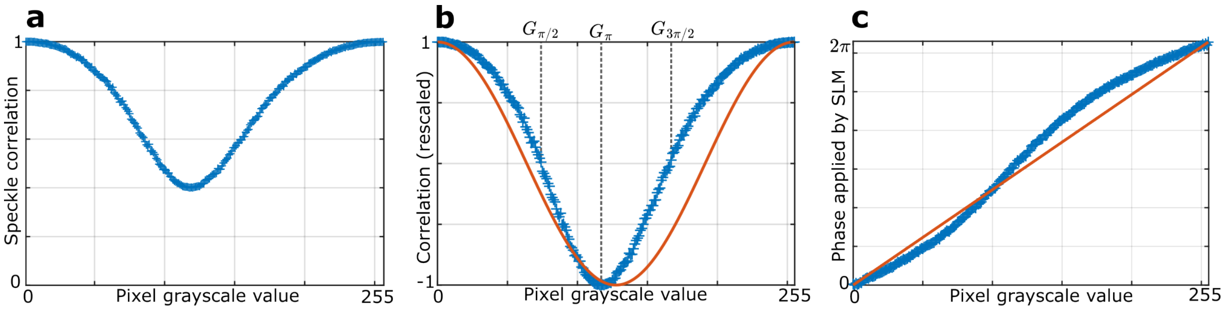

Figure A.2: **Pixel response of SLM measured via speckle correlation. a,** Speckle correlation computed between a reference speckle and speckles from each pixel grayscale value. **b,** Rescaled speckle correlation vs pixel grayscale value. Grayscale values corresponding to $\pi/2, \pi, 3\pi/2$ phase shifts are indicated. Solid red line is the cosine that the data would follow if the pixel response was linear. **c,** Actual phase shift applied by the SLM, computed from the inverse cosine of the rescaled speckle correlation data. Solid red line is a straight line to illustrate the nonlinearity of the pixel response.

As shown in Figure A.2a, the correlation as a function of the grayscale level G closely resembles that of a cosine. A cosine is what we would expect to observe if the SLM was already perfectly calibrated. More precisely, it should be:

$$M = A + B\cos\left(\frac{2\pi}{255}G\right), \tag{A.1}$$

where A^{final} and B are two constants. Indeed, the intensity at a position $\mathbf{r}$ on the camera results from the interference between a speckle s_P generated by the passive part of the SLM and a speckle s_A generated by the active part. When we phase-shift the active part with respect to the passive part by a global phase θ, then the intensity measured on the camera can be written as follows: $I_\theta(\mathbf{r}) = |s_P|^2 + |s_A|^2 + 2|s_P s_A|\cos\left(\alpha_A(\mathbf{r}) - \alpha_P(\mathbf{r}) + \theta\right)$, where $\alpha_P(\mathbf{r})$ and $\alpha_A(\mathbf{r})$ are the phase components of $s_A(\mathbf{r})$ and $S_P(\mathbf{r})$, respectively. Calculating the correlation M between I_θ and I_0 using Matlab's `corr2` function involves spatially averaging the products $I_\theta(\mathbf{r})$ and $I_0(\mathbf{r}')$ for all pairs of positions $\mathbf{r}$ and $\mathbf{r}'$. Assuming that each speckle is well developed, then phases α_P and α_A are randomly distributed between 0 and 2π across all the camera pixels, leading to the following results:

$$\begin{aligned}
M(\theta) &= \langle I_\theta(\mathbf{r}) I_\theta(\mathbf{r}')\rangle_{\mathbf{r},\mathbf{r}'} \\
&= \langle [|s_A(\mathbf{r})|^2 + |s_P(\mathbf{r})|^2] + [|s_A(\mathbf{r}')|^2 + |s_P(\mathbf{r}')|^2]\rangle_{\mathbf{r},\mathbf{r}'} \\
&\quad + 2\langle [|s_A(\mathbf{r})|^2 + |s_P(\mathbf{r})|^2]|s_A(\mathbf{r}')||s_P(\mathbf{r}')\cos\left(\alpha_A(\mathbf{r}') - \alpha_P(\mathbf{r}')\right. + \theta)\rangle_{\mathbf{r},\mathbf{r}'} \\
&\quad + 2\langle [|s_A(\mathbf{r}')|^2 + |s_P(\mathbf{r}')|^2]|s_A(\mathbf{r})||s_P(\mathbf{r})\cos\left(\alpha_A(\mathbf{r}) - \alpha_P(\mathbf{r})\right)\rangle_{\mathbf{r},\mathbf{r}'} \\
&\quad + 2\langle |s_A(\mathbf{r}) s_P(\mathbf{r}) s_A(\mathbf{r}') s_P(\mathbf{r}')|\cos\left(\alpha_A(\mathbf{r}) - \alpha_P(\mathbf{r} - \alpha_A(\mathbf{r}') + \alpha_P(\mathbf{r}')\right)\rangle_{\mathbf{r},\mathbf{r}'} \\
&\quad + 2\langle |s_A(\mathbf{r}) s_P(\mathbf{r}) s_A(\mathbf{r}') s_P(\mathbf{r}')|\cos(\theta)\rangle_{\mathbf{r},\mathbf{r}'} \\
&= A + B\cos(\theta).
\end{aligned} \tag{A.2}$$

If the SLM is perfectly calibrated, then $\theta = \frac{255}{2\pi}G$, leading to equation A.1. However, in practice this is never the case, and the relationship between θ and G i.e. $\theta = f(G)$, is not so simple. It is precisely this function f that we are aiming to experimentally measure and determine here.

To achieve this, we then start form the correlation curve measured in Figure A.2a. Firstly, it is necessary to ensure that the SLM implements sufficient phase shifting, i.e. if the cosine is cut off before reaching a maximum, then the pixels are not modulating all the way to 2π. Generally, an SLM will come with software to control the voltage that is applied across the pixels. If possible, use this to adjust the maximum applied voltage so you get one full oscillation, erring towards more than a full oscillation. Once a calibration curve with more than one oscillation is obtained, the curve is unlikely to be a perfect cosine because f is generally not linear. f is determined using the following procedure:

1. Rescale the data so that M ranges between -1 and 1. Figure A.2b shows such a re-scaled curve (blue).

2. Record the gray values G of the first maximum, labelled G_0; the minimum, labelled G_π; and the second maximum, labelled $G_{2\pi}$. Record the G values where $M = 0$ (or closest). Label the lower $G_{\pi/2}$ and higher $G_{3\pi/2}$. See Figure A.2b.

3. Split the data in half at G_π, so we have $M_{left} = M(G_{left})$ for $G_{left} \in [G_0, G_\pi]$ and $M_{right} = M(G_{right})$ for $G_{right} \in [G_\pi + 1, G_{2\pi}]$.

4. Compute $Y_{left} = \arccos(M_{left})$ and $Y_{right} = -\arccos(M_{right}) + 2\pi$, and plot Y vs G, as shown in Figure A.2c. This is the pixel response of the SLM i.e. the function f.

5. Fit Y_{left} and Y_{right} as functions of G_{left} and G_{right}, respectively. It is usually sufficient to use quadratic polynomials for the models. In the example code, to improve the fit consistency, we shift the right data so that the first point is at the origin. That is, we fit $Y'_{right} = Y_{right} - \pi$ as a function of $G'_{right} = G_{right} - G_\pi$. The results can be re-shifted after the fit. Figures A.3ab show examples of fitted models.

6. Now you have two models describing the pixel response from 0 to G_π and G_π to $G_{2\pi}$. If they are quadratics, they are of the form

$$Y_{model} = a_1 G^2 + a_2 G + a_3. \tag{A.3}$$

   For the right-side model, if the fit was done with shifted data, then the coefficients can be redefined:

$$a_1 = a_1, \quad a_2 = -2G_\pi a_1 + a_2, \quad a_3 = -a_2 G_\pi + a_1 G_\pi^2 + Y_0 \tag{A.4}$$

   with $Y_0 = max(Y_{left})$ ensuring the fits can be merged at G_π. We use these models to create the function f (e.g. in the form of a Matlab function) that transforms a grayscale level G into its corresponding phase value.

7. Similarly, we need to create a function corresponding to f^{-1}. For this, the models must be inverted. If they are quadratics, then

$$G_{model} = \frac{-a_2 + \sqrt{a_2^2 - 4a_1(a_3 - Y)}}{2a_1}. \tag{A.5}$$

   Now you can define a function that computes $G_{model-left}$ for $Y \in [0, \pi]$, using the coefficients for the left side fit, and $G_{model-right}$ for $Y \in [\pi, 2\pi]$ for the right-side fit. See Figure A.3c for the final combined model.

8. At the end of the calibration, we have two functions corresponding to f and f^{-1} which represent the grayscale values programmed onto the SLM and the actual phase shift that the SLM implements. To check the calibration, repeat the speckle measurements above

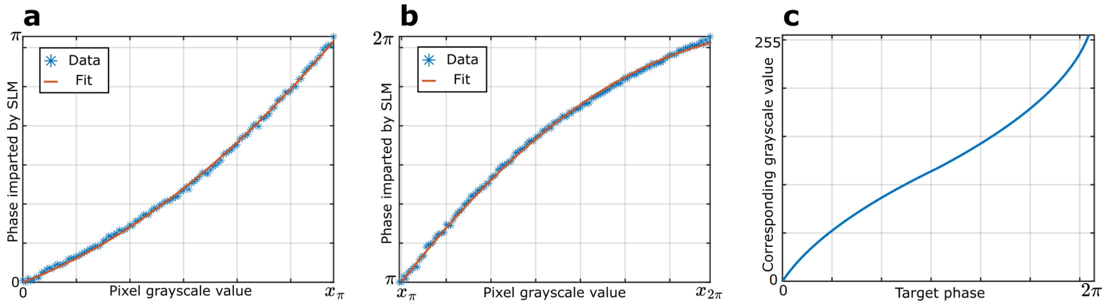

Figure A.3: **Quadratic fits of the measured SLM pixel response. a,b,** Data points and fitted functions for the left and right data, respectively. **c,** Combined inverse function that maps the target phase to the grayscale pixel value that gives this phase.

with grayscale values $G_{pix} = G_{model}(Y)$, with Y being a linear vector of phases from 0 to 2π. If the calibration was successful, this should result in a perfect cosine shape.

Appendix B

Details on Simulations

Throughout my PhD I have also performed simulations of the experiments described in the main body of this thesis. I give details on these simulations here.

All simulations are performed in 1 spatial dimension i.e. $\mathbf{r} \to x$. These simulations are performed with Matlab. We first choose the number of spatial elements, i.e. the spatial discretisation, N. The main components are described in the following:

- **Spatial coordinates:** This is an N-element column vector that determines the size of the space being simulated, i.e. it ranges from x_{min} to x_{max}. Typically it is generated using `linspace`(x_{min}, x_{max}, N).
- **Classical electric field:** An electric field is written analytically as $E(x)$. This takes the form of an N-element column vector whose i^{th} element is denoted E_i. For example, for a Gaussian beam with amplitude A, width σ, E is defined as

$$E_i = A\exp(-x_i^2/2\sigma^2). \tag{B.1}$$

- **Two-photon state:** The two-photon wavefunction written analytically as $\phi(x_1, x_2)$. In simulations it is represented as an $N \times N$ array Φ. For a state with perfect spatial correlations we have $\Phi_{ij} = \delta_{ij}$.
- **Object:** In Matlab, an object t takes the form of a vector with N elements. Each element takes a value between 0 and 1 representing the transmittance of the object at that location. Its also convenient to encode this object in a diagonal matrix $O_{ii} = t_i$.
- **Phase mask:** An SLM or layer of aberration imparts a phase to the incident field. This is represented as a complex diagonal array (i.e. one whose non-diagonal elements are 0), which I will denote D. For a phase profile $\theta_i = \theta(x_i)$, the i^{th} diagonal element (i.e. element

D_{ii}) is

$$D_{ii} = \exp(i\theta_i), \tag{B.2}$$

where the non-subscript i is the imaginary number $i = \sqrt{-1}$, and all other elements $D_{i,j\neq i} = 0$.

- **Fourier lens:** Recall that the field at the back focal plane of a lens is related to the field at the front focal plane by $E_{out}(2x'/f\lambda) = \mathcal{F}[E_{in}(x)]$ where f is the focal length of the lens. This 2-f system is represented by an $N \times N$ complex array F, where the ij^{th} element is given by

$$F_{ij} = \frac{1}{N}\exp\left[-\frac{2i\pi}{f\lambda}x_i x_j\right] \tag{B.3}$$

- **Coherent Propagation:** For an electric field, propagation is done performing a matrix multiplication. For example, the field at the output plane of a system comprised of object t, followed by a 2-f lens system, a layer of aberration D then another 2-f lens is computed via

$$E^{out} = FDFOE^{in}. \tag{B.4}$$

The two-photon wavefunction at the output plane of the same system is computed via:

$$\Phi^{out} = FDFO\Phi^{in}(FDFO)^T, \tag{B.5}$$

where A^T denotes the matrix transpose of A.

- **Point spread function:** In Matlab, the point spread function $h(x' - x)$ takes the form of an $N \times N$ element array, denoted T. This array can be found by taking the matrix multiplication of all of the arrays composing the system, in order. For the example system above we would have $T = FDFO$. Propagation can be written more succinctly as e.g. $\Phi^{out} = T\Phi^{in}T^T$

- **Incoherent propagation:** The intensity at the output plane of a system described by T for an incoherent input I^{in} is found by

$$I^{out} = |T|^2 I^{in}. \tag{B.6}$$

Bibliography

1. Defienne, H., Cameron, P., Ndagano, B., *et al.* Pixel super-resolution with spatially entangled photons. *Nature Communications* **13,** 3566. doi:`10.1038/s41467-022-31052-6` (June 2022) (cit. on pp. iii, 12, 20, 47, 50, 55, 80).
2. Courme, B., Cameron, P., Faccio, D., Gigan, S. & Defienne, H. Manipulation and Certification of High-Dimensional Entanglement through a Scattering Medium. *PRX Quantum* **4,** 010308. doi:`10.1103/PRXQuantum.4.010308` (Jan. 2023) (cit. on pp. iii, 18, 72–75, 105, 111, 112, 114, 115, 118).
3. Cameron, P., Courme, B., Vernière, C., *et al.* Adaptive optical imaging with entangled photons. *Science* **383,** 1142–1148. doi:`10.1126/science.adk7825` (Mar. 2024) (cit. on pp. iii, 74, 79, 81, 118).
4. Cameron, P., Courme, B., Faccio, D. & Defienne, H. Shaping the spatial correlations of entangled photon pairs. *Journal of Physics: Photonics* **6,** 033001. doi:`10.1088/2515-7647/ad50b1` (July 2024) (cit. on pp. iii, 57).
5. Einstein, A. Über einen die Erzeugung und Verwandlung des Lichtes betreffenden heuristischen Gesichtspunkt. *Annalen der Physik* **322,** 132–148. doi:`10.1002/andp.19053220607` (Jan. 1905) (cit. on p. 2).
6. Broglie, L. D. *Recherches sur la théorie des Quanta* PhD Thesis (Migration - université en cours d'affectation, Nov. 1924) (cit. on p. 2).
7. Griffiths, D. J. & Schroeter, D. F. *Introduction to Quantum Mechanics* Third (Cambridge University Press, 2018) (cit. on p. 3).
8. Cohen-Tannoudji, C., Diu, B. & Laloë, F. *Quantum Mechanics* 2nd ed. (John Wiley & Sons, 2019) (cit. on p. 3).
9. Einstein, A., Podolsky, B. & Rosen, N. Can Quantum-Mechanical Description of Physical Reality Be Considered Complete? *Physical Review* **47,** 777–780. doi:`10.1103/PhysRev.47.777` (May 1935) (cit. on p. 4).
10. *2022 Physics Nobel Prize, Alain Aspect Photo gallery* Nobel Prize website. Copyright: Collections, Ecole Polytechnique. (cit. on p. 4).

11. Bell, J. S. On the Einstein Podolsky Rosen paradox. *Physics Physique Fizika* **1.** Publisher: American Physical Society, 195–200. doi:`10.1103/PhysicsPhysiqueFizika.1.195` (Nov. 1964) (cit. on p. 4).
12. Aspect, A., Grangier, P. & Roger, G. Experimental realization of Einstein-Podolsky-Rosen-Bohm Gedankenexperiment: a new violation of Bell's inequalities. *Physical Review Letters* **49,** 91–94. doi:`10.1103/PhysRevLett.49.91` (July 1982) (cit. on p. 5).
13. Kocher, C. A. & Commins, E. D. Polarization Correlation of Photons Emitted in an Atomic Cascade. *Physical Review Letters* **18,** 575–577. doi:`10.1103/PhysRevLett.18.575` (Apr. 1967) (cit. on p. 5).
14. Burnham, D. C. & Weinberg, D. L. Observation of Simultaneity in Parametric Production of Optical Photon Pairs. *Physical Review Letters* **25,** 84–87. doi:`10.1103/PhysRevLett.25.84` (July 1970) (cit. on p. 5).
15. Slusher, R. E., Hollberg, L. W., Yurke, B., Mertz, J. C. & Valley, J. F. Observation of Squeezed States Generated by Four-Wave Mixing in an Optical Cavity. *Physical Review Letters* **55.** Publisher: American Physical Society, 2409–2412. doi:`10.1103/PhysRevLett.55.2409` (Nov. 1985) (cit. on pp. 5, 10).
16. Andersen, U. L., Gehring, T., Marquardt, C. & Leuchs, G. 30 years of squeezed light generation. *Physica Scripta* **91.** Publisher: IOP Publishing, 053001. doi:`10.1088/0031-8949/91/5/053001` (Apr. 2016) (cit. on p. 6).
17. Xiao, M., Wu, L.-A. & Kimble, H. J. Precision measurement beyond the shot-noise limit. *Physical Review Letters* **59,** 278–281. doi:`10.1103/PhysRevLett.59.278` (July 1987) (cit. on pp. 6, 7).
18. Breitenbach, G., Schiller, S. & Mlynek, J. Measurement of the quantum states of squeezed light. *Nature* **387.** Number: 6632 Publisher: Nature Publishing Group, 471–475. doi:`10.1038/387471a0` (May 1997) (cit. on p. 6).
19. Kolobov, M. I. & Sokolov, I. V. Multimode Squeezing, Antibunching in Space and Noise-Free Optical Images. *Europhysics Letters (EPL)* **15,** 271–276. doi:`10.1209/0295-5075/15/3/007` (June 1991) (cit. on p. 7).
20. Schwartz, O., Levitt, J. M., Tenne, R., *et al.* Superresolution Microscopy with Quantum Emitters. *Nano Letters* **13,** 5832–5836. doi:`10.1021/nl402552m` (Dec. 2013) (cit. on pp. 7, 11).
21. Gatto Monticone, D., Katamadze, K., Traina, P., *et al.* Beating the Abbe Diffraction Limit in Confocal Microscopy via Nonclassical Photon Statistics. *Physical Review Letters* **113,** 143602. doi:`10.1103/PhysRevLett.113.143602` (Sept. 2014) (cit. on p. 7).
22. Opatrny, T. Number-phase uncertainty relations. *Journal of Physics A: Mathematical and General* **28,** 6961. doi:`10.1088/0305-4470/28/23/034` (Dec. 1995) (cit. on p. 7).

23. Pittman, T. B., Shih, Y. H., Strekalov, D. V. & Sergienko, A. V. Optical imaging by means of two-photon quantum entanglement. *Physical Review A* **52,** R3429–R3432. doi:`10.1103/PhysRevA.52.R3429` (Nov. 1995) (cit. on p. 7).
24. Bennink, R. S., Bentley, S. J. & Boyd, R. W. "Two-Photon" Coincidence Imaging with a Classical Source. *Physical Review Letters* **89,** 113601. doi:`10.1103/PhysRevLett.89.113601` (Aug. 2002) (cit. on p. 8).
25. Ferri, F., Magatti, D., Gatti, A., *et al.* High-Resolution Ghost Image and Ghost Diffraction Experiments with Thermal Light. *Physical Review Letters* **94,** 183602. doi:`10.1103/PhysRevLett.94.183602` (May 2005) (cit. on p. 8).
26. Valencia, A., Scarcelli, G., D'Angelo, M. & Shih, Y. Two-Photon Imaging with Thermal Light. *Physical Review Letters* **94,** 063601. doi:`10.1103/PhysRevLett.94.063601` (Feb. 2005) (cit. on p. 8).
27. Boto, A. N., Kok, P., Abrams, D. S., *et al.* Quantum Interferometric Optical Lithography: Exploiting Entanglement to Beat The Diffraction Limit. *Physical Review Letters* **85,** 2733–2736. doi:`10.1103/PhysRevLett.85.2733` (Sept. 2000) (cit. on pp. 8, 11, 57, 80).
28. D'Angelo, M., Chekhova, M. V. & Shih, Y. Two-Photon Diffraction and Quantum Lithography. *Physical Review Letters* **87.** Publisher: American Physical Society, 013602. doi:`10.1103/PhysRevLett.87.013602` (June 2001) (cit. on p. 8).
29. Unternährer, M., Bessire, B., Gasparini, L., Perenzoni, M. & Stefanov, A. Super-resolution quantum imaging at the Heisenberg limit. *Optica* **5,** 1150. doi:`10.1364/OPTICA.5.001150` (Sept. 2018) (cit. on p. 8).
30. Brambilla, E., Caspani, L., Jedrkiewicz, O., Lugiato, L. A. & Gatti, A. High-sensitivity imaging with multi-mode twin beams. *Physical Review A* **77,** 053807. doi:`10.1103/PhysRevA.77.053807` (May 2008) (cit. on p. 8).
31. Brida, G., Genovese, M. & Ruo Berchera, I. Experimental realization of sub-shot-noise quantum imaging. *Nature Photonics* **4,** 227–230. doi:`10.1038/nphoton.2010.29` (Apr. 2010) (cit. on pp. 8, 11, 80).
32. Lemos, G. B., Borish, V., Cole, G. D., *et al.* Quantum imaging with undetected photons. *Nature* **512,** 409–412. doi:`10.1038/nature13586` (Aug. 2014) (cit. on pp. 8, 9).
33. Wang, L. J., Zou, X. Y. & Mandel, L. Induced coherence without induced emission. *Physical Review A* **44,** 4614–4622. doi:`10.1103/PhysRevA.44.4614` (Oct. 1991) (cit. on p. 8).
34. Casacio, C. A., Madsen, L. S., Terrasson, A., *et al.* Quantum-enhanced nonlinear microscopy. *Nature* **594,** 201–206. doi:`10.1038/s41586-021-03528-w` (June 2021) (cit. on pp. 10, 11).
35. Tenne, R., Rossman, U., Rephael, B., *et al.* Super-resolution enhancement by quantum image scanning microscopy. *Nature Photonics* **13.** Number: 2 Publisher: Nature Publishing

Group, 116–122. doi:`10.1038/s41566-018-0324-z` (Feb. 2019) (cit. on pp. 10, 11).

36. Wu, L.-A., Kimble, H. J., Hall, J. L. & Wu, H. Generation of Squeezed States by Parametric Down Conversion. *Physical Review Letters* **57.** Publisher: American Physical Society, 2520–2523. doi:`10.1103/PhysRevLett.57.2520` (Nov. 1986) (cit. on p. 10).
37. McKenzie, K., Grosse, N., Bowen, W. P., *et al.* Squeezing in the Audio Gravitational-Wave Detection Band. *Physical Review Letters* **93,** 161105. doi:`10.1103/PhysRevLett.93.161105` (Oct. 2004) (cit. on pp. 10, 11).
38. Bowen, W. P., Schnabel, R., Treps, N., Bachor, H.-A. & Lam, P. K. Recovery of continuous wave squeezing at low frequencies. *Journal of Optics B: Quantum and Semiclassical Optics* **4.** doi:`10.1088/1464-4266/4/6/309` (2022) (cit. on pp. 10, 11).
39. Shelby, R. M., Levenson, M. D., Perlmutter, S. H., DeVoe, R. G. & Walls, D. F. Broad-Band Parametric Deamplification of Quantum Noise in an Optical Fiber. *Physical Review Letters* **57.** Publisher: American Physical Society, 691–694. doi:`10.1103/PhysRevLett.57.691` (Aug. 1986) (cit. on p. 10).
40. McCormick, C. F., Boyer, V., Arimondo, E. & Lett, P. D. Strong relative intensity squeezing by four-wave mixing in rubidium vapor. *Optics Letters* **32,** 178. doi:`10.1364/OL.32.000178` (Jan. 2007) (cit. on p. 10).
41. Vahlbruch, H., Mehmet, M., Danzmann, K. & Schnabel, R. Detection of 15 dB Squeezed States of Light and their Application for the Absolute Calibration of Photoelectric Quantum Efficiency. *Physical Review Letters* **117.** Publisher: American Physical Society. doi:`10.1103/PhysRevLett.117.110801` (Sept. 2016) (cit. on p. 10).
42. Harry, G. M. & forthe LIGO Scientific Collaboration et al. Advanced LIGO: the next generation of gravitational wave detectors. *Classical and Quantum Gravity* **27.** doi:`10.1088/0264-9381/27/8/084006` (2010) (cit. on p. 11).
43. Dwyer, S. E., Mansell, G. L. & McCuller, L. Squeezing in Gravitational Wave Detectors. *Galaxies* **10,** 46. doi:`10.3390/galaxies10020046` (Mar. 2022) (cit. on p. 11).
44. Barsotti, L., Harms, J. & Schnabel, R. Squeezed vacuum states of light for gravitational wave detectors. *Reports on Progress in Physics* **82,** 016905. doi:`10.1088/1361-6633/aab906` (Jan. 2019) (cit. on p. 11).
45. Taylor, M. A. & Bowen, W. P. Quantum metrology and its application in biology. *Physics Reports. Quantum metrology and its application in biology* **615,** 1–59. doi:`10.1016/j.physrep.2015.12.002` (Feb. 2016) (cit. on p. 11).
46. Taylor, M. A., Janousek, J., Daria, V., *et al.* Biological measurement beyond the quantum limit. *Nature Photonics* **7,** 229–233. doi:`10.1038/nphoton.2012.346` (Mar. 2013) (cit. on p. 11).

47. Taylor, M. A., Janousek, J., Daria, V., *et al.* Subdiffraction-Limited Quantum Imaging within a Living Cell. *Physical Review X* **4,** 011017. doi:`10.1103/PhysRevX.4.011017` (Feb. 2014) (cit. on p. 11).
48. Cheng, J.-X. & Xie, X. S. Vibrational spectroscopic imaging of living systems: An emerging platform for biology and medicine. *Science* **350,** aaa8870–aaa8870. doi:`10.1126/science.aaa8870` (Nov. 2015) (cit. on p. 11).
49. Camp Jr, C. H. & Cicerone, M. T. Chemically sensitive bioimaging with coherent Raman scattering. *Nature Photonics* **9,** 295–305. doi:`10.1038/nphoton.2015.60` (May 2015) (cit. on p. 11).
50. Stockert, J. C. & Blázquez-Castro, A. *Fluorescence Microscopy in Life Sciences* 1st (Bentham Science Publishers, 2017) (cit. on p. 11).
51. Hanbury Brown, R. & Twiss, R. Q. A Test of a New Type of Stellar Interferometer on Sirius. *Nature* **178,** 1046–1048. doi:`10.1038/1781046a0` (Nov. 1956) (cit. on p. 11).
52. Basché, T., Moerner, W. E., Orrit, M. & Talon, H. Photon antibunching in the fluorescence of a single dye molecule trapped in a solid. *Physical Review Letters* **69,** 1516–1519. doi:`10.1103/PhysRevLett.69.1516` (Sept. 1992) (cit. on p. 11).
53. Sroda, A., Makowski, A., Tenne, R., *et al.* SOFISM: Super-resolution optical fluctuation image scanning microscopy. *Optica* **7.** Publisher: Optica Publishing Group, 1308–1316. doi:`10.1364/OPTICA.399600` (Oct. 2020) (cit. on p. 11).
54. Israel, Y., Tenne, R., Oron, D. & Silberberg, Y. Quantum correlation enhanced super-resolution localization microscopy enabled by a fibre bundle camera. *Nature Communications* **8.** Number: 1 Publisher: Nature Publishing Group, 14786. doi:`10.1038/ncomms14786` (Mar. 2017) (cit. on p. 11).
55. Reichert, M., Defienne, H. & Fleischer, J. W. Massively Parallel Coincidence Counting of High-Dimensional Entangled States. *Scientific Reports* **8,** 7925. doi:`10.1038/s41598-018-26144-7` (May 2018) (cit. on pp. 12, 13).
56. Toninelli, E., Moreau, P.-A., Gregory, T., *et al.* Resolution-enhanced quantum imaging by centroid estimation of biphotons. *Optica* **6,** 347–353. doi:`10.1364/OPTICA.6.000347` (Mar. 2019) (cit. on pp. 12, 80).
57. Giovannetti, V., Lloyd, S. & Maccone, L. Advances in quantum metrology. *Nature Photonics* **5,** 222–229. doi:`10.1038/nphoton.2011.35` (Apr. 2011) (cit. on p. 12).
58. Ono, T., Okamoto, R. & Takeuchi, S. An entanglement-enhanced microscope. *Nature Communications* **4,** 2426. doi:`10.1038/ncomms3426` (Sept. 2013) (cit. on pp. 12, 80).
59. Israel, Y., Rosen, S. & Silberberg, Y. Supersensitive Polarization Microscopy Using NOON States of Light. *Physical Review Letters* **112,** 103604. doi:`10.1103/PhysRevLett.112.103604` (Mar. 2014) (cit. on p. 12).

60. Camphausen, R., Cuevas, A., Duempelmann, L., *et al.* A quantum-enhanced wide-field phase imager. *Science Advances* **7,** eabj2155. doi:`10.1126/sciadv.abj2155` (Nov. 2021) (cit. on pp. 12, 80, 106).
61. Ndagano, B., Defienne, H., Branford, D., *et al.* Quantum microscopy based on Hong–Ou–Mandel interference. *Nature Photonics* **16,** 384–389. doi:`10.1038/s41566-022-00980-6` (May 2022) (cit. on pp. 12, 80, 106, 107).
62. Devaux, F., Mosset, A., Moreau, P.-A. & Lantz, E. Imaging Spatiotemporal Hong-Ou-Mandel Interference of Biphoton States of Extremely High Schmidt Number. *Physical Review X* **10.** Publisher: American Physical Society, 031031. doi:`10.1103/PhysRevX.10.031031` (Aug. 2020) (cit. on pp. 12, 51).
63. Hong, C. K., Ou, Z. Y. & Mandel, L. Measurement of subpicosecond time intervals between two photons by interference. *Phys. Rev. Lett.* **59,** 2044–2046. doi:`10.1103/PhysRevLett.59.2044` (Nov. 1987) (cit. on p. 12).
64. Devaux, F., Mosset, A., Bassignot, F. & Lantz, E. Quantum holography with biphotons of high Schmidt number. *Physical Review A* **99,** 033854. doi:`10.1103/PhysRevA.99.033854` (Mar. 2019) (cit. on pp. 12, 51).
65. Defienne, H., Ndagano, B., Lyons, A. & Faccio, D. Polarization entanglement-enabled quantum holography. *Nature Physics* **17,** 591–597. doi:`10.1038/s41567-020-01156-1` (May 2021) (cit. on pp. 12–14, 54, 80, 102).
66. Gabor, D. A new microscopic principle. *Nature* **161,** 777–778 (1948) (cit. on p. 12).
67. Yamaguchi, I. & Zhang, T. Phase-shifting digital holography. *Optics Letters* **22,** 1268–1270. doi:`10.1364/OL.22.001268` (Aug. 1997) (cit. on p. 12).
68. Brida, G., Cagliero, E., Falzetta, G., *et al.* Biphoton double-slit experiment. *Physical Review A* **68,** 033803. doi:`10.1103/PhysRevA.68.033803` (Sept. 2003) (cit. on pp. 13, 57).
69. Aspden, R. S., Gemmell, N. R., Morris, P. A., *et al.* Photon-sparse microscopy: visible light imaging using infrared illumination. *Optica* **2,** 1049–1052. doi:`10.1364/OPTICA.2.001049` (Dec. 2015) (cit. on pp. 13, 14).
70. Defienne, H., Reichert, M., Fleischer, J. W. & Faccio, D. Quantum image distillation. *Science Advances* **5,** eaax0307. doi:`10.1126/sciadv.aax0307` (Oct. 2019) (cit. on pp. 13, 14, 49, 54, 55, 80).
71. Lloyd, S. Enhanced Sensitivity of Photodetection via Quantum Illumination. *Science* **321,** 1463–1465. doi:`10.1126/science.1160627` (Sept. 2008) (cit. on p. 14).
72. Lopaeva, E. D., Ruo Berchera, I., Degiovanni, I. P., *et al.* Experimental Realization of Quantum Illumination. *Physical Review Letters* **110,** 153603. doi:`10.1103/PhysRevLett.110.153603` (Apr. 2013) (cit. on p. 14).

73. Gregory, T., Moreau, P.-A., Toninelli, E. & Padgett, M. J. Imaging through noise with quantum illumination. *Science Advances* **6,** eaay2652. doi:`10.1126/sciadv.aay2652` (Feb. 2020) (cit. on pp. 14, 80, 102).
74. Zhang, Y., England, D., Nomerotski, A., *et al.* Multidimensional quantum-enhanced target detection via spectrotemporal-correlation measurements. *Physical Review A* **101,** 053808. doi:`10.1103/PhysRevA.101.053808` (May 2020) (cit. on p. 14).
75. Zhao, J., Lyons, A., Ulku, A. C., *et al.* Light detection and ranging with entangled photons. *Optics Express* **30,** 3675–3683. doi:`10.1364/OE.435898` (Jan. 2022) (cit. on p. 14).
76. Liu, H., Qin, C., Papangelakis, G., Iu, M. L. & Helmy, A. S. Compact all-fiber quantum-inspired LiDAR with over 100 dB noise rejection and single photon sensitivity. *Nature Communications* **14.** Number: 1 Publisher: Nature Publishing Group, 5344. doi:`10.1038/s41467-023-40914-6` (Sept. 2023) (cit. on p. 14).
77. Johnson, S., McMillan, A., Frick, S., Rarity, J. & Padgett, M. Hiding images in noise. *Optics Express* **31.** Publisher: Optica Publishing Group, 5290–5296. doi:`10.1364/OE.480881` (Feb. 2023) (cit. on p. 14).
78. Zhang, Y., England, D. & Sussman, B. Snapshot hyperspectral imaging with quantum correlated photons. *Optics Express* **31,** 2282–2291. doi:`10.1364/OE.462587` (Jan. 2023) (cit. on p. 14).
79. Hodgson, H., Zhang, Y., England, D. & Sussman, B. Reconfigurable phase contrast microscopy with correlated photon pairs. *Applied Physics Letters* **122.** arXiv:2212.10918 [physics, physics:quant-ph], 034001. doi:`10.1063/5.0133980` (Jan. 2023) (cit. on pp. 14, 80, 106).
80. Bornman, N., Agnew, M., Zhu, F., *et al.* Ghost imaging using entanglement-swapped photons. *npj Quantum Information* **5,** 1–6. doi:`10.1038/s41534-019-0176-5` (July 2019) (cit. on p. 14).
81. Schneeloch, J., Knarr, S. H., Bogorin, D. F., *et al.* Introduction to the absolute brightness and number statistics in spontaneous parametric down-conversion. *Journal of Optics* **21,** 043501. doi:`10.1088/2040-8986/ab05a8` (Feb. 2019) (cit. on pp. 15, 22).
82. Gustafsson, M. G. L. Surpassing the lateral resolution limit by a factor of two using structured illumination microscopy. *Journal of Microscopy* **198,** 82–87. doi:`https://doi.org/10.1046/j.1365-2818.2000.00710.x` (2000) (cit. on pp. 15, 58).
83. Booth, M. J. Adaptive optical microscopy: the ongoing quest for a perfect image. *Light: Science & Applications* **3,** e165–e165. doi:`10.1038/lsa.2014.46` (Apr. 2014) (cit. on pp. 15, 58).
84. Gigan, S., Katz, O., Aguiar, H. B. d., *et al.* Roadmap on wavefront shaping and deep imaging in complex media. *Journal of Physics: Photonics* **4,** 042501. doi:`10.1088/2515-7647/ac76f9` (Aug. 2022) (cit. on p. 15).

85. Popoff, S. M., Lerosey, G., Fink, M., Boccara, A. C. & Gigan, S. Controlling light through optical disordered media: transmission matrix approach. *New Journal of Physics* **13.** doi:`10.1088/1367-2630/13/12/123021` (Dec. 2011) (cit. on pp. 15, 114).
86. Vellekoop, I. M. & Mosk, A. P. Focusing coherent light through opaque strongly scattering media. *Optics Letters* **32,** 2309. doi:`10.1364/OL.32.002309` (Aug. 2007) (cit. on pp. 15, 74, 105, 114).
87. Plöschner, M., Tyc, T. & Čižmár, T. Seeing through chaos in multimode fibres. *Nature Photonics* **9,** 529. doi:`10.1038/nphoton.2015.112` (Aug. 2015) (cit. on p. 15).
88. Forbes, A., de Oliveira, M. & Dennis, M. R. Structured light. *Nature Photonics* **15.** Number: 4 Publisher: Nature Publishing Group, 253–262. doi:`10.1038/s41566-021-00780-4` (Apr. 2021) (cit. on p. 15).
89. Trichili, A., Park, K.-H., Zghal, M., Ooi, B. S. & Alouini, M.-S. Communicating Using Spatial Mode Multiplexing: Potentials, Challenges, and Perspectives. *IEEE Communications Surveys & Tutorials* **21.** Conference Name: IEEE Communications Surveys & Tutorials, 3175–3203. doi:`10.1109/COMST.2019.2915981` (2019) (cit. on p. 15).
90. Allen, L., Beijersbergen, M. W., Spreeuw, R. J. C. & Woerdman, J. P. Orbital angular momentum of light and the transformation of Laguerre-Gaussian laser modes. *Physical Review A* **45.** Publisher: American Physical Society, 8185–8189. doi:`10.1103/PhysRevA.45.8185` (June 1992) (cit. on p. 16).
91. Beijersbergen, M. W., Coerwinkel, R. P. C., Kristensen, M. & Woerdman, J. P. Helical-wavefront laser beams produced with a spiral phaseplate. *Optics Communications* **112,** 321–327. doi:`10.1016/0030-4018(94)90638-6` (Dec. 1994) (cit. on p. 16).
92. Massari, M., Ruffato, G., Gintoli, M., Ricci, F. & Romanato, F. Fabrication and characterization of high-quality spiral phase plates for optical applications. *Applied Optics* **54.** Publisher: Optica Publishing Group, 4077–4083. doi:`10.1364/AO.54.004077` (May 2015) (cit. on p. 16).
93. Heckenberg, N. R., McDuff, R., Smith, C. P. & White, A. G. Generation of optical phase singularities by computer-generated holograms. *Optics Letters* **17.** Publisher: Optica Publishing Group, 221–223. doi:`10.1364/OL.17.000221` (Feb. 1992) (cit. on p. 16).
94. Ohtake, Y., Ando, T., Fukuchi, N., *et al.* Universal generation of higher-order multiringed Laguerre-Gaussian beams by using a spatial light modulator. *Optics Letters* **32.** Publisher: Optica Publishing Group, 1411–1413. doi:`10.1364/OL.32.001411` (June 2007) (cit. on p. 16).
95. He, H., Friese, M. E. J., Heckenberg, N. R. & Rubinsztein-Dunlop, H. Direct Observation of Transfer of Angular Momentum to Absorptive Particles from a Laser Beam with a Phase Singularity. *Physical Review Letters* **75.** Publisher: American Physical Society, 826–829. doi:`10.1103/PhysRevLett.75.826` (July 1995) (cit. on p. 16).

96. O'Neil, A. T., MacVicar, I., Allen, L. & Padgett, M. J. Intrinsic and Extrinsic Nature of the Orbital Angular Momentum of a Light Beam. *Physical Review Letters* **88.** Publisher: American Physical Society, 053601. doi:`10.1103/PhysRevLett.88.053601` (Jan. 2002) (cit. on p. 16).
97. Nape, I., Sephton, B., Ornelas, P., Moodley, C. & Forbes, A. Quantum structured light in high dimensions. *APL Photonics* **8,** 051101. doi:`10.1063/5.0138224` (May 2023) (cit. on p. 16).
98. Mair, A., Vaziri, A., Weihs, G. & Zeilinger, A. Entanglement of the orbital angular momentum states of photons. *Nature* **412,** 313–316. doi:`10.1038/35085529` (July 2001) (cit. on p. 16).
99. Wootters, W. K. & Zurek, W. H. The no-cloning theorem. *Physics Today* **62,** 76–77. doi:`10.1063/1.3086114` (Feb. 2009) (cit. on p. 16).
100. Mafu, M., Dudley, A., Goyal, S., *et al.* Higher-dimensional orbital-angular-momentum-based quantum key distribution with mutually unbiased bases. *Physical Review A* **88,** 032305. doi:`10.1103/PhysRevA.88.032305` (Sept. 2013) (cit. on p. 16).
101. Mirhosseini, M., Magaña-Loaiza, O. S., O'Sullivan, M. N., *et al.* High-dimensional quantum cryptography with twisted light. *New Journal of Physics* **17.** Publisher: IOP Publishing, 033033. doi:`10.1088/1367-2630/17/3/033033` (Mar. 2015) (cit. on pp. 16, 71).
102. Sit, A., Bouchard, F., Fickler, R., *et al.* High-dimensional intracity quantum cryptography with structured photons. *Optica* **4,** 1006–1010. doi:`10.1364/OPTICA.4.001006` (Sept. 2017) (cit. on p. 16).
103. Nape, I., Otte, E., Vallés, A., *et al.* Self-healing high-dimensional quantum key distribution using hybrid spin-orbit Bessel states. *Optics Express* **26.** Publisher: Optica Publishing Group, 26946–26960. doi:`10.1364/OE.26.026946` (Oct. 2018) (cit. on p. 16).
104. Bonato, C., Sergienko, A. V., Saleh, B. E. A., Bonora, S. & Villoresi, P. Even-Order Aberration Cancellation in Quantum Interferometry. *Physical Review Letters* **101,** 233603. doi:`10.1103/PhysRevLett.101.233603` (Dec. 2008) (cit. on pp. 17, 18, 106).
105. Simon, D. S. & Sergienko, A. V. Spatial-dispersion cancellation in quantum interferometry. *Physical Review A* **80.** Publisher: American Physical Society, 053813. doi:`10.1103/PhysRevA.80.053813` (Nov. 2009) (cit. on pp. 18, 106).
106. Simon, D. S. & Sergienko, A. V. Correlated-photon imaging with cancellation of object-induced aberration. *JOSA B* **28.** Publisher: Optica Publishing Group, 247–252. doi:`10.1364/JOSAB.28.000247` (Feb. 2011) (cit. on pp. 18, 106).
107. Filpi, L. A. P., Pereira, M. V. d. C. & Monken, C. H. Experimental observation of aberration cancellation in entangled two-photon beams. *Optics Express* **23,** 3841–3850. doi:`10.1364/OE.23.003841` (Feb. 2015) (cit. on pp. 18, 106).

108. Cao, Y., Li, Y.-H., Yang, K.-X., *et al.* Long-Distance Free-Space Measurement-Device-Independent Quantum Key Distribution. *Physical Review Letters* **125,** 260503. doi:`10.1103/PhysRevLett.125.260503` (Dec. 2020) (cit. on p. 18).
109. Popoff, S. M., Lerosey, G., Carminati, R., *et al.* Measuring the Transmission Matrix in Optics: An Approach to the Study and Control of Light Propagation in Disordered Media. *Physical Review Letters* **104,** 100601. doi:`10.1103/PhysRevLett.104.100601` (Mar. 2010) (cit. on pp. 18, 74).
110. Defienne, H., Reichert, M. & Fleischer, J. W. Adaptive Quantum Optics with Spatially Entangled Photon Pairs. *Physical Review Letters* **121,** 233601. doi:`10.1103/PhysRevLett.121.233601` (Dec. 2018) (cit. on pp. 18, 105).
111. Valencia, N. H., Goel, S., McCutcheon, W., Defienne, H. & Malik, M. Unscrambling entanglement through a complex medium. *Nature Physics* **16,** 1112–1116. doi:`10.1038/s41567-020-0970-1` (Nov. 2020) (cit. on p. 18).
112. Black, A. N., Giese, E., Braverman, B., *et al.* Quantum Nonlocal Aberration Cancellation. *Physical Review Letters* **123,** 143603. doi:`10.1103/PhysRevLett.123.143603` (Sept. 2019) (cit. on pp. 18, 106).
113. Lib, O., Hasson, G. & Bromberg, Y. Real-time shaping of entangled photons by classical control and feedback. *Science Advances* **6,** eabb6298. doi:`10.1126/sciadv.abb6298` (Sept. 2020) (cit. on pp. 19, 105).
114. Weiss, U. & Katz, O. Two-photon lensless micro-endoscopy with in-situ wavefront correction. *Optics Express* **26.** Publisher: Optica Publishing Group, 28808–28817. doi:`10.1364/OE.26.028808` (Oct. 2018) (cit. on p. 19).
115. Couteau, C. Spontaneous parametric down-conversion. *Contemporary Physics* **59.** Publisher: Taylor & Francis _eprint: https://doi.org/10.1080/00107514.2018.1488463, 291–304. doi:`10.1080/00107514.2018.1488463` (July 2018) (cit. on pp. 20, 22, 23).
116. Boyd, R. W. *Nonlinear Optics* Third (Acadmic Press, 2008) (cit. on pp. 20, 21).
117. Loudon, R. *The Quantum Theory of Light* (OUP Oxford, Sept. 2000) (cit. on p. 21).
118. James Schneeloch, J. C. H. Introduction to the Transverse Spatial Correlations in Spontaneous Parametric Down-Conversion through the Biphoton Birth Zone. *Journal of Optics* **18,** 053501. doi:`10.1088/2040-8978/18/5/053501` (Apr. 2016) (cit. on pp. 24, 25, 84).
119. Fedorov, M. V., Mikhailova, Y. M. & Volkov, P. A. Gaussian modeling and Schmidt modes of SPDS biphoton states. *Journal of Physics B: Atomic, Molecular and Optical Physics* **42,** 175503. doi:`10.1088/0953-4075/42/17/175503` (Sept. 2009) (cit. on p. 25).
120. Coates, C. & Mullan, A. *What is an EMCCD Camera?* Oxford Instruments Andor website, URL: https://andor.oxinst.com/learning/view/article/electron-multiplying-ccd-cameras (cit. on p. 25).

121. Defienne, H., Reichert, M. & Fleischer, J. W. General model of photon-pair detection with an image sensor. *Physical Review Letters* **120,** 203604. doi:`10.1103/PhysRevLett.120.203604` (May 2018) (cit. on pp. 26, 27, 29, 30, 41, 60, 61, 92, 117).
122. Madonini, F., Severini, F., Zappa, F. & Villa, F. Single Photon Avalanche Diode Arrays for Quantum Imaging and Microscopy. *Advanced Quantum Technologies* **4,** 2100005. doi:`10.1002/qute.202100005` (2021) (cit. on pp. 27, 28).
123. Madonini, F., Cusini, I., Severini, F. & Villa, F. *Event-Driven SPAD Array for Quantum-Enhanced Imaging* in *Conference on Lasers and Electro-Optics (2022), paper FM4C.4* (Optica Publishing Group, May 2022), FM4C.4. doi:`10.1364/CLEO_QELS.2022.FM4C.4` (cit. on p. 28).
124. Global, C. *Canon Successfully Develops Key Devices for Future Society - SPAD Sensor* Technology Highlight Article. Oct. 2023 (cit. on p. 28).
125. Chrapkiewicz, R., Wasilewski, W. & Banaszek, K. High-fidelity spatially resolved multiphoton counting for quantum imaging applications. *Optics Letters* **39,** 5090–5093. doi:`10.1364/OL.39.005090` (Sept. 2014) (cit. on p. 28).
126. Wolley, O., Gregory, T., Beer, S., Higuchi, T. & Padgett, M. Quantum imaging with a photon counting camera. *Scientific Reports* **12.** Number: 1 Publisher: Nature Publishing Group, 8286. doi:`10.1038/s41598-022-10037-x` (May 2022) (cit. on p. 28).
127. Zhang, Y., Orth, A., England, D. & Sussman, B. Ray tracing with quantum correlated photons to image a three-dimensional scene. *Physical Review A* **105,** L011701. doi:`10.1103/PhysRevA.105.L011701` (Jan. 2022) (cit. on pp. 29, 80, 100, 105).
128. Courme, B., Vernière, C., Svihra, P., *et al.* Quantifying high-dimensional spatial entanglement with a single-photon-sensitive time-stamping camera. *Optics Letters* **48,** 3439–3442. doi:`10.1364/OL.487182` (July 2023) (cit. on pp. 29, 105).
129. Hadfield, R. H. Superfast photon counting. *Nature Photonics* **14,** 201–202. doi:`10.1038/s41566-020-0614-0` (Apr. 2020) (cit. on p. 29).
130. Esmaeil Zadeh, I., Chang, J., Los, J. W. N., *et al.* Superconducting nanowire single-photon detectors: A perspective on evolution, state-of-the-art, future developments, and applications. *Applied Physics Letters* **118,** 190502. doi:`10.1063/5.0045990` (May 2021) (cit. on p. 29).
131. Oripov, B. G., Rampini, D. S., Allmaras, J., *et al.* A superconducting nanowire single-photon camera with 400,000 pixels. *Nature* **622.** Number: 7984 Publisher: Nature Publishing Group, 730–734. doi:`10.1038/s41586-023-06550-2` (Oct. 2023) (cit. on p. 29).
132. Hadfield, R. H. Single-photon detectors for optical quantum information applications. *Nature Photonics* **3,** 696–705. doi:`10.1038/nphoton.2009.230` (Dec. 2009) (cit. on p. 29).

133. Reichert, M., Defienne, H. & Fleischer, J. W. Optimizing the signal-to-noise ratio of biphoton distribution measurements. *Physical Review A* **98,** 013841. doi:`10.1103/PhysRevA.98.013841` (July 2018) (cit. on pp. 39, 41).
134. Goodman, J. W. *Introduction to Fourier Optics* (Roberts and Company Publishers, 2005) (cit. on p. 42).
135. Toninelli, E. *Quantum-enhanced imaging and sensing with spatially correlated biphotons* PhD Thesis (University of Glasgow, 2020) (cit. on p. 49).
136. Voelz, D. G. *Computational Fourier Optics: A MATLAB® Tutorial* doi:`10.1117/3.858456` (SPIE, 1000 20th Street, Bellingham, WA 98227-0010 USA, Jan. 2011) (cit. on p. 51).
137. ISO Central Secretary. *Photography — Electronic still picture imaging — Resolution and spatial frequency responses* Standard ISO 12233:2014(E) (International Organization for Standardization, Geneva, CH, 2014) (cit. on p. 53).
138. Masaoka, K., Yamashita, T., Nishida, Y. & Sugawara, M. Modified slanted-edge method and multidirectional modulation transfer function estimation. *Optics Express* **22,** 6040. doi:`10.1364/OE.22.006040` (Mar. 2014) (cit. on p. 53).
139. Brida, G., Cavanna, A., Degiovanni, I. P., Genovese, M. & Traina, P. Experimental realization of counterfactual quantum cryptography. *Laser Physics Letters* **9,** 247–252. doi:`https://doi.org/10.1002/lapl.201110120` (2012) (cit. on p. 57).
140. Maurer, C., Jesacher, A., Bernet, S. & Ritsch-Marte, M. What spatial light modulators can do for optical microscopy. *Laser & Photonics Reviews* **5,** 81–101. doi:`10.1002/lpor.200900047` (2011) (cit. on p. 58).
141. Yoon, S., Kim, M., Jang, M., *et al.* Deep optical imaging within complex scattering media. *Nature Reviews Physics* **2,** 141–158. doi:`10.1038/s42254-019-0143-2` (Mar. 2020) (cit. on p. 58).
142. Zernike, F. & Stratton, F. Diffraction Theory of the Knife-Edge Test and its Improved Form, The Phase-Contrast Method. *Monthly Notices of the Royal Astronomical Society* **94,** 377–384. doi:`10.1093/mnras/94.5.377` (Mar. 1934) (cit. on p. 58).
143. Bernet, S., Jesacher, A., Fürhapter, S., Maurer, C. & Ritsch-Marte, M. Quantitative imaging of complex samples by spiral phase contrast microscopy. *Optics Express* **14.** Publisher: Optica Publishing Group, 3792–3805. doi:`10.1364/OE.14.003792` (May 2006) (cit. on p. 58).
144. Glauber, R. J. The Quantum Theory of Optical Coherence. *Physical Review* **130.** Publisher: American Physical Society, 2529–2539. doi:`10.1103/PhysRev.130.2529` (June 1963) (cit. on pp. 61, 62).
145. Siegert, A. J. F. & Massachusetts Institute of Technology Radiation Laboratory. *On the fluctuations in signals returned by many independently moving scatterers* (Radiation Laboratory, Massachusetts Institute of Technology [Cambridge, Mass.], 1943) (cit. on p. 64).

146. Abouraddy, A. F., Saleh, B. E. A., Sergienko, A. V. & Teich, M. C. Entangled-photon Fourier optics. *Journal of the Optical Society of America B* **19,** 1174. doi:`10.1364/JOSAB.19.001174` (May 2002) (cit. on pp. 65, 84).
147. Saleh, B. E. A., Abouraddy, A. F., Sergienko, A. V. & Teich, M. C. Duality between partial coherence and partial entanglement. *Physical Review A* **62,** 043816. doi:`10.1103/PhysRevA.62.043816` (Sept. 2000) (cit. on p. 65).
148. Gisin, N. & Thew, R. Quantum communication. *Nature Photonics,* 165–171. doi:`https://doi.org/10.1038/nphoton.2007.22` (2007) (cit. on p. 71).
149. Fedorov, M. V., Efremov, M. A., Volkov, P. A., *et al.* Anisotropically and High Entanglement of Biphoton States Generated in Spontaneous Parametric Down-Conversion. *Physical Review Letters* **99,** 063901. doi:`10.1103/PhysRevLett.99.063901` (Aug. 2007) (cit. on p. 71).
150. Ecker, S., Bouchard, F., Bulla, L., *et al.* Overcoming Noise in Entanglement Distribution. *Physical Review X* **9.** Publisher: American Physical Society, 041042. doi:`10.1103/PhysRevX.9.041042` (Nov. 2019) (cit. on p. 71).
151. Acín, A., Brunner, N., Gisin, N., *et al.* Device-Independent Security of Quantum Cryptography against Collective Attacks. *Physical Review Letters* **98,** 230501. doi:`10.1103/PhysRevLett.98.230501` (June 2007) (cit. on p. 71).
152. Giovannetti, V., Mancini, S., Vitali, D. & Tombesi, P. Characterizing the entanglement of bipartite quantum systems. *Physical Review A* **67,** 022320. doi:`10.1103/PhysRevA.67.022320` (Feb. 2003) (cit. on p. 73).
153. Helmchen, F. & Denk, W. Deep tissue two-photon microscopy. *Nature Methods* **2,** 932–940. doi:`10.1038/nmeth818` (Dec. 2005) (cit. on p. 76).
154. LaFratta, C. N., Fourkas, J. T., Baldacchini, T. & Farrer, R. A. Multiphoton Fabrication. *Angewandte Chemie International Edition* **46,** 6238–6258. doi:`10.1002/anie.200603995` (2007) (cit. on p. 76).
155. Qin, Y., Schnedermann, C., Tasior, M., Gryko, D. T. & Nocera, D. G. Direct Observation of Different One- and Two-Photon Fluorescent States in a Pyrrolo[3,2-b]pyrrole Fluorophore. *The Journal of Physical Chemistry Letters* **11.** Publisher: American Chemical Society, 4866–4872. doi:`10.1021/acs.jpclett.0c00669` (June 2020) (cit. on p. 76).
156. Javanainen, J. & Gould, P. L. Linear intensity dependence of a two-photon transition rate. *Physical Review A* **41.** Publisher: American Physical Society, 5088–5091. doi:`10.1103/PhysRevA.41.5088` (May 1990) (cit. on p. 76).
157. Dorfman, K. E., Schlawin, F. & Mukamel, S. Nonlinear optical signals and spectroscopy with quantum light. *Reviews of Modern Physics* **88.** Publisher: American Physical Society, 045008. doi:`10.1103/RevModPhys.88.045008` (Dec. 2016) (cit. on p. 76).

158. Schlawin, F., Dorfman, K. E. & Mukamel, S. Entangled Two-Photon Absorption Spectroscopy. *Accounts of Chemical Research* **51.** Publisher: American Chemical Society, 2207–2214. doi:`10.1021/acs.accounts.8b00173` (Sept. 2018) (cit. on p. 76).
159. Varnavski, O., Pinsky, B. & Goodson, T. I. Entangled Photon Excited Fluorescence in Organic Materials: An Ultrafast Coincidence Detector. *The Journal of Physical Chemistry Letters* **8.** Publisher: American Chemical Society, 388–393. doi:`10.1021/acs.jpclett.6b02378` (Jan. 2017) (cit. on p. 76).
160. Villabona-Monsalve, J. P., Varnavski, O., Palfey, B. A. & Goodson, T. Two-Photon Excitation of Flavins and Flavoproteins with Classical and Quantum Light. *Journal of the American Chemical Society* **140,** 14562–14566. doi:`10.1021/jacs.8b08515` (Nov. 2018) (cit. on p. 76).
161. Tabakaev, D., Montagnese, M., Haack, G., *et al.* Energy-time-entangled two-photon molecular absorption. *Physical Review A* **103.** Publisher: American Physical Society, 033701. doi:`10.1103/PhysRevA.103.033701` (Mar. 2021) (cit. on p. 76).
162. Landes, T., Allgaier, M., Merkouche, S., *et al.* Experimental feasibility of molecular two-photon absorption with isolated time-frequency-entangled photon pairs. *Physical Review Research* **3.** Publisher: American Physical Society, 033154. doi:`10.1103/PhysRevResearch.3.033154` (Aug. 2021) (cit. on p. 76).
163. Raymer, M. G., Landes, T., Allgaier, M., *et al.* How large is the quantum enhancement of two-photon absorption by time-frequency entanglement of photon pairs? *Optica* **8.** Publisher: Optica Publishing Group, 757–758. doi:`10.1364/OPTICA.426674` (May 2021) (cit. on p. 76).
164. Born, M. & Wolf, E. *Principles of Optics* 7th (Cambridge University Press, 1999) (cit. on p. 79).
165. He, Z., Zhang, Y., Tong, X., Li, L. & Wang, L. V. Quantum microscopy of cells at the Heisenberg limit. *Nature Communications* **14,** 2441. doi:`10.1038/s41467-023-38191-4` (Apr. 2023) (cit. on pp. 80, 102).
166. Black, A. N., Nguyen, L. D., Braverman, B., *et al.* Quantum-enhanced phase imaging without coincidence counting. *Optica* **10,** 952–958. doi:`10.1364/OPTICA.482926` (July 2023) (cit. on pp. 80, 106).
167. Töpfer, S., Gilaberte Basset, M., Fuenzalida, J., *et al.* Quantum holography with undetected light. *Science Advances* **8,** eabl4301. doi:`10.1126/sciadv.abl4301` (Jan. 2022) (cit. on p. 80).
168. Nasr, M. B., Saleh, B. E. A., Sergienko, A. V. & Teich, M. C. Demonstration of Dispersion-Canceled Quantum-Optical Coherence Tomography. *Physical Review Letters* **91,** 083601. doi:`10.1103/PhysRevLett.91.083601` (Aug. 2003) (cit. on pp. 80, 106).

169. Abouraddy, A. F., Nasr, M. B., Saleh, B. E. A., Sergienko, A. V. & Teich, M. C. Quantum-optical coherence tomography with dispersion cancellation. *Physical Review A* **65,** 053817. doi:`10.1103/PhysRevA.65.053817` (May 2002) (cit. on pp. 80, 106).
170. Duffner, R. W. *The Adaptive Optics Revolution: A History* First (University of New Mexico Press, 2009) (cit. on p. 80).
171. Ji, N. Adaptive optical fluorescence microscopy. *Nature Methods* **14,** 374–380. doi:`10.1038/nmeth.4218` (Apr. 2017) (cit. on p. 81).
172. Zhang, Q., Hu, Q., Berlage, C., *et al.* Adaptive optics for optical microscopy [Invited]. *Biomedical Optics Express* **14,** 1732–1756. doi:`10.1364/BOE.479886` (Apr. 2023) (cit. on pp. 81, 113).
173. Hampson, K. M., Antonello, J., Lane, R. & Booth, M. Sensorless Adaptive Optics. *Technical note: DOI 10.5281/zenodo.4065529.* doi:`10.5281/zenodo.4066425` (Oct. 2020) (cit. on p. 81).
174. Booth, M. J. Wave front sensor-less adaptive optics: a model-based approach using sphere packings. *Optics Express* **14.** Publisher: Optica Publishing Group, 1339–1352. doi:`10.1364/OE.14.001339` (Feb. 2006) (cit. on pp. 81, 95).
175. Débarre, D., Botcherby, E. J., Watanabe, T., *et al.* Image-based adaptive optics for two-photon microscopy. *Optics letters* **34,** 2495–2497 (Aug. 2009) (cit. on pp. 81, 99).
176. Zhou, X., Bedggood, P., Bui, B., *et al.* Contrast-based sensorless adaptive optics for retinal imaging. *Biomedical Optics Express* **6,** 3577–3595. doi:`10.1364/BOE.6.003577` (Sept. 2015) (cit. on pp. 81, 99).
177. Debarre, D., Booth, M. J. & Wilson, T. Image based adaptive optics through optimisation of low spatial frequencies. *Optics Express* **15,** 8176. doi:`10.1364/OE.15.008176` (2007) (cit. on pp. 81, 99).
178. Fienup, J. R. & Miller, J. J. Aberration correction by maximizing generalized sharpness metrics. *JOSA A* **20.** Publisher: Optica Publishing Group, 609–620. doi:`10.1364/JOSAA.20.000609` (Apr. 2003) (cit. on p. 81).
179. Murray, L. P., Dainty, J. C. & Daly, E. *Wavefront correction through image sharpness maximisation* in *Opto-Ireland 2005: Imaging and Vision* **5823** (SPIE, June 2005), 40–47. doi:`10.1117/12.605161` (cit. on p. 81).
180. Shu, Y., Sun, J., Lyu, J., *et al.* Adaptive optical quantitative phase imaging based on annular illumination Fourier ptychographic microscopy. *PhotoniX* **3,** 24. doi:`10.1186/s43074-022-00071-3` (Oct. 2022) (cit. on p. 81).
181. Kam, Z., Hanser, B., Gustafsson, M. G. L., Agard, D. A. & Sedat, J. W. Computational adaptive optics for live three-dimensional biological imaging. *Proceedings of the National Academy of Sciences* **98,** 3790–3795. doi:`10.1073/pnas.071275698` (Mar. 2001) (cit. on p. 81).

182. Jian, Y., Xu, J., Gradowski, M. A., *et al.* Wavefront sensorless adaptive optics optical coherence tomography for in vivo retinal imaging in mice. *Biomedical Optics Express* **5,** 547–559. doi:`10.1364/BOE.5.000547` (Feb. 2014) (cit. on p. 81).
183. Walborn, S. P., Monken, C. H., Pádua, S. & Souto Ribeiro, P. H. Spatial correlations in parametric down-conversion. *Physics Reports* **495,** 87–139. doi:`10.1016/j.physrep.2010.06.003` (Oct. 2010) (cit. on p. 83).
184. Booth, M. J. Adaptive optics in microscopy. *Philosophical Transactions of the Royal Society A: Mathematical, Physical and Engineering Sciences* **365,** 2829–2843. doi:`10.1098/rsta.2007.0013` (Dec. 2007) (cit. on p. 93).
185. Booth, M. J. Wavefront sensorless adaptive optics for large aberrations. *Optics Letters* **32,** 5. doi:`10.1364/OL.32.000005` (Jan. 2007) (cit. on p. 95).
186. Wang, Z., Bovik, A., Sheikh, H. & Simoncelli, E. Image Quality Assessment: From Error Visibility to Structural Similarity. *IEEE Transactions on Image Processing* **13,** 600–612. doi:`10.1109/TIP.2003.819861` (Apr. 2004) (cit. on p. 97).
187. Xiao, P., Fink, M. & Boccara, A. C. Adaptive optics full-field optical coherence tomography. *Journal of Biomedical Optics* **21.** Publisher: SPIE, 121505. doi:`10.1117/1.JBO.21.12.121505` (Sept. 2016) (cit. on p. 105).
188. Mertz, J., Paudel, H. & Bifano, T. G. Field of view advantage of conjugate adaptive optics in microscopy applications. *Applied Optics* **54,** 3498–3506. doi:`10.1364/AO.54.003498` (Apr. 2015) (cit. on p. 105).
189. Simmonds, R. D. & Booth, M. J. Modelling of multi-conjugate adaptive optics for spatially variant aberrations in microscopy. *Journal of Optics* **15.** Publisher: IOP Publishing, 094010. doi:`10.1088/2040-8978/15/9/094010` (Sept. 2013) (cit. on p. 105).
190. Frenkel, N., Scharf, E., Lubin, G., *et al.* Two Biexciton Types Coexisting in Coupled Quantum Dot Molecules. *ACS Nano* **17,** 14990–15000. doi:`10.1021/acsnano.3c03921` (Aug. 2023) (cit. on p. 105).
191. Ndagano, B., Defienne, H., Lyons, A., *et al.* Imaging and certifying high-dimensional entanglement with a single-photon avalanche diode camera. *npj Quantum Information* **6.** Number: 1 Publisher: Nature Publishing Group, 1–8. doi:`10.1038/s41534-020-00324-8` (Dec. 2020) (cit. on p. 105).
192. Camphausen, R., Perna, A. S., Cuevas, A., *et al.* Fast quantum-enhanced imaging with visible-wavelength entangled photons. *Optics Express* **31,** 6039–6050. doi:`10.1364/OE.471429` (Feb. 2023) (cit. on p. 105).
193. Nomerotski, A., Chekhlov, M., Dolzhenko, D., *et al.* Intensified Tpx3Cam, a fast data-driven optical camera with nanosecond timing resolution for single photon detection in quantum applications. *Journal of Instrumentation* **18,** C01023. doi:`10.1088/1748-0221/18/01/C01023` (Jan. 2023) (cit. on p. 105).

194. Vidyapin, V., Zhang, Y., England, D. & Sussman, B. Characterisation of a single photon event camera for quantum imaging. *Scientific Reports* **13,** 1009. doi:`10.1038/s41598-023-27842-7` (Jan. 2023) (cit. on p. 105).

195. Hu, Q., Wang, J., Antonello, J., *et al.* A universal framework for microscope sensorless adaptive optics: Generalized aberration representations. *APL Photonics* **5,** 100801. doi:`10.1063/5.0022523` (Oct. 2020) (cit. on p. 105).

196. Yeminy, T. & Katz, O. Guidestar-free image-guided wavefront shaping. *Science Advances* **7,** eabf5364. doi:`10.1126/sciadv.abf5364` (May 2021) (cit. on p. 105).

197. Vorontsov, M. A., Carhart, G. W. & Ricklin, J. C. Adaptive phase-distortion correction based on parallel gradient-descent optimization. *Optics Letters* **22,** 907–909. doi:`10.1364/OL.22.000907` (June 1997) (cit. on p. 113).

198. Conkey, D. B., Brown, A. N., Caravaca-Aguirre, A. M. & Piestun, R. Genetic algorithm optimization for focusing through turbid media in noisy environments. *Optics Express* **20,** 4840. doi:`10.1364/OE.20.004840` (Feb. 2012) (cit. on p. 113).

199. Guo, Y., Zhong, L., Min, L., *et al.* Adaptive optics based on machine learning: a review. *Opto-Electronic Advances* **5,** 200082–200082. doi:`10.29026/oea.2022.200082` (2022) (cit. on p. 113).

200. *See repository http://dx.doi.org/10.5525/gla.researchdata.1576 for example code and accompanying data.* doi:`10.5525/gla.researchdata.1576` (cit. on p. 121).